Strange dibaryon system produced in the $d(\pi^+, K^+)$ reaction at J-PARC

A dissertation

by

Yudai Ichikawa

Submitted to
Department of Physics, Kyoto University
in partial fulfillment of the requirements
for the Degree of Doctor of Science

February, 2015

Abstract

The strange dibaryon systems (strangeness $S = -1$ and baryon number $B = 2$) such as a $\bar{K}NN$ system, in which a bound state of K^-pp is expected to exist, are experimentally not well explored, yet. We have searched for a strange dibaryon systems by using the $\pi^+ d \to K^+ X$ reaction at 1.69 GeV/c in the laboratory angles between 2° and 16°. We achieved the missing-mass resolution of 2.7 MeV/c^2 (FWHM). This experiment was carried out at the K1.8 beam line of the J-PARC hadron experimental facility. The K1.8 beam line spectrometer and the SKS spectrometer were used with a good momentum resolution of $\Delta p/p \sim 10^{-3}$ to measure π^+ and K^+ momenta.

In this reaction, $\Lambda(1405)$ hyperon resonance is expected to be produced as a doorway to form the K^-pp through the $\Lambda^* p \to K^-pp$ process. However, most of the produced $\Lambda(1405)$'s would escape from deuterons without secondary reactions. Therefore, coincidence of high-momentum (> 250 MeV/c) proton(s) in large emission angles ($39° < \theta_{lab.} < 122°$) is requested to enhance the signal-to-background ratio. It is because such proton(s) can be produced from the K^-pp but not from the quasi-free hyperon production (background).

We have measured the inclusive missing-mass spectrum at this beam energy in high statistics and high energy resolution for the first time. The present data covers with a wide missing-mass range from the Λ mass threshold to the $\Lambda(1405)/\Sigma(1385)$ region. While a gross structure is well understood with a simple quasi-free picture based on the known elementary processes, we have observed two distinct deviations; one peculiar enhancement at 2.13 GeV/c^2 is due to the ΣN cusp, and the other notable feature is a "shift" of a broad bump structure, mainly originating from hyperon resonance productions of $\Lambda(1405)$ and $\Sigma(1385)^{+/0}$.

We have measured a mass distribution of a "K^-pp"-like structure in the $\pi^+ d \to K^+$"K^-pp", "K^-pp"$\to \Sigma^0 p$ mode in a two-proton coincidence analysis, for the first time. By fitting the mass distribution with a relativistic Breit Wigner function, the mass and width have been evaluated to be 2275 $^{+17}_{-18}$ (stat.) $^{+21}_{-30}$ (syst.) MeV/c^2 and 162 $^{+87}_{-45}$ (stat.) $^{+66}_{-78}$ (syst.) MeV, respectively. It corresponds to the K^-pp binding energy of 95 $^{+18}_{-17}$ (stat.) $^{+30}_{-21}$ (syst.) MeV.

Contents

1 Introduction **1**
- 1.1 $\bar{K}N$ interaction . . . 2
- 1.2 $\Lambda(1405)$ . . . 5
- 1.3 $\bar{K}$-nucleus interaction . . . 7
- 1.4 Kaonic nuclei: Experiments and Theory . . . 9
  - 1.4.1 Past experiments of the K^-pp . . . 10
  - 1.4.2 Current situation of the K^-pp . . . 17
  - 1.4.3 Theoretical studies of the K^-pp . . . 19
- 1.5 J-PARC E27 experiment . . . 20
- 1.6 Thesis composition . . . 21

2 Experiment **22**
- 2.1 Outline . . . 22
- 2.2 J-PARC and hadron experimental facility . . . 22
- 2.3 K1.8 beam line . . . 25
- 2.4 K1.8 beam line spectrometer . . . 29
- 2.5 Superconducting kaon spectrometer (SKS) . . . 35
- 2.6 Liquid hydrogen and deuterium target . . . 44
- 2.7 Range counter array (RCA) . . . 46
- 2.8 Trigger . . . 49
- 2.9 Data-acquisition system . . . 54
- 2.10 Data summary . . . 56

3 Analysis I - inclusive analysis **57**
- 3.1 Outline . . . 57
- 3.2 Analysis of π^+ beam . . . 60
  - 3.2.1 Identification of triggered beam particles . . . 60
  - 3.2.2 BC1 and BC2 local tracking . . . 61
  - 3.2.3 BC3 and BC4 local tracking . . . 63
  - 3.2.4 Beam momentum reconstruction . . . 66
  - 3.2.5 Efficiency for the π^+ beam . . . 68
- 3.3 Analysis of emitted K^+ . . . 71
  - 3.3.1 SDC1 and SDC2 local tracking . . . 71
  - 3.3.2 SDC3 and SDC4 local tracking . . . 71
  - 3.3.3 Momentum reconstruction of scattered particles . . . 73

3.3.4 Efficiency for K^+ trigger counters . . . 75
3.3.5 Kaon identification in the SKS . . . 77
3.4 Vertex reconstruction . . . 80
3.5 Momentum correction . . . 84
3.5.1 Momentum correction of K^+ . . . 84
3.5.2 Momentum correction of π^+ and systematic error . . . 85
3.6 Missing-mass resolution . . . 88
3.7 Cross section . . . 90
3.7.1 Data acquisition efficiency (ϵ_{DAQ}) . . . 90
3.7.2 Efficiency of the trigger bias (ϵ_{trig}) . . . 90
3.7.3 K^+ decay factor (f_{decay}) . . . 92
3.7.4 Acceptance of the SKS . . . 93
3.7.5 Systematic errors . . . 95
3.8 The Σ^+ production cross section . . . 97

4 Analysis II - Coincidence analysis 100
4.1 Outline . . . 100
4.2 Velocity calibration . . . 101
4.3 Gain calibration . . . 104
4.3.1 PID parameter . . . 106
4.4 Particle identification in RCA . . . 108
4.4.1 Analysis for stopping layer $i_{stop} = 2 \sim 4$ . . . 108
4.4.2 Analysis for stopping layer $i_{stop} = 1$ . . . 109
4.4.3 Analysis for stopping layer $i_{stop} = 5$ . . . 111
4.5 Detection efficiency of RCA . . . 113

5 Experimental results and discussion 117
5.1 Inclusive analysis: results and discussion . . . 117
5.1.1 Inclusive missing-mass spectra of the $d(\pi^+, K^+)$ reaction . . . 117
5.1.2 Quasi-free processes in the $d(\pi^+, K^+)$ reactions . . . 119
5.1.3 Discussion on inclusive spectra . . . 124
5.2 Coincidence analysis: results and discussion . . . 134
5.2.1 π coincidence analysis . . . 134
5.2.2 One-proton coincidence analysis . . . 135
5.2.3 Two-proton coincidence analysis . . . 137
5.2.4 Identification of final states in two-proton coincidence . . . 137
5.2.5 Cross section in two-proton coincidence . . . 140
5.2.6 Results on proton coincidence spectra . . . 143
5.2.7 Discussion on proton coincidence spectra . . . 146

6 Conclusion 150

A BH1 filter tracking 154

B Accuracy of time offset of RCA 156

C ΣN cusp for two-proton coincidence analysis **158**

D Two-proton coincidence analysis using the E_X spectrum **160**

List of Figures

1.1 The hadron spectrum of a strangeness -1 and baryon number $B = 2$ systems. . . . 1
1.2 The low energy K^-p scattering data and the curves calculated from the M-matrix parameters. . . . 3
1.3 Comparison of the ΔE_{1s}'s and Γ_{1s}'s of the kaonic hydrogen together with recent theoretical calculated values. . . . 4
1.4 The $K^-p \to K^-p$ forward scattering amplitude extrapolated to the sub-threshold region. . . . 5
1.5 Comparison between the measured masses and the predicted one from the constituent quark model of the strangeness $S = -1$ negative parity baryons. 6
1.6 The level-shifts and widths of the K^- atom with the best-fit density dependent optical potentials. . . . 8
1.7 Comparison between the DWIA calculation of the $1s_\Lambda$ hypernuclear formation rates in stopped K^- reaction on several p-shell targets and measured values from the FINUDA Collaboration . . . 8
1.8 The missing mass spectra of the $^4\mathrm{He}(K^-_{stopped}, p)$ and $^4\mathrm{He}(K^-_{stopped}, n)$ reactions obtained by KEK E549 experiment. . . . 10
1.9 The Λp invariant mass spectrum obtained from the FINUDA experiment. 11
1.10 The deviation spectrum (DEV) of the of missing-mass spectrum of K^+ constructed from the DISTO experiment. . . . 12
1.11 The $(pp\pi^-)$ invariant-mass spectrum corresponding to the Λp state obtained from the OBELIX experiment. . . . 13
1.12 The $d(\gamma, K^+\pi^-)$ missing-mass spectrum of the LEPS experiment. . . . 14
1.13 The obtained (ΛK^+, pK^+, $p\Lambda$) invariant mass spectra with the solution of PWA evaluated from HADES experiment. . . . 15
1.14 The *semi*-inclusive $^3\mathrm{He}(K^-, n)$ missing mass spectrum with estimated backgrounds of the J-PARC E15 experiment. . . . 16
1.15 Summary of the calculated binding energy and width together with the experimental values. . . . 19
1.16 The $\Sigma^\pm\pi^\mp$ invariant mass spectrum and the angular distribution of $\Lambda(1405)$ measured by the old hydrogen bubble chamber experiment. . . 21

2.1 Schematic view of J-PARC . . . 23
2.2 Schematic view of hadron experimental facility as of 2012. . . . 23
2.3 Schematic view of K1.8 Beam line. . . . 25
2.4 Typical beam momentum distribution of π^+ in the present experiment. . 28

2.5 Typical beam profile of this experiment. 28
2.6 Schematic view of K1.8 beam spectrometer. 29
2.7 Schematic view of GC. 31
2.8 Schematic view of BH1. 32
2.9 Schematic view of BH2. 32
2.10 Schematic view of tracking chambers of K1.8 beam line spectrometer. . . 34
2.11 Schematic view of the SKS. 36
2.12 Schematic view of TOF. 38
2.13 Threshold and refractive index for Čerenkov radiation as a function of the momentum. 39
2.14 Schematic view of LAC. 39
2.15 Schematic view of LC. 40
2.16 Schematic view of BVH. 41
2.17 Typical trajectories of the background particles. 42
2.18 The cell structure of SDC3, 4. 43
2.19 Schematic view of the liquid hydrogen and deuterium target. 45
2.20 The scatter plot between momentum and scattering angle in xz plane of proton for the background and K^-pp. 46
2.21 Schematic view of RCA. 47
2.22 Schematic view of one unit of range counter array and the range as a function of β for the pion and proton. 48
2.23 Trigger logic diagram of this experiment. 49
2.24 The selected TOF and LC segments region with the matrix trigger 50
2.25 The horizontal direction cosine at SDC3, 4 position for each hit combination of TOF and LC segment. 51
2.26 Typical accepted and rejected region of the mass trigger. 52
2.27 Logic Scheme of the 2nd-level mass trigger 53
2.28 The diagram of the data-acquisition system. 54

3.1 Flow chart of the offline analysis for inclusive (π^+, K^+) spectrum. 59
3.2 Time-of-flight spectrum of the incident beam particles. 60
3.3 Typical reduced χ^2 distribution of the BC1, 2 local tracking. 62
3.4 Typical residual distribution of the BC1 layers. 62
3.5 Typical TDC distributions of BC3 and BC4. 63
3.6 A scatter plot between the drift time and the drift length of the BC3 layers. 64
3.7 Typical reduced χ^2 distribution of the BC3, 4 local tracking. 65
3.8 Typical residual distribution of the BC3 layers. 65
3.9 Typical distribution of the momentum of π^+ beam. 67
3.10 Typical reduced χ^2 distribution of the K1.8 tracking. 67
3.11 Summary of the ϵ_{K18} of the χ^2 cut value dependence. 68
3.12 The y distribution at the BC4 position. 69
3.13 A summary of f_μ of $\chi^2_{K18\ track}$ cut value. 70
3.14 The analysis efficiency of beam particles. 70
3.15 The reduced χ^2 distribution of the SDC1, 2 and SDC3, 4 local tracking. . 72
3.16 Proton selection for the estimation of ϵ_{SDC34}. 73
3.17 Initial momentum function of the SKS tracking. 74

3.18 Typical reduced χ^2 distributions of the SKS tracking. 74
3.19 The SKS tracking efficiency as a function of scattering angle. 75
3.20 Scatter plot between the horizontal direction cosine measured by SDC1, 2 and the flight time of BH2-TOF. 77
3.21 Mass squared distributions for the outgoing particles. 78
3.22 The mass square distribution for the $p(\pi^+, K^+)\Sigma^+$ data. 79
3.23 The distribution of the difference of the dx/dz (a) and dy/dz (b) between the K1.8 and SKS tracking. 80
3.24 The vertex distribution of x and y direction. 81
3.25 The summary of z-vertex resolution. 81
3.26 The vertex distribution of z direction. 82
3.27 The vertex cut efficiency. 83
3.28 Scatter plots between the direction cosines and the missing mass of $p(\pi^+, K^+)\Sigma^+$ reaction. 84
3.29 The momentum difference measured by the K1.8 beam line and the SKS. 86
3.30 The missing-mass spectrum of the $p(\pi^+, K^+)$ reaction in the $\Sigma^+(1385)$ mass region. 87
3.31 The momentum difference after the correction. 87
3.32 The momentum resolution of K1.8 beam line spectrometer and the SKS. 89
3.33 Comparison between (π, K) inclusive trigger data and the unbiased (π, K) trigger data. 91
3.34 Efficiency of the Matrix trigger, Mass trigger and BVH accidental veto factor. 91
3.35 The obtained decay factor as a function of MM_d. 92
3.36 The acceptance table for the $d(\pi^+, K^+)$ at 1.69 GeV/c data. 94
3.37 The acceptance table for the $p(\pi^+, K^+)$ at 1.69 GeV/c data. 94
3.38 The systematic error of the efficiency correcting event by event. 96
3.39 The total systematic error $(\Delta\epsilon/\epsilon)$ for the double differential cross section. 96
3.40 The obtained missing-mass spectra (MM_p) for the $p(\pi^+, K^+)\Sigma^+$. 97
3.41 Acceptance of SKS with the three kinematical lines of K^+. 98
3.42 The differential cross section of Σ^+ production at 1.58 GeV/c. 99
3.43 The differential cross section of Σ^+ production at 1.69 GeV/c. 99

4.1 A typical scatter plot of the ADC and flight time after the slewing correction of BH2. 102
4.2 A typical scatter plot of the ADC and flight time after the slewing correction of RCA. 102
4.3 A typical time difference spectrum between the up and down PMT's of the first layer of RCA. 103
4.4 A typical $1/\beta$ spectrum around the Σ production region compared with simulation. 103
4.5 A typical correlation plot between the normalized ADC values of the third layer fourth layer of RCA. 104
4.6 A typical obtained normalized ADC and simulated energy deposit spectra of the fourth layer of RCA for the stopping proton at this layer. 105

4.7 A typical obtained normalized ADC and simulated energy deposit spectra of the second layer of RCA for the stopping proton at fourth layer. 105
4.8 The correlation between the normalized ADC values and the energy deposit fitted with the second polynomial. 106
4.9 A typical scatter plot between the energy deposit of the first layer and the PID. 107
4.10 A typical χ^2 distribution as a function of α. 107
4.11 A typical scatter plot between the $1/\beta$ and PID for the $i_{stop} = 2 \sim 4$ events. 108
4.12 A typical PID spectra for the $i_{stop} = 2 \sim 4$ events. 109
4.13 A typical scatter plot between the $1/\beta$ and energy deposit in the first layer of RCA and typical proton selection gate. 110
4.14 The effective range for the pion and proton. 111
4.15 A typical scatter plot between PID and energy deposit of the fifth layer of RCA. 112
4.16 The simulated correlation plot between produced angle and the momentum of proton and π^+ from the Σ^+ decay. 113
4.17 The obtained $1/\beta$ spectrum for the Seg1 and 4 of RCA in coincidence with Σ^+ production compared with the simulation. 114
4.18 The π^+ coincidence probability of each segment of RCA compared with the simulation. 115

5.1 The obtained inclusive missing-mass spectra of the $d(\pi^+, K^+)$ reaction at 1.69 GeV/c for the MM_d. 118
5.2 The obtained inclusive missing-mass spectra of the $d(\pi^+, K^+)$ reaction at 1.69 GeV/c for the MM_p. 118
5.3 The momentum distribution of a nucleon inside of deuteron obtained from the Bonn Potential. 119
5.4 Considered elementary differential cross sections of the two-body reaction for the quasi-free processes. 121
5.5 The differential cross section of the Σ^0 production for the forward scattering angle. 122
5.6 A simulated differential cross section of the $d(\pi^+, K^+)$ reaction for the quasi-free processes. 123
5.7 A simulated differential cross section of the $d(\pi^+, K^+)$ reaction of the Region Ⅲ. 123
5.8 The missing-mass spectrum (MM_d) of the $d(\pi^+, K^+)$ reaction compared with the simulation. 124
5.9 The missing-mass spectrum (MM_d) for the fitting of ΣN cusp. 125
5.10 The obtained Λp invariant mass spectrum of the old experiment. 126
5.11 The contour plot of the χ^2 of the fitting as a function of the peak position and width. 127
5.12 A summary of the peak positions and widths from the fit with one Lorentzian function by the author of Ref. [107]. 128
5.13 A summary of peak positions and widths from the fit with two Lorentzian functions by the author of Ref. [107]. 128

5.14 The obtained double differential cross section (MM_d) for each scattering angle compared with the simulated spectra. 131
5.15 The obtained double differential cross section (MM_p) for each scattering angle compared with the simulated spectra. 132
5.16 The peak positions of the Y^* bump for each scattering angle obtained from the present data and simulated spectra. 133
5.17 A comparison of the π coincidence spectra between data and simulation. 134
5.18 The detection efficiency of a proton for each segment of RCA. 135
5.19 The one proton coincidence and coincidence probability spectra for the middle segment of RCA. 136
5.20 The two protons coincidence and coincidence probability spectra. 137
5.21 Missing-mass squared spectra of X obtained from the two proton coincidence events in the reaction of the $d(\pi^+, K^+pp)X$. 139
5.22 Detection efficiency of two protons for Λp and $\Sigma^0 p$ modes. 141
5.23 Detection efficiency of two protons for each mode as a function of MM_d. 141
5.24 The double differential cross section for the Λp and $\Sigma^0 p$ final state modes estimated from the fitting of M_X^2. 142
5.25 The double differential cross section for the Λp and $\Sigma^0 p$ final state modes fitted with the relativistic Breit Winger function. 143
5.26 The contour plot of the χ^2 of the fitting as a function of the mass and width of the "K^-pp"-like structure. 144
5.27 Comparison of the double differential cross sections between the inclusive spectrum and "K^-pp"-like structure. 146
5.28 The one proton coincidence probability spectrum of the middle segment of RCA with the interpreted spectrum. 147
5.29 Comparison of the binding energy and width of the K^-pp. 148

A.1 Schematic view of BH1Filter. 155
A.2 Typical hit position gate of BH1Filter. 155

B.1 The M_X^2 spectrum for each time-offset condition compared with the simulation. 157

C.1 The double differential cross section for the Λp final state mode around 2.13 GeV/c^2 compared with the past experiment. 159

D.1 Energy spectra of X obtained from the two proton coincidence events in the reaction of the $d(\pi^+, K^+pp)X$. 161
D.2 The double differential cross section for the Λp and $\Sigma^0 p$ final state modes estimated from the fitting of E_X. 162

List of Tables

2.1 Design specifications of the K1.8 beam line spectrometer 30
2.2 Specifications of the trigger counters of the K1.8 beam line spectrometer 30
2.3 Specifications of the trackers of the K1.8 beam line spectrometer 33
2.4 Design specifications of the SKS spectrometer at the 2.36 T mode. 35
2.5 Specifications of the particle identification counters in the SKS spectrometer 37
2.6 Specifications of the drift chambers of the SKS. 43
2.7 Specifications of the liquid hydrogen and deuterium target. 44
2.8 Summary of the obtained data with different combinations of experimental targets, incident π^+ momenta P_{beam}, and beam intensities. N_{beam} means the total number of π^+ beam irradiated on the target. 56

3.1 The position resolution of each layer. 61
3.2 The position resolution of each layer. 64
3.3 The scattering-angle resolutions and the missing mass resolutions of the Σ^+ production at 1.58 GeV/c data. 89
3.4 The list of the experimental efficiency and systematic error for the common factor (ϵ_{com}). 95

5.1 The elementary total cross sections of hyperon productions. 120

Chapter 1

Introduction

A multi-hadron spectrum of strangeness $S = -1$ and baryon number $B = 2$ system is displayed in Figure. 1.1. In the low mass region, there are ΛN (2.05 GeV/c^2) and ΣN (2.13 GeV/c^2) systems which are composed in octet baryons. The Λ-nucleon system forms bound states called Λ-hypernuclei starting from three baryon system of ${}^{3}_{\Lambda}\mathrm{H}$ ($p + n + \Lambda$). The Λ single particle energy in nuclear matter is obtained to be about 30 MeV from the study of Λ-hypernuclei. This system is the ground state of $S = -1$, $B = 2$ systems. The ΣN system is about 80 MeV heavier than the ΛN system. It has a bound state of four baryons ${}^{4}_{\Sigma}\mathrm{He}$. In heavier systems, the ΣN interaction is repulsive, and there would be no bound states.

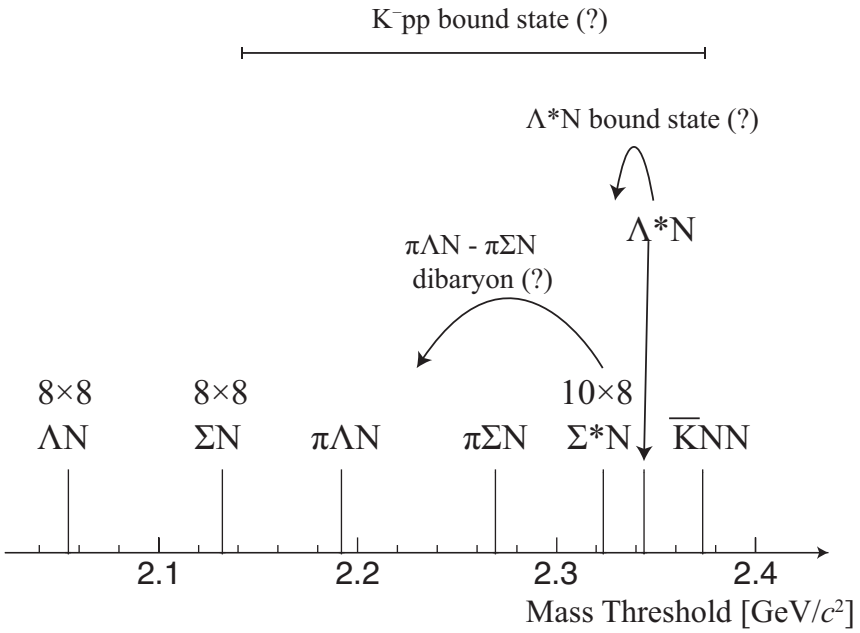

Figure 1.1: The hadron spectrum of a strangeness $S = -1$ and baryon number $B = 2$ system.

In the higher mass region, there is an energy threshold composed of $\Sigma(1385)$, which is a decuplet baryon with $J^P = \frac{3}{2}^+$ and $S = -1$, and nucleon at 2.32 GeV/c^2. We can also

see a threshold of $\Lambda(1405)$ and nucleon at about 2.34 GeV/c^2. The $\Lambda(1405)$ is considered as the first excited state of Λ particle with $J^P = \frac{1}{2}^-$ in a quark model. Above the two thresholds at 2.37 GeV/c^2, we also have a new type of threshold of $\bar{K}NN$. In the $\bar{K}NN$ system, a bound state which is called as a K^-pp bound state is theoretically predicted to exist as the $J^P = 0^-$, isospin $I = 1/2$ and total charge +1 because of the strong attraction of the $\bar{K}N$ interaction in $I = 0$ [1]. The $\bar{K}NN$ system sits on above about 49 MeV and 27 MeV from the $\Sigma(1385)N$ and $\Lambda(1405)N$ systems, respectively. These situations make it difficult to theoretically study the K^-pp bound state. On the other hand, a $\pi\Lambda N$–$\pi\Sigma N$ dibaryon, which is the bound state of the decuplet and octet baryons, is theoretically predicted in the $\Sigma(1385)N$ system with $I = 3/2$ and $J^P = 2^+$ [2]. There is also a theoretical prediction of a bound state of the $\Lambda(1405)N$ system [3]. Its quantum number is $I = 1/2$ and $J^P = 0^-$. We can not distinguish the $\Lambda(1405)N$ from the K^-pp bound state when we consider the $\Lambda(1405)$ is the bound state of the $\bar{K}N$ system. It is no wonder that these three bound states would appear in anyplace between the ΣN and $\Sigma(1385)N$ thresholds. Of course, the bound states are unstable; they decay into light systems such as ΛN, ΣN, $\pi\Lambda N$, and $\pi\Sigma N$. In this thesis, we aim to investigate the states in the strangeness $S = -1$ and baryon number $B = 2$ system around this energy region. It is expected that strangeness degree of freedom plays an important role in high density nuclear matter realized in core of neutron star. For example, Λ hypereon might appear at around twice the normal nuclear matter density. Beyond that density, the system we are investigating can take an important role. Therefore, it is an important subject to understand the whole energy spectrum of strange dibaryon systems.

1.1 $\bar{K}N$ interaction

Information on the $\bar{K}N$ interaction was obtained from K^-p scattering data in low-energy region. In particular, Martin estimated the scattering length by using the self-consistent M-matrix description for the low energy $\bar{K}N$ data of $K^-p \to K^-p$ (elastic), $K^-p \to \bar{K}N$ (charge exchange), and $K^-p \to \Lambda\pi^0, \Sigma^0\pi^0, \Sigma^\pm\pi^\mp$ (inelastic) with the $K^\pm p$ and $K^\pm n$ dispersion relation as shown in Figure 1.2 [5]. The estimated scattering lengths[1] at the K^-p threshold are

$$\begin{aligned} a^{I=0} &= -1.70 + i0.65 \text{ fm}, \\ a^{I=1} &= 0.37 + i0.60 \text{ fm}, \end{aligned} \tag{1.1}$$

where $a^{I=0}$ and $a^{I=1}$ are the scattering lenghts with $I = 0$ and $I = 1$, respectively.

The information of $\bar{K}N$ is also obtained from the measurement of the K_α X-ray ($2p \to 1s$ transition) of kaonic hydrogen. The energy level shift from the electromagnetic calculation ($\Delta E_{1s} = E_{1s}^{measured} - E_{1s}^{e.m.}$) and the width ($\Gamma_{1s}$) of the ground state give us information of S-wave $\bar{K}N$ interaction. These values can be compared with the K^-p scattering data. The scattering length can be deduced from the ΔE_{1s} and Γ_{1s} through

[1] In this definition, the scattering length is attractive for Re $a > 0$ and vice versa.

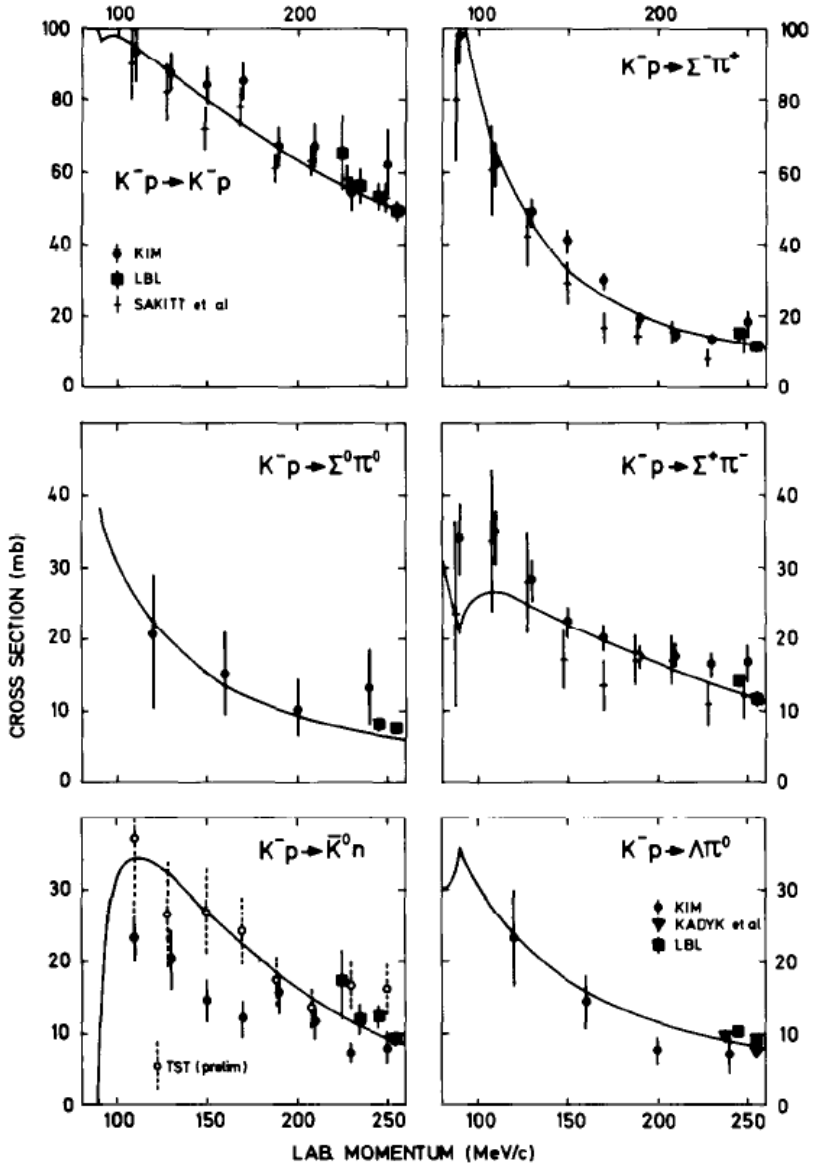

Figure 1.2: The low energy K^-p scattering data and the curves calculated from the M-matrix parameters. This figure is taken from Ref. [5].

the Deser relation [6, 7] as:

$$\Delta E_{1s} + \frac{i}{2}\Gamma_{1s} = 2\alpha^3\mu^2 a_{K^-p}, \tag{1.2}$$

$$a_{K^-p} = \frac{1}{2}(a^{I=0} + a^{I=1}), \tag{1.3}$$

where α is the fine structure constant and μ is the reduced mass of the K^-p system. The deduced scattering length from the kaonic hydrogen data was not consistent with the Martin's result until 1997. Especially, the sign of the real part was in disagreement with each other, whose discrepancy was called as " kaonic hydrogen puzzle".

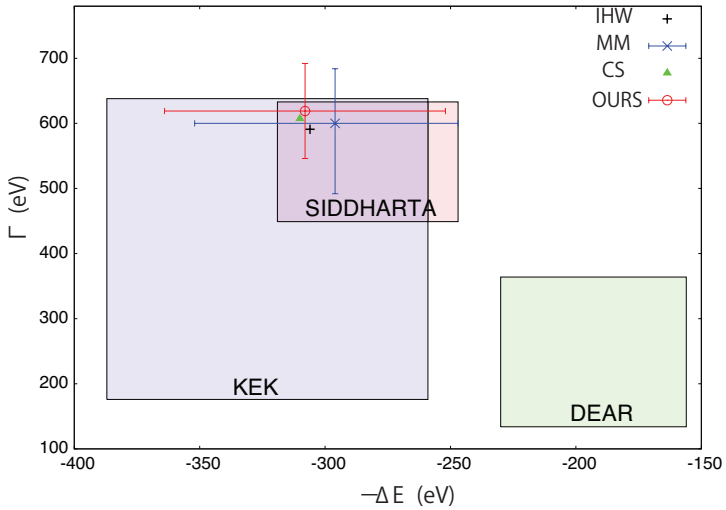

Figure 1.3: The comparison of the ΔE_{1s}'s and Γ_{1s}'s of the kaonic hydrogen reported by three groups (taken from Ref. [14]). The experimental data with errors are indicated by the sides of the rectangles corresponding to the KEK-PS E228 [8], DEAR [9] and SIDDHARTA [10] experiment. The recent theoretical values are also shown with a black plus symbol [11], a blue cross [12], a green solid triangle [13] and a red empty circle [14].

This "kaonic hydrogen puzzle" was solved by KEK-PS E228 (KpX) experiment in 1997. They observed a clear K_α peak by using a gaseous hydrogen target in order to reduce the backgrounds [8]. Later, the DEAR collaboration also published the kaonic hydrogen atom data [9], whose obtained value was not so far from the value of KEK-PS E228 experiment. Recently, the SIDDHARTA group measured the kaonic hydrogen X-ray in high precision by using the silicon drift detectors (SDDs), which had both good energy resolution of about 150 eV and good time resolution of about 1 μs [10]. These ΔE_{1s}'s and Γ_{1s}'s are summarized in Figure 1.3. In this figure, the recently calculated values using the coupled-channel approach based on the chiral effective theory (chiral unitary model) with the interaction kernel up to NLO level are also shown [11, 12, 13, 14]. Furthermore, in these theoretical works, they discuss the extrapolation of $\bar{K}N$ amplitude into sub-threshold energy region. Here, we show the result in Figure 1.4 of Ref. [11, 15]. These theoretical models well reproduce the experimental values (kaonic hydrogen data, K^-p cross sections, and branching ratios), although details of models and fitting schemes

are different. However, some deviations are seen in the subthreshold extrapolations as shown in Fig. 1.4. These uncertainties may be attributed to the difference of the model setup [14, 15]. Therefore, the $\bar{K}N$ interaction in the sub-threshold region is not well constrained at present and a new experimental constraint is necessary.

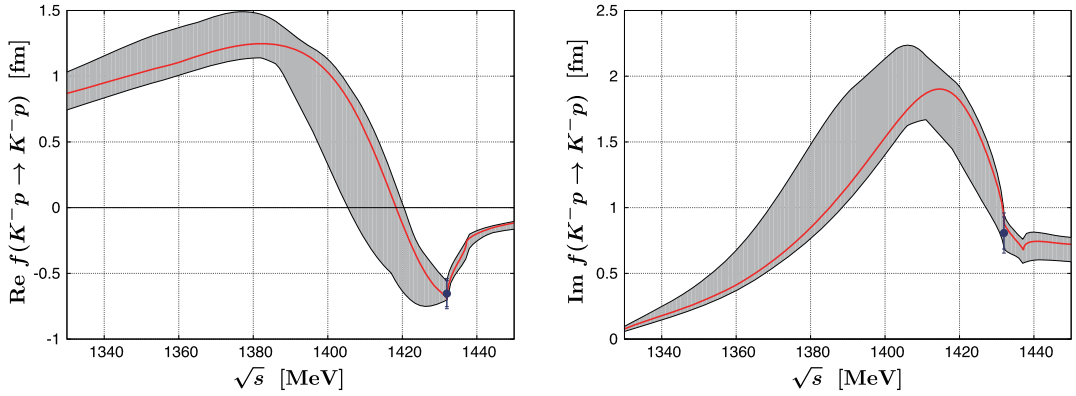

Figure 1.4: The $K^-p \to K^-p$ forward scattering amplitude extrapolated to the subthreshold region taken from Ref. [15]. The constraints from the result of SIDDHARTA experiment are indicated by the dots. The shaded bands represent theoretical uncertainties.

1.2 $\Lambda(1405)$

In the constituent quark model, $\Lambda(1405)$ is assigned as a negative parity excited three quark baryon of u, d, and s-quarks with isospin $I = 0$, and spin parity $J^P = \frac{1}{2}^-$. The constituent quark model correctly predicted many of existing hadron masses of the ground and excited states [16]. However, the quark model is difficult to reproduce the mass of $\Lambda(1405)$. In Figure 1.5, it is compared between the measured masses and the predictions of the quark model for the strangeness $S = -1$ negative parity baryons. Mass of the negative parity baryons was reproduced well with the quark model except for the $\Lambda(1405)$ ($\Lambda^*\frac{1}{2}^-$). According to the model, the $\Lambda(1405)$ is the spin-multiplet partner of the $\Lambda(1520)$, which is the $J^P = \frac{3}{2}^-$ state, and these $\frac{1}{2}^-$ and $\frac{3}{2}^-$ states should almost degenerate in mass at about 1490 MeV as shown in Figure 1.5.

However, the observed mass of $\Lambda(1405)$ is smaller by about 80 MeV than the theoretical prediction. The mass difference between $\Lambda(1405)$ and $\Lambda(1520)$ is too large to explain it with the LS splitting between quarks. Moreover, the mass of $\Lambda(1405)$ is lighter than $N(1535)$, which is a nucleon excited state with the same spin and parity $J^P = \frac{1}{2}^-$, although $\Lambda(1405)$ has a strange quark. Then, the $\Lambda(1405)$ is considered not three quark state. In meson-baryon picture, the $\Lambda(1405)$ is interpreted as a $\bar{K}N$ quasi-bound state with $I = 0$ embedded in the $\Sigma\pi$ continuum, which was discussed in coupled-channel meson-baryon scattering models [17]. This is in some sense reasonable, because the mass of $\Lambda(1405)$ is located just below the $\bar{K}N$ threshold and the $\bar{K}N$ interaction is strongly attractive in the $I = 0$ channel.

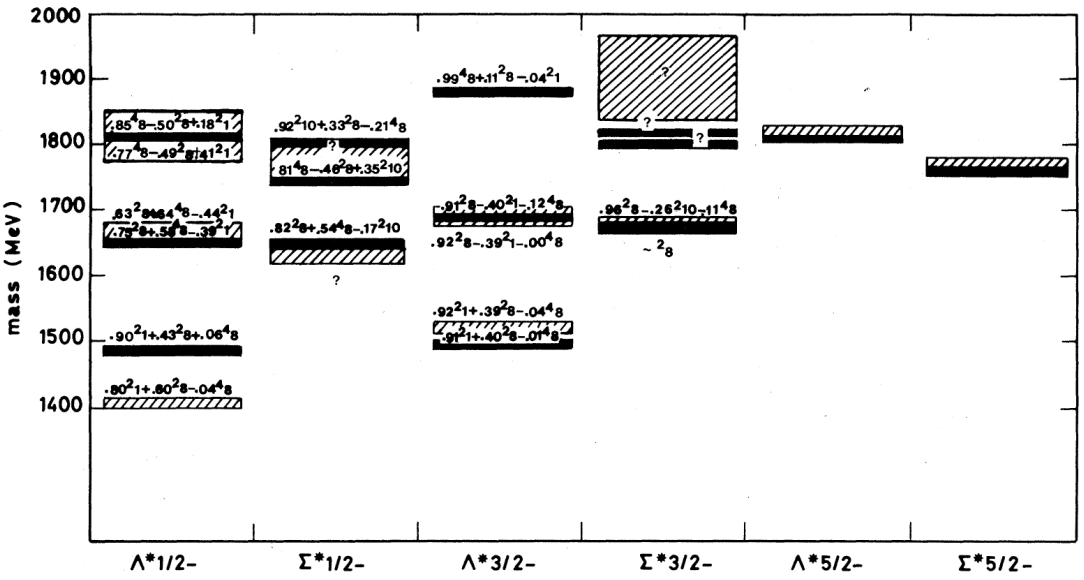

Figure 1.5: Comparison between the measured masses and the predicted one from the constituent quark model of the strangeness $S = -1$ negative parity baryons taken from Ref. [16]. The shadow boxes show the measured masses and the black bars show the predicted masses from this model.

Recently, the $\Lambda(1405)$ is discussed by using the chiral unitary model [18]. In this study, the $\Lambda(1405)$ is composed of two poles located between $\bar{K}N$ and $\pi\Sigma$ thresholds. Both poles contribute the observed experimental invariant mass distribution. In the recent result in the NLO scheme including the constraints of SIDDARTA measurement, one pole is located at $1424\ ^{+7}_{-23} - i26\ ^{+3}_{-14}$ MeV with a dominant coupling to $\bar{K}N$ and the other pole is at $1381\ ^{+18}_{-6} - i81\ ^{+19}_{-8}$ MeV with a strong coupling to $\pi\Sigma$ [11]. Moreover, it is understood that the strong energy dependence of the scattering amplitude shown in Figure 1.4 is induced from the existence of $\Lambda(1405)$.

In the experimental side, the existence of $\Lambda(1405)$ was confirmed from Bubble-chamber experiments using a π^- and K^- beam at Brookhaven [19] and CERN [20], respectively. In the recent years, several results with high statistics using the magnetic spectrometer were reported. The $\Sigma^0\pi^0$ line shape was reported for the $p + p$ reaction at a 3.65 GeV/c at the Cooler Synchrotron (COSY) [21]. The $\Sigma^{\pm}\pi^{\mp}$ line shapes were measured in the $p + p$ collisions at Gesellschaft für Schwerionenforschung (GSI) by the HADES collaboration [22] and the photo-production at the Super Photon ring-8 GeV (SPring-8) by the LEPS collaboration [23, 24]. From the LEPS data [24], the difference between the line shapes of $\Sigma^+\pi^-$ and $\Sigma^-\pi^+$ was reported, although the exact contribution from the $\Lambda(1405)$ was not clear. Moreover, both $\Sigma^{\pm}\pi^{\mp}$ and $\Sigma^0\pi^0$ line shapes in high statistics were measured by using the photo-production reaction at Thomas Jefferson National Accelerator Facility (JLab) by the CLAS collaboration [25]. These observed line shapes are not always consistent with each other and these inconsistencies might be originated from the structure of the $\Lambda(1405)$.

1.3 $\bar{K}$-nucleus interaction

An important tool to study the $\bar{K}$-nucleus interaction in low-energy region is kaonic atoms, which are coulombic bound state of the K^- and nucleus with influence of strong interaction, obtained by the X-ray spectroscopy. Recently, high precision experiments were carried out to measure the kaonic ^{4}He and ^{3}He by KEK-PS E570 [26] and SIDDHARTA [27] experiments. The simple $t\rho$ approach, where t is the free space zero energy t matrix and ρ is the nuclear density, is widely used to obtain the hadron-nucleus interaction. In this approach, global fits were carried out for a large set of data using an optical potential V_{opt} with the Klien-Gordon equation,

$$[\Delta - 2\mu(B + V_{opt} + V_c) + (V_c + B)^2]\Psi = 0, \tag{1.4}$$

where V_c is the static Coulomb potential for the $\bar{K}$ due to the finite charge distribution of the nucleus, μ is the reduced mass of K^--nucleus system and $B = B_{\bar{K}+i\Gamma_{\bar{K}}}/2$ ($B_{\bar{K}}$ and $\Gamma_{\bar{K}}$ are the binding energy and the width, respectively). The simple $t\rho$ optical potential is given by,

$$2\mu V_{opt}(r) = -4\pi\Big(1 + \frac{\mu}{m}\frac{A-1}{A}\Big)b_0\rho(r), \tag{1.5}$$

where m is the mass of nucleon and $\rho(r)$ is the nucleon density distribution normalized to the mass number A. The b_0 is the fitting parameter which is equal to the $\bar{K}$-nucleon isoscalar scattering length in the impulse approximation. The $t\rho$ best-fit potentials had the real parts depth of about -80 MeV for a typical medium-weight to heavy nucleus [28]. Such a "shallow" potential was obtained from the chirally inspired approaches which fit the low-energy K^-p reaction data [29]. Much shallower potential was derived by additionally requiring self-consistency in the construction of the optical potential [30, 31].

The generic $t\rho$ potential in Eq. 1.5 was greatly improved by adopting a density dependent (DD) potential, where the fixed b_0 was replaced by $b_0 \rightarrow b_0 + B_0[\rho(r)/\rho_0]$. The parameters b_0, B_0 and $\alpha \geq 0$ were determined from the fit. In this global fits, 65 level-shifts and widths of the K^- atom data from ^{7}Li to ^{238}U were used as shown in Figure 1.6. The density dependent optical potentials turned to give the "deep" potential, whose depth of the real parts was $-$(150–200) MeV. The $t\rho$ with the multiplicative function approach [32] and the model independent Fourier-Bessel method [33] also provided such a "deep" potential.

Recently, a $\bar{K}$ nuclear potential study was carried out by using the Ikeda-Hyodo-Weise (IHW) NLO chiral K^-N subthreshold scattering amplitude [11] as shown in Figure 1.4 [34]. In this study, the single-nucleon density-dependent potential $V^{(1)}_{K^-}(\rho)$ was generated using the IHW amplitudes and a phenomenological density-dependent interaction potential $V^{(2)}_{K^-}(\rho)$ was added to reproduce multi-nucleon dispersive and absorptive processes. Both $V^{(1)}_{K^-}(\rho)$ and $V^{(2)}_{K^-}(\rho)$ are coupled implicitly within a self-consistent cycle built into the kaonic atom fitting procedure. Finally, the IHW-based $(V^{(1)}_{K^-}(\rho) + V^{(2)}_{K^-}(\rho))$ potential produced the deeply attractive real potential, whose depth at the center of Ni was -191 MeV [34].

The other tool to investigate the $\bar{K}$-nucleus interaction is the excitation spectrum in the in-flight (K^-, N) reaction with nuclear targets. In KEK-PS E548 experiment [37], they measured the energy spectra both of the ^{12}C(K^-, n) and ^{12}C(K^-, p) reactions

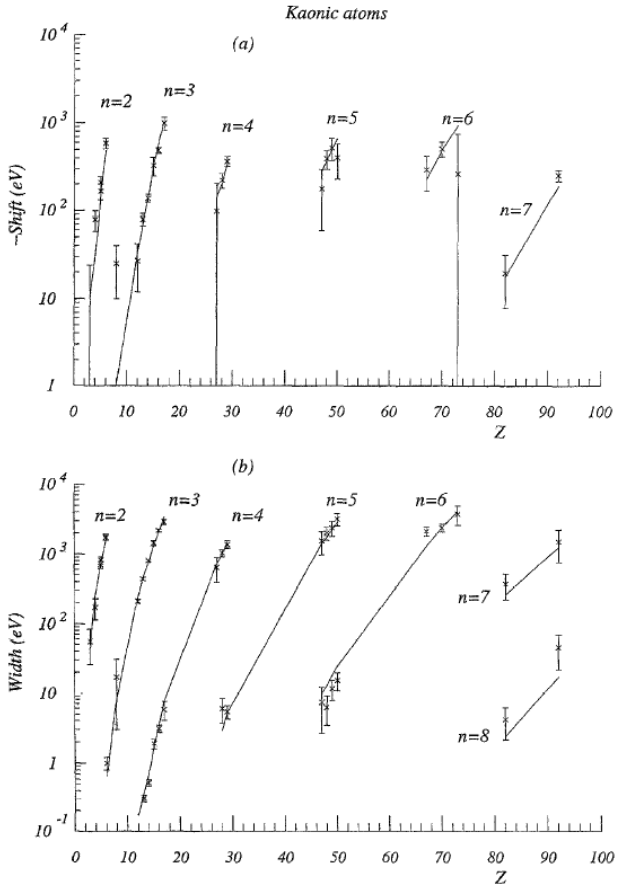

Figure 1.6: The level-shifts (a) and widths (b) of the K^- atom with the best-fit density dependent optical potentials taken from Ref. [28].

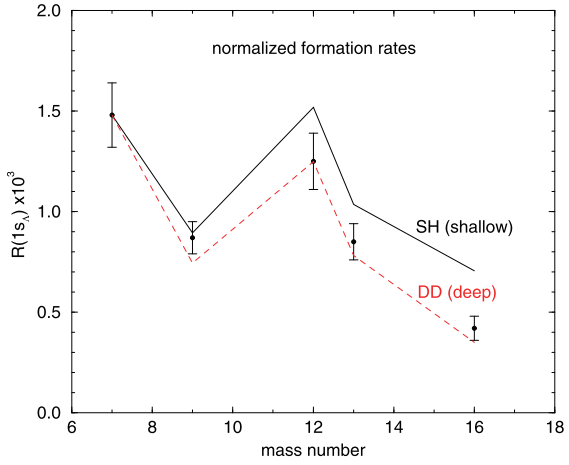

Figure 1.7: Comparison between the DWIA calculation of the $1s_\Lambda$ hypernuclear formation rates in stopped K^- reaction on several p-shell targets and measured values from the FINUDA Collaboration [35]. This plots were normalized to the $1s_\Lambda$ formation rate of the ${}^{7}_{\Lambda}$Li. Taken from Ref. [36].

and the potential depths were obtained as -190 MeV for the $^{12}\mathrm{C}(K^-, n)$ reaction and -160 MeV for the $^{12}\mathrm{C}(K^-, p)$ reaction with the Greens function method. However, there is a paper to point out a serious drawback in this experimental setup [38]. In KEK-PS E548 experiment, at least one charged particle detected in their decay counter was required. The paper pointed out that this requirement can appreciably distort the spectrum shape.

Recently, the distinction between "deep" and "shallow" K^--nucleus potentials was discussed by comparing the calculated $1s_\Lambda$ hypernuclear formation rates in stopped K^- reaction on several p-shell targets with measured values from the FINUDA Collaboration as shown in Figure 1.7 [36]. This comparison favors deep potentials to shallow ones. However, it is not conclusive whether $\bar{K}$-nucleus interaction potential is "deep" or "shallow" in the current situation. The study of the kaonic nuclei, which is the bound states of kaon and nucleus, will help to solve this problem because the binding energies and the width of each kaonic nucleus should depend on the potential depth and have the information of inner behavior of the strong interaction potential.

1.4 Kaonic nuclei: Experiments and Theory

The kaonic nuclei in medium-weight nucleus system was discussed by Kishimoto in 1999 [39]. Akaishi and Yamazaki predicted the possible existence of the deeply bound kaonic nuclei for few body systems in 2002 [1]. From these period, a study of the kaonic nuclei have been actively conducted from both theoretical and experimental sides. The kaonic nuclei should have the rich information such as the $\bar{K}N$ strong interaction in sub-threshold region, the strong interaction potential of the $\bar{K}$ nucleus system and the behavior of the $\Lambda(1405)$ in many body systems.

In the Akaishi and Yamazaki's theoretical work [1], they constructed a phenomenological $\bar{K}N$ interaction model using the $\bar{K}N$ scattering data, kaonic hydrogen data of the KEK-PS E228 (KpX) experiment and the binding energy and width of the $\Lambda(1405)$ by assuming the $\Lambda(1405)$ as isospin $I = 0$ bound state of the $\bar{K}N$ system. They predicted the kaonic nuclei with narrow widths of the $K^-+{}^3\mathrm{He}$, $K^-+{}^4\mathrm{He}$, and $K^-+{}^8\mathrm{Be}$ systems with binding energies of 108, 86, and 113 MeV and narrow widths of 20, 34, and 38 MeV, respectively. In the paper [1], they also proposed an experimental method to populate the $K^-+{}^3\mathrm{He}$ by using the $^4\mathrm{He}(K^-_{stopped}, n)$ reaction. Moreover, in Ref. [40], they discussed the kaonic nuclei in proton-rich system. The K^- with two protons system, namely the K^-pp bound state, was calculated with the binding energy of 48 MeV and the width of 61 MeV using their formalism. In this discussion [40], they proposed the (K^-, π^-) and (π^+, K^+) reactions to produce the proton-rich kaonic nuclei, where $\Lambda(1405)$ and $\Lambda(1520)$ might play important roles as door-ways. This prediction inspires the present work.

After the Akaishi and Yamazaki's prediction, several experiments to search the kaonic nuclei were carried out. In KEK-PS E549 experiment [41, 42], they measured the missing-mass spectra of the $^4\mathrm{He}(K^-_{stopped}, p)$ and $^4\mathrm{He}(K^-_{stopped}, n)$ reactions to search for the K^-ppn and K^-pnn bound states. However, no peak structures were observed in both spectra as shown in Figure 1.8. The upper limits for the formation branch were obtained to be a few $\%/(stopped\ K^-)$.

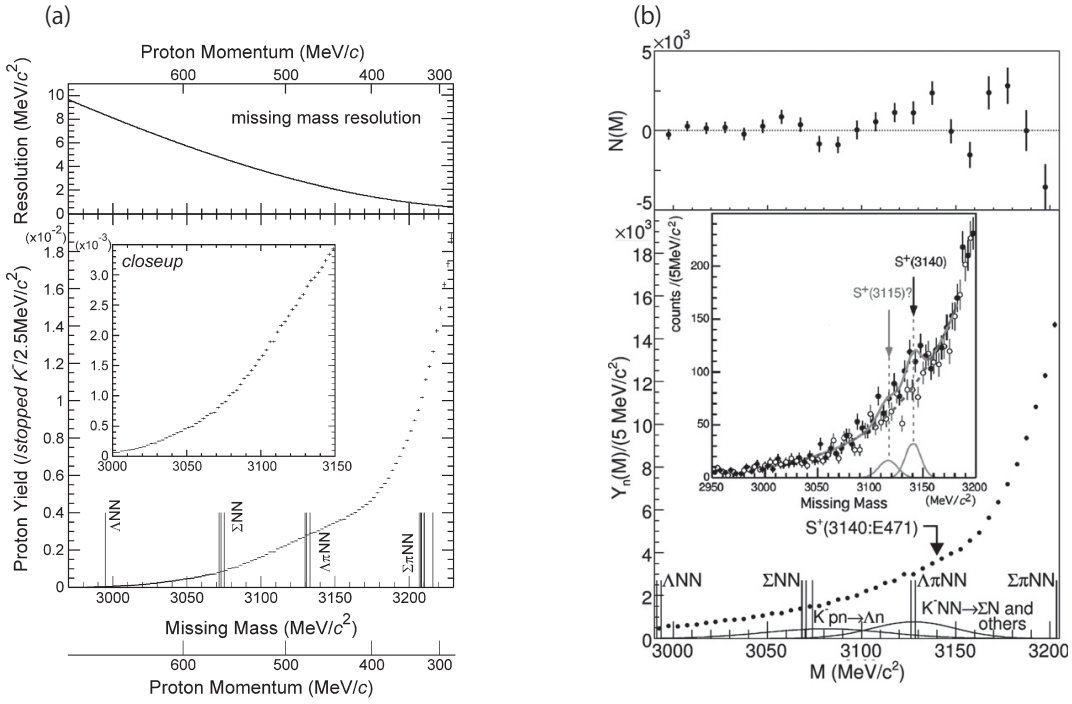

Figure 1.8: The missing mass spectra of the ^{4}He$(K^-_{stopped}, p)$ (a) and ^{4}He$(K^-_{stopped}, n)$ (b) reactions obtained by KEK E549 experiment. Taken from Ref. [41, 42].

1.4.1 Past experiments of the K^-pp

FINUDA experiment

The first evidence of the K^-pp was reported by the Fisica Nucleare a DAΦNE (FINUDA) Collaboration [43] at DAΦNE, which is the e^+e^- collider at the Laboratori Naziali di Frascati (LNF) and produces copious $\phi(1020)$ mesons. In this experiment, almost monochromatic K^-'s produced from the decay of $\phi(1020)$ mesons were stopped in five kinds of thin targets (^{6}Li, ^{7}Li, ^{12}C, ^{27}Al, and ^{51}V). They measured a lot of Λp pairs emitted in the opposite direction ($\cos\theta^{Lab} < -0.8$) from the light nuclear targets (^{6}Li, ^{7}Li, and ^{12}C). They observed a bump structure in the invariant mass spectrum of the Λp pairs as shown in Figure 1.9. The obtained binding energy and the width, which were estimated by fitting with a Lorentzian function folded with a Gaussian with the experimental invariant mass resolution $\sigma = 4$ MeV, were $B_{K^-pp} = 115\ ^{+6}_{-5}$ (stat.) $^{+3}_{-4}$ (syst.) MeV and $\Gamma_{K^-pp} = 67\ ^{+14}_{-11}$ (stat.) $^{+2}_{-3}$ (syst.) MeV, respectively. This experiment is the first experiment to detect the $K^-pp \to \Lambda p$ mode. Since the obtained width was large, to measure the invariant-mass spectrum leads to prosperity. After the FINUDA experiment, $K^-pp \to \Lambda p$ mode is mainly used to search for the K^-pp bound state.

In this analysis, there was a theoretical criticism that the obtained invariant mass spectrum can be explained without K^-pp [44]. They point out that a final state interaction of proton and Λ after the quasi-free two nucleon absorption can also produce the similar invariant mass distribution of FINUDA experiment. However, for their criticism, there is also counterargument that the bump structure around this region was observed

in the Λp spectrum but not in the Λn spectrum and the large difference between the Λp and Λn spectra is difficult to explain with the final state interactions [45]. Therefore, the interpretation of the observed spectrum of the FINUDA experiment seems to be not conclusive at present.

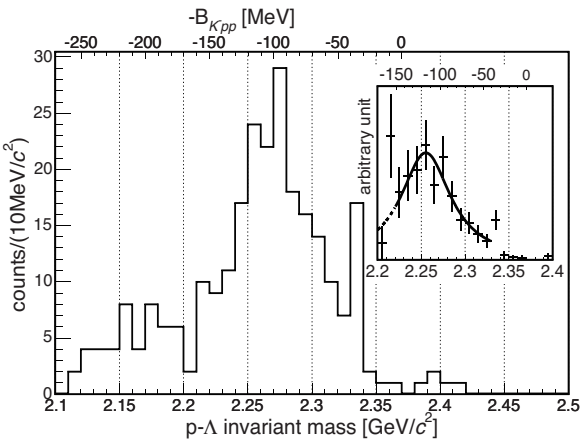

Figure 1.9: The Λp invariant mass spectrum obtained from the FINUDA experiment (taken from Ref. [43]).

DISTO experiment

After the report of FINUDA experiment, a possible signal of the K^-pp was discussed by the DISTO experiment [46], which was carried out at the SATURNE accelerator at Saclay. They used the $pp \to K^+p\Lambda$ reaction at $T_p = 2.85$ GeV and measured both K^+ missing mass and Λp invariant mass. Deviation spectra were obtained from the measured experimental spectra, which was not corrected experimental acceptance, divided by simulated phase space spectra of the $p\Lambda K^+$ process taking into account of the acceptance.

A large broad peak in the deviation spectrum of missing-mass spectrum of K^+ was observed by applying cut of the large proton angle ($|\cos\theta_{cm}(p)| < 0.6$) and large-angle of K^+ emission ($-0.2 < \cos\theta_{cm}(K^+) < 0.4$) as shown in Figure. 1.10. The obtained mass and width were $M = 2267 \pm 3$ (stat.) ± 5 (syst.) MeV/c^2 and $\Gamma = 118 \pm 8$ (stat.) ± 10 (syst.) MeV, respectively, with the statistical significance of 26σ. The obtained mass corresponds to a binding energy of 103 ± 3 (stat.) ± 5 (syst.) MeV for the K^-pp. The production rate of this broad peak was found to be as much as the $\Lambda(1405)$ production rate, which is roughly 20% of the total Λ production rate. They also analyzed the same reaction data at $T_p = 2.5$ GeV [47]. However, they did not observe such a signal at this beam energy; may be due to the small production cross section of $\Lambda(1405)$ at $T_p = 2.5$ GeV.

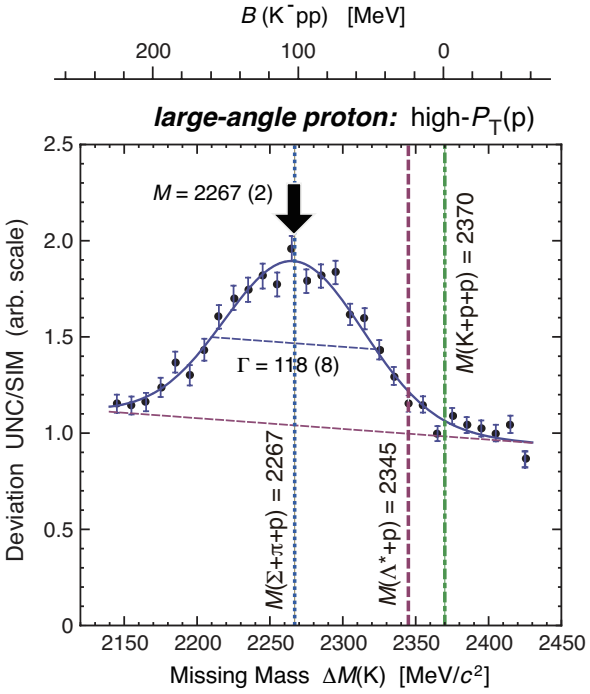

Figure 1.10: The deviation spectrum (DEV) of the of missing-mass spectrum of K^+ constructed from the DISTO experiment (taken from Ref. [46]).

OBELIX experiment

The OBELIX experiment [48, 49] was carried out at the LEAR complex at CERN using the $\bar{p}$ annihilation reaction on ^{4}He target. Especially, they discussed the $\bar{p} + ^4\mathrm{He} \to p\pi^- p\pi^+\pi^- nX$ reaction, which corresponds to the $\bar{p} + ^4\mathrm{He} \to [K^- pp]K^0_s nX \to \Lambda p K^0_s nX$ reaction. In Ref. [48], they observed a peak with the statistical significance of 3.7σ at the mass of 2212.1 ± 4.9 MeV, which corresponding to the K^-pp binding energy of 160.9 ± 4.9 MeV, and width of $< 24.4 \pm 8.0$ MeV in the $(pp\pi^-)$ invariant-mass spectrum by selecting the events with the $p\pi^-$ invariant mass close to the Λ mass (1115 ± 30 MeV), although they did not observe clear Λ peak directly in the $p\pi^-$ invariant-mass spectra due to the poor resolution.

In Ref. [49], they reported the results which was improved the signal/background by changing the analysis method. The main difference was in the selection of Λ. In this analysis, the Λ produced event was selected by checking not only the invariant mass of $p\pi^-$ but also the scatter plot of p_{tot} and E_{tot}, which corresponded to the momentum and energy of the Λp system respectively, characterized by missing K^0. Figure 1.11 shows the obtained $(pp\pi^-)$ invariant-mass spectrum with several cuts to achieve the best statistical significance of 4.7σ by fitting with two Gaussian functions. The obtained peak position and width were 2223.2 ± 3.2 (stat.) ± 1.2 (syst.) MeV, which corresponds to the K^-pp binding energy of -151.0 ± 3.2 (stat.) ± 1.2 (syst.) MeV, and $< 33.9 \pm 6.2$ MeV, respectively. (On the other hand, the obtained peak of the OBELIX experiment might be attributed to a threshold cusp effect at the $\Lambda p\pi$ system [50].)

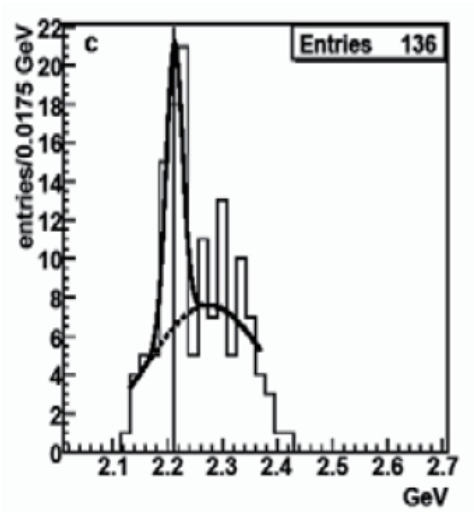

Figure 1.11: The $(pp\pi^-)$ invariant-mass spectrum corresponding to the Λp state obtained from the OBELIX experiment (taken from Ref. [49]).

LEPS experiment

The K^-pp was also searched by using the photo-production at the LEPS/SPring-8 [51]. In this experiment, they used the $d(\gamma, K^+\pi^-)$ reaction at $E_\gamma = 1.5$–2.4 GeV and totally 7.6×10^{12} tagged photons were irradiated on a liquid deuterium target. The beam energy E_γ was measured for each event with a tagging counter, whose energy resolution was approximately 12 MeV, and the K^+ and π^- which were produced in the forward angle ($\cos\theta^{lab}_{K^+,\ \pi^-} > 0.95$) were detected with the LEPS spectrometer. The $d(\gamma, K^+\pi^-)$ reaction can be regarded as the virtual $d(K^-, \pi^-)$ or $d(K^{*-}, \pi^-)$ reactions when t-channel reaction modes are dominant.

A peak of the K^-pp was searched by using the Log-likelihood ratio method by assuming the background process as $\gamma n \to \Lambda K^+\pi^-$, $\gamma p \to \Sigma^+ K^+\pi^-$, $\gamma p \to \Lambda(1520)K^+$, $\gamma n \to \Lambda\pi^0 K^+\pi^-$, $\gamma n \to \Sigma^0\pi^0 K^+\pi^-$ and $\gamma p \to \Sigma(1385)^0 K^+\pi^-$, whose yields were taken into account as free parameters. The obtained spectrum could be fitted with only these background processes and no peak structure was observed from 2.22 to 2.36 GeV/c^2 as shown in Figure 1.12. The upper limits of the differential cross section of the K^-pp was determined to be 0.17–0.55, 0.55–1.7 and 1.1–2.9 μb at 95% confidence level with the assumed width of $\Gamma = 20$, 60 and 100 MeV, respectively.

Furthermore, in order to investigate the background precisely, they fitted missing-mass spectra of $d(\gamma, K^+\pi^-)$ and $d(\gamma, K^+)$ reactions assuming the proton mass for the target mass simultaneously by supposing the total 12 quasi-free processes. In the fit result, they found that the main contribution to the missing-mass spectrum in the K^-pp search region was originated from the $\gamma p \to \Lambda(1520)K^+$ process ($22 \pm 3\%$) and non-resonant hyperon production processes of $\gamma N \to \Lambda/\Sigma\pi K^+\pi^-$ ($24 \pm 5\%$).

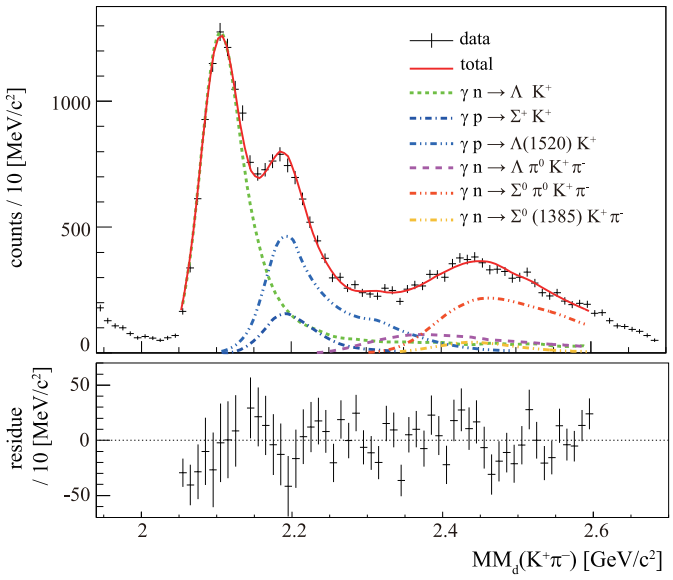

Figure 1.12: The $d(\gamma, K^+\pi^-)$ missing-mass spectrum of the LEPS experiment (taken from Ref. [51]).

HADES experiment

The HADES Collaboration at GSI also searched for the K^-pp by using the $pp \to p\Lambda K^+$ reaction at $T_p = 3.5$ GeV [52, 53], whose beam energy was higher than the one of the DISTO experiment. In Ref. [52], they compared the obtained invariant mass of ΛK^+, pK^+ and Λp system and angular distribution spectra with the simulated one calculated with a pure phase-space event generator. They found that the phase-space simulation could not reproduce the obtained invariant mass and angular distributions. The disagreement could not be overcome by adding the contribution of (one) resonances. Furthermore, since the obtained $K^+\Lambda$ invariant mass spectrum showed two peaks around 1700 and 1900 MeV/c^2, they added incoherently the phase space production to the N(1720) and N(1900) contributions. Then, they achieved a better description of the experimental data. Moreover, they built the deviation spectra (DEV) by dividing the experimental data with the simulation including the N^* contribution, although the DISTO experiment assumed the pure-phase space distribution. The deviation spectrum of the Λp invariant mass showed a wide bump around 2400 MeV/c^2. They pointed out that the obtained bump at the deviation spectrum of the HADES experiment jeopardized the solidity of the deviation method used by the DISTO collaboration.

Recently, they reported the result employing the Bonn-Gatchina partial wave analysis framework (PWA) in Ref. [53]. In the PWA, they used ten versions of the non-resonant production waves and twelve versions of N^* resonances as the PWA inputs. They fitted the data with their combination of 120 different ansatzes. The four best PWA solutions were obtained with a null hypothesis of the existence of the K^-pp which decayed to Λp mode. Figure 1.13 shows the comparison between the obtained (black dotes) and the PWA solutions (gray band), whose error band shows the systematic differences of the four best PWA solutions, of the (ΛK^+, pK^+, Λp) invariant mass spectra which are

one of the spectra used for the fitting. Finally, they evaluated the upper limits on the K^-pp in the mass range of 2220–2370 MeV/c^2 and assuming the widths of 30, 50 and 70 MeV for the three possible production waves of J^P =$0^+, 1^-, 2^+$, where the quantum numbers of the K^-pp was assumed as $J^P = 0^-$. The evaluated upper limits of the K^-pp decaying to Λp mode were 1.8–3.9 μb ($J^P = 0^+$), 2.1–4.2 μb ($J^P = 1^-$) and 0.7–2.1 μb ($J^P = 2^+$). Moreover, the obtained upper limits about 4 μb was discussed by comparing the measured production cross section of the $\Lambda(1405)$ of about 10 μb from evaluated from the same experiment [22].

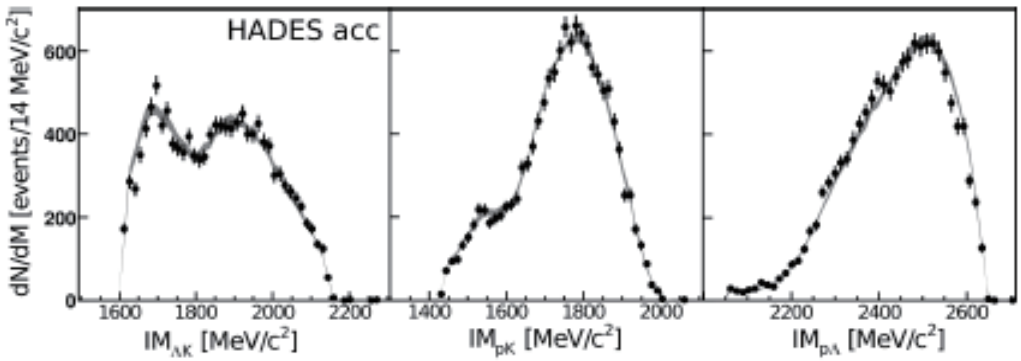

Figure 1.13: The obtained (ΛK^+, pK^+, $p\Lambda$) invariant-mass spectra with the solution of PWA evaluated from HADES experiment (taken from Ref. [53]).

J-PARC E15 experiment

In the E15 experiment, they have used the in-flight ^{3}He(K^-, n) reaction at 1 GeV/c [54]. They measured not only the missing-mass spectrum of the ^{3}He(K^-, n) reaction but also an invariant-mass spectrum of the decay particles such as Λp pairs. The outgoing neutron at $\theta_n^{lab} = 0^\circ$ was measured by the time-of-flight method using a neutron counter hodoscope placed at a distance of about 15 m from the liquid ^{3}He target. The decay particles were detected by using the Cylindrical Detector System (CDS), which surrounded the target.

The first physics run of this experiment was carried out in May 2013. In this data taking, they irradiated 5.3 $\times$ 10^9 kaons, which corresponds to about 1% of statistics requested in the original proposal. In Ref. [54], a result of the ^{3}He(K^-, n) missing-mass distribution based on a *semi*-inclusive condition by requesting at least one charged track in the CDS was discussed. Figure 1.14 shows the reported ^{3}He(K^-, n) *semi*-inclusive missing-mass distribution together with the estimated backgrounds for the K^-pp bound region. They confirmed the observed events in the missing-mass region below 2.29 GeV/c^2 were explained by the background such as a neutron event from the $\Sigma^\pm$ decay. On the other hand, they pointed out that the yield of the tail like component above 2.29 GeV/c^2 cannot be totally reproduced. It might originate from the imaginary part of the attractive $\bar{K}N$ interaction and/or hyperon resonance production via the non-mesonic two-nucleon absorption processes. They evaluated the upper limits of the production cross section of the K^-pp assuming the isotropic decay of the $K^-pp \to \Lambda p$ at

95% confidence level in the missing-mass range from 2.06 to 2.29 GeV/c^2. The obtained upper limits were 30–180, 70–250, and 100–270 μb/sr, for the widths of 20, 60, and 100 MeV, respectively. The analysis using the CDS for the decay particles are on going. (This analysis result will be also reported in near future.)

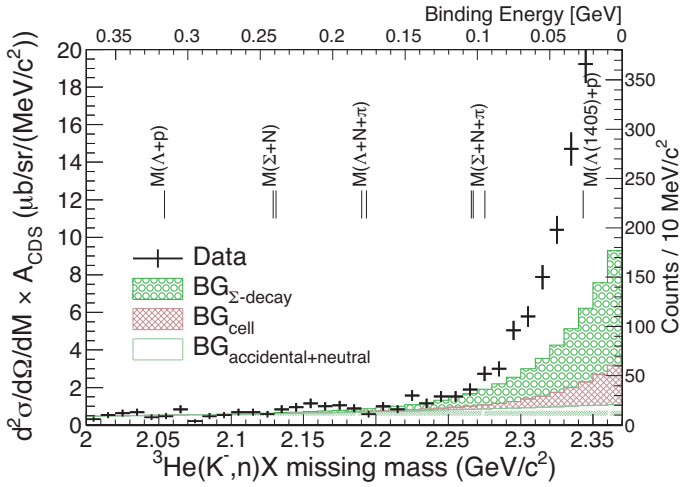

Figure 1.14: The *semi*-inclusive ^{3}He(K^-, n) missing mass spectrum with estimated backgrounds of the J-PARC E15 experiment (taken from Ref. [54]).

1.4.2 Current situation of the K^-pp

FINUDA, DISTO and OBELIX experiments observed the peak structure which can be attributed to the signal of the K^-pp. However, the obtained experimental values are not consistent with each other. There are no experimental evidence which can conclude the existence of the K^-pp. In the FINUDA experiment [43], there is a theoretical criticism that the final state interaction of proton and Λ after the quasi-free two nucleon absorption can produce the similar bump structure [44]. Since they used nuclear targets such as ^{12}C, the contribution of the final state interaction could be larger. In order to reduce the final state interaction effect, it is better to use the lighter targets. Note that there is further experiment to search for the K^-pp using the stopped K^- reaction at DAΦNE (AMADEUS experiment [55]) using ^{4}He target to reduce the final state interaction effect. Furthermore, the reaction mechanism to produce the K^-pp from the stopped K^- reaction was not investigated. In this view, OBELIX experiment [48, 49] also has the same problem in the $\bar{p}$ annihilation reaction. In addition, they did not observe clear Λ peak directly in the $p\pi^-$ invariant-mass spectra due to the poor resolution. Moreover, the peak structure measured by OBELIX experiment might be the threshold cusp of the $\Lambda p\pi$ system [50].

The DISTO experiment introduced the deviation spectra which were made from the measured spectra divided by simulated spectra [46]. They assumed the phase space $p\Lambda K^+$ production reaction in the simulation as for the background reaction. However, it seems there is an ambiguity of the background assumption because they used the $pp \to K^+p\Lambda$ reaction at $T_p = 2.85$ GeV. In this reaction, there should be additional background processes such as N^* production, which is pointed out by the HADES collaboration [52, 53]. The HADES collaboration, which also used the $pp \to K^+p\Lambda$ reaction at $T_p = 3.5$ GeV, performed the partial wave analysis (PWA) using the components of non-resonant production waves and N^* resonances in order to understand this reaction. They found the four best PWA solutions without the hypothesis of the K^-pp when they fitted with 120 different ansatzs. Thus, there are a lot of background reactions in the pp reaction at these energy region. By using the pp reaction, FOPI experiment also searches the K^-pp at $T_p = 3.1$ GeV at GSI [56].

The LEPS collaboration evaluated the upper limit using the inclusive spectrum in the $d(\gamma, K^+\pi^-)$ reaction [51] . Since they used the inclusive spectrum, there were a lot of background processes of the hyperon and hyperon resonance productions. Thus, the inclusive measurement seems less sensitive to search for the K^-pp. Note that they are considering a further experiment for the K^-pp search with the exclusive measurement in the $\gamma d \to K^+\pi^-\Lambda p$ reaction at LEPS2 [64].

In the J-PARC E15 experiment [54], they used ^{3}He(K^-, n) reaction to search for the K^-pp. They supposed the K^-pp is expected to be produced directly from a ^{3}He nucleus in this reaction. However, we do not know whether this reaction model is valid or not. In order to clarify the reaction mechanism, it is important to investigate an elementary cross section of the $\Lambda(1405)$ production. They measured missing-mass spectrum of the ^{3}He(K^-, n) reaction and invariant-mass spectrum of decay particles such as Λp pairs. In the semi-inclusive analysis, they evaluated the upper limits for the K^-pp production in the missing-mass range from 2.06 to 2.29 GeV/c^2. The analysis constructing the invariant mass spectrum of the Λp pairs by requiring the final state to be Λpn, whose

spectrum is expected to have less background, is on going.

In order to investigate whether the K^-pp exists or not, we should know the reaction mechanism to produce the K^-pp. Moreover, it is important to investigate the K^-pp by using the different reactions in order to reduce the other possibility such as a final state interaction. Here, it is better to use the lighter target to reduce the component of the final state interaction. In addition, the background reactions should be controlled. In this view, we proposed a new experiment to search for the K^-pp using the $d(\pi^+, K^+)$ reaction.

1.4.3 Theoretical studies of the K^-pp

The K^-pp has been also studied from the theoretical side using different treatments of the $\bar{K}N$ interactions and a few-body calculation methods [40, 57, 58, 59, 60, 61, 62]. For the $\bar{K}N$ interaction, usually two types of potentials are used, namely chiral SU(3)-based energy-dependent potentials and the energy-independent potentials, whose potential is constructed with the phenomenological treatment. There are also two types of the calculation methods: one is a variational method with effective single-channel potential and the other is Faddeev coupled-channel method.

The calculated binding energy and width of the K^-pp was summarized in Ref. [63] (especially Table 1) characterized of the types of $\bar{K}N$ interaction and calculation method. We plot these predicted binding energies and widths in Figure 1.15 together with the experimental values reported from the FINUDA [43], DISTO [46] and OBELIX [49] experiments. In this plot, the values using the chiral SU(3)-based energy dependent potentials are shown with circles and the ones calculated with the energy independent potentials are indicated with triangles. Moreover, the values obtained using the calculation method of the variational and the Faddeev approach are shown in black and white colors, respectively. The experimental values are indicated with red squares.

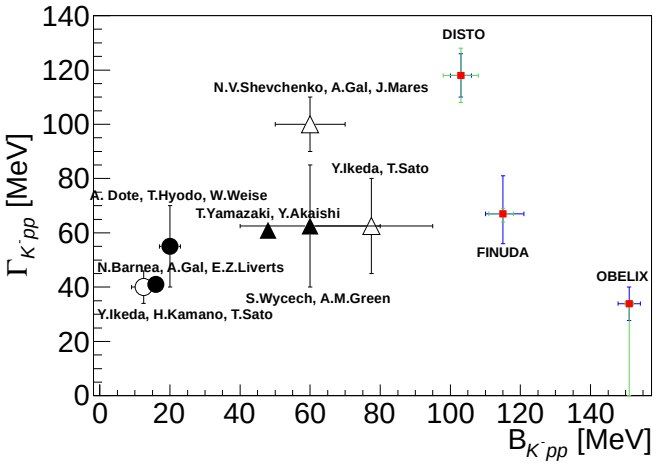

Figure 1.15: Summary of the calculated binding energy and width, which were listed in Ref. [63], together with the experimental values of the FINUDA [43], DISTO [46] and OBELIX [49] data. For the experimental values, the statistical and systematic errors are shown with the blue and green lines, respectively. See the text for the detail.

Although all of the theoretical predictions listed in Ref. [63] agrees in the existence of the K^-pp bound state, the predicted binding energy and the width are not consistent with each other. Especially, the calculated binding energy using the chiral energy dependent potentials (shown in circles) seems to be lower than the values of the energy independent potentials (shown in triangles). It is discussed that this tendency appears because of the difference between the $(\bar{K}N)_{I=0}$ interaction strengths which yield a quasi-bound state at about 1420 MeV in the former case and at about 1405 MeV in the latter

case [63]. Note that theoretical calculations of the K^-pp are difficult to reproduce the measured binding energy about 100 MeV.

In the other view of the $S = -1$ and $B = 2$ system, the $\pi\Lambda N$–$\pi\Sigma N$ dibaryon, which can be a quasi-bound state of $\Sigma(1385)N$ and $\Delta(1232)Y$ component, is discussed theoretically [2]. A quantum number of this state is isospin $I = 3/2$ and spin parity $J^P = 2^+$. The mass is predicted to be about 2.27 GeV/c^2 which is 50 MeV below the $\Sigma(1385)N$ threshold. Moreover, the $\Lambda(1405)N$ bound state is also discussed [3]. In this study, they found the quasi-bound state slightly below the $\Lambda(1405)N$ threshold in the total spin 0 channel.

1.5 J-PARC E27 experiment

The J-PARC E27 experiment was proposed to investigate the K^-pp bound state by using the (π^+, K^+) reaction on a liquid deuterium target at 1.69 GeV/c. In this reaction, a production mechanism for the K^-pp was discussed in Ref. [69]; a hyperon resonance $\Lambda(1405)$ is produced in the π^+"n"$\rightarrow K^+\Lambda(1405)$ process as a doorway to the K^-pp formation through $\Lambda(1405)$"p"$\rightarrow K^-pp$. Here, "n" and "p" indicate a neutron and a proton in a deuteron, respectively. It should be noted that an elementary cross section of the π^+"n"$\rightarrow K^+\Lambda(1405)$ reaction can be estimated from the cross section of the $\pi^-\ p\ \rightarrow\ K^0\Lambda(1405)$ reaction assuming the isospin symmetry. The elementary cross section of $\Lambda(1405)$ has already been measured by using the hydrogen bubble chamber at $p_{\pi^-} = 1.69$ GeV/c [19]. Figure 1.16 (a) shows the $\Sigma^\pm\pi^\mp$ invariant-mass spectrum obtained in this old experiment [19]. The $\Lambda(1405)$ mass distribution was clearly observed in this spectrum. Moreover, the angular distribution of $\Lambda(1405)$ production was also measured as shown in Figure 1.16 (b). We can find the elementary $\Lambda(1405)$ production cross section is large at the very forward scattering angle. Thus, in the E27 experiment, we measured the (π^+, K^+) reaction in the forward scattering-angle, where a lot of $\Lambda(1405)$'s were produced. We have an advantage to be able to compare the K^-pp cross section with the elementary production cross section of the $\Lambda(1405)$. It is a unique advantage compared with any other experiments.

In addition, we can control the background process. In the $d(\pi^+, K^+)$ reaction, possible main background components are hyperons and hyperon resonances production in quasi-free processes of π^+"N"$\rightarrow K^+Y(Y^*)$ reaction, where "N" is a nucleon in the deuteron. The elementary cross sections of the π^+p reactions have already been measured in the old bubble chamber experiment [65]. In case of the π^+n elementary cross sections, we can estimate the ones from the $\pi^-p \rightarrow K^0Y(Y^*)$ reaction as same as the $\Lambda(1405)$. These π^-p cross sections were also measured by using a bubble chamber [19]. Thus, we can reliably estimate these quasi-free background processes by using the measured elementary cross sections. Moreover, the kinematics, especially the proton kinematics, between the quasi-free backgrounds and the K^-pp is different. A proton can be produced from the decay of hyperon such as $\Lambda \rightarrow p\pi^-$ in the quasi-free hyperon production (background). Such a proton's scattering angle in the quasi-free processes concentrates in the forward angle ($\theta_{p(Lab)} \lesssim 30^\circ$) according to our simulation. On the other hand, a proton produced from the K^-pp decay such as $K^-pp \rightarrow \Lambda(\Sigma^0)p$ process can distribute in a wide scattering-angle region. Therefore, we can reduce the quasi-free background components

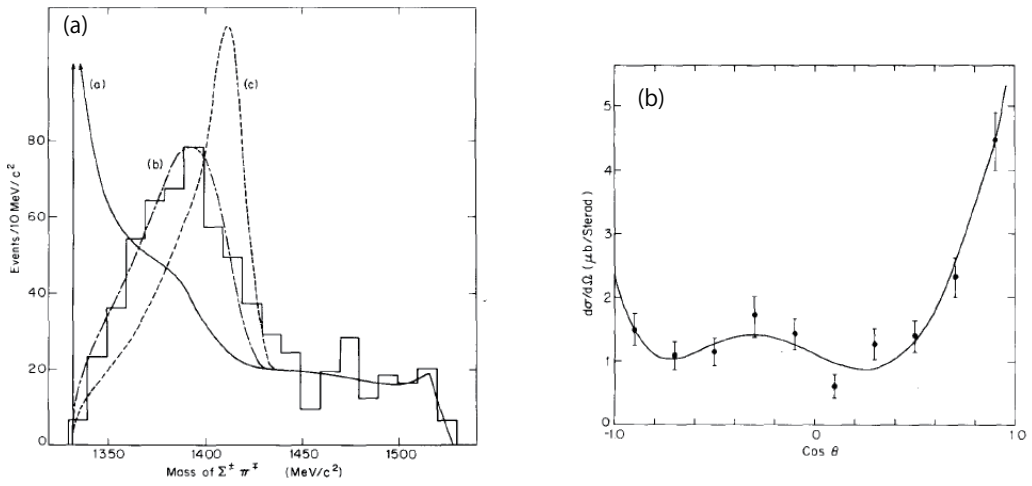

Figure 1.16: The $\Sigma^{\pm}\pi^{\mp}$ invariant mass spectrum (a) and the angular distribution (b) of $\Lambda(1405)$ measured by the old hydrogen bubble chamber experiment. Taken from Ref. [19].

by tagging the large scattering-angle ($\theta_{p(Lab)} \gtrsim 30^{\circ}$) proton. Note that we can detect the $K^{-}pp$ signal free from the quasi-free backgrounds by measuring the two-protons in the scattering angles $\theta_{p(Lab)} \gtrsim 30^{\circ}$. Furthermore, we can eliminate the final state interaction for the $K^{-}pp$ because we use the liquid deuterium target.

This experiment was carried out at K1.8 beam line [66, 67] of the hadron experimental hall at J-PARC [68] in 2012. We reconstructed the missing mass by measuring the incident beam π^{+} momentum with the K1.8 beam line spectrometer and the emitted K^{+} momentum with the superconducting Kaon Spectrometer (SKS). The SKS has a good momentum resolution about 0.2% (FWHM) and wide acceptance about 100 msr. Therefore, we can measure the missing mass spectrum of $d(\pi^{+}, K^{+})$ reaction with the good missing-mass resolution of about 3 MeV (FWHM) and the wide missing-mass region from quasi-free Λ production region ($\sim$2.05 GeV/c^2) to Y^{*} production region ($\sim$2.5 GeV/c^2). This experiment can overcome all the problems which hampered other experiments. It is because we know the reaction mechanism to produce the $K^{-}pp$ and the elementary cross section of the $\Lambda(1405)$. Moreover, we can control the background processes and eliminate the final state interaction for the $K^{-}pp$.

1.6 Thesis composition

This thesis is arranged by the following order. The J-PARC E27 experiment and the experimental setup are described in Chapter. 2. The detail of the inclusive analysis of the (π^{+}, K^{+}) reaction is described in Chapter. 3. The coincidence analysis by using the range counter array (RCA) to detect the proton(s) is shown in Chapter. 4. The results of both inclusive and coincidence analyses are shown in Chapter. 5. We also discuss physics interpretations for the obtained results. Finally, the conclusion is given in Chapter. 6.

Chapter 2

Experiment

2.1 Outline

The J-PARC E27 experiment was carried out at the K1.8 beam line of the J-PARC hadron experimental hall in 2012. The goal of this experiment is to search for the K^-pp bound state by using the (π^+, K^+) reaction on a liquid deuterium target at $p_{\pi^+} = 1.69$ GeV/c. A typical beam intensity was 3×10^6 per 6-second per spill cycle with a spill length of about 2 seconds.

In order to measure the momenta of beam pion and emitted kaon, the K1.8 beam line spectrometer and the superconducting Kaon Spectrometer (SKS) were used, respectively. Furthermore, a range counter array (RCA) was installed surrounding the liquid deuterium target in order to suppress a large backgrounds coming from quasi-free productions of hyperon (Λ and Σ's) and hyperon resonances ($\Lambda(1405)$ and $\Sigma(1385)$'s).

In Chap.2.2, J-PARC accelerator facility and hadron experimental facility are described. In Chap.2.3, the detail of K1.8 beam line is described. The details of the K1.8 beam line spectrometer, SKS, the liquid target and RCA are shown in Chap.2.4, Chap.2.5, Chap.2.6 and Chap.2.7, respectively.

2.2 J-PARC and hadron experimental facility

The Japan Proton Accelerator Research Complex (J-PARC) (Figure 2.1) is a multi-purpose proton accelerator facility which aims to pursue frontier in nuclear physics, particle physics, materials and life sciences and nuclear technology using MW-class, proton beams in these proton energies; 400 MeV, 3 GeV and 30 GeV [68]. The J-PARC consists of three accelerators (a linac, a 3 GeV rapid-cycle synchrotron: RCS, and the main ring: MR) and three experimental facilities (a materials and life science facility: MLF, a neutrino facility: NU, and a hadron experimental facility: HD).

The linac is composed of an H^- ion source (IS), a radio frequency quadrupole (RFQ), a drift tube linac (DTL) and a separated-type DTL (SDTL) [70]. H^- was produced at the IS and accelerated up to 181 MeV with a peak current 30 mA as of 2012. The beam energy of the linac was upgraded to 400 MeV in 2013.

The H^- beam from the linac was delivered to the RCS and converted to proton (H^+) by using a carbon stripper foil [71]. The RCS accelerates the injected proton up to

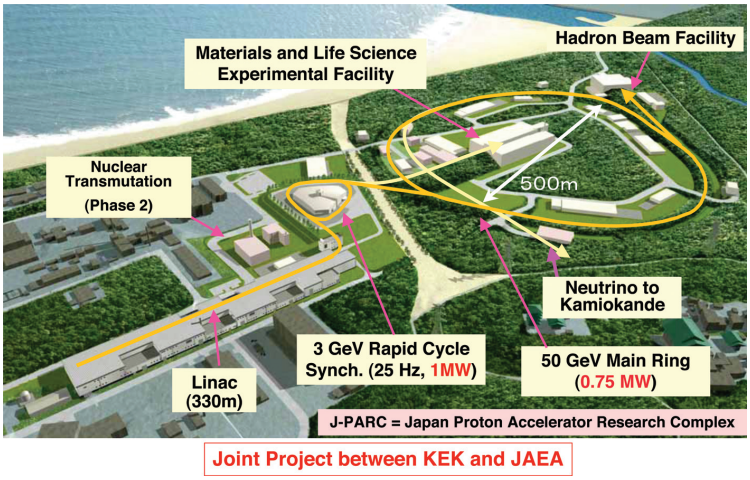

Figure 2.1: Schematic view of J-PARC (taken from Ref. [68]).

3 GeV. The 3 GeV beam from the RCS is mainly transported to the MLF and a part of the RCS beam is transported to the MR [72]. The MR accelerates up to 30 GeV, and delivers it to the NU by fast extraction and to the HD by slow extraction. The operation of the J-PARC accelerator was started in 2009.

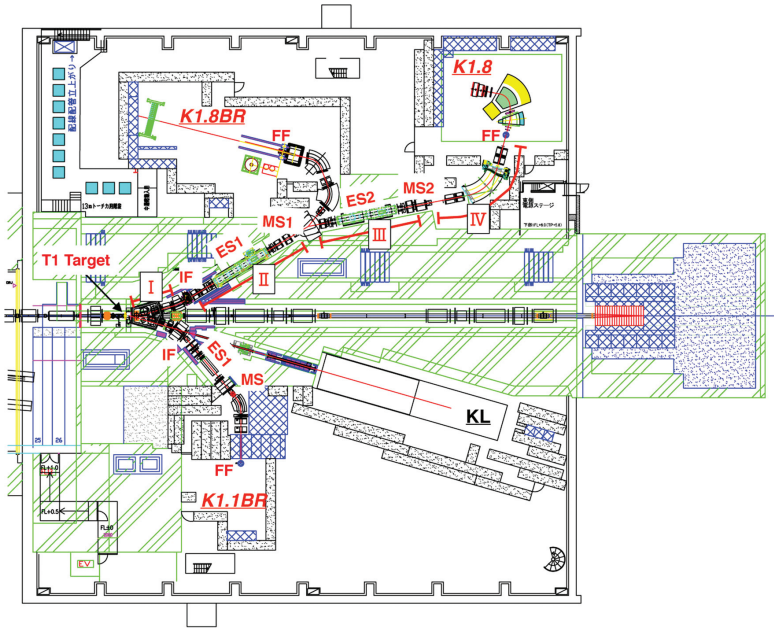

Figure 2.2: Schematic view of hadron experimental facility (taken from Ref. [66]).

The primary proton beam from the main ring was extracted to HD for a duration of 2 seconds in every 6 seconds, which is synchronized to the J-PARC 30-GeV PS operation cycle. The duration of the beam extraction is called a spill. The HD consists of a primary beam line, three charged secondary beam lines (K1.8, K1.8BR and K1.1BR)

and one neutral secondary beam line (KL) as shown in Figure 2.2. The proton beam is transported from the MR to the HD and bombarded to the production target, T1 [73]. In the present experiment, the production target was a platinum rod (ϕ6 mm $\times$60 mm). Secondary hadron beams such as kaon and pion produced at T1 were delivered to experimental areas through the secondary beam lines [66].

2.3 K1.8 beam line

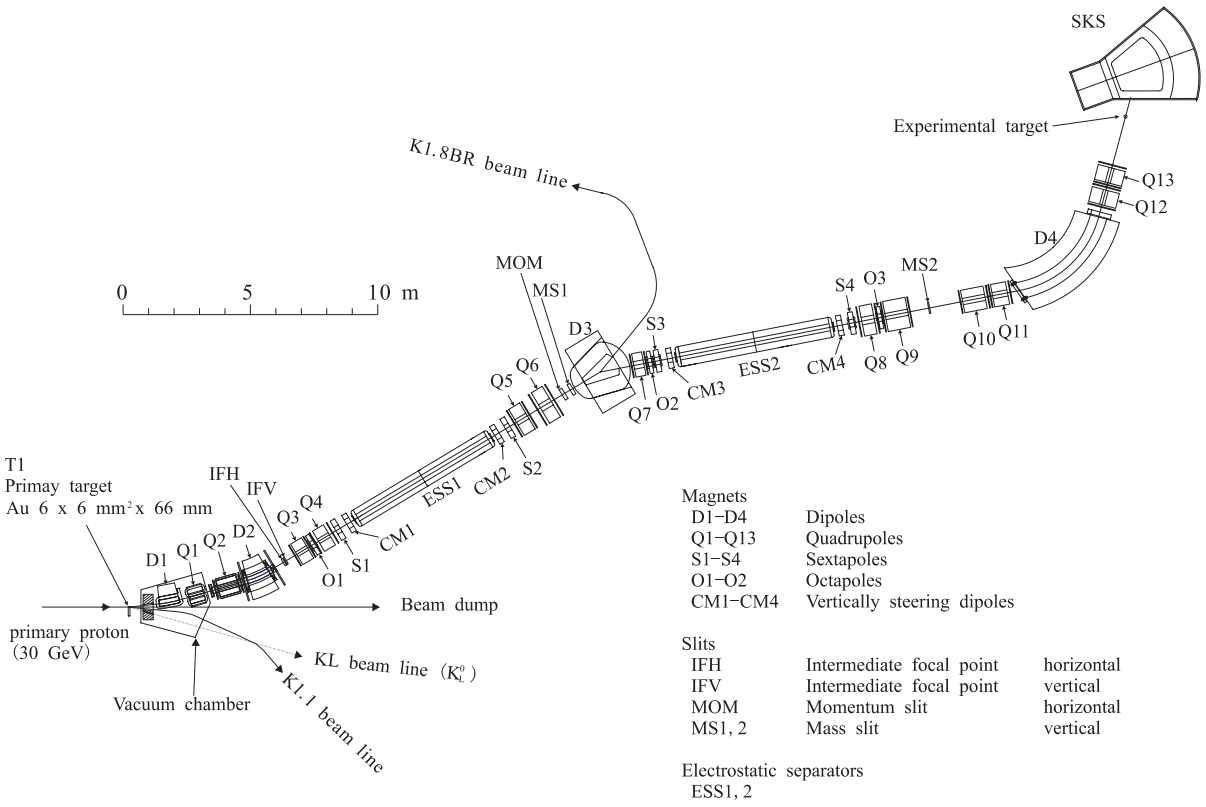

Figure 2.3: Schematic view of K1.8 Beam line.

The K1.8 beam line is a general-purpose mass-separated beam line that can supply secondary hadron beams of $K^{\pm}$, $\pi^{\pm}$, p and $\bar{p}$ up to 2.0 GeV/c [66, 67]. It was designed for a spectroscopic study of Ξ hypernuclei and a systematic study of the double strangeness systems by using the (K^-, K^+) reaction by achieving the $K^-/(\pi^- + \mu^-)$ ratio of larger than 1 at the kaon beam intensity of 10 MHz on an experimental target. In the present experiment, we used the π^+ beam at 1.69 GeV/c with a typical beam intensity of 3×10^6 per spill, where it was limited due to a non-uniform time structure of the beam.

Figure 2.3 shows a schematic view of the K1.8 beam line. The K1.8 beam line is composed of 4 sections: the front-end section, the first mass separation section, the second mass separation section, and the beam analyzer section. The total length of the beam line is about 46 m. The primary beam intensity on the production target was typically of 7.5×10^{12} proton/spill for the present experiment.

Front-end section

Front-end section from D1 to IFV is shown in Figure 2.3. Two dipole magnets (D1 and D2) and two quadruple magnets (Q1 and Q2) are installed. The extraction angle is chosen to be 6°, where the kaon production cross section is expected to be at the maximum.

Some of the beam line elements in this section are operated in a large vacuum tank of ∼1Pa.

The transported beam is vertically focused at the intermediate focus (IF) point. Both horizontal and vertical beam profiles are shaped with a horizontal (IFH) slit and a vertical (IFV) slit. The so-called cloud pions which are produced by the decay of K^0_s and the scattered pions by materials of the upstream section are rejected by these slits. This is one of the essential components in order to enhanced the purity of kaon. For the IF slits, 30-cm thick brass blocks are used.

Mass separation section

The first mass separation section is from Q3 to D3 and the second mass separation section is from Q7 to MS2 in Figure 2.3. The double-stage mass separation system is an essential component of the K1.8 beam line. In the mass separation section, a dipole magnet (D3), seven quadruple magnets (Q3–Q9), four sextuple magnets (S1–S4), three octupole magnets (O1–O3) and two electrostatic separators (ESS1 and ESS2) with four correction magnets (CM1–CM4) are located.

Two electrostatic separators are employed to separate kaons from pions in the first and second mass separation sections. An electrostatic separator generates a transverse electric field along the beam axis to separate particles of the same momentum by their mass differences. Each electrostatic separator generates an electric field in the 10 cm gap between parallel electrode plates with a size of 30 cm in width and 6 m in length. The maximum gradient of the electric field is 750 kV/cm adding He(36.9%)/Ne insulating gas in the chamber up to a few times 10^{-2} Pa. In this condition, the number ratio of the kaon over other particles such as pion and muon in the beam is expected to be 3.5 at the beam momentum of 1.8 GeV/c. In the present experiment, ESS1 and ESS2 were set at 200 kV/cm and 150 kV/cm, respectively.

The particle orbits are corrected by correction magnets (CM1–CM4) located both at the entrance and the exit of the electrostatic separators. After ESS1 and ESS2, the beam is focused in the vertical direction at each mass slit (MS1 and MS2). For the present pion beam experiment, the setting of correction magnets were adjusted to let pions only pass through the slit. A horizontal momentum slit (MOM) determines the momentum bite of the secondary particles.

Beam analyzer section

Beam analyzer section which is called as K1.8 beam line spectrometer with a QQDQQ magnet configuration is placed after the second mass slit, MS2. The beam is focused on an experimental target and the beam momenta are analyzed particle by particle.

In the present experiment, the central beam momentum was set at 1.69 GeV/c for the $d(\pi^+, K^+)$ reaction and a typical momentum bite was about 1.6% (FWHM), as shown in Figure 2.4. Figure 2.5 shows typical beam profiles at the experimental target in the present experiment. A typical beam size was 7.6 mm (horizontal)×4.2 mm (vertical) in σ. A liquid target, whose shape was cylindrical with 67.3 mm in diameter, fully covered the incident beam. The derivatives of the horizontal (dx/dz) and vertical (dy/dz)

directions on the experimental target position were 0.01 rad and 0.004 rad in rms (root-mean-square), respectively. Here, in the coordination system, x, y and z coordinates correspond to the horizontal, vertical and beam directions, respectively.

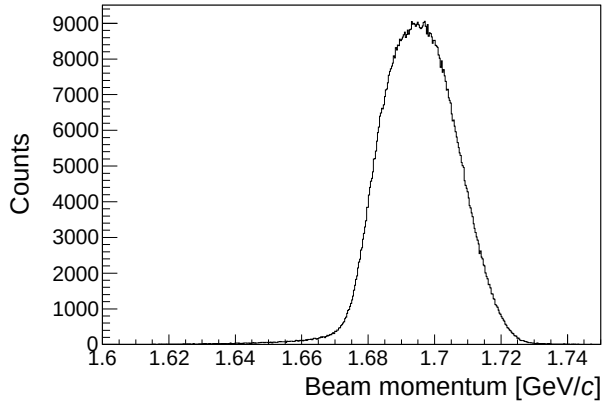

Figure 2.4: Typical beam momentum distribution of π^+ in the present experiment.

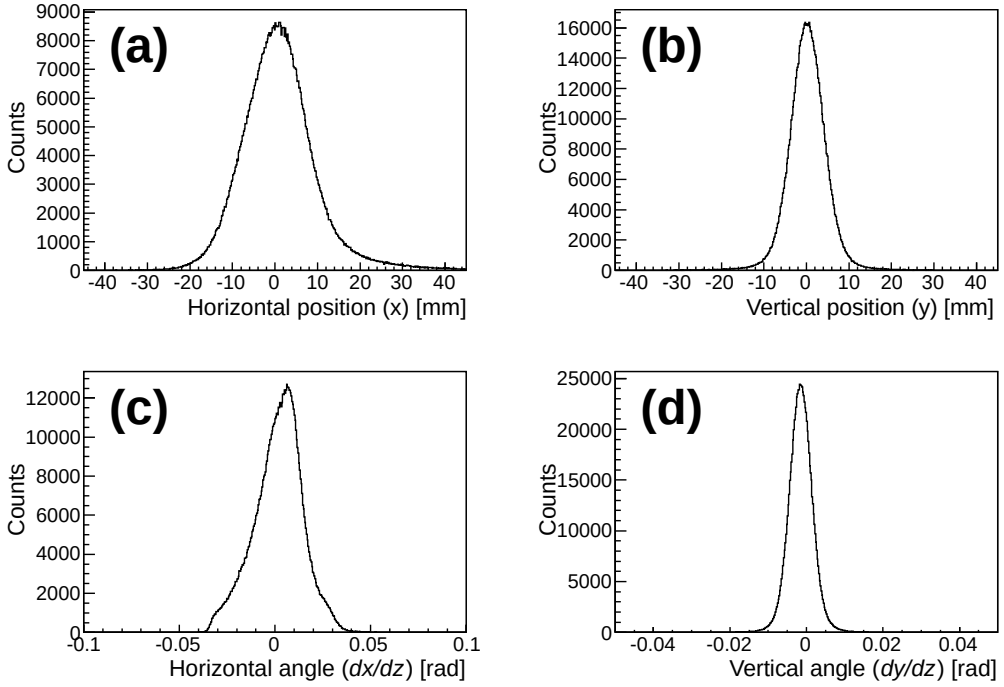

Figure 2.5: Typical beam profile at the experimental target in the E27 experiment measured by tracking chambers at the down stream of the K1.8 beam line spectrometer. The horizontal and vertical positions are shown in (a) and (b), respectively. The derivatives of the horizontal (dx/dz) and vertical (dy/dz) directions are shown in (c) and (d).

2.4 K1.8 beam line spectrometer

Overview

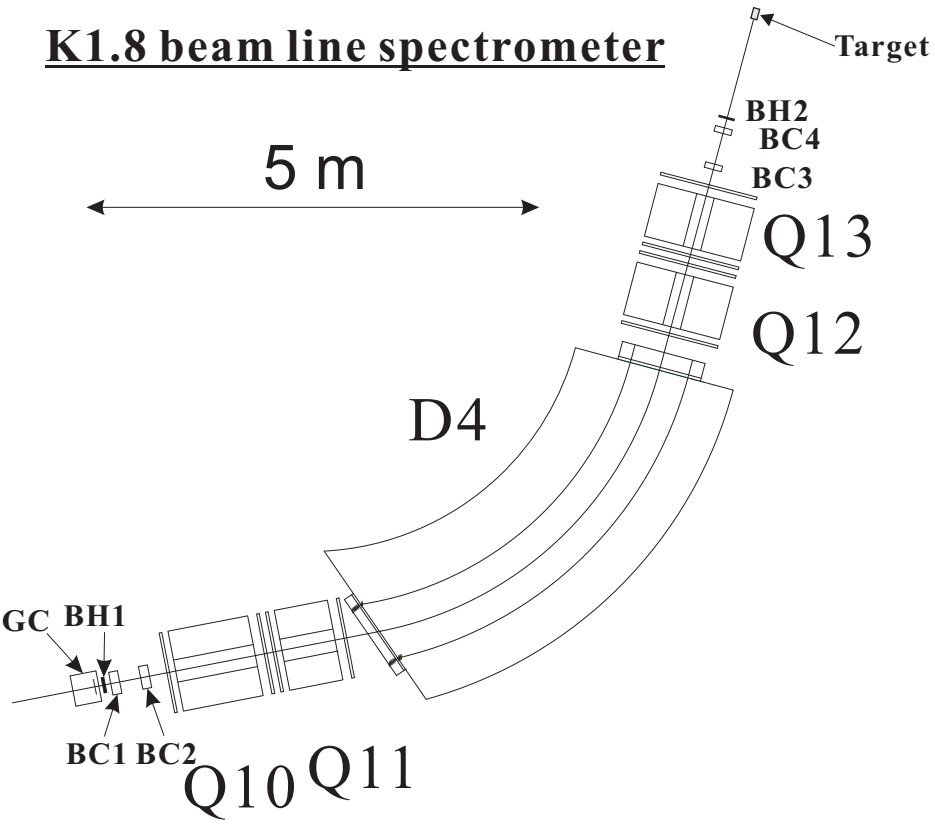

Figure 2.6: Schematic view of K1.8 beam spectrometer.

The end-part of the K1.8 beam line is used as a beam spectrometer [75] to analyze momentum and trajectory of each beam particle. Figure 2.6 shows a schematic view of the K1.8 beam spectrometer. The K1.8 beam line spectrometer consisted of a gas Čerenkov counter (GC), a timing plastic scintillation hodoscope (BH1 and BH2), two MWPCs (BC1 and BC2), QQDQQ magnets and two drift chambers (BC3 and BC4).

Beam trajectories are measured by two sets of wire chambers at the entrance (BC1, 2) and exit (BC3, 4) of the K1.8 beam line spectrometer for momentum analysis and reaction vertex reconstruction. For the momentum reconstruction, a third-order transfer matrix was used through the QQDQQ system. A vacuum chamber and ducts are installed in the magnet region and the vacuum windows are made of 0.1 mm thick SUS. Point-to-point optics is realized between the entrance and exit of the QQDQQ system. Therefore, the multiple scattering at the entrance and exit of the QQDQQ does not affect the momentum resolution to the first order. The design momentum resolution is 3.3×10^{-4}(FWHM) with the position accuracy of 0.2 mm(rms) [75]. The magnetic field of the dipole magnet (D4) was monitored during the experiment with a high-precision Hall probe [Digital Teslameter 151 (DTM-151)] with the accuracy of 1.7×10^{-6} [76]. The

Table 2.1: Design specifications of the K1.8 beam line spectrometer

Momentum resolution	3.3×10^{-4}(FWHM)
Maximum momentum	2.0 GeV/c
Bending angle	64°
Flight path (BH1−BH2)	10.4 m
Effective length (D4)	4 m

observed fluctuation ($\frac{\Delta B}{B}$) was less than 0.05%. Design specifications of the K1.8 beam line spectrometer are listed in Table 2.1.

Trigger counters

Three sets of trigger counters (GC, BH1, and BH2) are installed for particle identification. Specifications of the trigger counters of K1.8 beam line spectrometer are listed in Table 2.2.

Table 2.2: Specifications of the trigger counters of the K1.8 beam line spectrometer

Name	Sensitive area W×H×T (mm)	Spec.	PMT (Hamamatsu)
GC	340×80(mirror), 290^L	iso-C_4H_{10}, n∼1.002 (1.5 atm)	R1250-03 (UV glass)
BH1	170×66×5	11 segments, 3-stage booster	H6524MOD
BH2	145×60×5	7 segments, 3-stage booster	H6524MOD

Gas Čerenkov counter

Although the beam particles are selected by using the time-of-flight between BH1 and BH2, electrons or positrons cannot be separated from pions over the beam momentum of 1 GeV/c. Thus, a gas Čerenkov counter (GC) is necessary for pion beam experiments in order to reject electrons or positrons. It was installed at the most upstream of the K1.8 beam line spectrometer. Figure 2.7 shows a schematic view of GC. An isobutane gas of 0.15 MPa was used as the radiator. The reflection mirror was a borosilicate glass evaporated with aluminum. In order to protect aluminum from the oxidation, the surface is coated with the manganese fluoride (MgF_2) which is transmissive to the ultraviolet-light region. In addition, the UV transparent window PMT was equipped in order to increase the detection efficiency. The configuration of the mirror and the PMT was optimized to focus the Čerenkov radiation on to the photo-cathode of the PMT.

The measured number of photo-electrons was approximately 5 for electrons of ≥ 0.5 GeV/c. The efficiency of GC for electrons and positrons was found to be 99.5%. It was enough to reject the electron (or positron) contamination of 12−14% in the beam.

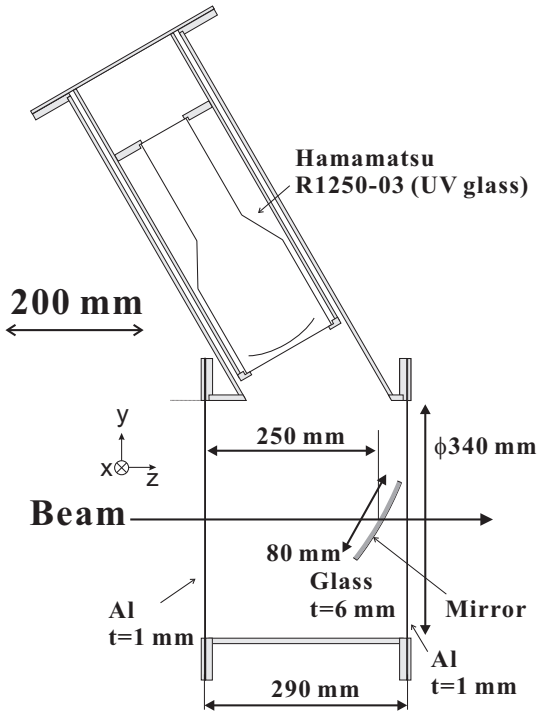

Figure 2.7: Schematic view of GC.

BH1 and BH2 counter

Beam particles were identified by the time-of-flight measurement between plastic scintillator hodoscopes of BH1 and BH2. BH1 and BH2 were installed upstream of BC1 and downstream of BC4, respectively. The flight length was 10.4 m, where the time difference between kaons and pions is 1.3 ns at 1.69 GeV/c.

BH1 was segmented into 11 vertical pieces of 5 mm-thick plastic scintillators with different widths of 8, 12, 16 and 20 mm, as shown in Figure 2.8. The width of each segment was adjusted for the single counting rate to be uniform. Each segment was overlapped with its adjacent segments by 1 mm to avoid a dead space and the effective area was 170 mm (horizontal) $\times$ 66 mm(vertical). H1650MOD phototubes equipped with a three-stage booster, were connected on both ends of each scintillator.

BH2 was composed of 7-segment plastic scintillators with 5-mm thickness and different widths of 15, 20 and 30 mm, as shown in Figure 2.8. It defined the start timing for all timing measurements. In the case of BH2, there were no overlapping in order to avoid the position dependence of the energy losses caused by the overlappings. The effective area was 145 mm (horizontal) $\times$ 60 mm(vertical). The same phototubes as the BH1 were connected on both ends of each scintillator.

Tracking wire chambers

Specifications of the tracking wire chambers in the K1.8 beam line spectrometer are summarized in Table 2.3. MWPCs (BC1, 2) were placed at the entrance of the QQDQQ

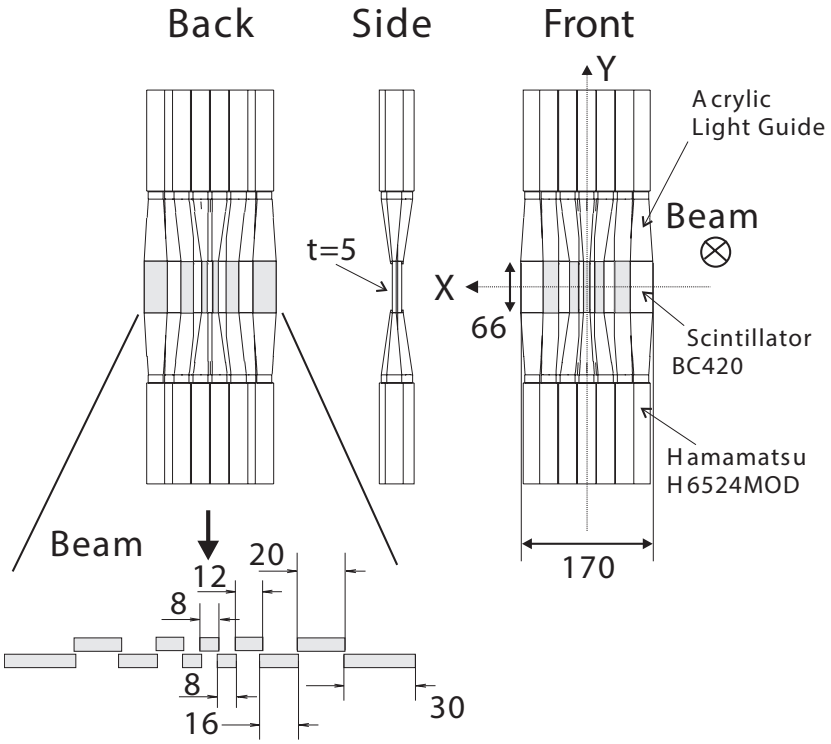

Figure 2.8: Schematic view of BH1.

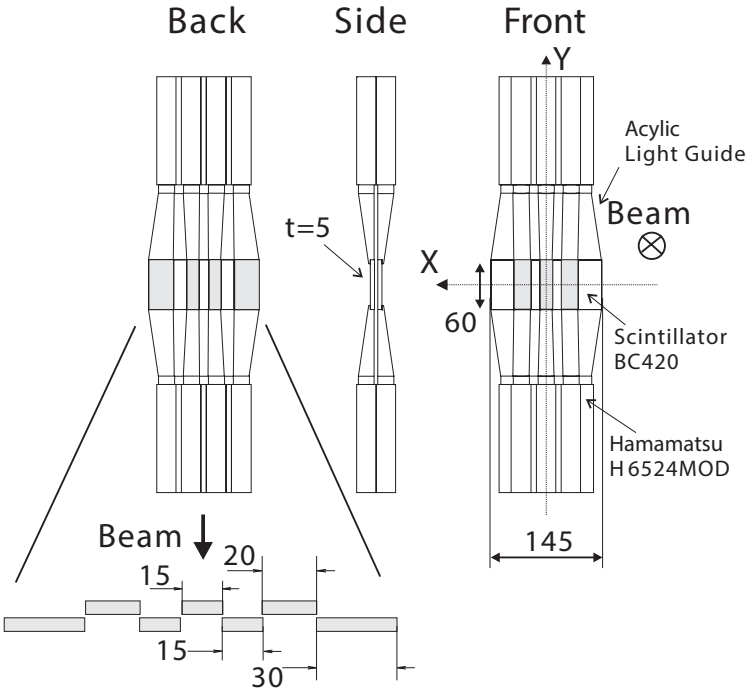

Figure 2.9: Schematic view of BH2.

magnet system and drift chambers (BC3, 4) at the exit. The structure of the tracking wire chambers are shown in Figure 2.10.

Table 2.3: Specifications of the MWPC (BC1, 2) and the drift chambers (BC3, 4) of the K1.8 beam line spectrometer

Name	Area W×H (mm)	Anode pitch or Drift length (mm)	Wires	Angle (x, u, v) (°)	Resol. (expected) (μm in σ)
BC1	256×150	1 mm pitch	$xvuxvu$	0, +15, −15	300
BC2	256×150	1 mm pitch	$vuxvux$	0, +15, −15	300
BC3	192×100	1.5	$xx'vv'uu'$	0, +15, −15	200
BC4	240×150	2.5	$vv'uu'xx'$	0, +15, −15	200

BC1, 2 (MWPC)

Tracking device should be operated under a very high counting rate of 10–20 MHz at the entrance of K1.8 beam line spectrometer. In order to handle such a high counting rate, MWPC with the anode pitch size of 1 mm and the cathode gap size of 3 mm was constructed. This pitch size is almost at the technical limit to allow some space for soldering. The gap between the anode wires and the cathode planes was determined to be 3 mm from a balance between preventing the discharge and maintaining the gain with a low operation voltage. The sense wires were a gold-plated 15 μm-diameter tungsten wire. These anode wires were fixed on the G10 frame with a thickness of 3 mm. In order to suppress damage of the cathode by discharge, the cathode planes were made of 20 μm-thick graphite pasted on 12 μm-thick aramid film.

The assembled structure of the BC1, 2 is shown in Figure 2.10(a). The MWPCs had 6 layers (x, u, v, x, u, v) configuration, where x plane measured the horizontal position. The u and v planes were tilted by $\pm 15°$ with respect to the x plane. The front-end read-out electronics for both MWPC and MWDC were made of ASD (Amplifier-Shaper-Discriminator) chips with 16 ns integration time developed for ATLAS Thin Gap Chamber [77]. The timing information of the BC1, 2 hit was digitized by the MWPC encoder installed in COPPER modules [78].

The gas mixture for both MWPCs and MWDCs was Ar (76%) + C_4H_{10} (20%) + Methylal (4%). The operation voltages of MWPCs were set to be −2.5 kV.

BC3, 4 (MWDC)

At the exit of the K1.8 beam spectrometer, the wire chambers have to be operated at several MHz. Thus, a 3-mm anode-wire-spacing (1.5 mm drift distance) drift chamber was chosen as BC3. Figures 2.10(b) and 2.10(c) show the structure of BC3. For BC4, we used a drift chamber with the anode wire pitch of 5 mm used in the previous KEK-PS experiments [79]. For both BC3 and BC4, the sense wire was a gold-plated 12.5 μm-diameter tungsten wire and the field wire was a gold-plated 75 μm-diameter copper-

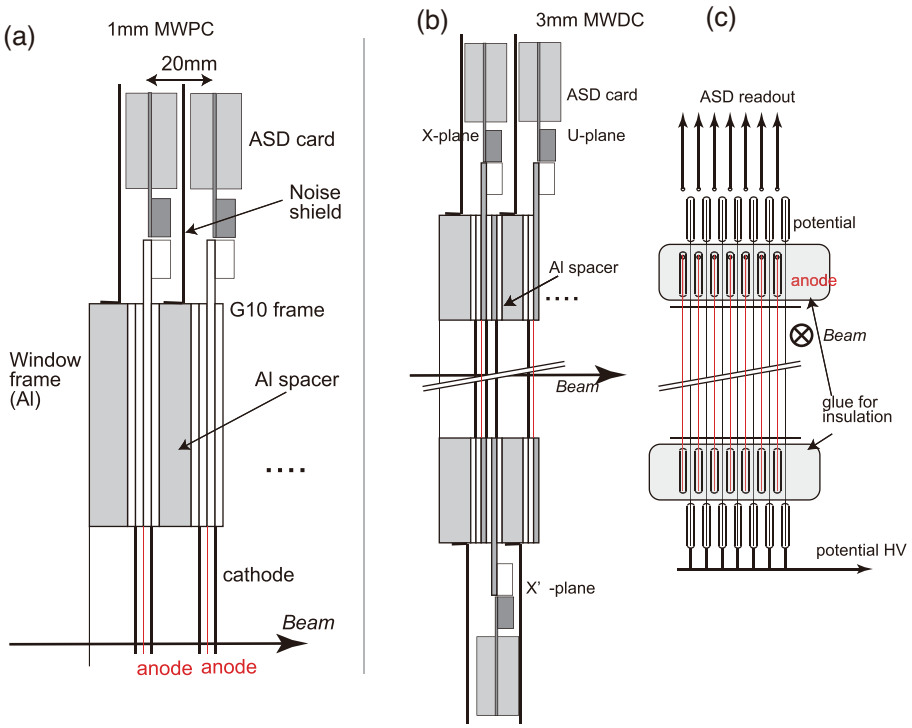

Figure 2.10: (a) Structure of the BC1, 2 (MWPC). (b) Side view of the BC3 (MWDC). (c) Front view of the wire frame of the BC3 (MWDC) [75].

beryllium wire. The cathode planes of BC3 were made of 20 μm-thick graphite pasted on 12 μm-thick aramid film. The optimal cathode pitch size was 1.7 mm based on the studies from the previously used drift chamber with the anode wire pitch of 5 mm. By considering the manufacturing accuracy, the pitch size was determined to be 2 mm. The drift chambers have 6 layers (xx', uu', vv') as same as the MWPCs. The wire position of each pair plane was shifted by a half of the cell size to resolve L/R ambiguity. The timing information of the BC3, 4 hit was digitized by the TKO Multi-hit TDC module. The BC3 was operated at the cathode and potential wire high voltage of -1.22 kV and -1.25 kV, respectively. In case of BC4, the high voltage of -1.40 kV were applied at both cathode and potential wires.

2.5 Superconducting kaon spectrometer (SKS)

Overview

The emitted kaon in the (π^+, K^+) reaction was measured by using the superconducting kaon spectrometer (SKS). The SKS was constructed for the study of Λ-hypernuclei with the (π^+, K^+) reaction [80].

In the present measurement, the SKS magnetic field was set at 2.36T. Design parameters of the SKS at the 2.36 T mode are summarized in Table 2.4. In this mode, emitted particles in the momentum range of 0.8–1.3 GeV/c with a scattering angle between 2° and 16° were analyzed. The very forward events (less than 2°) were cut out in order to keep good vertex resolution and suppress beam-oriented backgrounds in the (π^+, K^+) events, such as μ^+ from π^+ decay and secondary particles produced from various support structures. By using SKS, the particle momenta were measured with a resolution of about 0.2% (FWHM) in an acceptance of about 100 msr. In addition, it kept the flight path as short as 5.5 m for the central trajectory in order to minimize kaon decay-in-flight. The SKS enables us to realize the high energy resolution and high statistic experiments.

Table 2.4: Design specifications of the SKS spectrometer at the 2.36 T mode.

Maximum magnetic field	2.5 T
Stored energy	6.3 MJ
Pole gap	49.75 cm
Conductor	NbTi/Cu
Ampere Turn	2.1 MA·T
Maximum current	400 A
Total weight	280 t
Momentum resolution	0.2% FWHM at 1.1 GeV/c
Momentum range	0.8–1.3 GeV/c
Bending angle	85° for central trajectory
Solid angle	∼100 msr
Flight path	∼5.5 m for central trajectory

The SKS spectrometer consisted of four sets of drift chambers (SDC1, SDC2, SDC3 and SDC4), a superconducting magnet (SKS magnet), a timing plastic scintillator hodoscope (TOF), a beam veto hodoscope (BVH) and two threshold-type Čerenkov counters (LAC and LC). The kaon momentum was calculated by using the Runge-Kutta method with a calculated field map. The kaon was identified by time-of-flight between BH2 and TOF in combination of with the flight-path length for each track. The background particles which were produced after the beam hit the SDC4 support frame were suppressed by using the BVH plastic scintillator hodoscope at the trigger level. In order to reduce multiple scattering effects on the momentum resolution, helium bags were installed in the spaces along the particle trajectory (the SKS pole gap and the space between SDC3 and the SKS magnet). The magnetic field was monitored with an NMR

probe during the experiment to correct for the fluctuation of the field in the offline analysis. The accuracy of the NMR probe is 1.0×10^{-6} [81].

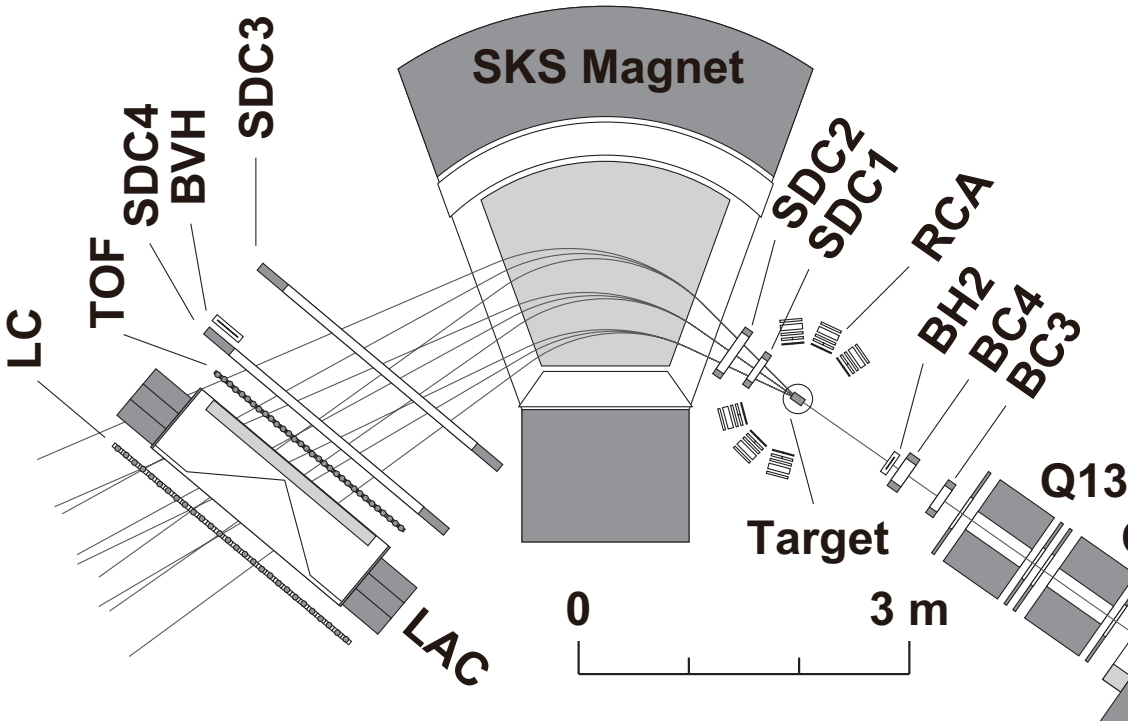

Figure 2.11: Schematic view of SKS. SDC1–4 were drift chambers. TOF was a plastic scintillation counter hodoscope for the time-of-flight measurement. LAC was aerogel Čerenkov counter (n=1.05). LC was a Lucite (Acrylic) Čerenkov counter (n=1.49). RCA was installed surrounding the target in order to detect the decayed particles.

Trigger counters

Specifications of the trigger counters in SKS are listed in Table 2.5. In the trigger, a combination of three kinds of trigger counters were used to identify pions, kaons and protons. The TOF counter is sensitive to all charged particles, LAC are sensitive only to pions, and LC is insensitive to protons.

Table 2.5: Specifications of the particle identification counters in the SKS spectrometer

Name	Sensitive area W×H×T (mm)	Specification	PMT (Hamamatsu)
TOF	2240×1000×30	32 segments	H1949
LAC	1050×1200×113	Aerogel; n=1.05	R1584-02, (Burle)-8854
LC	2800×1400×40	28 segments, Acrylic; n=1.49	H1949, H6410
BVH	240×150×5	4 segments	H6524MOD

TOF

TOF is a segmented plastic scintillation hodoscope located at just a downstream of SDC4 to identify scattered particles by the time-of-flight measurement with BH2. Figure 2.12 shows a schematic view of TOF. The TOF counter was horizontally segmented into 32 pieces of 70×1000×30 mm^3 scintillators. The signal of each segment was detected by phototubes (H1949) on the top and bottom sides. A typical time-of-flight resolution between TOF and BH2 was measured to be 150 ps (rms). This is sufficient to separate the scattered pions, kaons and protons.

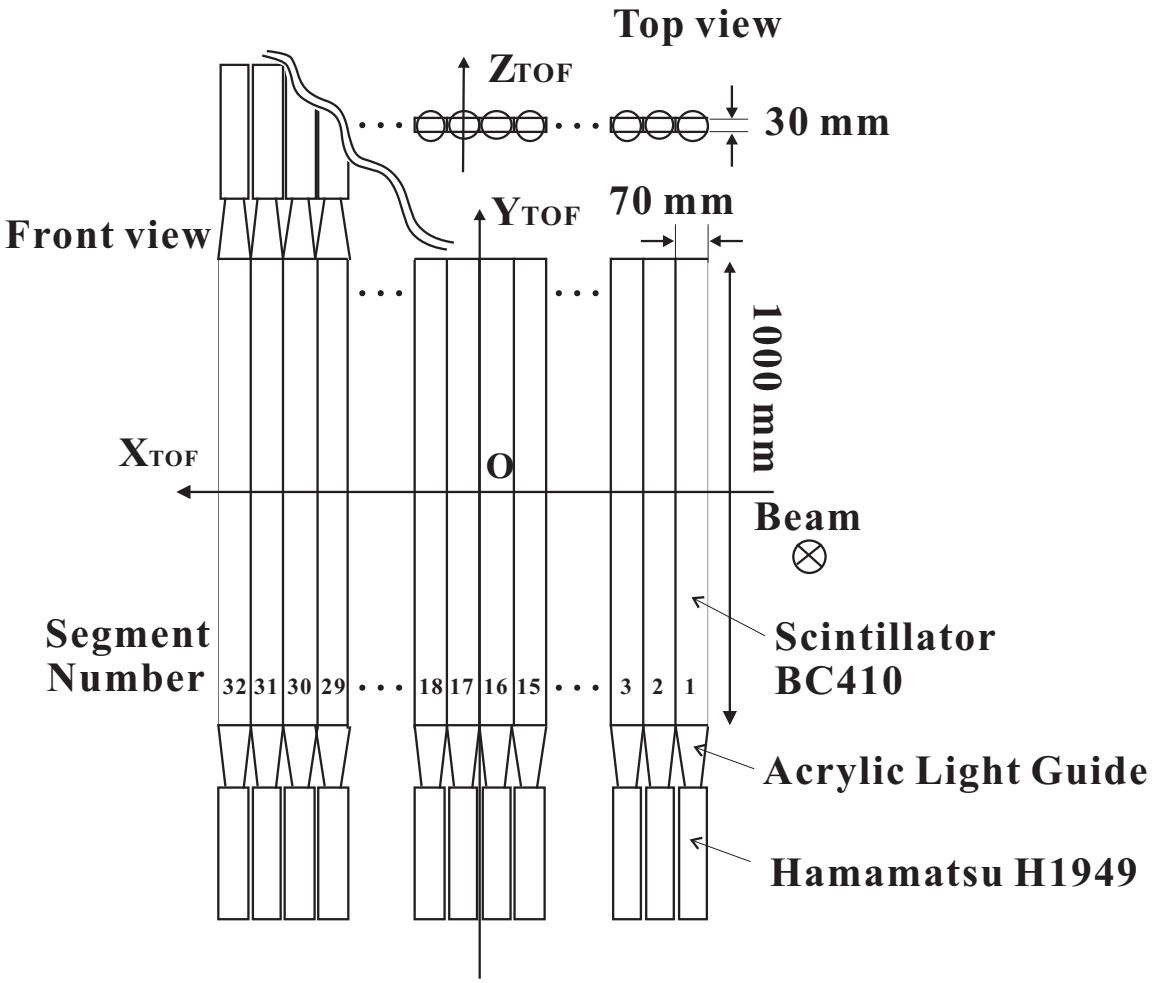

Figure 2.12: Schematic view of TOF.

LAC

LAC is a threshold-type silica aerogel Čerenkov counter to select kaons in the trigger level. As shown in Figure 2.13, pions with a threshold of 0.45 GeV/c were rejected by the reflactive index of silica aerogel of 1.05. LAC was installed just behind of the TOF counter. Figure 2.14 shows a schematic view of LAC. The sensitive area of LAC was 1050×1200×113 mm^3. For the uniform efficiency without any dead space over a large sensitive area, LAC was not segmented but of a large one-box type. 5-inch phototubes (Hamamatsu-R1584 and Burle-8854) which were sensitive to a single photon were placed on both sides. The number of photo electrons was typically 6 over the whole area for scattered pions at 0.9 GeV/c.

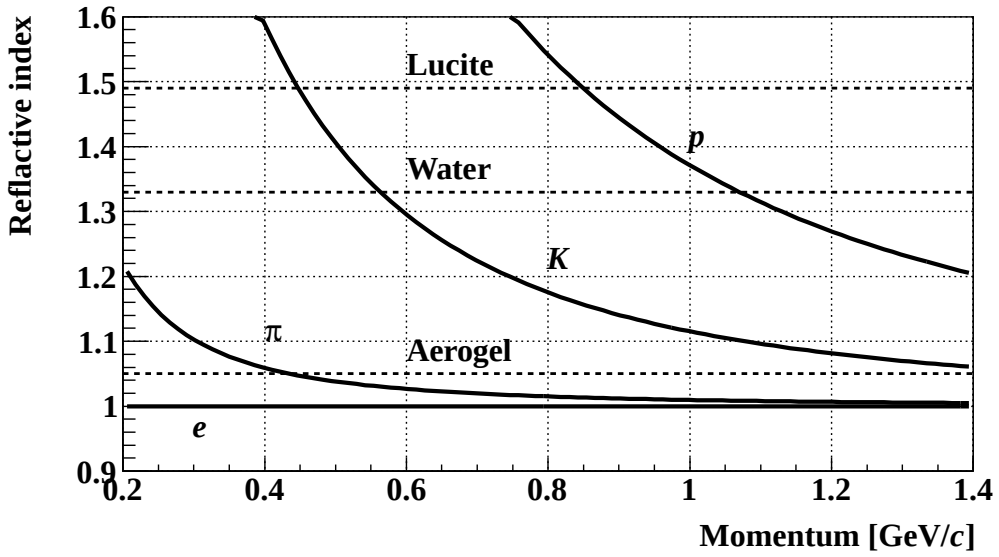

Figure 2.13: Threshold and refractive index for Čerenkov radiation as a function of the momentum.

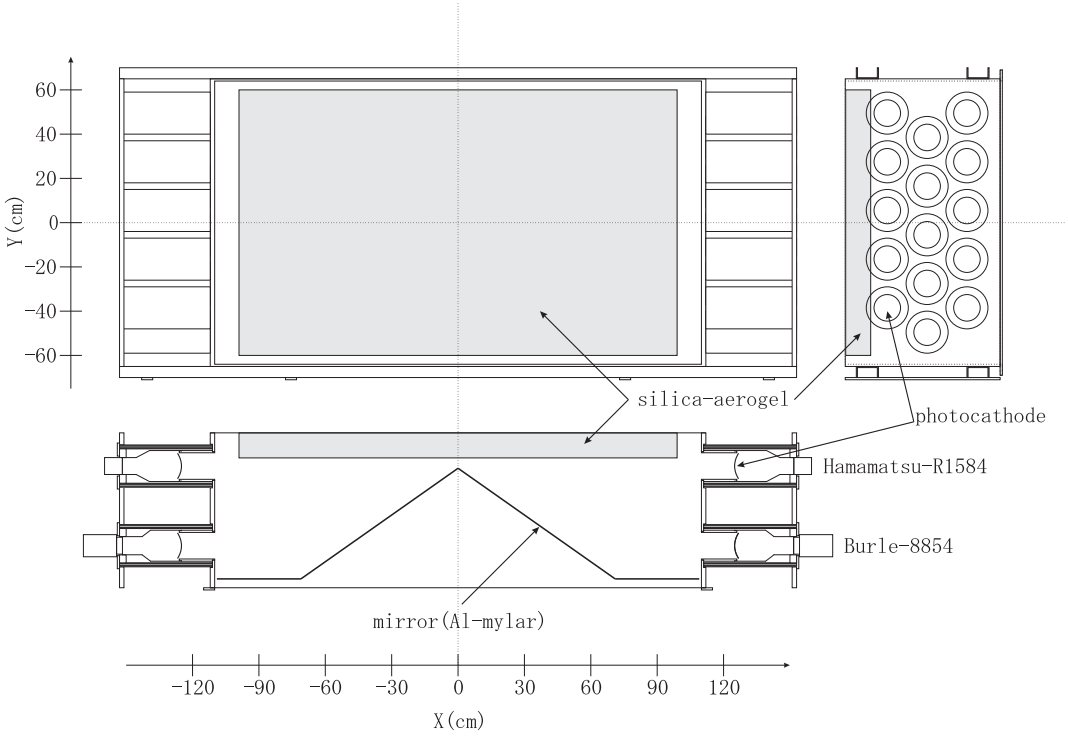

Figure 2.14: Schematic view of LAC.

LC

LC is a threshold-type Čerenkov counter installed just downstream of LAC. Figure 2.15 shows a schematic view of LC. It was segmented into 28 vertical pieces of 100×1400×40 mm^3 Lucite (Acrylic) radiator with the reflection index of 1.49. Each segment is equipped with fast phototubes (H1949) on the top and bottom sides. As shown in Figure 2.13, most of protons slower than 0.85 GeV/c were rejected.

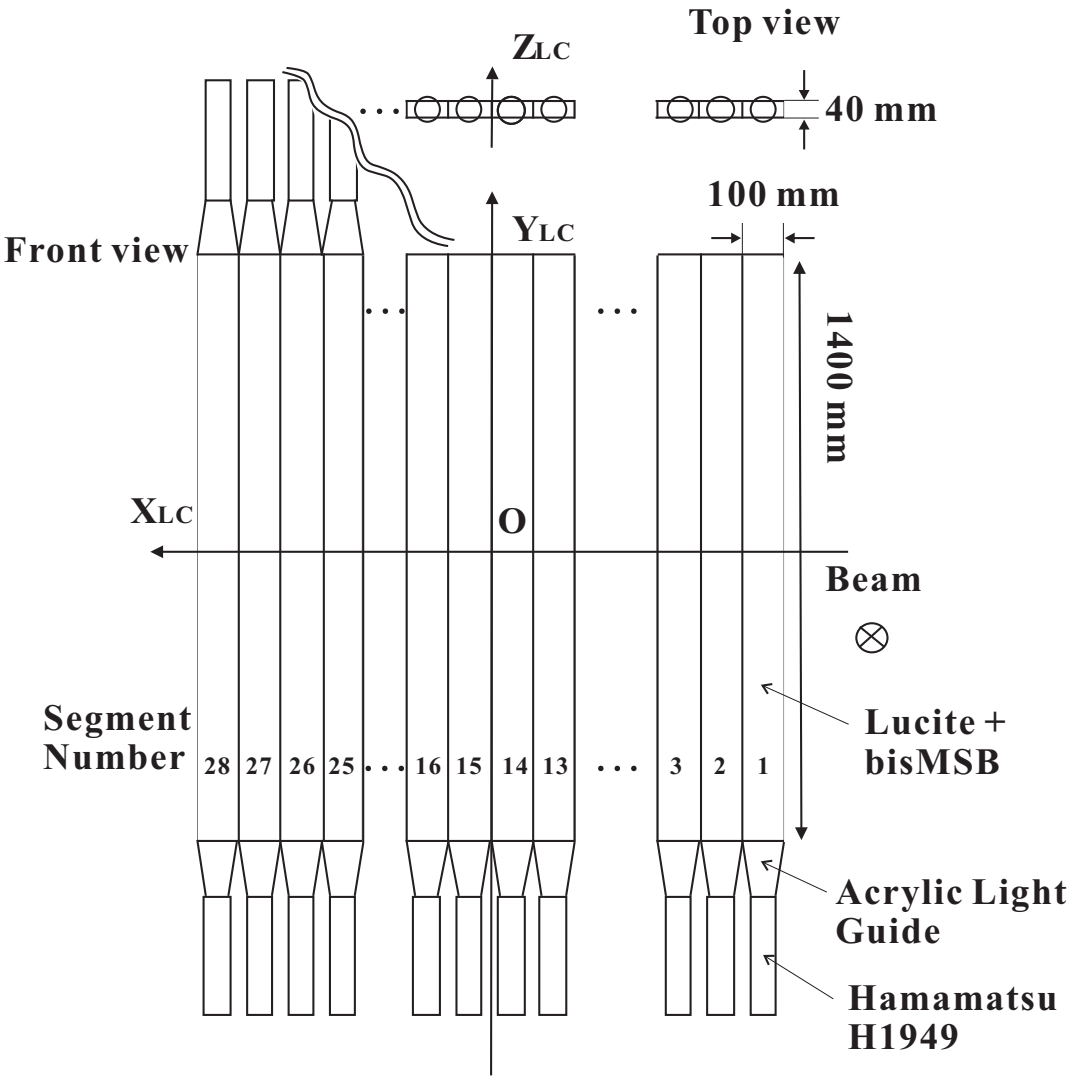

Figure 2.15: Schematic view of LC.

BVH

BVH is a segmented plastic scintillation hodoscope located at just upstream of SDC4 to reduce the background trigger rate. Figure 2.16 shows a schematic view of BVH. BVH was horizontally segmented into 4 pieces of $60 \times 150 \times 5$ mm^3 scintillators. Phototube (H6524MOD), which was same as BH1 and 2, was connected on bottom side of each segment.

Figure 2.17 shows the typical trajectories of the background particles produced after the beam hits the SDC4 frame and made fake triggers. The green arrows show the typical trajectories of these background particles. BVH was installed on the beam trajectories at $p_{\pi^+} = 1.69$ GeV/c as shown in Figure 2.17.

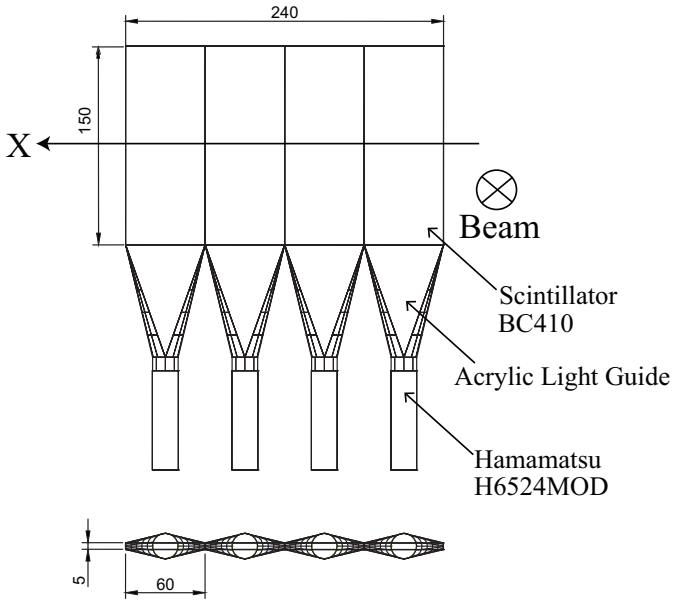

Figure 2.16: Schematic view of BVH.

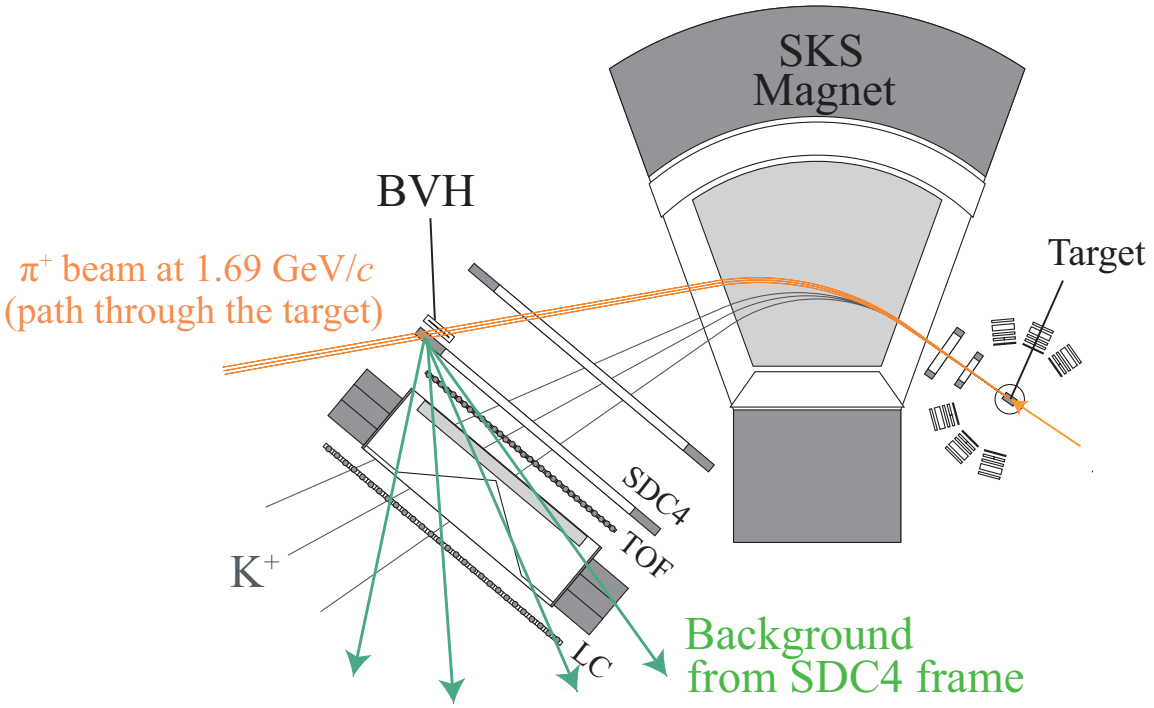

Figure 2.17: Typical trajectories of the background particles. The beam trajectories in the SKS with beam momentum of 1.69 GeV/c are shown in orange lines. The background particles were produced after the beam hits the SDC4 frame and made fake triggers, as shown in green arrows. Typical tracks of emitted K^+ are also shown in black lines.

Tracking chambers

Specifications of the tracking chambers of the SKS are summarized in Table 2.6.

SDC1, 2

At the entrance of the SKS magnet, two sets of drift chambers (SDC1 and SDC2) were installed. SDC1 was the same as BC3 except that it has four layers (v, v', u, u') configuration. The SDC2 was similar to SDC1 except for its wire spacing, the anode wire pitch of SDC2 was 5 mm. For both SDC1 and SDC2, the sense wire was gold-plated 12.5 μm-diameter tungsten wire, and the field wire was gold-plated 75 μm-diameter copper-beryllium wire, and the cathode planes were made of 20 μm-thick graphite pasted on 12 μm-thick aramid films. The SDC2 had 6 layers of xx', uu', vv', where u and v wires were tilted $\pm 15°$ with respect to the x wires. Since the SDC1 and SDC2 were in line with the beam, the gas mixture and read-out electronics were the same as those of beam line chambers.

Table 2.6: Specifications of the drift chambers of the SKS.

Name	Area W×H (mm)	Anode pitch or Drift length (mm)	Wires	Angle (x, u, v) (°)	Resol. (μm in r.m.s)
SDC1	192×100	1.5	$vv'uu'$	0, +15, −15	200
SDC2	400×150	2.5	$vv'uu'xx'$	0, +15, −15	200
SDC3	2140×1140	10	$vxuvxu$	0, +30, −30	300
SDC4	2140×1140	10	$vxuvxu$	0, +30, −30	300

Gas mixture (SDC1, 2); Ar(76%) + C_4H_{10}(20%) + Methylal(4%)
Gas mixture (SDC3, 4); Ar(50%) + C_2H_6(50%)

SDC3, 4

Large-sized drift chambers (SDC3, 4) were installed at the exit of the SKS magnet. These drift chambers, which had been used in the BNL-AGS experiment [82], were moved to J-PARC. The size of the effective area was 2140×1140 mm^2, being twice larger in length than in the previous SKS one. All anode wires were replaced to the larger diameter (20μm → 25μm) wires for more strength. The drift space was 10 mm and its cell structure is shown in Figure 2.18. The high voltage of potential wires was set at −350 V and −450 V and the anode high voltage was applied at +2.2 kV. The anode wire was a gold-plated 25 μm-diameter tungsten wire, and both field wire and cathode wire were gold-plated 80 μm-diameter copper-beryllium wire. The pith of the cathode wires was 2 mm. SDC3 and SDC4 had 6 layers (x, x, u, u, v, v), where u and v wires were tilted ±30° with respect to the x wires. The front-end read-out electronics of SDC3, 4 was made of ASD chips. The timing information of the SDC3, 4 hit was digitized by the TKO Dr.TII TDC module

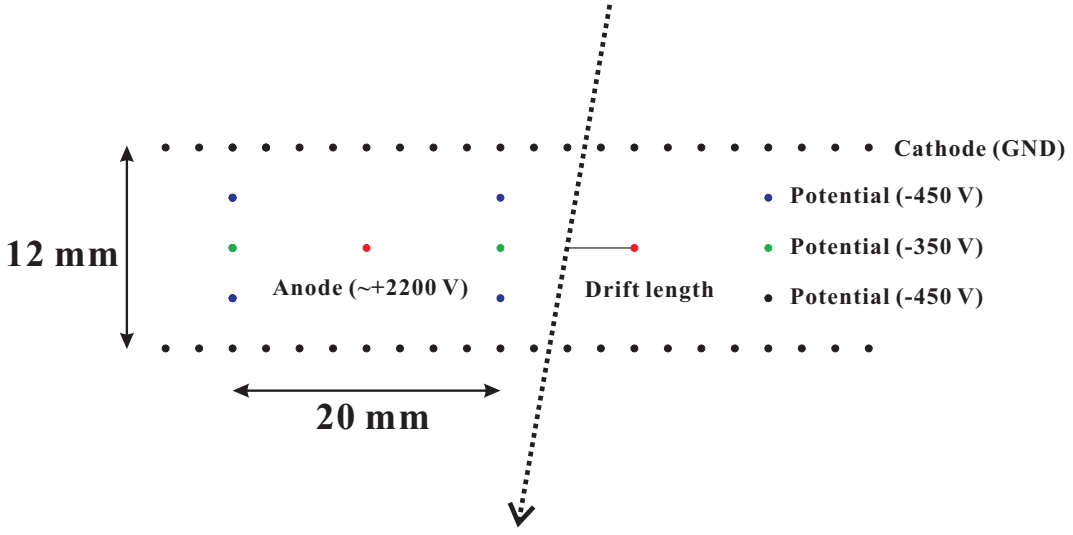

Figure 2.18: The cell structure of SDC3, 4.

2.6 Liquid hydrogen and deuterium target

In order to use pure proton and deuteron targets, we used the liquid target system which was used in the KEK E559 experiment [83]. A liquid deuterium target of 1.99-g/cm^2 thickness was used for the $d(\pi^+, K^+)$ reaction at 1.69 GeV/c, and a liquid hydrogen target of 0.85-g/cm^2 thickness for the $p(\pi^+, K^+)$ reactions at 1.58 and 1.69 GeV/c for calibrations. Specifications of the liquid hydrogen and deuterium target were listed in Table 2.7.

Table 2.7: Specifications of the liquid hydrogen and deuterium target.

Size	$\phi 67.3 \times 120^L$ mm
Capacity	427 cm^3
Material	PET(cylinder), Mylar(end cap)
Average thickness	0.3 mm(cylinder), 0.25 mm(end cap)
Target chamber	Aluminium; t=3 mm, ϕ270 mm
	Window(Mylar); t=0.25 mm
Vacuum	$\sim 1.0 \times 10^{-7}$ mbar
LH_2 thickness	0.85 g/cm^2 (0.0708 g/cm^3 $\times$12 cm)
LD_2 thickness	1.99 g/cm^2 (0.166 g/cm^3 $\times$12 cm)
Mylar thickness	0.0695 g/cm^2 (1.39 g/cm^3 $\times$0.025 cm$\times$2)

Figure 2.19 shows a schematic view of the liquid hydrogen target. The target shape was cylindrical; 67.3 mm in diameter and 120 mm in length. The target fully covered the incident beam with a typical beam size of $\sigma_{\rm H} = 7.6$ mm (horizontal) and $\sigma_{\rm V} = 4.2$ mm (horizontal). Its cooling system uses liquid helium. The hydrogen vessel was made from PET (polyethylene terephthalate) of 0.30 mm thickness for the cylinder part, and Mylar of 0.25 mm thickness for the end cap. The pressure of the target was monitored during the experimental period.

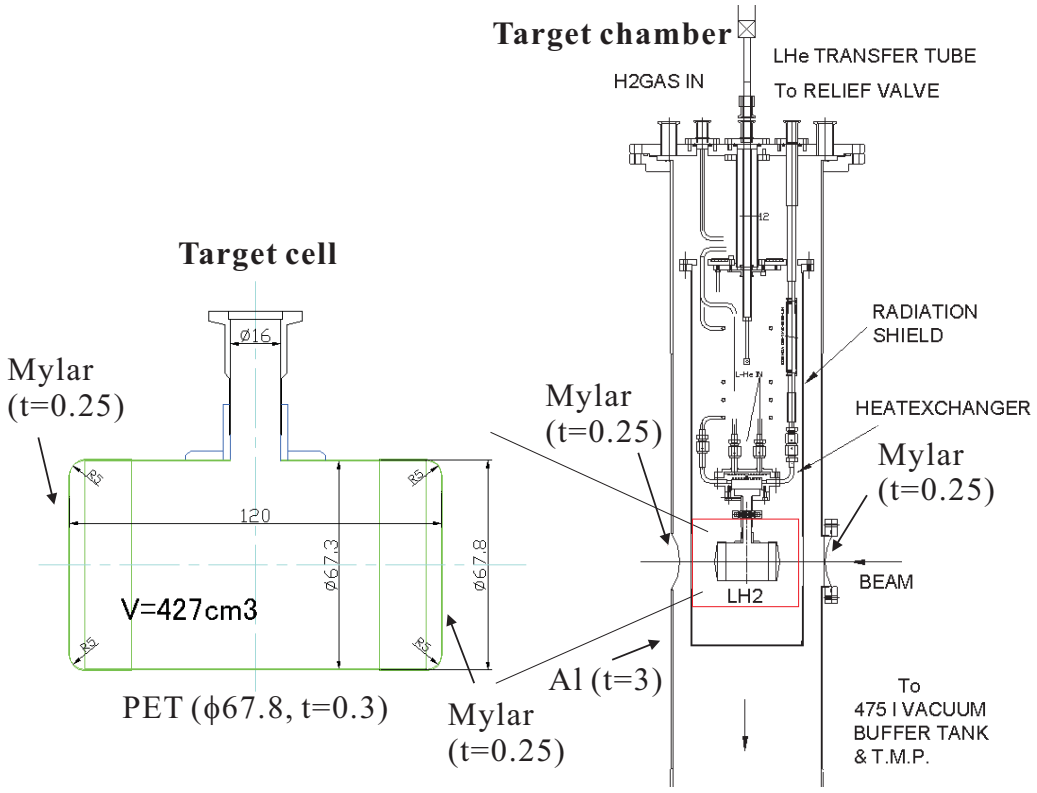

Figure 2.19: Schematic view of the liquid hydrogen and deuterium target (units in mm).

2.7 Range counter array (RCA)

In the $d(\pi^+, K^+)$ reaction, there are background processes of quasi-free hyperons (Λ and Σ's), hyperon resonances ($\Lambda(1405)$ and $\Sigma(1385)$'s) and non-resonant ($\Lambda\pi$ and $\Sigma\pi$) productions. Thus, we have to reduce these background processes by detecting the decay particles of the K^-pp. The K^-pp is expected to decay to non-mesonic modes such as Λp and $\Sigma^0 p$. In such non-mesonic decays of the K^-pp, a proton or two protons can be produced as "K^-pp"$\rightarrow \Lambda p \rightarrow p\pi^- p$. On the other hand, a proton can be produced from the decay of hyperon such as $\Lambda \rightarrow p\pi^-$ in the quasi-free processes (background). Moreover, a proton can be also produced as a spectator in the quasi-free backgrounds. However, the proton kinematics between the K^-pp and quasi-free backgrounds is different.

Figure 2.20 (a) shows a scatter plot between momentum and scattering angle in xz plane, where x and z coordinates correspond to the horizontal and beam directions, of the proton from the decay of Λ in one of the quasi-free processes of π^+"n"$\rightarrow K^+\Lambda\pi^0$ reaction. Figure 2.20 (b) shows the same scatter plot of the proton from the "K^-pp"$\rightarrow \Lambda p \rightarrow p\pi^- p$ mode. As shown in these figures, the proton's scattering angle in the quasi-free background processes concentrates in the forward angle. On the other hand, the proton produced from the K^-pp decay such as $K^-pp \rightarrow \Lambda(\Sigma^0)p$ can distribute in a wide scattering-angle region. Moreover, the proton's momentum of the spectator is small ($p_{proton} \lesssim 250$ MeV/c). Almost all the spectator protons would stop in the deuterium target. Thus, we can reduce the quasi-free background processes by measuring the large scattering angle and high-momentum proton. Furthermore, we can detect the K^-pp signal free from the quasi-free backgrounds by measuring two protons in large scattering angles.

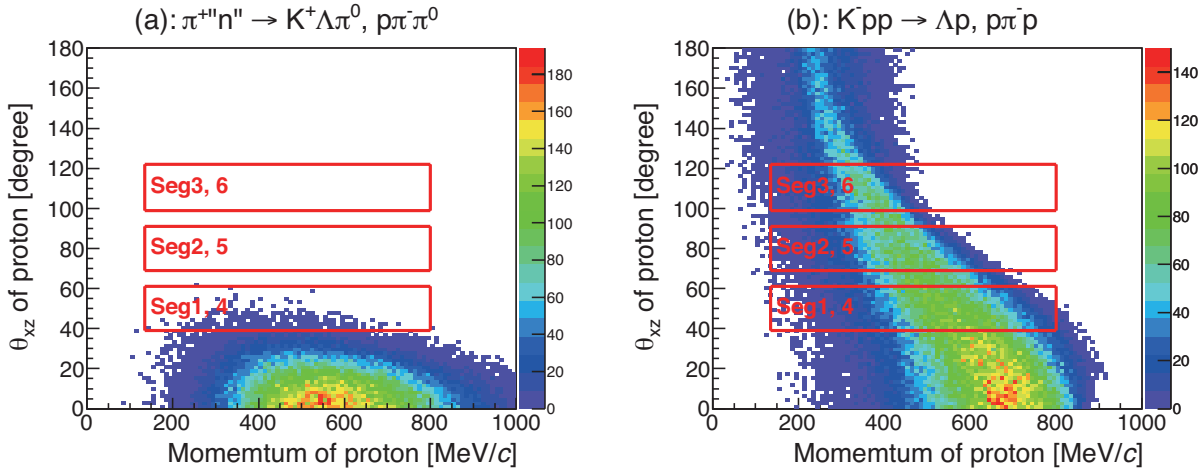

Figure 2.20: (a) Scatter plot between momentum and scattering angle in xz plane of the proton from the typical quasi-free process of π^+"n"$\rightarrow K^+\Lambda\pi^0, \Lambda \rightarrow p\pi^-$. In (b), the same scatter plot for the $K^-pp \rightarrow \Lambda p, \Lambda \rightarrow p\pi^-$ reaction is shown. The acceptance for each segment of RCA is also shown with red boxes. These correlation plots were made from a Monte Carlo simulation.

In the E27 experiment, we installed the six range counter arrays (RCA's) surrounding the liquid target system to detect the proton from the K^-pp. The six range counter arrays composed of three in the left (Seg1 to Seg3) and three in the right (Seg4 to Seg6) of the beam (z) axis as shown in Figure 2.21. According to our simulation, the proton from the quasi-free background can not produce in scattering angle $\theta_{xz(Lab)} \gtrsim 70°$ as shown in Figure 2.20 (a). Thus, the Seg2 and 5 of RCA was installed at $\theta_{xz(Lab)} \gtrsim 70°$. Note that the forward segments (Seg1 and 4) of RCA conflict to the SDC1 and 2, especially support frame of SDC1 and 2, geometrically. Therefore, in order to install the RCA at the forward angle, we have to move the target position backward. On the other hand, the K^+ acceptance of the SKS strongly depends on the target position. The K^+ acceptance becomes small when we move the target position backward. Finally, we determined the target and RCA positions to optimize the acceptance of K^+ and proton(s). In this experiment, the RCA was installed in the laboratory angles ($\theta_{xz(Lab)}$) between 39° and 122° as shown in Figure 2.21. Its geometrical coverage was about 26%.

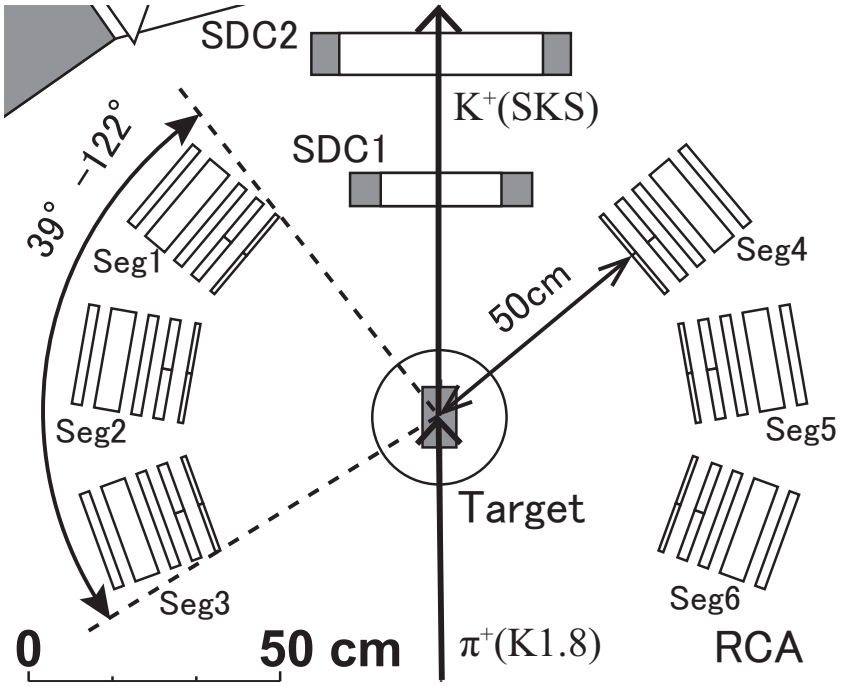

Figure 2.21: Schematic view of the range counter system (RCA) in the xz plane. It was composed of six range counter arrays; three in the left (Seg1 to Seg3) and three in the right (Seg4 to Seg6) of the beam axis.

Each range counter array had five layers of plastic scintillation counters; the thickness of each scintillator was 1 cm, 2 cm, 2 cm, 5 cm and 2 cm, respectively, with a height of 100 cm. The width of each layer was 20 cm. Schematic view of the one unit of range counter array is shown in Figure 2.22 (a). The first two layers were segmented into two slabs; each slab had 10-cm width. Therefore, we had seven (2+2+1+1+1) scintillation counters in one range counter array. Every scintillation counter was read out from both sides (up and down) by a phototube; H1949 was used for the first layers and H6410 was

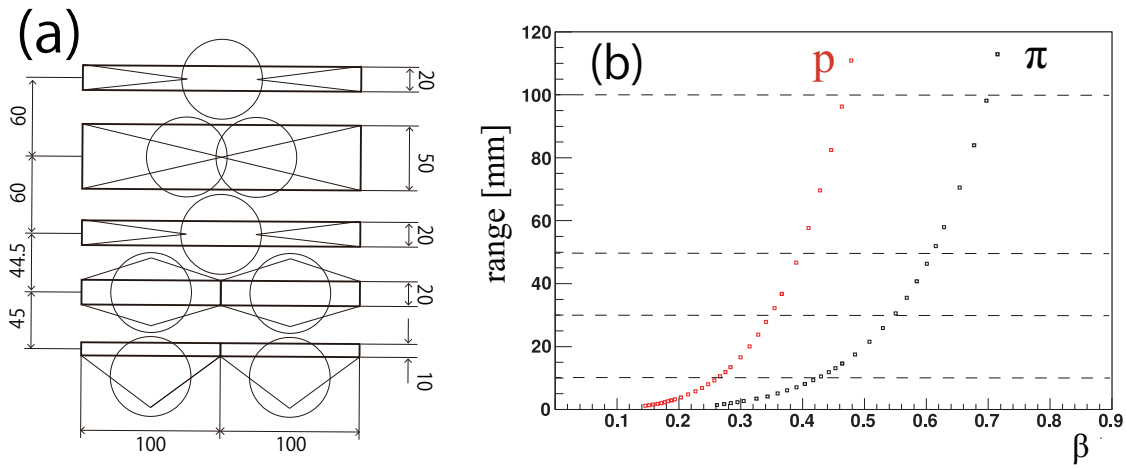

Figure 2.22: (a) Schematic view of one unit of range counter array. (b) The range as a function of β for the pion and proton. The thickness of range counter (10+20+20+50+20) mm are also indicated with a dashed-line.

used for the other layers.

From each PMT, both hit timing and pulse height information was obtained. The discriminator threshold for the timing information was set at less than the one tenth level of the minimum ionizing particles. The timing information from the first layer was used for the on-line trigger and the time-of-flight analysis in off-line. The distance from the liquid target center to the first layer was about 50 cm.

The time-of-flight (TOF) of each particle was obtained with the hit timing in the first layer with a resolution of 160 ps. The flight path length was measured from the vertex position of the (π^+, K^+) reaction to the hit position on the first layer, which was obtained with the time difference between the up and down PMT's. Then, the velocity of the particle (β) was obtained as $\beta = (\text{path length})/(\text{TOF}\cdot c)$, where c is the light speed. Moreover, we can define the stopping layer, i_{stop}, for each range counter array from a hit pattern of five layers.

Figure 2.22 (b) shows the range as a function of β for the pion and proton. The thickness of our range counter (1+2+2+5+2) cm are also indicated with a dashed-line in this figure. We can separate the pion and proton by using the information of the stopping layer and the velocity of particles.

Furthermore, in order to improve the separation between pion and proton, we set up a particle identification parameter, PID, as,

$$PID = \left((\widetilde{dE}_{i_{stop}} + \widetilde{dE}_{(i_{stop}-1)})^{\alpha} - (\widetilde{dE}_{i_{stop}})^{\alpha}\right) \cdot \cos\theta, \tag{2.1}$$

where $\widetilde{dE}_i$ shows the energy deposit in the i-th layer of the plastic scintillators and θ is the incident angle for RCA. The α is the constant parameter, where $\sim$1.75 is empirically used. The PID corresponds to the range of the previous layer of the stopping one and it should depend on not momentum but charge and mass of the particle. Finally, the proton was selected by combining the information of the stopping layer, the velocity and the PID.

2.8 Trigger

In the (π^+, K^+) reaction, many background particles are produced through the pion-nucleon reactions, such as (π^+, p)X and (π^+, π^+)X reaction. Typical cross sections of such background reactions are two or three orders of magnitude larger than that of the (π^+, K^+) reaction. Moreover, $\pi^+ \rightarrow \mu^+ + \nu_\mu$ decay in flight was not trivial to make the fake trigger. Therefore, a powerful trigger system is very important.

In the present experiment, we used two main triggers: the (π, K) inclusive trigger and the (π, K) coincidence trigger. In both triggers, the 1st level trigger, TOF-LC matrix trigger and 2nd level mass-trigger systems were introduced. These triggers are described later in this subsection. The inclusive trigger was prescaled 1/3 in order to decreased a trigger rate. The trigger logic diagram of these main triggers are shown in Figure 2.23. Prescaled beam trigger, (π, π) trigger, unbiased (π, K) trigger and TOF-RCA trigger as the calibration trigger were mixed into them.

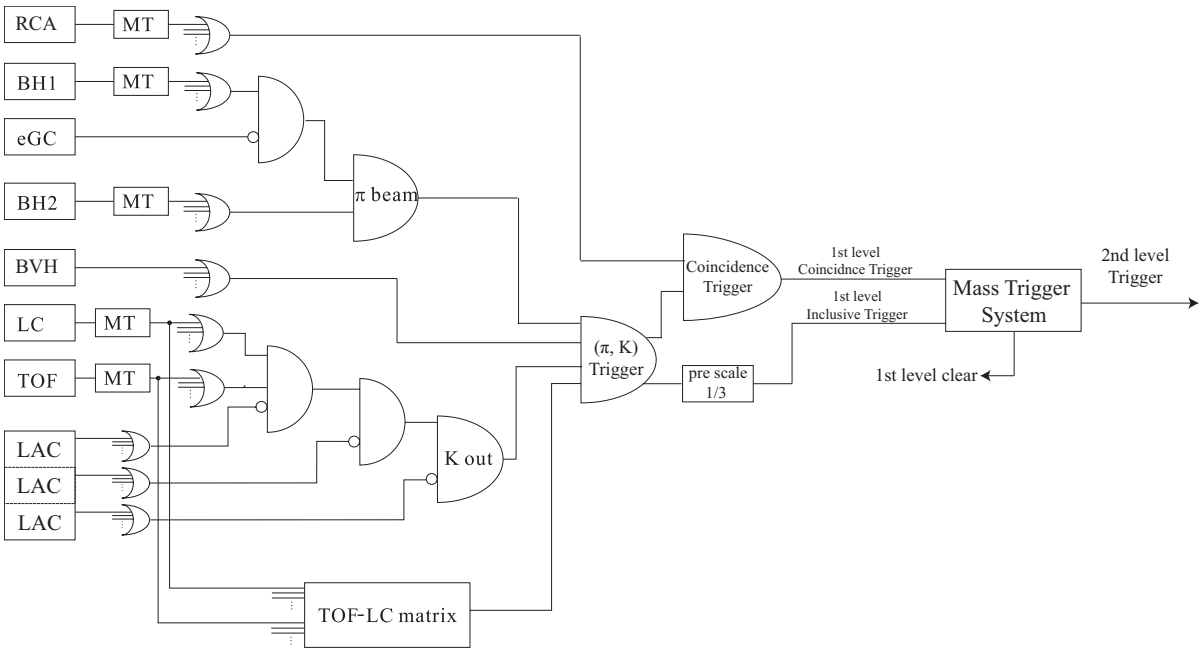

Figure 2.23: Trigger logic diagram of the (π, K) inclusive trigger and the (π, K) coincidence trigger.

The 1st level trigger

The 1st level trigger of (π, K) inclusive trigger was comprised of a π beam part, an outgoing K part and the TOF-LC matrix trigger.

The π beam part was defined as:

$$BEAM \equiv \overline{GC} \times BH1 \times BH2. \tag{2.2}$$

BH1 an BH2 had two PMTs at both end, and then mean timer modules were used to remove the incident position dependence of the trigger timing. The coincidence timing

between BH1 and BH2 was adjusted with a coincidence width less than 5 ns. The proton contamination was completely rejected by precisely adjusting the coincidence timing between BH1 and BH2 for pions. This was possible for the momentum of less than 1.5 GeV/c, which corresponds to the time difference between BH1 and BH2 of $\sim$7 ns.

The outgoing K part was defined as:

$$KOUT \equiv TOF \times LC \times \overline{LAC} \times \overline{BVH}. \tag{2.3}$$

Mean timer modules were also used for the same reason for the TOF and LC counters. Finally, the 1st level (π, K) inclusive trigger was defined as:

$$PIK \equiv BEAM \times KOUT \times MATRIX, \tag{2.4}$$

where $MATRIX$ was the TOF-LC matrix trigger.

The 1st level (π, K) coincidence trigger was additionally required at least one hit among 12 first-layer scintillators of RCA, which also used mean timer modules for the same reason, as:

$$PIK(COIN) \equiv PIK \times RCA. \tag{2.5}$$

By requiring the hit of RCA, the trigger rate could be decreased about 1/4 and it helped to reduce the DAQ dead time.

The BH2 timing was used as the STOP signal of the TDC's for BCs and SDC1, 2, while the TOF timing was used as the stop signal for SDC3, 4 because the flight time from BH2 to TOF varies according to the flight path and momenta of scatted particles.

TOF-LC matrix trigger

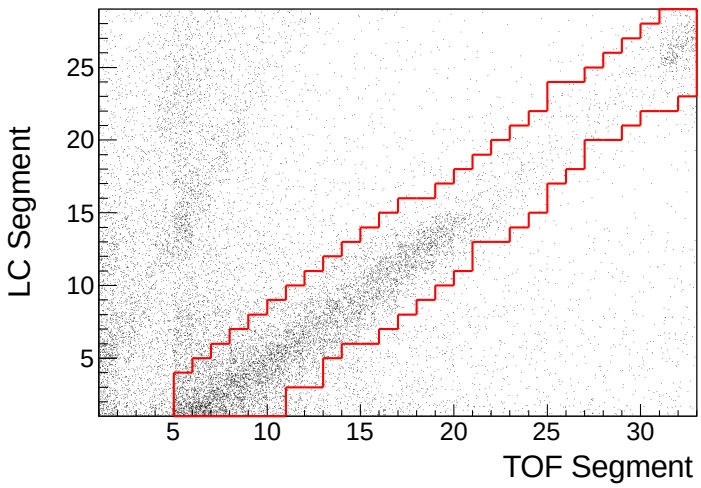

Figure 2.24: The hit patteren of TOF and LC segments without the matrix trigger. The selected TOF and LC segment region for the matrix trigger was indicated in red lines.

The matrix trigger was generated when the appropriate hit combinations between TOF and LC segments were matched. For constructing the matrix trigger, we used an FPGA module called TUL (Tohoku Universal Logic Module) [85]. Figure 2.24 shows hit patteren of TOF and LC segments without the matrix trigger. In the figure, the selected region is also indicated with solid lines and the background events are located out of the region. The 1st level (π, K) trigger was reduced by 30% with the matrix trigger.

The 2nd level mass trigger

The outgoing proton was roughly rejected by using the 2nd level mass trigger system. The momentum of the outgoing particles were correlated to the horizontal direction cosine (dx/dz) at SDC3, 4 position. The dx/dz was roughly estimated with the hit combination of TOF and LC segments as shown in Figure 2.25. Then, the mass of the outgoing particle was estimated with their time-of-flight between BH2 and TOF and momentum by the hit combination of TOF and LC segments.

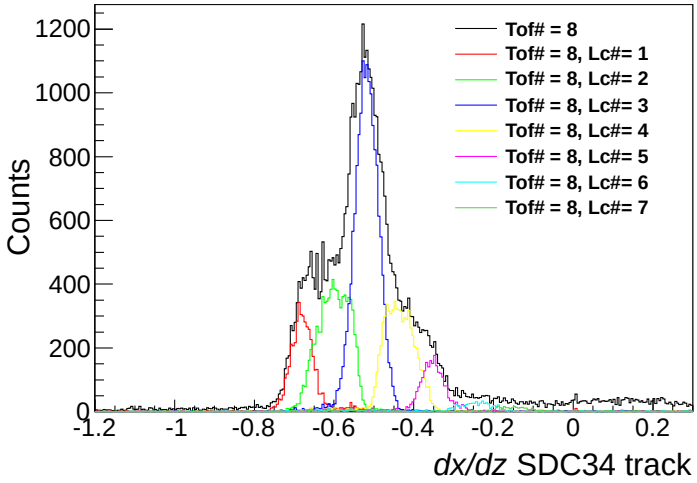

Figure 2.25: The horizontal direction cosine at SDC3, 4 position for each hit combination of TOF and LC segment in each color. The color lines for each corresponding segment are listed in the figure. The horizontal direction cosine could be determined by checking with the hit combination of TOF and LC segment roughly.

The emitted K^+ was selected by setting a suitable window against time-of-flight between BH2 and TOF for each hit combination. Typical accepted and rejected region are shown with red and black lines, respectively, in Figure 2.26. Almost half of outgoing protons could be rejected by using the mass-trigger system.

The trigger scheme for the mass trigger is illustrated in Figure 2.27. This mass trigger system was introduced to the PIK and $PIK(COIN)$ triggers. The timing information of the TOF signals was digitized with a LeCroy 4303 TFC (Time-to-Fera Converter) module.

The hit addresses and the timing information of TOF were stored in the memories in the FERA driver, and the hit information of LC was stored in TUL. The FERA driver

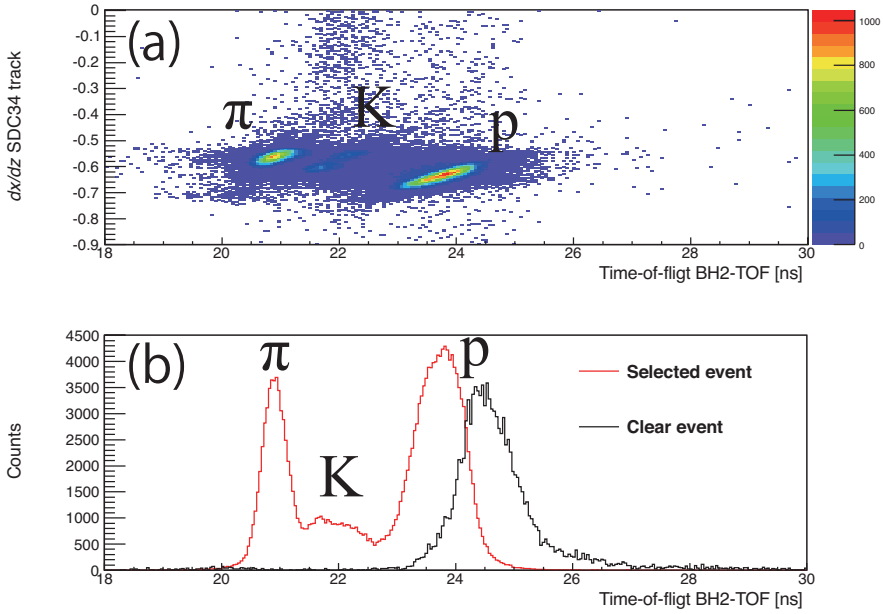

Figure 2.26: (a) The scatter plot between the (dx/dz) obtained from SDC3, 4 tracking and the time-of-flight between BH2 and TOF when we required the hit of TOF 4 segment and LC 2 segment. The outgoing pions, kaons and protons are seen in this figure. (b) The accepted and rejected region are shown with red and black lines, respectively. In this figure, we also required the hit of TOF 4 segment and LC 2 segment.

sent the 4 bits of hit address information and 9 bits of time-of-flight information to TUL. If the time-of-flight of TOF was in the time window we set the 2nd level (π, K) trigger. If not, the 1st-level trigger clear signal was generated and all the stored data in each DAQ modules were cleared. The decision time of the mass trigger was about 15 μs.

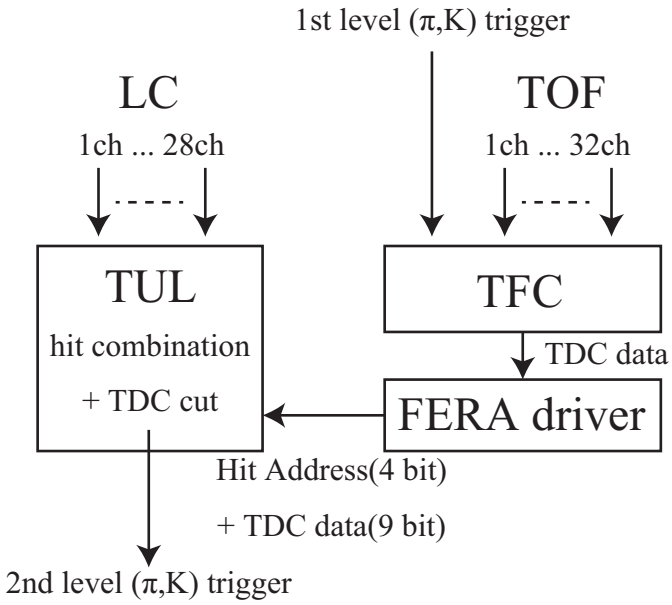

Figure 2.27: Logic Scheme of the 2nd-level mass trigger.

Calibration triggers

In order to monitor the efficiency of each detector and adjust the calibration parameters, calibration triggers were mixed with prescale factors in the main trigger. These calibration triggers mean the beam, (π, π), unbiased (π, K) and TOF-RCA triggers defined as:

$$PIPI \equiv BEAM \times TOF \times LC, \tag{2.6}$$

$$PIK(unbiased) \equiv BEAM \times TOF \times LC \times \overline{LAC}, \tag{2.7}$$

$$TOF{-}RCA \equiv BEAM \times TOF \times RCA. \tag{2.8}$$

The prescale factors were $1/(256 \times 256 \times 2)$ for the beam trigger, $1/(256 \times 30)$ for the (π, π) trigger, $1/100$ for the unbiased (π, K) trigger and $1/500$ for the TOF-RCA trigger. The 2nd-level mass trigger system was not used for these calibration triggers.

2.9 Data-acquisition system

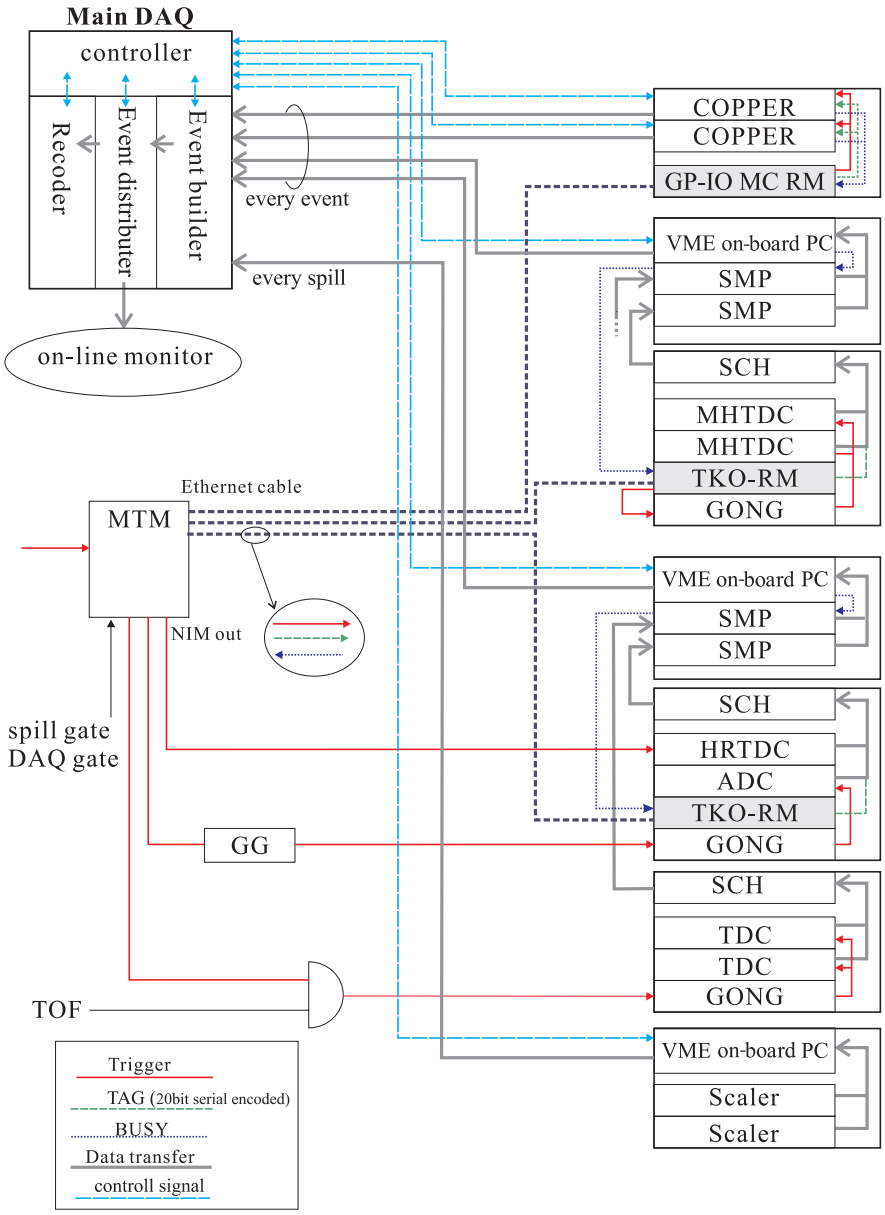

Figure 2.28: The diagram of the data-acquisition system.

Figure 2.28 shows a diagram of the data-acquisition system. The raw signals of RCA, trigger counters and SDC3, 4 were digitized with the TKO TDC and ADC modules and the TKO TDC (Dr.TII) modules, respectively, while the signals of BC3, 4 were digitized with the TKO Multi-hit TDC (MHTDC) modules. For the TKO modules, those digitized signals were transfered to the VME-SMP (Super Memory Partner) which was installed in the VME box together with a VME-CPU module. The data were read out by the VME-CPU module and transfered to the host computer. The timing information of the BC1, 2 hit was digitized by the MWPC encoder installed in the COPPER modules. COPPER

(COmmon Pipelined Platform for Electronics Readout) [78] is a new platform module for the KEK-VME specification that realizes various types of analog-to-digital conversion and pipelines digital data processing functions within a unified scheme. Although the COPPER is a VME slave module, it works as a standalone system without any additional VME processor on the VME bus. The BC1, 2 data on the COPPER modules were directly transfered to the host computer. The data-acquisition cycle was processed event by event. The single counting of each trigger counter was recorded by VME scalers, which were transfered at the end of spill.

For the early stage of J-PARC hadron experiments, we needed to use several conventional DAQ subsystems, such as TKO, together with a new network oriented DAQ module, KEK-VME/COPPER. It was necessary to integrate these different data acquisition readouts. In addition, most readout systems (VME-CPU and COPPER) have network interfaces and communicate via the TCP/IP protocol. Under this situation, we developed a network-based DAQ system [86] with a DAQ software using the TCP/IP protocol and a trigger/tag distribution system.

For building up an event by combining data sets coming from the different modules, we needed to write the event number and the spill number to each data set and to check their consistency event by event in the event building. For this purpose, we developed a trigger/tag distribution system. When the trigger signal was generated, the Master Trigger Module (MTM) accepted the trigger signal and distributed the event and spill numbers to Receiver Modules (RM) in each node by using the Ethernet cables. After finishing the analogue to digital conversion of all the modules in each node, MTM distributed the read-out signal to all the RMs and the event data with the same event and spill numbers were transfered to the host computer. The event and spill numbers were distributed to the data bus by RM in each node. The information of those numbers were transfered together with the digitized raw data to the host computer. However, in the present experiment, we did not use these event and spill numbers for an event building in the host computer, because the data read-out was successfully carried out without any event slipping.

The data transfered from each module to the host computer were at first processed by the Event-Builder. Then they were transfered to the Event-Distributor and to downstream processes.

2.10 Data summary

The K^-pp production data of the $d(\pi^+, K^+)$ reaction at 1.69 GeV/c was taken in June 2012 as listed in Table. 2.8. The total number of pions irradiated on the liquid deuterium target was 3.3×10^{11}.

In this experiment, we took beam-through data at beam momentum of 0.9 GeV/c with and without experimental target and $p(\pi^+, K^+)\Sigma^+$ data with liquid hydrogen target at $p_{\pi^+} = 1.58$ GeV/c for calibrations. This beam momentum was selected in order to have a good overlap of the kinematics of K^+ in the Σ^+ production reaction with the $d(\pi^+, K^+)K^-pp$ reaction. Furthermore, we measured the $p(\pi^+, K^+)$ reaction at 1.69 GeV/c, which is the same beam momentum of K^-pp production, by using the liquid hydrogen target. We adjusted the missing-mass scale of the $d(\pi^+, K^+)$ reaction and evaluated the missing-mass resolution by using these data. In addition, we could check the validity of energy calibration and cross section normalization by looking at the Σ^+ mass and cross sections because these values were well known.

Table 2.8: Summary of the obtained data with different combinations of experimental targets, incident π^+ momenta P_{beam}, and beam intensities. N_{beam} means the total number of π^+ beam irradiated on the target.

Reaction	Target	Thickness [g/cm^2]	P_{beam} [GeV/c]	Beam intensity [pion/spill]	N_{beam}
$d(\pi^+, K^+)$	LD_2	1.99	1.69	3.0-3.3$\times10^6$	3.3×10^{11}
$p(\pi^+, K^+)$	LH_2	0.85	1.69	3.0×10^6	7.6×10^9
$p(\pi^+, K^+)\Sigma^+$	LH_2	0.85	1.58	3.0×10^6	1.2×10^9
beam-through	none	–	0.9	$\sim 10^4$	$\sim 10^5$

Chapter 3

Analysis I - inclusive analysis

The data analysis can be separated into two parts, namely the analysis of the magnetic spectrometers and the coincidence analysis of the RCA. The analysis of the K1.8 beam line spectrometer and the SKS is described in this chapter. The goal of this part is to obtain a missing mass spectrum of the (π^+, K^+) reaction as an inclusive spectrum. The analysis of the RCA for the coincidence measurement is described in the next chapter.

3.1 Outline

A missing-mass spectrum is obtained as a double differential cross section of $d^2\bar{\sigma}_{\theta_1-\theta_2}/d\Omega/dM$ averaged over the scattering angle of the (π^+, K^+) reaction from θ_1 to θ_2. The double differential cross section is calculated as:

$$\frac{d^2\bar{\sigma}_{\theta_1-\theta_2}}{d\Omega dM} = \frac{A}{N_A(\rho x)} \frac{N_{\pi K}}{N_{beam}\Delta\Omega_{\theta_1-\theta_2}\Delta M\epsilon}, \tag{3.1}$$

where A is the target mass number, N_A the Avogadro constant, ρx the target mass thickness, $N_{\pi K}$ the number of good (π^+, K^+) events in the missing-mass interval ΔM, N_{beam} the number of beam pions on the target, $\Delta\Omega_{\theta_1-\theta_2}$ the solid angle of SKS between θ_1 and θ_2 and ϵ the overall experimental efficiency. In the whole offline analysis, the error of efficiency is estimated for the systematic uncertainty. The statistical error is negligibly small compared with the systematical one. The mass of the produced particle (MM_d) in the $d(\pi^+, K^+)X$ reaction is obtained as a missing mass by calculating the following equation in the laboratory frame

$$M = MM_d = \sqrt{(E_\pi + M_d - E_K)^2 - (p_\pi^2 + p_K^2 - 2p_\pi p_K \cos\theta_{\pi K})}, \tag{3.2}$$

where E_π and p_π are the total energy and momentum of a pion, E_K and p_K are those of a kaon, M_d is the deuteron rest mass, and $\theta_{\pi K}$ is the scattering angle of the reaction. Thus, we need to measure three kinematic variables, p_π, p_K and $\theta_{\pi K}$, through the momentum reconstruction.

Figure 3.1 shows a flowchart of the offline analysis. First, good (π^+, K^+) events should be distinguished from a large number of background events. We request all counters have good hits and an incident beam π^+ is selected by using the time-of-flight between BH1

and BH2 within the time window of ± 2 ns. The emitted K^+ is roughly selected by using the information of the TOF, LC counters combining with the tracking information in SDCs. Then, the beam π^+ momentum and emitted kaon momentum are reconstructed with the K1.8 beam line spectrometer and SKS, respectively. For each spectrometer system, a local track assuming the straight line is selected using the hit positions of the tracking chambers installed both at the entrance and exit of the spectrometer. Then good tracks are selected by connecting those local track candidates so as to give the least chi-squares in the track reconstruction. For the track reconstruction of the K1.8 beam spectrometer, a third-order transfer matrix is used. In the track reconstruction of SKS, we used a calculated magnetic field map for the Runge-Kutta tracking method [88]. After the track reconstruction, the final identification of K^+ is carried out by using the time-of-flight with the flight path and the reconstructed momentum of SKS. Then, a vertex point of the (π^+, K^+) reaction event is reconstructed from the trajectories of the π^+ and K^+. Thus, the missing mass is obtained.

Finally, we obtained the missing-mass spectrum as a double differential cross section of $d^2\bar{\sigma}/d\Omega/dM$ after correcting the efficiency of detectors and the acceptance of the SKS spectrometer. These analysis results are described in this chapter.

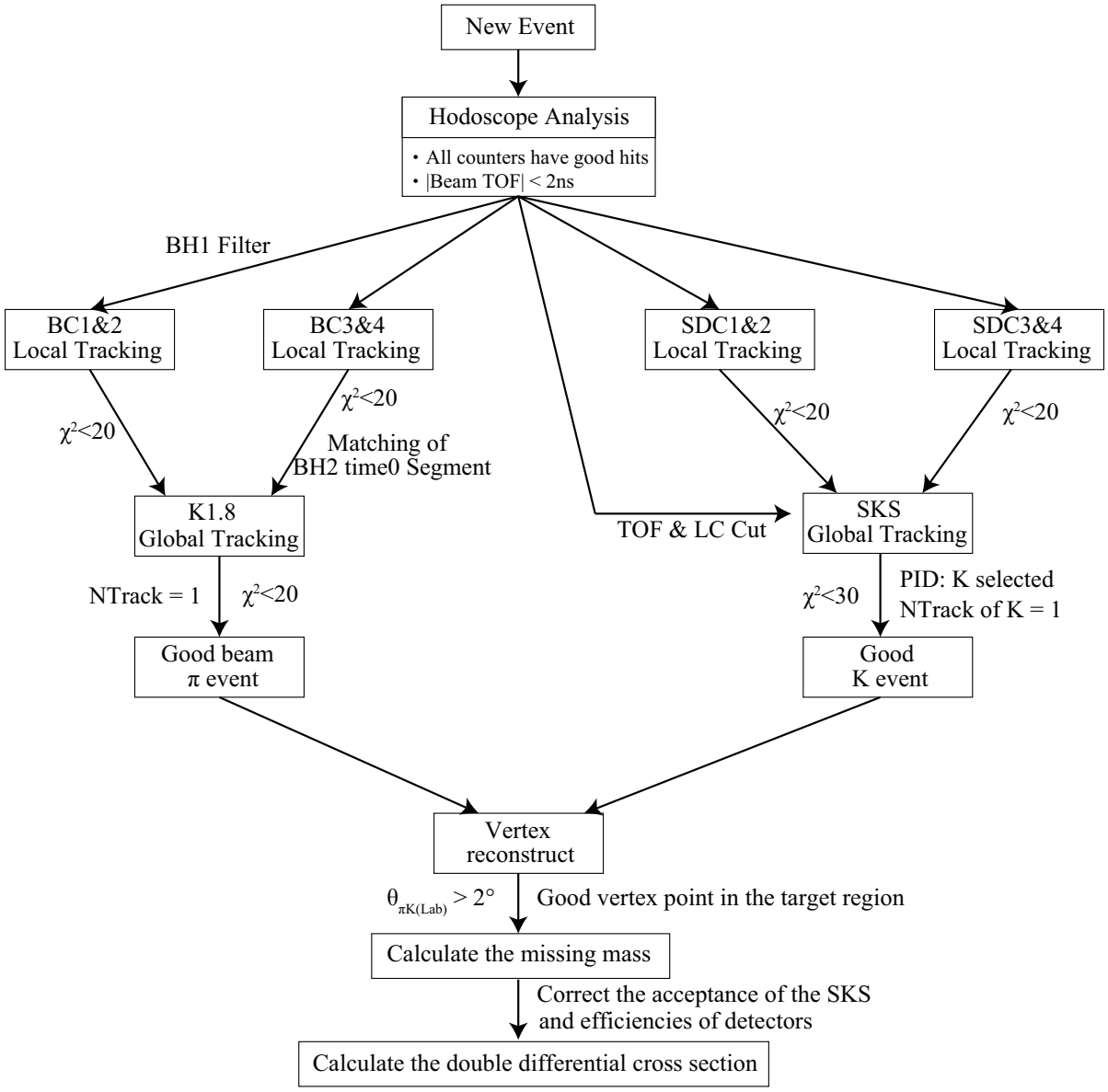

Figure 3.1: Flow chart of the offline analysis for inclusive (π^+, K^+) spectrum.

3.2 Analysis of π^+ beam

3.2.1 Identification of triggered beam particles

N_{beam} in Eq. 3.1 is the number of triggers of $BH1 \times BH2 \times \overline{GC}$. The incident hadron beam such as pion, kaon and proton was separated with the electro static separator (ESS1, 2) written in Sec. 2.2. In addition, the positron was rejected by requiring no hit of the GC at the trigger level. Figure 3.2 show the time-of-flight spectrum between BH1 and BH2 with the flight pass of 10.4 m. The flight time difference between pion and kaon is 1.3 ns for the momentum of 1.69 GeV/c and that of pion and proton is 4.9 ns. Thus, we found that the proton and kaon in π was rejected in the electro magnetic separator and time-of-flight. We set the time window, ± 2 ns, as shown in Figure 3.2 in order to keep a π detection efficiency. The beam TOF efficiency which is the analysis efficiency of time-of-flight cut between BH1 and BH2 ($|\text{Beam TOF}| < 2$ ns) was estimated to be 99.6 ± 0.1 (syst.) %[1]. The systematic error was estimated from the fluctuation of the efficiency during the experimental period.

The main background of the π^+ beam was μ's from the $\pi \to \mu$ decay in flight inside the QQDQQ magnet. The contamination of the background was estimated by checking the y profile at BC4 as described in Sec. 3.2.4.

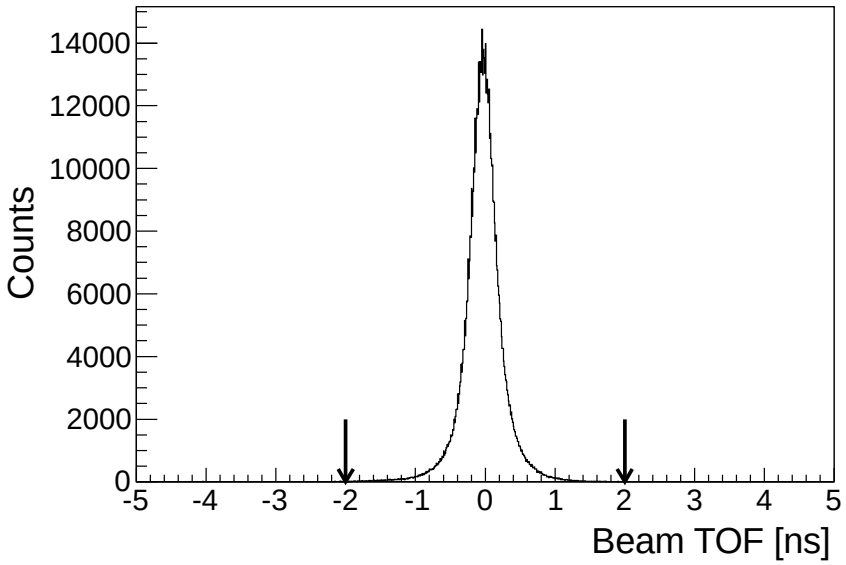

Figure 3.2: Typical time-of-flight spectrum of the incident beam particles. The selected time window was indicated by arrows.

[1]We found that this factor became worse ($\sim$90%) in a few experimental periods. This effect was corrected to calculate the double differential cross section.

3.2.2 BC1 and BC2 local tracking

The BC1 and BC2 were MWPCs installed at the entrance of the K1.8 beam line spectrometer. In the BC1, 2 local tracking, hits on adjoining wires within a proper timing was made up as a cluster hit. Timing information of BC1, 2 was digitized by the MWPC encoder with the sampling time interval of 10 ns (100 MHz sampling). In the digitalization, both leading edge and trailing edge information of raw signals were recorded for making up cluster hits. In the present analysis, the time gate for the leading edge timing with a 80 ns was set for the clustering. For the tracking analysis, the central position in a cluster was used. In finding the BC1, 2 track, we applied the hit position gate for each layer by checking consistency of hit position with the BH1 hit segment. We call this tracking method as BH1 filter tracking. The detail of BH1 filter tracking is described in Appendix A.

Local straight track fitting was performed by using the least squares method. The tracking χ^2 was defined as:

$$\begin{aligned} \chi^2 &= \frac{1}{n-4}\sum_{i=1}^{12}\left(\frac{cor - f(z_i)}{\sigma_i}\right)^2, \\ f(z_i) &= x(z_i)\cos(\theta) + y(z_i)\sin(\theta), \\ x(z_i) &= x_0 + u_0 \times z_i, \\ y(z_i) &= y_0 + v_0 \times z_i, \end{aligned} \tag{3.3}$$

where *cor* is the position of the cluster center wire σ_i the position resolution of each layer, θ wire tilt angle of each plane (x, u, v for 0°, 15°, -15°). The optimum parameters (x_0, y_0, $u_0(dx/dz)$, $v_0(dy/dz)$) which minimize the reduced χ^2 were obtained by the least squares method.

Figure 3.3 shows a typical reduced χ^2 distribution of the BC1, 2 local tracking. In the local track search, the accepted reduced χ^2 value was selected to be less than 20.

Figure 3.4 shows a typical residual distribution of one of the BC1, 2 layers. In the calculation of the residual in Figure 3.4(a), the calculated layer was included in the tracking analysis. In case of Figure 3.4(b), the calculated layer was not included. The intrinsic resolution, σ_i in Eq. 3.3, was estimated from the geometric average of the resolutions obtained from these two types of tracking. The obtained position resolutions of BC1, 2 chambers are listed in Table. 3.1.

Table 3.1: The position resolution of each layer.

BC1-Layer	resolution [μm]	BC2-Layer	resolution [μm]
BC1-x	268.3 ± 1.4	BC2-v	268.7 ± 1.4
BC1-v	267.4 ± 1.4	BC2-u	270.2 ± 1.4
BC1-u	271.6 ± 1.4	BC2-x	275.7 ± 1.8
BC1-x	276.9 ± 1.7	BC2-v	272.7 ± 1.4
BC1-v	273.4 ± 1.5	BC2-u	271.0 ± 1.4
BC1-u	269.4 ± 1.4	BC2-x	269.1 ± 1.5

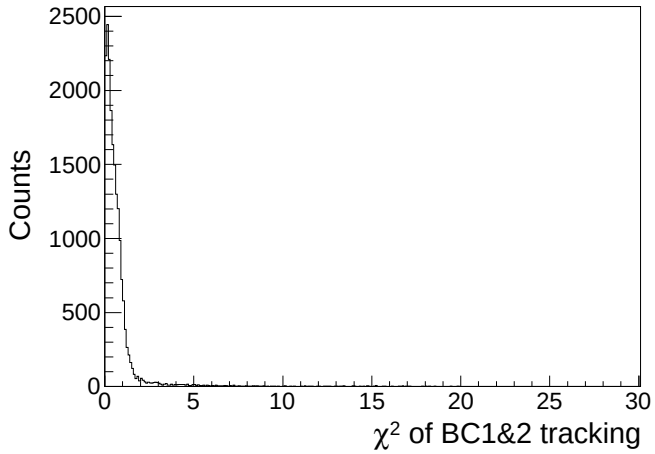

Figure 3.3: Typical reduced χ^2 distribution of the BC1, 2 local tracking. The tracks were accepted to be less than 20 of the χ^2 value.

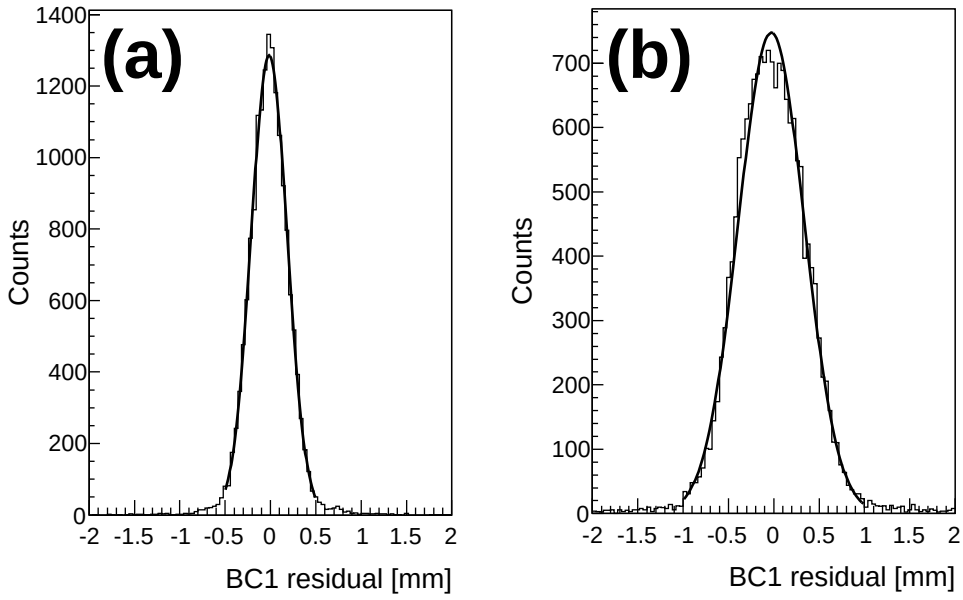

Figure 3.4: Typical residual distributions of the BC1 layers. (a) The calculated layer was included in the tracking analysis. (b) The calculated layer was not included in the tracking analysis. These residual spectra were fitted with a Gaussian function to estimate the resolution shown in black solid lines.

3.2.3 BC3 and BC4 local tracking

The BC3 and BC4 were drift chambers installed at the exit of the K1.8 beam line spectrometer. The drift time information of BC3, 4 was digitized by the TKO Multi-hit TDC (MHTDC) modules. Figure 3.5(a) and (b) show typical TDC distributions of one of the BC3 layers (3-mm wire spacing) and one of the BC4 layers (5-mm wire spacing), respectively.

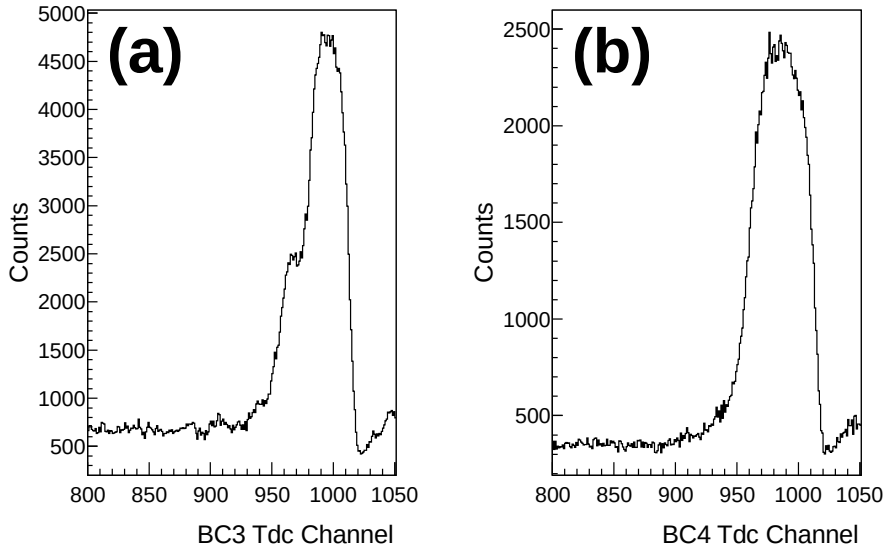

Figure 3.5: Typical TDC distributions of one of the BC3 layers (a) and one of the BC4 layers (b). The TDC distribution was the sum of all hits in a layer, and all multi-hit signal were shown in the spectrum.

The TDC information was converted to the drift time distribution in order to calculate the drift length. The origin of the drift timing was roughly determined to the edge of the TDC distribution (∼1020 ch in Fig. 3.5) and TDC channels (t) were converted to the time using the MHTDC conversion width of 0.78 ns/ch. The conversion function from the drift time to drift length was determined by assuming the uniform hit distribution with the following equation:

$$DL(t) = \frac{\int_{t_0}^{t} dtDT(t)}{\int_{t_0}^{t_{max}} dtDT(t)} \times max\ drift\ length, \tag{3.4}$$

$$DT(t) = (t - t_0) \times 0.78, \tag{3.5}$$

where t_0 is the time origin, t_{max} is the maximum drift time for the maximum drift length, and $DT(t)$ is the observed drift time distribution. The maximum drift length was determined by the wire spacing (3 mm/5 mm).

Figure 3.6 shows a typical scatter plot between the drift time and the drift length ($DL(t)$). The scatter plot was fitted by using a 5th-order polynomial function, which was optimized by minimizing the residual in each plane iteratively.

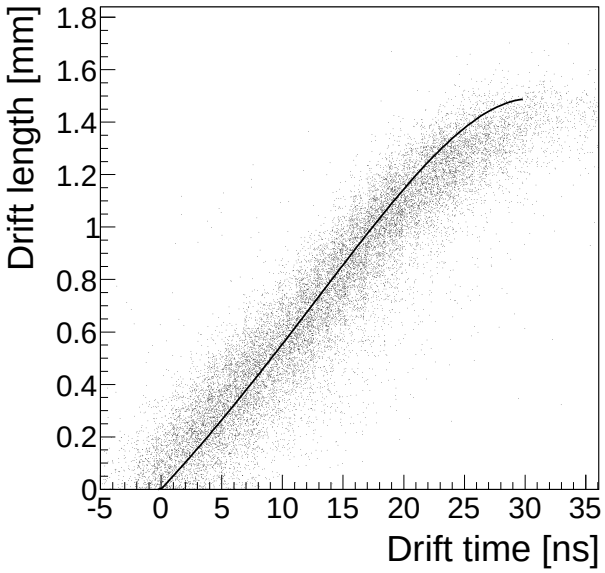

Figure 3.6: A scatter plot between the drift time and the drift length of one of the BC3 layers with the fitting result in black line. The scatter plot was the sum of all hits in a layer.

Before the straight line fitting of BC3, 4, we searched the track candidates in each layer. At first, we resolved the left or right (L/R) by checking the hit pattern in the pair plains (x-x', u-u', v-v'). If the pair plain did not have the corresponding hits, both (L/R) hit positions were considered as the track candidates. All combination of the hit positions were examined to find a BC3, 4 local track.

Figure 3.8 shows a typical residual distribution of one of the BC3, 4 layers. The accepted reduced χ^2 value was less than 20. Figure 3.4 shows the residual distribution of the tracking. From this distribution, the intrinsic resolutions were estimated as listed in Table. 3.2. Finally, hit consistency between the track and the BH2 hit segment was examined.

Table 3.2: The position resolution of each layer.

BC3-Layer	resolution [μm]	BC4-Layer	resolution [μm]
BC3-x	146.0 $\pm$ 0.6	BC4-v	168.6 $\pm$ 0.8
BC3-x'	150.1 $\pm$ 0.7	BC4-v'	169.4 $\pm$ 0.8
BC3-v	175.1 $\pm$ 0.7	BC4-u	186.1 $\pm$ 0.8
BC3-v'	174.0 $\pm$ 0.7	BC4-u'	194.2 $\pm$ 0.9
BC3-u	168.7 $\pm$ 0.7	BC4-x	175.6 $\pm$ 0.8
BC3-u'	178.3 $\pm$ 0.7	BC4-x'	196.7 $\pm$ 0.9

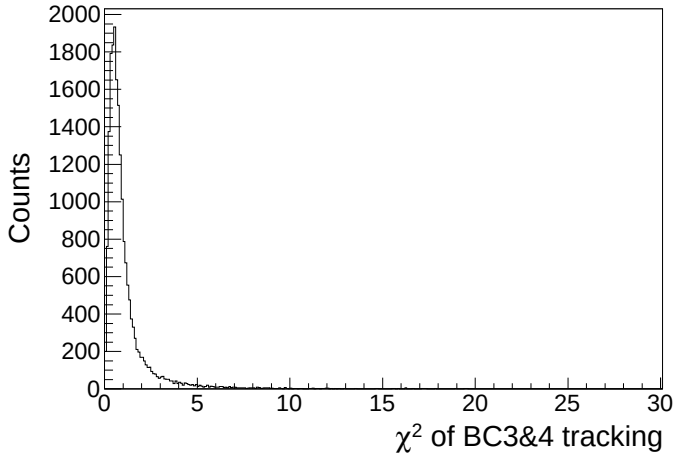

Figure 3.7: Typical reduced χ^2 distribution of the BC3, 4 local tracking. The tracks were accepted to be less than 20 of the χ^2 value.

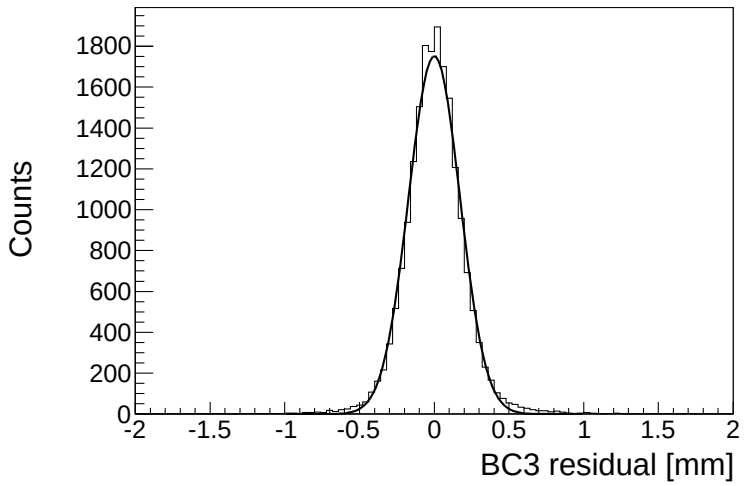

Figure 3.8: Typical residual distributions of the BC3 layers fitted with a Gaussian function to estimate the resolution.

3.2.4 Beam momentum reconstruction

After selecting the straight track candidates at the entrance and exit of the K1.8 beam line spectrometer, those tracks were reconstructed by using the 3rd-order transfer matrix M calculated by the ORBIT code [87] as follow:

$$\begin{aligned} \vec{X}_{out} &= M(\vec{X}_{in}, \delta), \\ \vec{X_{in}} &= (x_{in}, y_{in}, \frac{dx_{in}}{dz}, \frac{dy_{in}}{dz}), \\ \vec{X_{out}} &= (x_{out}, y_{out}, \frac{dx_{out}}{dz}, \frac{dy_{out}}{dz}), \end{aligned} \tag{3.6}$$

where $\vec{X}_{in}$ and $\vec{X}_{out}$ are the horizontal and vertical positions and their derivatives at the entrance and the exit of the K1.8 beam line spectrometer and δ is momentum deviation from the central momentum denoted as $p = p_0(1+\delta)$, where p_0 is the central momentum. The momentum of a K1.8 track was determined by minimizing the reduced χ^2 value as:

$$\begin{aligned} \chi^2_{K1.8} &\equiv \frac{1}{n-5}\left(\sum_{i=1}^{12} H_i \left(\frac{P_i - f_i(\vec{X}_{in})}{\sigma_i}\right)^2 + \sum_{i=13}^{24} H_i \left(\frac{P_i - g_i(\vec{X}_{out})}{\sigma_i}\right)^2\right), \\ n &= \sum_{i=1}^{24} H_i, \\ H_i &= \left\{ \begin{array}{l} 1 \text{ if } i-\text{th plane has a hit} \\ \\ 0 \text{ if } i-\text{th plane has no hit} \end{array} \right\}, \end{aligned} \tag{3.7}$$

where P_i and σ_i denote the hit position and resolution of the i-th layer. The calculated position by the transport matrix at the i-th plane is denoted by $f_i(\vec{X}_{in})$ and $g_i(\vec{X}_{out})$.

In the ORBIT code, the properties of the K1.8 beam line spectrometer magnets such as the effective magnetic length, aperture, field strength of the central ray, and bending angle and the radius of central orbit for the dipole magnet were the input parameters. The effective magnetic length was obtained from a measured magnetic field distribution. The aperture was taken from the design value of the spectrometer magnets.

After the beam momentum reconstruction, we obtained the beam momentum spectra of 1.69 and 1.58 GeV/c as shown in Figure .3.9. A typical reduced χ^2 distribution of the K1.8 tracking at 1.69 GeV/c is shown in Figure 3.10.

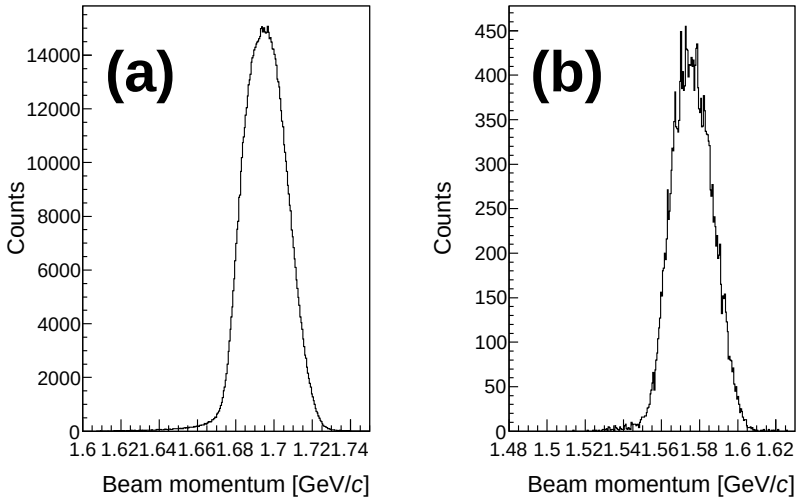

Figure 3.9: The beam momentum distribution of 1.69 GeV/c (a) and 1.58 GeV/c (b).

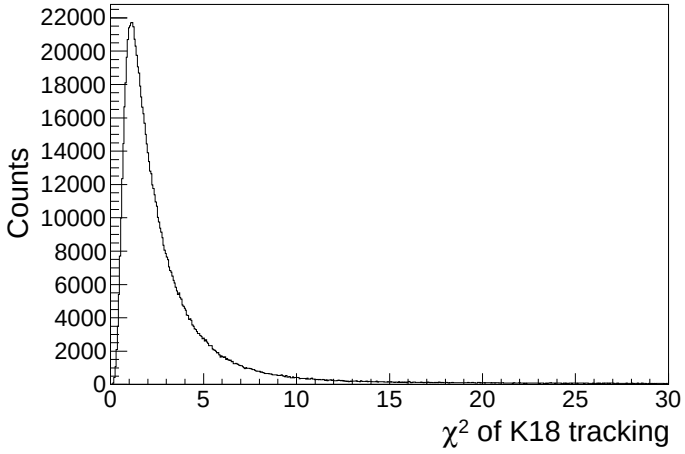

Figure 3.10: Typical reduced χ^2 distribution of the K1.8 tracking.

3.2.5 Efficiency for the π^+ beam

The single track events were selected at this stage. The overall tracking efficiency of the K1.8 beam line spectrometer is expressed as

$$\epsilon_{K18} = \epsilon_{BC12} \times \epsilon_{BC34} \times \epsilon_{K18Track}, \tag{3.8}$$

where ϵ_{BC12} and ϵ_{BC34} are the local tracking efficiency of each detector, and $\epsilon_{K18Track}$ is the single track efficiency of the K1.8 global tracking. Each efficiency is determined as:

$$\epsilon_{BC12} = \frac{N(BC12Track \geq 1)}{N(\pi Beam)}, \tag{3.9}$$

$$\epsilon_{BC34} = \frac{N(BC34Track \geq 1)}{N(\pi Beam)}, \tag{3.10}$$

$$\epsilon_{K18Track} = \frac{N(K18Track = 1)}{N(BC12Track \geq 1 \times BC34Track \geq 1)}, \tag{3.11}$$

where $N(\pi\ Beam)$ is the number of pions selected by BH1-BH2 time window. The overall tracking efficiency of the K1.8 beam line spectrometer, ϵ_{K18}, depends on the maximum allowed reduced χ^2 values as shown in Figure 3.11.

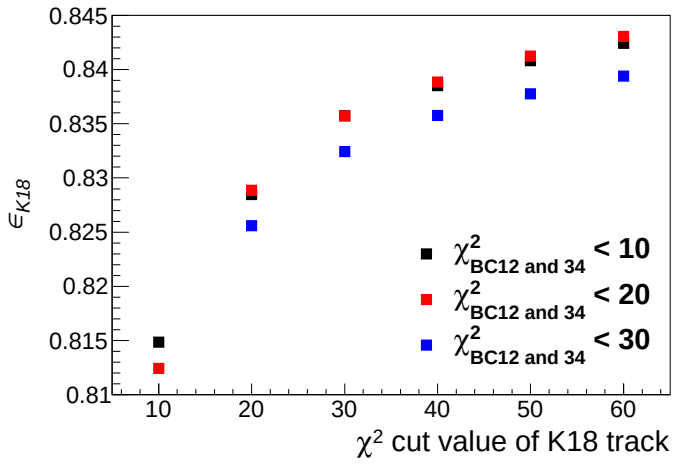

Figure 3.11: Summary of the ϵ_{K18} of the χ^2 cut value dependence.

The total analysis efficiency of beam particles is given by

$$\epsilon_{\pi} = \epsilon_{K18} \times \epsilon_{BeamTOF} \times (1 - f_{\mu}), \tag{3.12}$$

where $\epsilon_{BeamTOF}$ is the analysis efficiency of time-of-flight cut between BH1 and BH2 (|Beam TOF| < 2 ns) and f_{μ} is the muon contamination in the π^+ beam. The contamination of muons was caused from two sources; those delivered from the upstream of the mass slit and those from the $\pi \rightarrow \mu$ decay between the QQDQQ magnet. However, the probability of muons coming from upstream of mass slit was small compared with those

from decay between QQDQQ magnet, which was estimated by using the Decay TURTLE code [89]. The muons coming from decay in flight were estimated from vertical (y) distribution at BC4 position. The y distributions of the π^+ beam and those of decay events were different according to the Decay TURTLE. Here, the reduced χ^2 of the K1.8 tracking for those decay events becomes worse. The y distributions of good ($\chi^2_{K18\ track} < 5$) and bad ($\chi^2_{K18\ track} > 30$) $\chi^2_{K18\ track}$ events are shown in Figure 3.12(a) and (b), respectively. The y distribution for decay events was broader than the one for π^+ beam events.

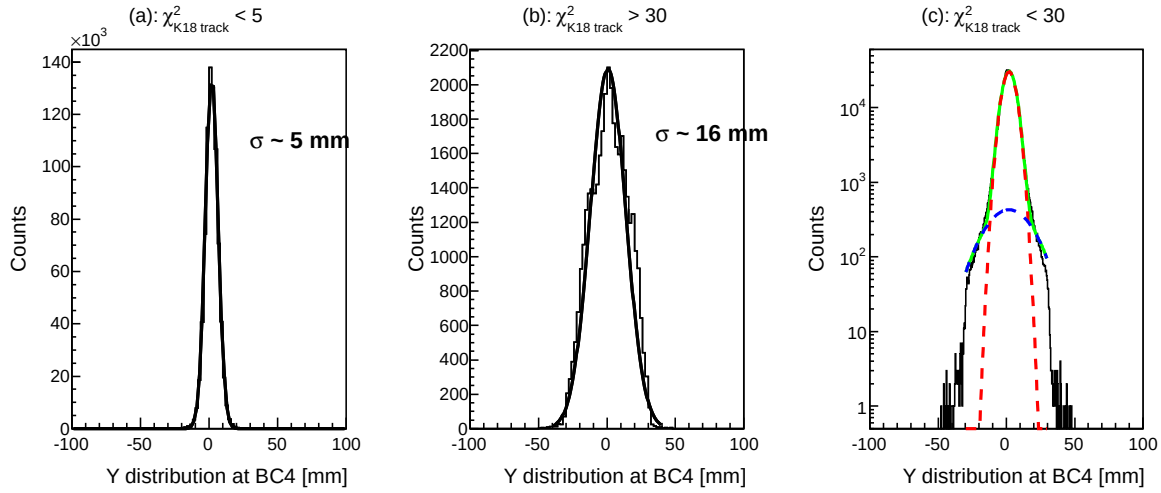

Figure 3.12: The y distribution at the BC4 position. (a) shows the one in case the χ^2 values are less than 5, which corresponds the y distribution of π^+ beam. (b) shows the one in case the χ^2 values are more than 30, which corresponds the y distribution of $\pi \to \mu$ decay events. (c) shows the one in case the χ^2 values are less than 30. This spectrum was fitted with 2 Gaussian functions for the π^+ beam (red-dashed line) and the muons component (blue-dashed line) to determine the fraction of muons contamination. The total fitting functions are shown in green-solid line.

Then, we estimated the muon contamination fraction f_μ by fitting the y distribution spectra with two Gaussian functions. A fit result for the $\chi^2_{K18\ track}$ cut value of 30 with Gaussian functions for the π^+ beam (red-dashed line) and the muon component (blue-dashed line) is shown in Figure 3.12 (c). The sum of two components is also shown with a green-solid line. The obtained f_μ values are summarized in Figure 3.13.

In order to determine the χ^2 cut value of each tracking, we had to consider the muon contamination fraction because it depended on the $\chi^2_{K18\ track}$ cut value. Then, we checked the analysis efficiency by changing the χ^2 cut values and these values are plotted in Figure 3.14. The total analysis efficiency was the best when we chose the all of accepted χ^2 values to be less than 20. Therefore, the accepted χ^2 values of the local and global tracking of the beam analysis were determined to be less than 20. In this cut condition, the local tracking efficiency of BC1, 2 and BC3, 4 chambers are found to be 93.8 $\pm$ 1.9 (syst.) % and 99.1 $\pm$ 0.1 (syst.) %, respectively. The global K1.8 tracking efficiency is 87.9 $\pm$ 1.2 (syst.) %. These systematic errors for the tracking are

estimated from the fluctuation of the efficiency during the experimental period. The muon contamination factor was found to be 3.4 ± 0.1 (syst.) %, whose systematic error was estimated by changing the fit method.

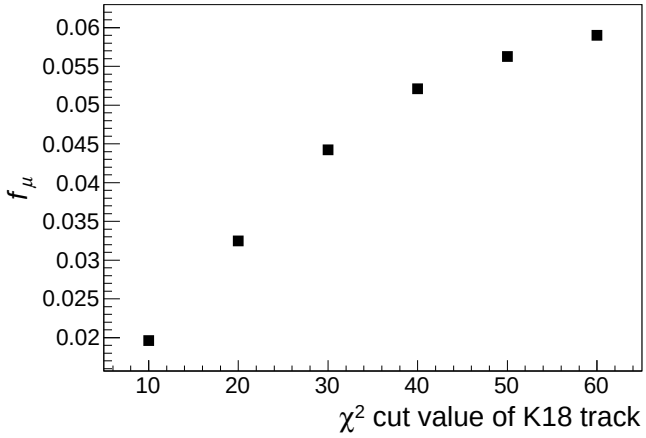

Figure 3.13: A summary of f_μ of $\chi^2_{K18\ track}$ cut value.

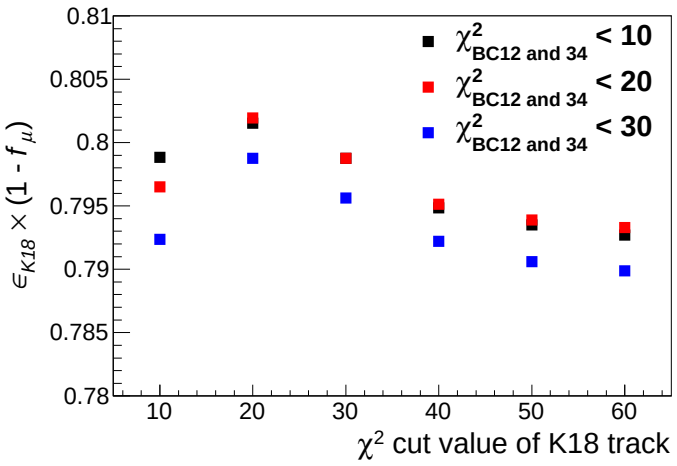

Figure 3.14: The analysis efficiency of beam particles. The efficiency, $\epsilon_{K18} \times (1 - f_\mu)$, for each χ^2 cut value are plotted in this figure.

3.3 Analysis of emitted K^+

3.3.1 SDC1 and SDC2 local tracking

The SDC1 and SDC2 were drift chambers installed at the entrance of the SKS magnet. By using these chambers, the local straight tracking was also carried out before the SKS global tracking.

The hit information of these chambers was obtained in the same method as BC3 and 4. However, the track through these chambers was slightly bent by the magnetic field because the SDC2 was installed near the SKS magnet gap. Thus, the drift velocity function was optimized in iteration not with the straight local tracking but with a help of the SKS global tracking using the Runge-Kutta method. Furthermore, the method to search the track candidates was different from BC3, 4 analysis. In case of BC3, 4 analysis, we used the pair-plane analysis to resolve the L/R (left or right) because the incident angles of the beam particles were almost perpendicular. On the other hand, the emitted particles into the SKS had wide scattering angles and the incident angles on SDC1 and 2 were not always perpendicular. Therefore, L/R was resolved from a straight pre-tracking using the same tilt angle plane (x, u, v) was performed before the straight line tracking in case of SDC1, 2 analysis. After the pre-tracking, the tracking procedure of the local tracking was same as BC3, 4 analysis.

Figure 3.15 (a) shows a typical reduced χ^2 distribution of the local SDC1, 2 tracking. The black and red histograms correspond to all the events and the single-track events, respectively. The reduced χ^2 value of less than 20 was accepted, which was determined to keep the sufficient single-track efficiency.

The efficiency of SDC1, 2 (ϵ_{SDC12}) is the efficiency including the detector efficiency and the analysis efficiency of local tracking. It was estimated from the beam trigger event by selecting the tracks which should pass through the effective area of SDC1 and SDC2 chosen from the straight track of BC3, 4 local tracking. The obtained efficiency was 95.7 ± 1.7 (syst.) %, whose systematic error was estimated from the hit position dependence. The fluctuation of the efficiency during the experimental period was sufficiently small compared with this error.

3.3.2 SDC3 and SDC4 local tracking

The SDC3 and SDC4 were drift chambers installed at the exit of the SKS magnet. The drift time information was digitized by the TKO Dr.II single-hit TDC modules. The analysis procedure of the local tracking of SDC3, 4 was same as that of SDC1, 2, although the drift velocity function was optimized in iteration with straight local tracking. The pre-tracking was necessary to resolve the L/R because the SDC3 and SDC4 have the same plane structure.

Figure 3.15 (b) shows a typical reduced χ^2 distribution of the local SDC3, 4 tracking. The black and red histograms correspond to all the events and the single-track events, respectively. χ^2 value of less than 20 was accepted, which was determined to keep the sufficient single-track efficiency. A typical residual width was 300 μm in σ.

The efficiency of SDC3, 4 (ϵ_{SDC34}) including the detector efficiency and local tracking efficiency was obtained from the (π^+, p) reaction events because proton did not decay in

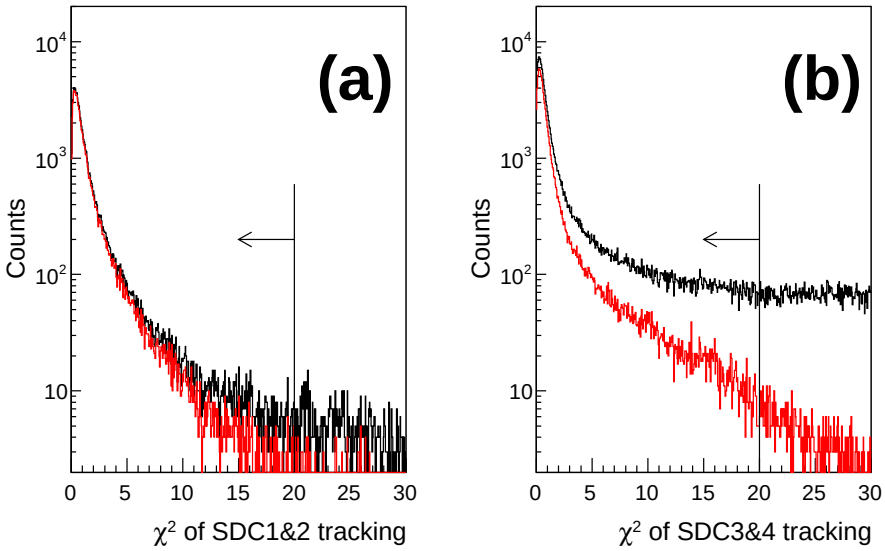

Figure 3.15: The reduced χ^2 distribution of the SDC1, 2 (a) and SDC3, 4 (b) local tracking. The black and red lines show the total and single-track events, respectively.

flight. It was obtained as:

$$\epsilon_{SDC34} = \frac{N(SDC34Track \times Proton)}{N(Proton)}. \tag{3.13}$$

The proton events, $N(Proton)$, was selected by using the information of the local tracking in SDC1, 2 and the flight time from BH2 to TOF. Figure 3.16 shows the scatter plot between the horizontal direction cosine (dx/dz) of the SDC1, 2 track and the flight time (BH2-TOF). Black and red markers show all events and proton selected events, respectively. The obtained efficiency was 99.2 $\pm$ 0.0 (syst.) %. The systematic error was estimated by checking the incident angle dependence of the SDC1, 2 tracks.

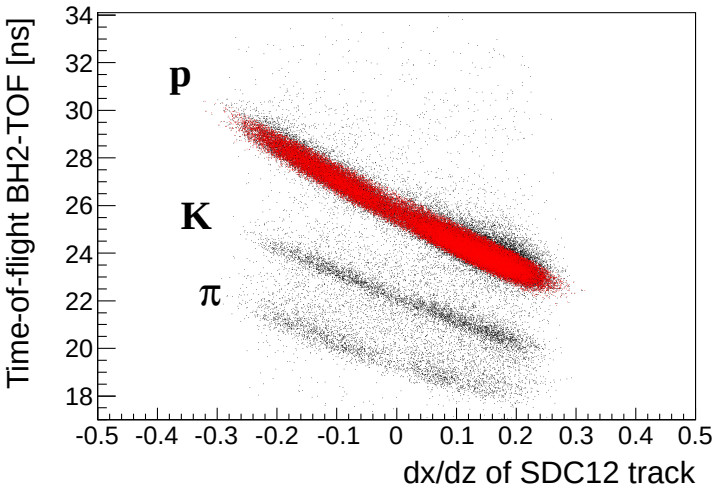

Figure 3.16: Proton selection by the correlation of the horizontal direction cosine (dx/dz) of the SDC1, 2 track and the time-of-flight (BH2-TOF). Black and red markers show all events and selected proton events, respectively.

3.3.3 Momentum reconstruction of scattered particles

The momentum vector of the emitted particles was determined by reconstructing trajectories from the hit positions of SDC1–4. The Runge-Kutta method [88] was used for track reconstruction with a magnetic filed map calculated by the ANSYS code [90]. The trajectory and the momentum were optimized by minimizing the following reduced χ^2 value iteratively. The fitting parameters were the momentum, the horizontal (x) and vertical (y) positions and their direction cosines (dx/dz, dy/dz) at the TOF position. The SKS tracking was started from the TOF position. The reduced χ^2 is defined as:

$$\chi^2_{SKS} \equiv \frac{1}{n-5} \sum_{i=1}^{n} \left(\frac{x_i^{hit} - x_i^{track}}{\sigma_i} \right)^2 , \tag{3.14}$$

where n is the number of SDC layers, x_i^{hit} and σ_i are the hit position and position resolution of each layer, respectively. x_i^{track} is the estimated hit position from the track reconstruction for each layer. The convergence criterion in the iteration is $\delta\chi^2 = (\chi^2_{k+1} - \chi^2_k)/\chi^2_k < 10^{-3}$, where k is the number of iteration and χ^2_k is the tracking χ^2 in the k-th iteration.

In the present analysis, the initial parameters of x, y, u and v were obtained from the SDC3, 4 local tracking. The initial momentum was set event by event by checking the horizontal direction cosine (dx/dz) of the SDC3, 4 track. We set the initial momentum which is higher about 100 MeV/c than the actual momentum as shown in Figure 3.17. Figure 3.18 shows a typical reduced χ^2 distribution of the SKS tracking. The black and red histograms correspond to all the events and kaon selected events, respectively. χ^2 value less than 30 was accepted, which was determined to keep the sufficient efficiency for kaon.

The SKS tracking efficiency was also estimated from the (π^+, p) reaction events be-

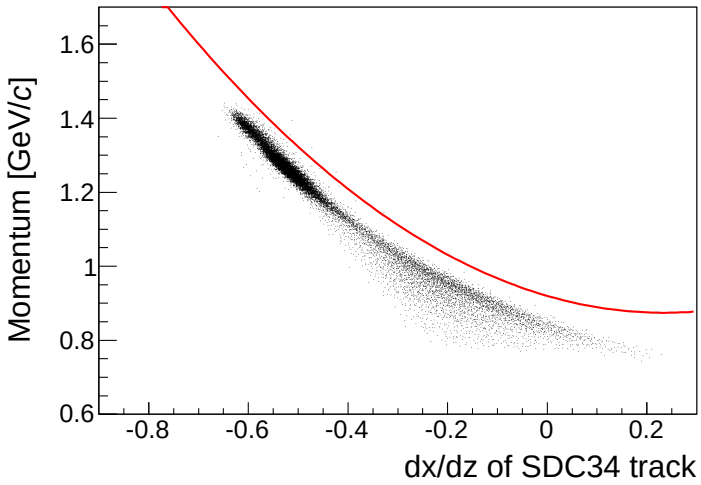

Figure 3.17: Initial momentum function of the SKS tracking as a function of horizontal direction cosine (dx/dz) of the SDC3, 4 track indicated with the red line. A correlation between momenta and dx/dz of SDC3, 4 track is also shown in this figure.

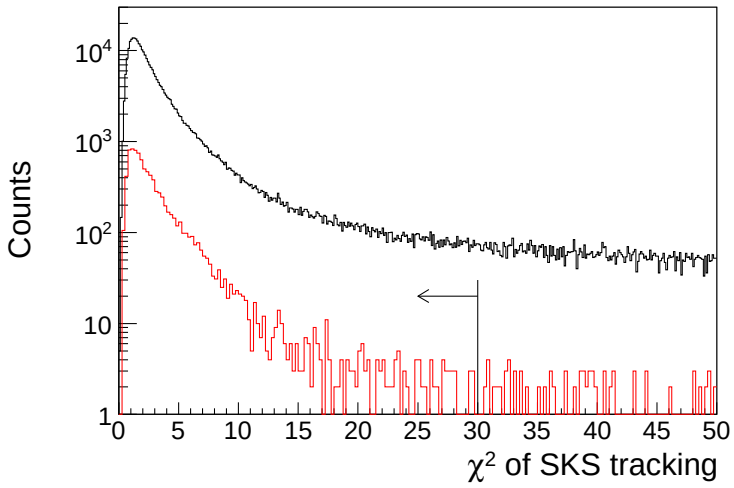

Figure 3.18: Typical reduced χ^2 distributions of the SKS tracking. The black and red lines indicate the distributions of total events and emitted kaon events, respectively.

cause the emitted particles which do not decay in flight should be selected to estimate the efficiency. The decay-in-flight particles such as pion make the χ^2 of SKS tracking worse. The procedure of the selection of emitted protons was same as that of SDC3, 4 in Figure 3.16.

In the present analysis, the SKS tracking efficiency was defined as the probability that the χ^2 of SKS tracking was less than 30 when there were good single tracks in SDC1, 2 and SDC3, 4 local tracking. Figure 3.19 shows the efficiency of the SKS tracking as a function of the scattering angle (θ_{SDC12}), which was obtained from the local tracking of BC3, 4 and SDC1, 2. Here, the SKS tracking efficiency depended on the scattering angle. Therefore, we corrected this efficiency event by event by checking the scattering angle to calculate the double differential cross section.

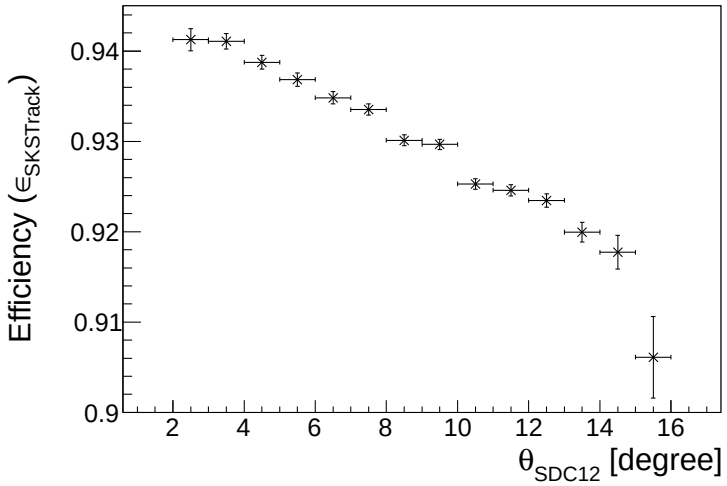

Figure 3.19: The SKS tracking efficiency as a function of scattering angle.

3.3.4 Efficiency for K^+ trigger counters

The detection efficiency and overkill factor of trigger counters for emitted K^+ (TOF, LC, LAC) were estimated from the controlled trigger data set.

The efficiency of TOF and LC counter was determined from the data set of these triggers as

$$\begin{aligned} LC\ Triger &\equiv BEAM \times LC, \\ TOF\ Triger &\equiv BEAM \times TOF, \end{aligned}$$

respectively. The hits of the estimated counters were not required in these controlled triggers. The TOF and LC efficiency was obtained as:

$$\epsilon_{TOF} = \frac{N(TOF \times Track \times LC)}{N(Track \times LC)}, \tag{3.15}$$

$$\epsilon_{LC} = \frac{N(LC \times Track \times TOF)}{N(Track \times TOF)}, \tag{3.16}$$

where $N(Track \times LC(TOF))$ is the number of tracks which should pass through the effective area of TOF (LC) selected from the local tracking of SDC3, 4 and $N(TOF(LC) \times Track \times LC(TOF))$ the number of those tracks detected by TOF (LC). When we estimated the LC efficiency, the outgoing particles were selected as π^+ with the mass squared (M^2). The LC efficiency is assumed to be same for K^+ because the sufficient yield of Čerenkov photons are obtained from K^+ with the momentum above the 0.8 GeV/c. The efficiency averaged in the whole segment of TOF and LC was estimated to be 99.5 $\pm$ 0.4 (syst.) % and 99.6 $\pm$ 0.1 (syst.) %, respectively. These systematic errors were obtained from the difference of the efficiency for each segment.

The factor of LAC was estimated by considering two origins of an accidental veto from the π^+ coincidence events and a δ-ray emission from the K^+ as

$$f_{LAC} = f_{LAC}^{Acc} \times f_{LAC}^{\delta-ray}. \tag{3.17}$$

The accidental veto factor (f_{LAC}^{Acc}) was obtained from $PIPI$ trigger indicated as Eq.2.6. This trigger was mixed during the physics data taking as the calibration trigger and did not required LAC anti-coincidence. In order to estimate the overkill factor, we used the emitted proton events which should not be detected by LAC and these protons were selected in mass squared (M^2). The overkill factor was obtained from

$$f_{LAC}^{Acc} = 1 - \frac{N(LAC \times Proton)}{N(Proton)}, \tag{3.18}$$

where $N(Proton)$ is the number of events at least one proton passing through the LAC and $N(LAC \times Proton)$ is the number of accidental-hit events in LAC in the coincidence width. The coincidence width was estimated by checking the TDC distribution of LAC with the PIK trigger, which required the anti-coincidence of LAC. The obtained accidental veto factor was 96.3 $\pm$ 0.5 (syst.) %. The systematic error was estimated by changing the coincidence width by $\pm$ 5 ns. The factor due to the δ-ray ($f_{LAC}^{\delta-ray}$) was estimated in a simulation with the Geant4 [91] and found to be 96.9 $\pm$ 0.1 (syst.) %. The systematic error was estimated by changing the incident momenta from 0.8 to 1.2 GeV/c and the incident positions and angles in the simulation. In total, the overall factor of LAC (f_{LAC}) was found to be 93.3 $\pm$ 0.5 (syst.) %.

3.3.5 Kaon identification in the SKS

The emitted kaon was roughly selected by using the information of SDC1, 2 tracking, TOF and LC counters. In this selection, the cuts were applied to TOF-ADC, LC-ADC and flight-time of BH2-TOF, BH2-LC, TOF-LC. In addition, the kaon was selected using the horizontal direction cosine (dx/dz) obtained from SDC1, 2 local tracking and the flight time between BH2 and TOF as shown in Figure 3.20. These cut regions were loosely selected so as to keep the kaon-selection efficiency about 100% because the kaon was strictly identified afterwards by a time-of-flight of BH2-TOF in combination with the flight path length obtained from the SKS global tracking. The total kaon-selection efficiency of these rough cuts was obtained to be 98.7%.

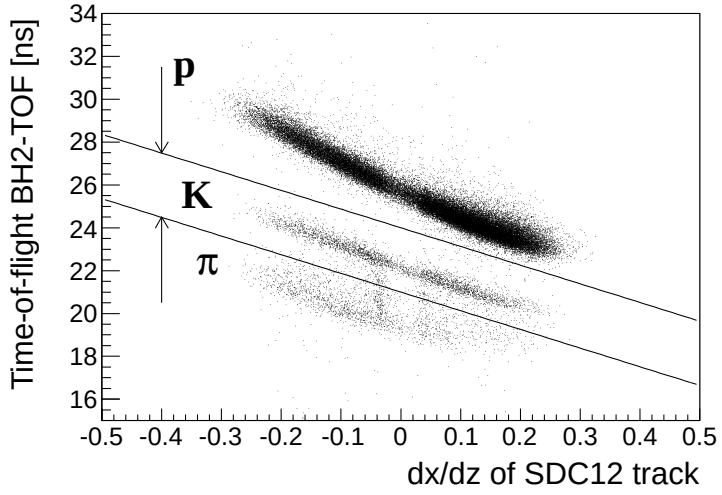

Figure 3.20: Scatter plot between the horizontal direction cosine measured by SDC1, 2 and the flight time of BH2-TOF. The selected region of kaon was also indicated in the figure.

The K^+ was finally identified by calculating the mass squared M^2 of the outgoing particles as:

$$M^2 = \left(\frac{p}{\beta}\right)^2 (1-\beta^2), \tag{3.19}$$

$$\beta = (\text{path length})/(\text{flight time} \cdot c), \tag{3.20}$$

where p and β are the momentum and the velocity of the outgoing particle, respectively. Here, p was obtained from the SKS tracking and β was calculated from the time-of-flight and the flight path between BH2 and TOF. Figure 3.21 shows an M^2 spectrum for the data set of the $p(\pi^+, K^+)$ reaction at 1.58 GeV/c (a) and the $d(\pi^+, K^+)$ reaction at 1.69 GeV/c (b) without any event selection by TOF and LC counters and local tracks. The kaon selection gate was set as $0.15 < M^2 < 0.45$ $(\text{GeV}/c^2)^2$. When there is one good kaon track, the other tracks are discarded in the analysis.

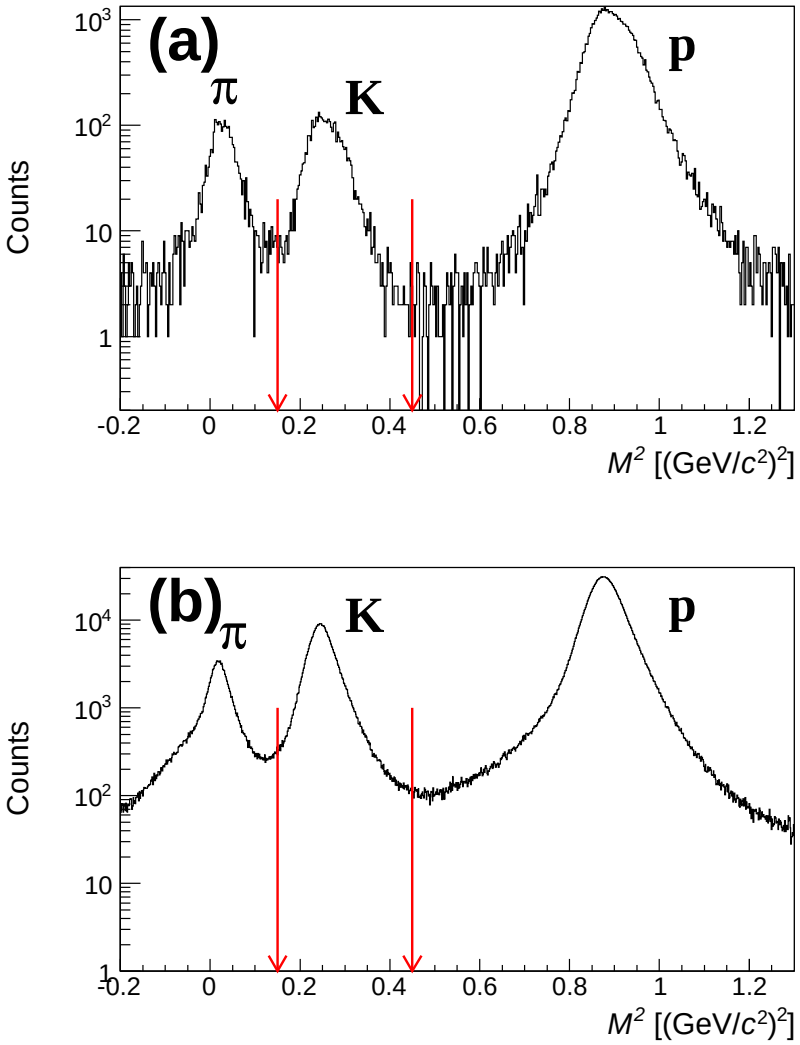

Figure 3.21: Mass squared distributions for the outgoing particles. The M^2 distribution without any TOF and LC cut for the data set of $p(\pi^+, K^+)$ at 1.58 GeV/c and $d(\pi^+, K^+)$ at 1.69 GeV/c are shown in (a) and (b), respectively.

Figure 3.22 shows a mass squared (M^2) spectrum for the $p(\pi^+, K^+)\Sigma^+$ reaction at 1.58 GeV/c. The black and red histograms indicate the mass squared spectrum before and after the pre-selections, respectively. The kaon selected region ($0.15 < M^2 < 0.45$ (GeV/c^2)^2) is shown in green arrows. The events after the pre-selections were free from proton as observed in the red histogram. Therefore, we chose the upper limit of the M^2 to be 0.45 (GeV/c^2)^2, which was less than -5σ from the proton peak. On the other hand, there is the tail in the low M^2 region. Therefore, we set the lower limit of the M^2 to be 0.15 (GeV/c^2)^2 to avoid the contamination of pion. It was -3σ from the kaon peak and more than $+4\sigma$ from the pion peak.

The K^+ identification efficiency (ϵ_{PID}) was obtained as

$$\epsilon_{PID} = \epsilon_{K-Hodo} \times \epsilon_{PID-M^2}, \tag{3.21}$$

$$\epsilon_{PID-M^2} = \frac{N(M^2 cut \times pre\text{–}cut)}{N(pre\text{–}cut)}, \tag{3.22}$$

where ϵ_{K-Hodo} is the rough cut efficiency using the TOF and LC. The efficiency for the mass squared cut (ϵ_{PID-M^2}) was estimated to be 98.5 $\pm$ 0.7 (syst.) %. The systematic error was estimated by changing the pre-cut conditions. Finally, the total kaon selection efficiency was estimated to be $\epsilon_{PID} = 97.2 \pm 0.7$ (syst.) %.

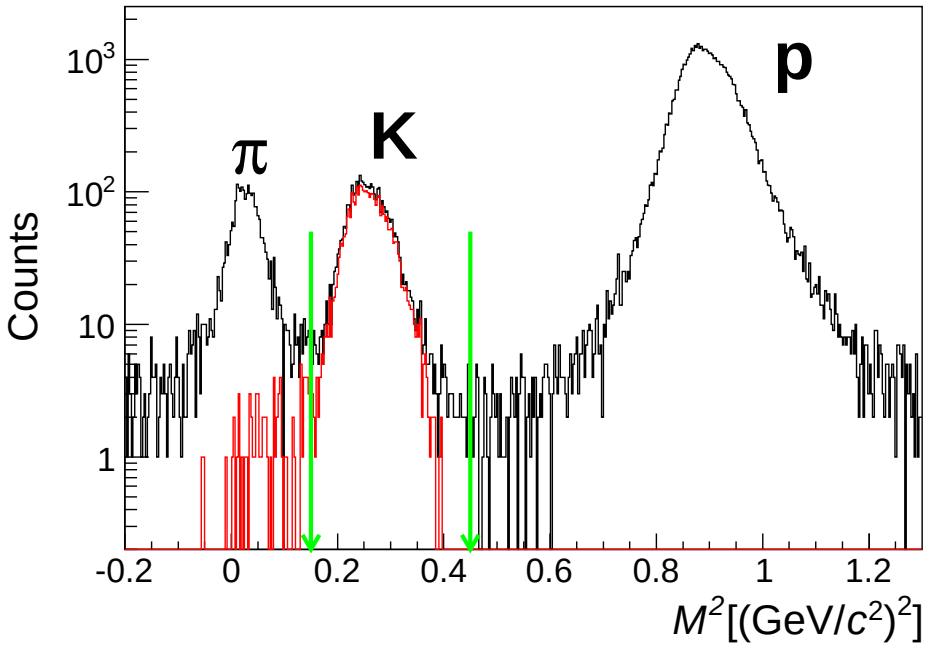

Figure 3.22: The mass square (M^2) distribution for the $p(\pi^+, K^+)\Sigma^+$ data. The black and red histogram are the mass square spectrum before and after the pre-selections.

3.4 Vertex reconstruction

In order to eliminate the background not coming from the target, the scattering angle and vertex point of the (π^+, K^+) reaction were reconstructed from both incident beam and outgoing particle trajectories obtained from the BC3, 4 and SKS tracking.

Figure 3.23 shows the difference distribution of the direction cosine between the BC3, 4 and SKS tracking measured in the beam-through data without target at $p_{\pi^+} = 0.9$ GeV/c. In this figure, the horizontal (dx/dz) one and vertical (dy/dz) one are shown in (a) and (b), respectively. We obtained the horizontal and vertical angular resolutions of 2.6 mrad and 3.3 mrad in σ, respectively. The vertical resolution was worse than the horizontal one because of the wire configuration of the drift chamber.

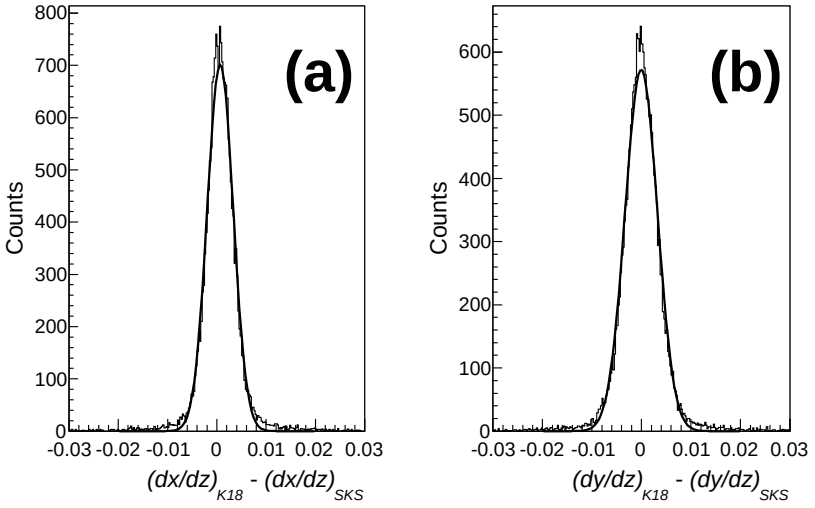

Figure 3.23: The distribution of the difference of the dx/dz (a) and dy/dz (b) between the BC3, 4 and SKS tracking. These spectra were obtained from beam-through data without the target.

The reaction vertex was determined from the closest distance between the BC3, 4 and SKS tracks. The vertex profile of the x (horizontal) and y (vertical) direction and the target size are shown in Figure 3.24, which was obtained from the $p(\pi^+, K^+)\Sigma^+$ data at 1.58 GeV/c. The liquid target was large enough for the incident beam with a typical beam size of 7.6 $\times$ 4.2 mm^2 in σ.

Figure 3.26 shows the z-vertex distribution of each scattering angle ($\theta_{\pi K}$) in laboratory system. The z-vertex resolutions of each scattering angle were estimated by the template fit as shown in red lines in Figure 3.26 and these results are summarized in Figure 3.25. These spectra were also obtained from the $p(\pi^+, K^+)\Sigma^+$ data at 1.58 GeV/c. The vertex resolution became worse for the small scattering angle. Moreover, the amount of background such as $\pi^+ \to \mu^+$ decay in flight increased for the small scattering angle. Therefore, the scattering angle cut ($\theta_{\pi K} > 2^\circ$) was applied. The vertex cuts in 3 direction were applied in the real target region shown by arrows.

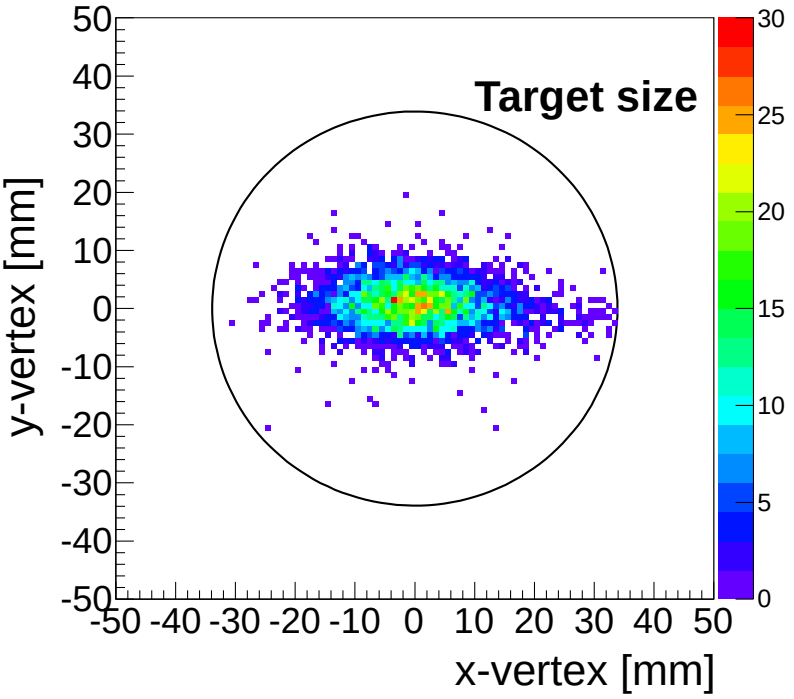

Figure 3.24: The vertex distribution of x and y direction, which was obtained from the $p(\pi^+, K^+)\Sigma^+$ reaction data at 1.58 GeV/c. The target size is also indicated with a solid line.

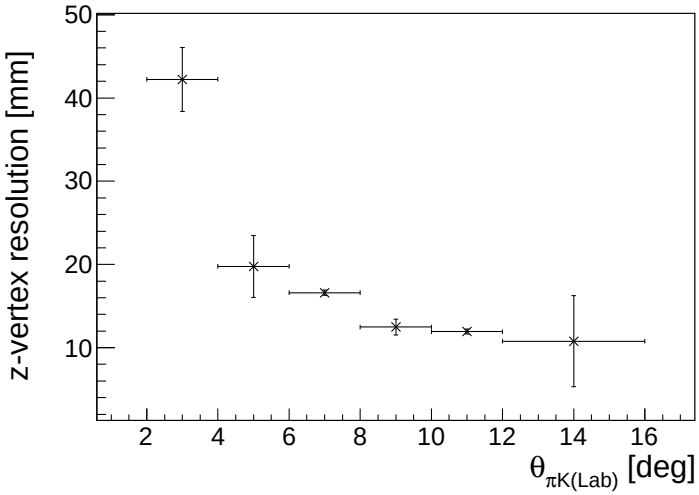

Figure 3.25: The summary of z-vertex resolution in each scattering angle. These values were estimated from the fitting shown in Figure 3.26.

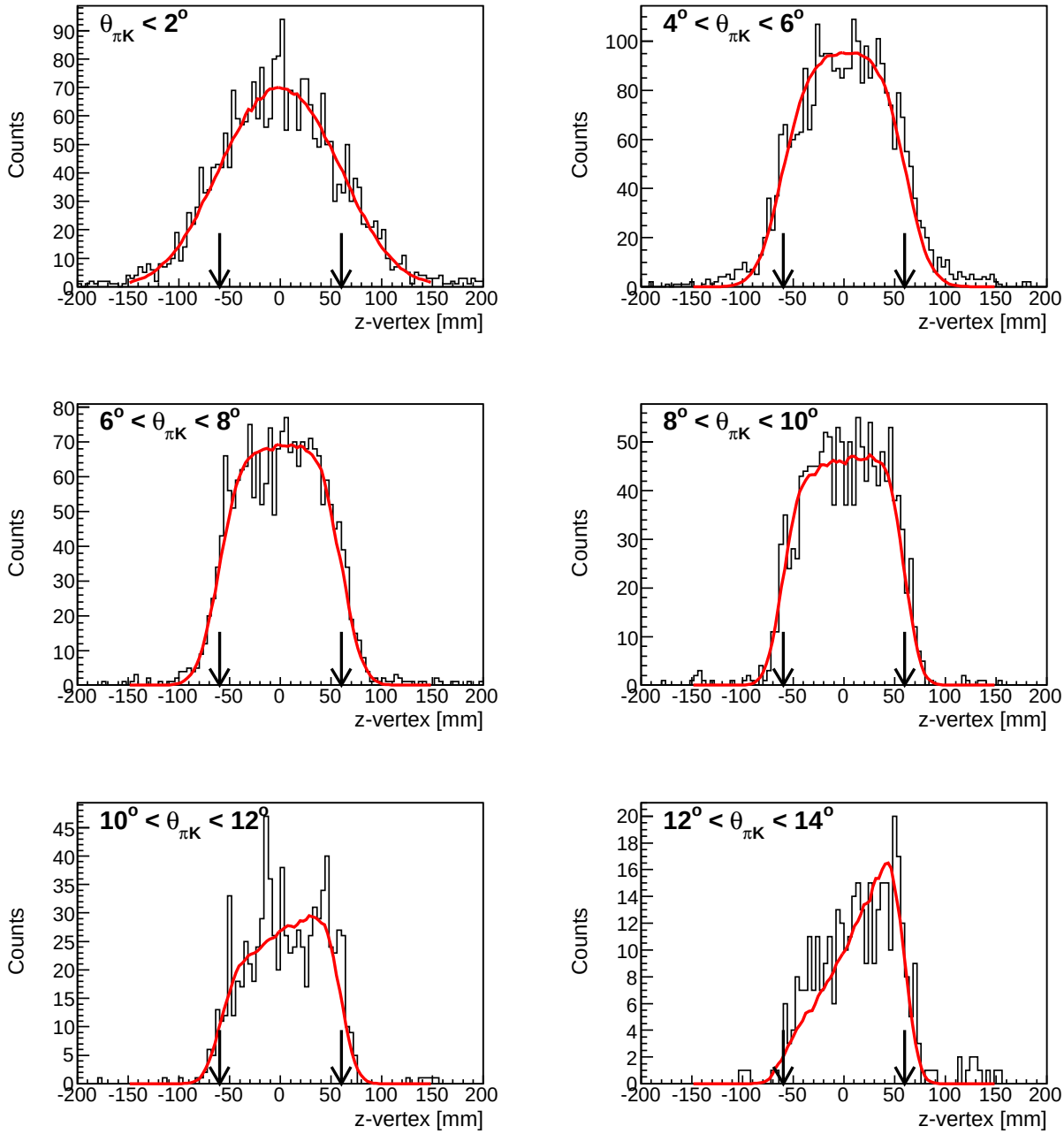

Figure 3.26: The vertex distribution of z direction of each scattering angle ($\theta_{\pi K}$) in laboratory system obtained from the $p(\pi^+, K^+)\Sigma^+$ data at 1.58 GeV/c . The vertex resolutions of z direction were estimated by the fitting as the red lines. The target size was indicated by arrows.

The efficiency of the x-vertex and y-vertex cuts were assumed to be 100%. Therefore, only the z-vertex selection, which was selected as the target size, was considered for the estimation of the vertex cut efficiency. The z-vertex selection efficiency was determined from the resolutions as shown in Figure 3.25. These efficiency as a function of scattering angle are plotted in Figure 3.27. We corrected the vertex cut efficiency event by event by using the scattering angle to calculate the double differential cross section.

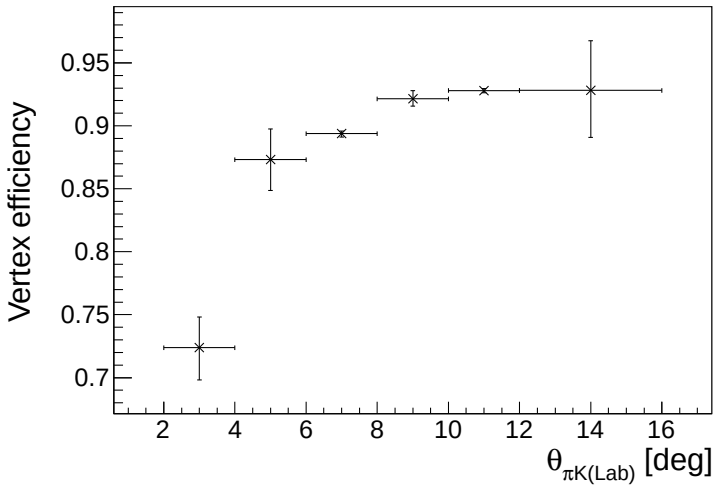

Figure 3.27: The vertex cut efficiency as a function of scattering angle. These values were estimated from the z-vertex resolution as shown in Figure 3.25.

3.5 Momentum correction

We applied two types of momentum corrections. One is the momentum correction of emitted K^+ in order to optimize the missing-mass resolution. It is because, we can see the correlation between the missing-mass and the scattering angle of the $p(\pi^+, K^+)\Sigma^+$ reaction. Next, we corrected the momenta of beam pions to obtain the absolute momentum by using the beam-through and Σ^+ productions data. It is necessary because the discrepancy of about 3 MeV/c^2 can be seen between the measured missing-mass of $p(\pi^+, K^+)\Sigma^+$ reaction and the PDG value [92].

3.5.1 Momentum correction of K^+

In the present experiment, the momenta of the outgoing particles were reconstructed by using the calculated magnetic field map for the SKS magnet. However, this calculated field map might not completely reproduce the real one. This effect may cause some correlation between the momentum and the scattering angle.

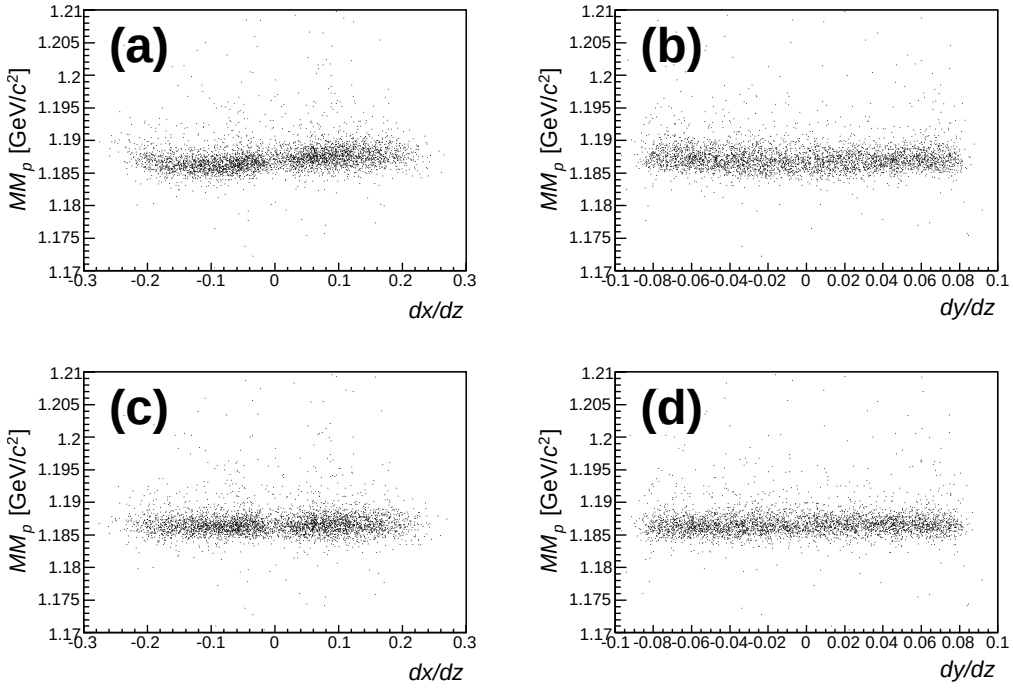

Figure 3.28: Scatter plots between the direction cosines and the missing mass in the $p(\pi^+, K^+)\Sigma^+$ reaction at 1.58 GeV/c. The figures (a) and (b) show the plot before correction and figures (c) and (d) show the plots after correction.

Figure 3.28(a) and (b) show scatter plots between the missing mass (MM_p) in the $p(\pi^+, K^+)\Sigma^+$ reaction at 1.58 GeV/c and the horizontal (dx/dz, a) or the vertical (dy/dz, b) direction cosines at the target position. This correlation was removed by introducing a phenomenological correction as the fifth order polynomial in both horizontal and vertical

direction cosines. These parameters were obtained by fitting the momentum difference, $dp_K = p_K^{calc} - p_K^{measured}$, as a function of dx/dz or dy/dz. The (p_K^{calc}) was the calculated K^+ momentum assuming the kinematics of the $p(\pi^+, K^+)\Sigma^+$ reaction and the $p_K^{measured}$ was the measured momentum from the SKS tracking. Figures 3.28(c) and (d) show scatter plots after this correction. This momentum correction of K^+ was applied to the analysis of whole data.

Energy loss correction

The energy loss in materials was corrected in order to reconstruct the real momentum and optimize the missing-mass resolution.

For the beam π^+, the energy loss corrections in BH2 and the targets were taken into account. These values were estimated from the π^+ beam-through data with and without target at 0.9 GeV/c. The energy loss of the target was obtained as the shift of the centroid of the momentum difference measured from the K1.8 tracking and the SKS tracking with and without the target in the beam-through data. The obtained sifts for the hydrogen and deuterium target were 3.2 $\pm$ 0.1 MeV/c and 3.6 $\pm$ 0.2 MeV/c, respectively. These values are about 10% lower than the values of Bethe-Bloch formula. The energy loss in BH2 was corrected using the Bethe-Bloch formula by considering this difference.

For the emitted K^+, the energy loss correction was applied with the Bethe-Bloch formula. In the present analysis, the energy loss in the target was corrected event-by-event by using the vertex position.

3.5.2 Momentum correction of π^+ and systematic error

The momenta of beam pions were corrected with a linear function by considering the result of the beam-through data at 0.9 GeV/c and $p(\pi^+, K^+)\Sigma^+$ data at 1.58 and 1.69 GeV/c in order to reduce the differences of Σ^+ masses between the measured values and the PDG value. Since the SKS magnetic field was fixed through the all data taking, the momentum of outgoing particle was not corrected in this analysis. The momentum difference between the K1.8 and SKS tracking, $dp = p_{K18} - p_{SKS}$, was obtained to be 1.8 $\pm$ 0.1 MeV/c from the beam-thorough data at 0.9 GeV/c and this value was considered of the energy loss in BH2. In the $p(\pi^+, K^+)\Sigma^+$ reaction, we obtained the Σ^+ mass as a peak. However, the measured Σ^+ masses had deviations from the PDG value. The deviations, $dM = (M_{\Sigma^+}^{measured} - M_{\Sigma^+}^{PDG})$, are $dM = -2.9 \pm 0.1$ MeV/c^2 at $p_{\pi^+} = 1.58$ GeV/c and $dM = -2.5 \pm 0.1$ MeV/c^2 at $p_{\pi^+} = 1.69$ GeV/c. Thus, we can estimated the beam momentum deviation as:

$$dp_\pi = \frac{dM}{(\partial M/\partial p_\pi)}, \tag{3.23}$$

$$\frac{\partial M}{\partial p_\pi} = \frac{1}{M}[\beta_\pi(M_{Target} - E_K) + p_K \cos\theta], \tag{3.24}$$

The beam momentum deviation (dp_π) for the beam-through and Σ^+ production data are summarized in Figure 3.29. The incident beam momentum was corrected with a

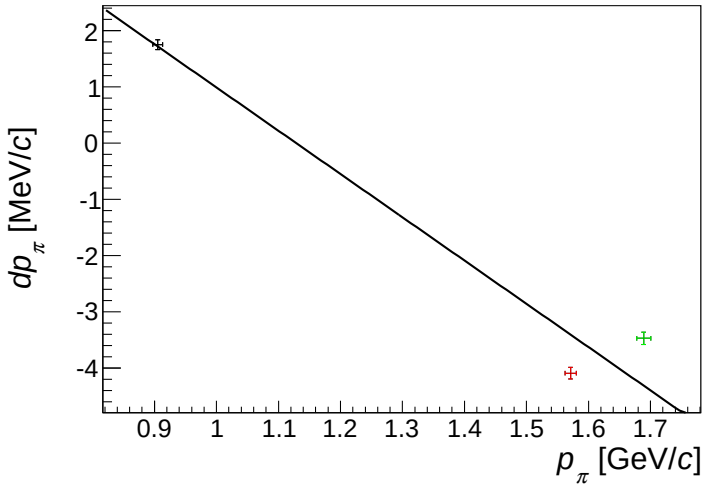

Figure 3.29: The momentum difference (dp_π) measured by the K1.8 beam line and the SKS. A black point with error bar shows the momentum difference between the K1.8 and SKS tracking obtained from the beam-through data. Red and green points with error bar show the momentum difference estimated from the Σ^+ data analysis at 1.58 and 1.69 GeV/c, respectively. The fitting result with the linear function to obtain the correcting parameter is also shown with black line.

linear function as:

$$p_{K18}^{corr} = 1.0077 \times p_{K18} - 0.0087 \text{ GeV}/c, \tag{3.25}$$

where p_{K18}^{corr} is the corrected beam momentum and p_{K18} is the measured beam momentum. This correcting function was obtained from the fit as shown in Figure 3.29.

After the absolute momentum adjustment, the validity of the corrections was tested in the $\pi^+ p \to K^+\Sigma(1385)^+$ production at 1.69 GeV/c. Figure 3.30 shows the missing mass spectrum in the $\Sigma(1385)^+$ region in the $p(\pi^+, K^+)$ reaction at 1.69 GeV/c. A fit result with a Lorentzian function for the $\Sigma(1385)^+$ (dashed line) and three-body phase space distributions for the $\Lambda\pi K^+$ (dotted line) and the $\Sigma\pi K^+$ (dot-dashed line) are also shown. The $\Sigma(1385)^+$ mass and width are found to be 1381.1 $\pm$ 3.6 (stat.) MeV/c^2 and 42 $\pm$ 13 (stat.) MeV, respectively, which are consistent with the PDG values [92] within the statistical errors.

The dp_π and dp_K values after correction are summarized in Figure 3.31, where dp_K is defined as:

$$dp_K = \frac{dM}{(\partial M/\partial p_K)}, \tag{3.26}$$

$$\frac{\partial M}{\partial p_K} = -\frac{1}{M}[\beta_K(M_{Target} + E_\pi) - p_\pi \cos\theta]. \tag{3.27}$$

Finally, the systematic uncertainty of the momentum scale was estimated to be 1.1 MeV/c from these values.

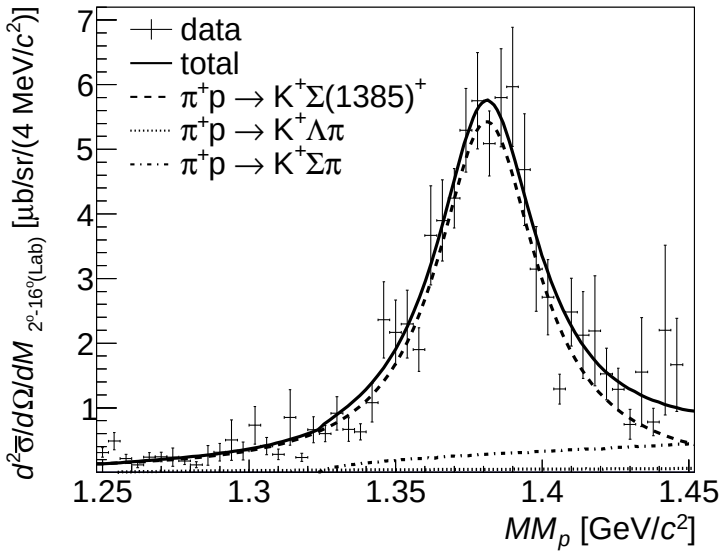

Figure 3.30: The missing-mass spectrum of the $p(\pi^+, K^+)$ reaction in the $\Sigma^+(1385)$ mass region. The experimental data are shown by black points with statistical errors. The spectrum was fitted with $\Sigma(1385)^+$ (dashed line), $\Lambda\pi$ (dotted line) and $\Sigma\pi$ (dot-dashed line) productions. Taken from Ref. [93].

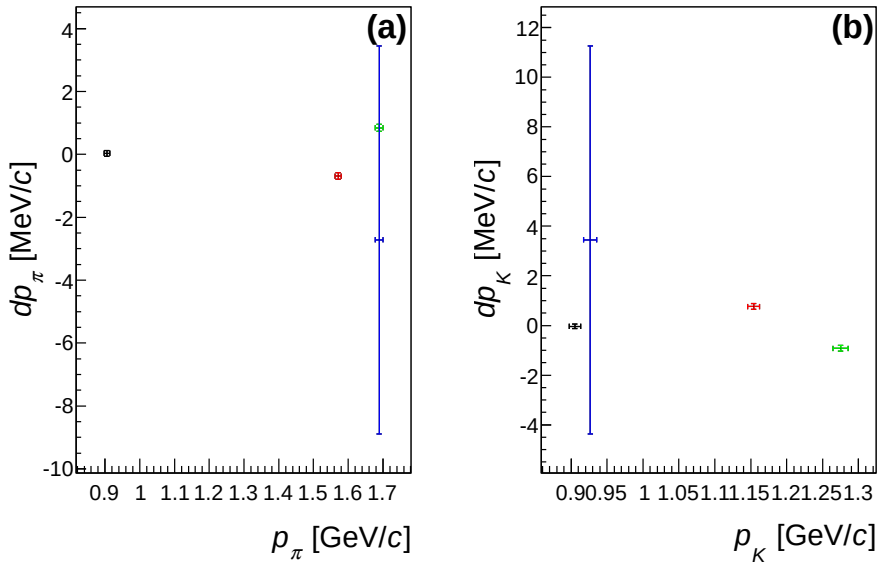

Figure 3.31: The momentum difference after the correction. The obtained values for the beam pions and emitted kaons are shown in (a) and (b), respectively. Black points with error bars show the momentum difference obtained from the beam-through data. Red and green points with error bars show the momentum difference estimated from the Σ^+ data analysis at 1.58 and 1.69 GeV/c, respectively. Blue points with error bars show the values estimated from the $\Sigma(1385)^+$ data analysis at 1.69 GeV/c.

3.6 Missing-mass resolution

In this subsection, we discuss a missing-mass resolution. The goal of this part is to estimate the missing-mass resolution of the $d(\pi^+, K^+)$ reaction by using the information of the beam-through and $p(\pi^+, K^+)\Sigma^+$ data. The missing mass resolution (ΔM) was estimated from:

$$\Delta M^2 = \Delta_{K18}^2 + \Delta_{SKS}^2 + \Delta_\theta^2 + \Delta E_{Target}^2. \tag{3.28}$$

Then, the missing-mass resolution can be divided to the contributions of the resolutions of K1.8 beam line spectrometer (Δ_{K18}), the SKS (Δ_{SKS}) and scattering angle (Δ_θ) and the energy loss straggling in the target (ΔE_{Target}). Further, each term in the equation can be expressed as:

$$\begin{aligned}
\Delta M^2 &= (\frac{\partial M}{\partial p_{K18}})^2 \Delta {p_{K18}}^2 + (\frac{\partial M}{\partial p_{SKS}})^2 \Delta {p_{SKS}}^2 + (\frac{\partial M}{\partial \theta})^2 \Delta\theta^2 + \Delta E_{Target}^2, \quad (3.29)\\
\frac{\partial M}{\partial p_{K18}} &= \frac{1}{M}[\beta_\pi (M_{Target} - E_K) + p_K \cos\theta],\\
\frac{\partial M}{\partial p_{SKS}} &= -\frac{1}{M}[\beta_K (M_{Target} + E_\pi) - p_\pi \cos\theta],\\
\frac{\partial M}{\partial \theta} &= -\frac{p_\pi p_K}{M} \sin\theta,
\end{aligned}$$

where E_π and p_π are the total energy and momentum of pions, E_K and p_K are those of kaons, M_{Target} is the rest mass of the target nucleus, and θ is the scattering angle of the reaction, Δp_{K18} and Δp_{SKS} the momentum resolution of the K1.8 beam line spectrometer and the SKS, respectively, and $\Delta\theta$ the resolution of the scattering angle.

Now, we estimate the resolution of each term. The resolution of the scattering angle was estimated from the resolution of horizontal direction cosines (Δu_{K18}, Δu_{SKS}) and vertical direction cosines (Δv_{K18}, Δv_{SKS}) as

$$\begin{aligned}
\Delta\theta^2 &= (\frac{\partial\theta}{\partial u_{K18}})^2 \Delta {u_{K18}}^2 + (\frac{\partial\theta}{\partial u_{SKS}})^2 \Delta {u_{SKS}}^2 + (\frac{\partial\theta}{\partial v_{K18}})^2 \Delta {v_{K18}}^2 + (\frac{\partial\theta}{\partial v_{SKS}})^2 \Delta {v_{SKS}}^2,\\
\theta &= \arccos\left(\frac{u_{K18}u_{SKS} + v_{K18}v_{SKS} + 1}{\sqrt{u_{K18}^2 + v_{K18}^2 + 1}\sqrt{u_{SKS}^2 + v_{SKS}^2 + 1}}\right),
\end{aligned}$$

where u_X and v_X are the direction cosines of each spectrometer. The total resolution of the horizontal and vertical ones were measured to be $\sqrt{u_{K18}^2 + u_{SKS}^2} = 2.6$ mrad and $\sqrt{v_{K18}^2 + v_{SKS}^2} = 3.3$ mrad in σ as described in Sec. 3.4. Further, the ratio of the distance of BC3, 4 and SDC1, 2 was about 10 : 7. Thus, each angular resolution was estimated to be $(\Delta u_{K18}, \Delta u_{SKS}, \Delta v_{K18}, \Delta v_{SKS})$ = (1.5, 2.2, 1.9, 2.7) mrad by combining these information.

The energy loss term ΔE_{Target} was estimated by the Geant4 [91] based Monte Carlo simulation. In this simulation, not only the energy loss straggling but also the difference of the path length in the target were included. The ΔE_{Target} values for three different kinematics: the Σ^+ production at 1.58 GeV/c, the $K^- pp$ production and the ΣN cusp, were obtained to be 0.6 MeV, 0.8 MeV and 0.8 MeV, respectively.

Table 3.3: The scattering-angle resolutions and the missing mass resolutions of the Σ^+ production at 1.58 GeV/c data.

θ [degree]	2–4	4–6	6–8	8–10	10–12
$\Delta\theta$ [mrad] (FWHM)	6.9±0.5	6.7±0.5	6.4±0.3	6.3±0.1	6.2±0.1
ΔM_{Σ^+} [MeV/c^2] (FWHM)	2.5±0.1	2.5±0.1	2.7±0.1	2.7±0.1	2.7±0.2

Total momentum resolution of the K1.8 beam line spectrometer and the SKS was estimated from the beam-through data without a target. The total resolution, $\Delta p^2_{beam\text{-}through} = \Delta p^2_{K18} + \Delta p^2_{SKS}$, was obtained from the width of the momentum difference measured from K1.8 tracking and the SKS tracking to be 2.2 MeV/c. Furthermore, we have information of the missing-mass resolution of the $p(\pi^+, K^+)\Sigma^+$ reaction. The measured missing-mass resolution of Σ^+ for each scattering angle is listed in Table. 3.3. Here, the resolution of the scattering angle in the $p(\pi^+, K^+)\Sigma^+$ kinematics for each angle was calculated by using the measured direction cosines event by event. These angular resolutions for the Σ^+ kinematics were also listed in Table. 3.3. Thus, we can estimate the momentum resolution of K1.8 beam line spectrometer (Δp_{K18}) and the SKS (Δp_{SKS}) by solving the Eq. 3.29 for the kinematics of $p(\pi^+, K^+)\Sigma^+$ reaction with the information of $\Delta p_{beam\text{-}through}$ and $\Delta\theta$ (in Table. 3.3). The momentum resolution of each spectrometer calculated in this scheme is summarized in Figure 3.32. The solid and dashed lines in this figure show the mean value and root mean square, respectively. Therefore, we estimated the resolutions of all components of Eq. 3.29. Finally, by using those resolutions, the missing mass resolution of $d(\pi^+, K^+)$ reaction for two different kinematics: the K^-pp (2.27 GeV/c^2) and the ΣN cusp (2.13 GeV/c^2), were estimated to be 2.7 ± 0.1 MeV/c^2 and 3.2 ± 0.2 MeV/c^2, respectively.

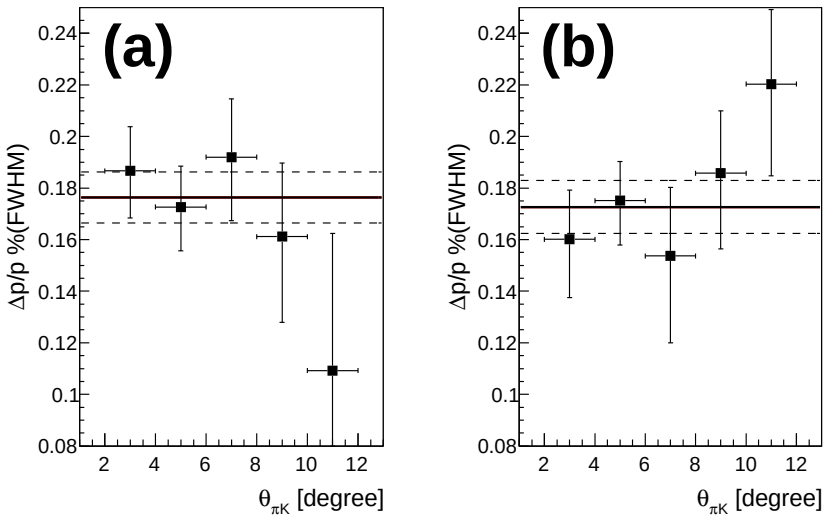

Figure 3.32: The momentum resolution of K1.8 beam line spectrometer (a) and the SKS (b). The solid and dashed lines are mean values and root mean squares, respectively.

3.7 Cross section

After selecting the (π^+, K^+) events, the missing-mass spectrum was obtained as a double differential cross section of $d^2\bar{\sigma}_{\theta_1-\theta_2}/d\Omega/dM$ averaged over the scattering angle from θ_1 to θ_2. The double differential cross section is calculated as:

$$\frac{d^2\bar{\sigma}_{\theta_1-\theta_2}}{d\Omega dM} = \frac{A}{N_A(\rho x)} \frac{N_{\pi K}}{N_{beam}\Delta\Omega_{\theta_1-\theta_2}\Delta M \epsilon}, \tag{3.30}$$

$$\begin{aligned}
\epsilon &= \epsilon_\pi \times \epsilon_K \times \epsilon_{DAQ} \times \epsilon_{trig} \times \epsilon_{vertex}, \\
\epsilon_\pi &= \epsilon_{BeamTOF} \times (1 - f_\mu) \times \epsilon_{BC12} \times \epsilon_{BC34} \times \epsilon_{K18Track}, \\
\epsilon_K &= \epsilon_{TOF} \times \epsilon_{LC} \times f_{LAC} \times \epsilon_{SDC12} \times \epsilon_{SDC34} \times \epsilon_{SKSTrack} \times \epsilon_{PID} \times f_{decay},
\end{aligned}$$

where A is the target mass number, N_A the Avogadro constant, ρx the target mass thickness, $N_{\pi K}$ the number of good (π^+, K^+) events in the missing-mass interval ΔM, N_{beam} the number of beam pions on the target, $\Delta\Omega_{\theta_1-\theta_2}$ the solid angle of SKS between θ_1 and θ_2 and ϵ the overall experimental efficiency resulting from DAQ, detectors, and analysis cuts including the K^+ decay factor. The experimental efficiency except for DAQ (ϵ_{DAQ}), the trigger bias (ϵ_{trig}), K^+ decay factor and acceptance of the SKS is already described in previous sections in this chapter. A typical value of the overall experimental efficiency is $\epsilon = 17.6 \pm 0.7$ ($syst.$) %. In this section, we describe procedures of the estimation of these remaining efficiency.

3.7.1 Data acquisition efficiency (ϵ_{DAQ})

The data acquisition efficiency, ϵ_{DAQ}, caused by the dead time of the data acquisition system, was obtained as a probability that 1st-level trigger is accepted when the data acquisition system generates triggers. ϵ_{DAQ} was obtained as a function of the trigger rate, and the typical value was 65.7 ± 1.0 (syst.) %. The main contribution of the dead time was the data transfer time of the TKO multi-hit TDC module.

3.7.2 Efficiency of the trigger bias (ϵ_{trig})

During the $d(\pi^+, K^+)$ data taking, the pre-scaled unbiased (π, K) trigger data without the matrix trigger, the mass trigger and BVH anti-coincidence was also taken with the pre-scaled factor of 100. Then, these trigger efficiency and accidental veto factor was determined by comparing the (π, K) inclusive trigger data and the unbiased (π, K) trigger data. Figure 3.33 shows the obtained missing mass (MM_d) spectra in each trigger condition. In this figure, the unbiased (π, K) trigger data was scaled by considering the pre-scaled factor and the difference of ϵ_{DAQ} in each trigger condition. Here, we checked the overall missing mass structure were consistent with each other. Finally, the overall efficiency of these trigger was evaluated by diving those spectra as shown in Figure 3.34. These values were averaged in whole MM_d region to be 91.6 ± 0.7 (syst.) %, whose systematic error was estimated from the difference in each MM_d region.

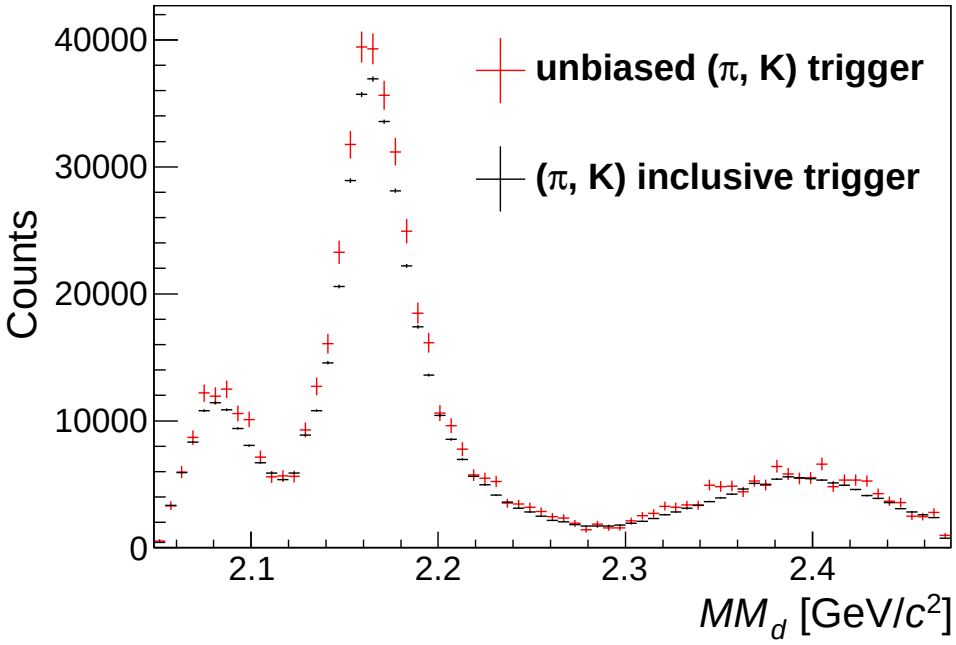

Figure 3.33: Comparison between (π, K) inclusive trigger data (black points) and the unbiased (π, K) trigger data (red points).

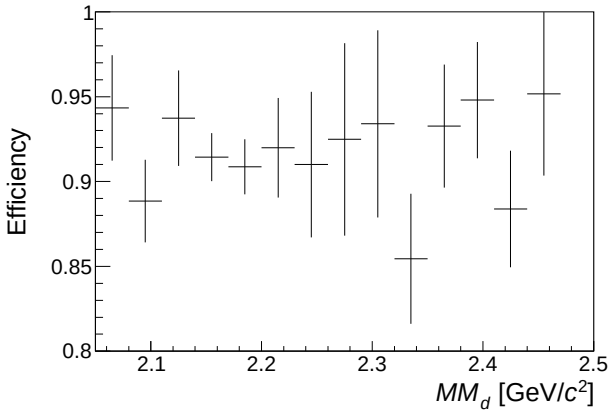

Figure 3.34: Efficiency of the Matrix trigger, Mass trigger and BVH accidental veto factor as a function of MM_d.

3.7.3 K^+ decay factor (f_{decay})

A part of K^+ produced in the target decayed in flight in the SKS magnet. Since the decay products such as μ^+ could be detected, the kaons which decayed before passing through the LAC were rejected in the trigger level. The survival rate until the LAC, f_{decay}, was estimated event by event as a function of the flight path length (L_K) of the kaons and its $\beta\gamma c\tau$ as:

$$f_{decay} = exp(-L_K/\beta\gamma c\tau), \tag{3.31}$$

where τ was life time of K^+. The obtained decay factor as a function of missing mass (MM_d) of the $d(\pi^+, K^+)$ data was shown in Figure 3.35. A typical value was 58.8 $\pm$ 0.3 (syst.) %. The systematic error was estimated by taking into account the radiator size of LAC.

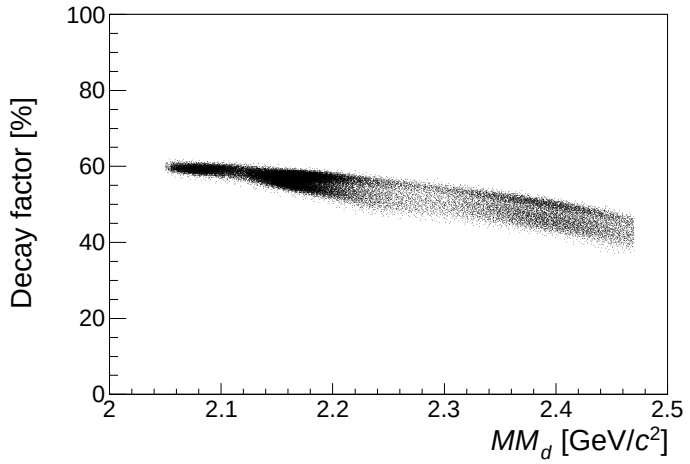

Figure 3.35: The obtained decay factor as a function of MM_d.

3.7.4 Acceptance of the SKS

The effective solid angle of the SKS ($\Delta\Omega_{\theta 1-\theta 2}$) was estimated with a Monte Carlo simulation based on the Geant4 [91]. The solid angle with the missing mass (MM_d or MM_p) and the scattering angle (θ) is defined as:

$$\Delta\Omega_{\theta 1-\theta 2}(MM,\ \theta) = 2\pi \int_{\theta 1}^{\theta 2} d\cos(\theta) \times \epsilon_{Acc}, \tag{3.32}$$

$$\epsilon_{Acc} = \frac{N(accepted\ events)}{N(generated\ events)}, \tag{3.33}$$

where $\theta 1$ and $\theta 2$ are expressed as $\theta - \frac{1}{2}\Delta\theta$ and $\theta + \frac{1}{2}\Delta\theta$ using a fixed interval ($\Delta\theta$).

In the event generation, the beam profiles of (x_b, y_b, $(dx/dz)_b$,$(dy/dz)_b$, p_b) were produced from the experimental data, where x_b, y_b, $(dx/dz)_b$,$(dy/dz)_b$, p_b are the horizontal and vertical position and their direction cosines and the momentum of a beam particle at the target, respectively. The distribution in the z-direction is generated assuming a flat distribution.

The scattered kaons were generated assuming the $\pi^+ + d\ (p) \rightarrow K^+ + X$ reaction. Then, we checked the mass of X in this reaction with missing mass and the scattering angle event by event. The obtained table of the ϵ_{Acc} in Eq. 3.32 as a function of the missing mass and the scattering angle is shown in Figure 3.36 for the deuteron target data and in Figure 3.37 for the proton target data. The incident momentum is 1.69 GeV/c in both cases.

In the simulation, the multiple-scattering effect, the energy loss and the hadronic interaction were taken into account. In the present analysis, a mesh size of the table is 2 MeV/c^2 in the missing mass axis and 0.1 degrees in the scattering angle axis.

In the present analysis, the upper limit of the MM_d (MM_p) was set to be 2.47 GeV/c^2 (1.44 GeV/c^2) because the SKS acceptance was small and changed rapidly in these large MM_d and MM_p regions. Moreover, we selected events in the scattering angle from 2° to 16° for the same reason.

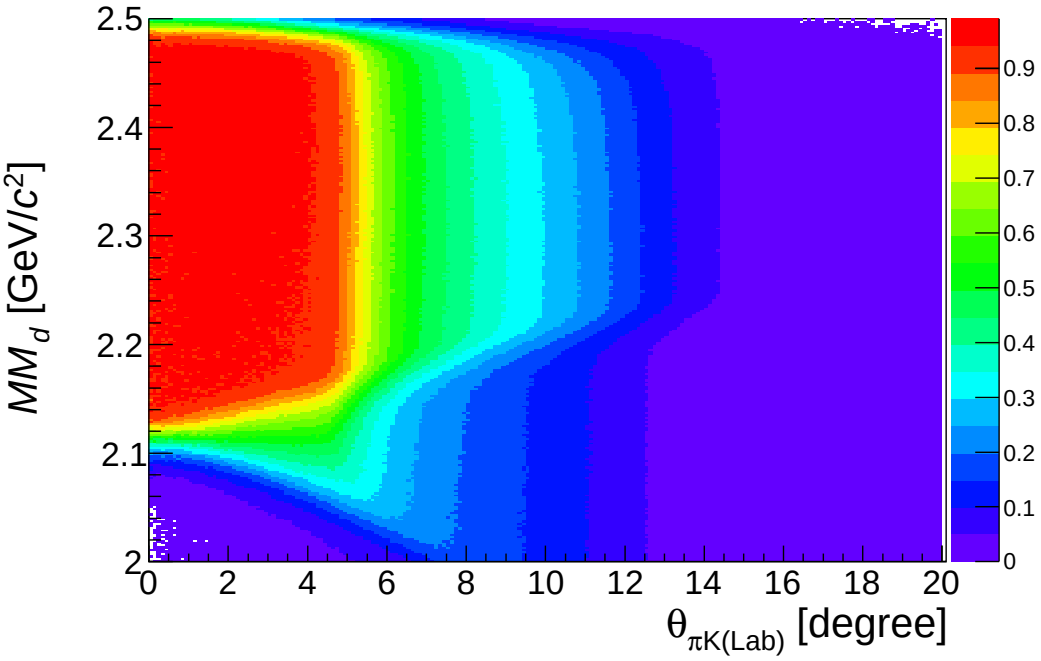

Figure 3.36: The acceptance table for the $d(\pi^+, K^+)$ at 1.69 GeV/c data.

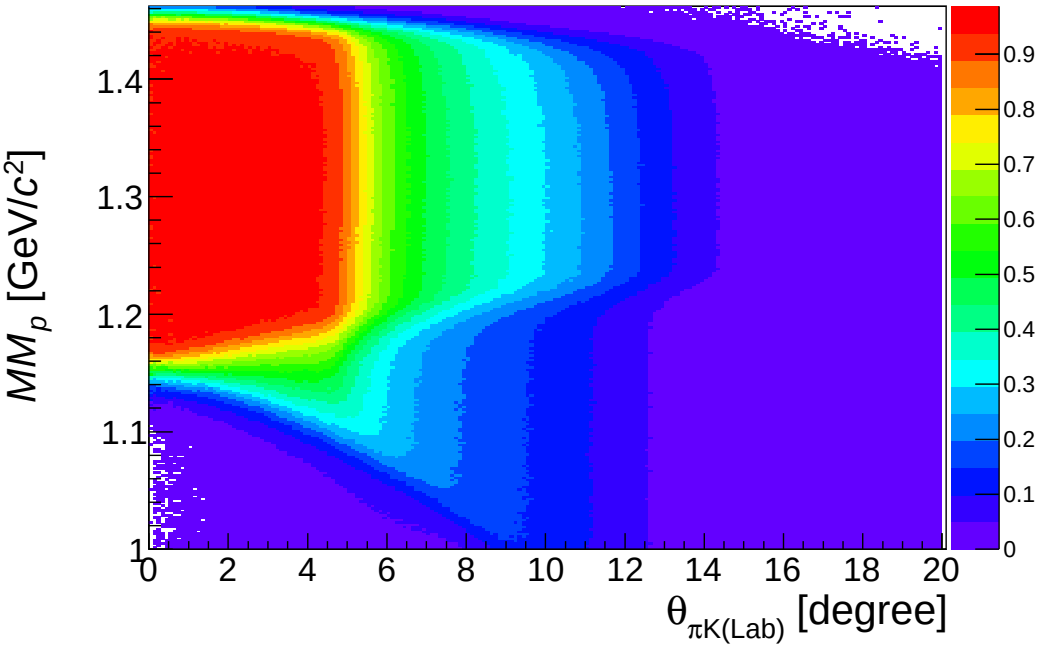

Figure 3.37: The acceptance table for the $p(\pi^+, K^+)$ at 1.69 GeV/c data.

Table 3.4: The list of the experimental efficiency and systematic error for the common factor (ϵ_{com}).

Factors	Meaning	Typical value (ϵ) [%]	$\Delta\epsilon/\epsilon$ [%]
$\epsilon_{BeamTOF}$	Beam TOF efficiency	99.6 ± 0.1	0.1
$1 - f_{\mu}$	μ contamination factor	96.6 ± 0.1	0.1
ϵ_{BC12}	BC1-2 efficiency	93.8 ± 1.9	2.0
ϵ_{BC34}	BC3-4 efficiency	99.1 ± 0.1	0.1
$\epsilon_{K18Track}$	K1.8 tracking efficiency	87.9 ± 1.2	1.4
ϵ_{TOF}	TOF efficiency	99.5 ± 0.4	0.4
ϵ_{LC}	LC efficiency	99.6 ± 0.1	0.1
f_{LAC}	LAC factor	93.3 ± 0.5	0.5
ϵ_{SDC12}	SDC1-2 efficiency	95.7 ± 1.7	1.8
ϵ_{SDC34}	SDC3-4 efficiency	99.2 ± 0.0	0.0
ϵ_{PID}	PID efficiency for K^+	97.2 ± 0.7	0.7
ϵ_{DAQ}	Data-acquisition efficiency	65.7 ± 1.0	1.5
ϵ_{trig}	Trigger efficiency (Matrix, Mass, BVH)	91.6 ± 0.7	0.8
	Total	$\epsilon_{com} = 40.4 \pm 1.5$	3.6

3.7.5 Systematic errors

There were two kinds of efficiency and factors in Eq. 3.30. One is the efficiency corrected event by event. It includes the SKS tracking efficiency ($\epsilon_{SKSTrack}$), the decay factor (f_{decay}), the vertex efficiency (ϵ_{vertex}) and the acceptance of SKS (ϵ_{Acc}). The other efficiency is common to all events. These common efficiency with systematic errors are summarized in Table 3.4 and found to be $\epsilon_{com} = 40.4 \pm 1.5$ (syst.) %. The total efficiency, ϵ, is described as

$$\epsilon = \epsilon_{com} \times \epsilon_{SKSTrack} \times \epsilon_{decay} \times \epsilon_{vertex} \times \epsilon_{Acc}. \tag{3.34}$$

The errors of efficiency corrected event by event are shown in Figure 3.38, whose errors were averaged in all events for each missing mass bin. Here, the error of ϵ_{Acc} was estimated by changing the mesh size of the acceptance table as (1, 2, 3) MeV/c^2 for the missing-mass mesh and (0.05, 0.1, 0.15) degrees for the scattering-angle mesh.

The total systematic error of correcting factors, ϵ, in Eq. 3.30, are shown in Figure 3.39 as a function of missing mass. The fluctuation of the systematic error in each missing-mass bin is small and the averaged value is $\Delta\epsilon/\epsilon = 4.4\%$.

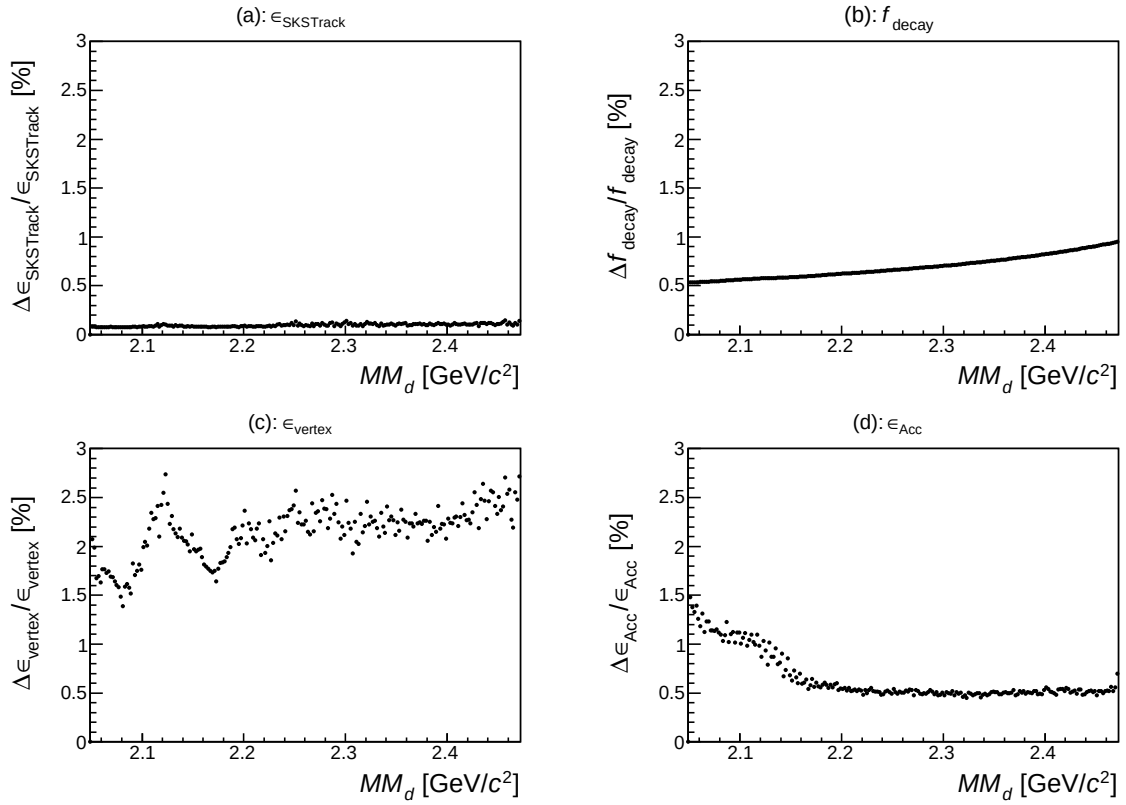

Figure 3.38: The systematic error of the $\epsilon_{SKSTrack}$, f_{decay}, ϵ_{vertex} and ϵ_{Acc} as functions of missing-mass for the $d(\pi^+K^+)$ at 1.69 GeV/c data.

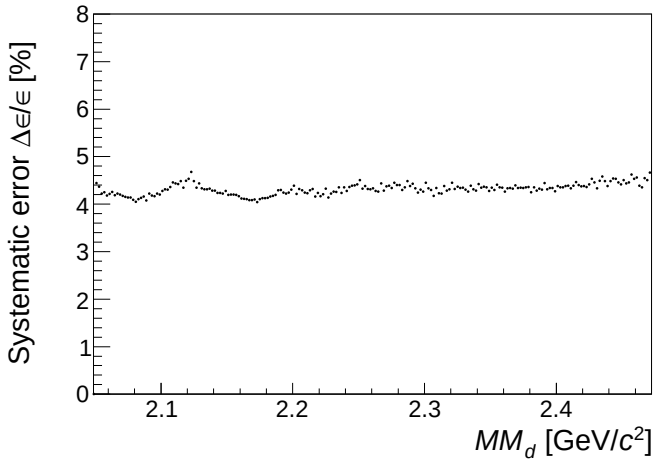

Figure 3.39: The total systematic error ($\Delta\epsilon/\epsilon$) for the double differential cross section as a function of missing-mass.

3.8 The Σ^+ production cross section

In order to check the overall validity of the efficiency correction, we compared the differential cross sections of the $p(\pi^+, K^+)\Sigma^+$ reaction between our measurement and old measurement at the same momenta of 1.58 and 1.69 GeV/c by Candlin *et al.* [94]. Figure 3.40 shows the missing-mass spectrum (MM_p) obtained from the incident beam momenta of 1.58 (1.69) GeV/c in (a)((b)). Thus, the Σ^+ peaks were clearly observed.

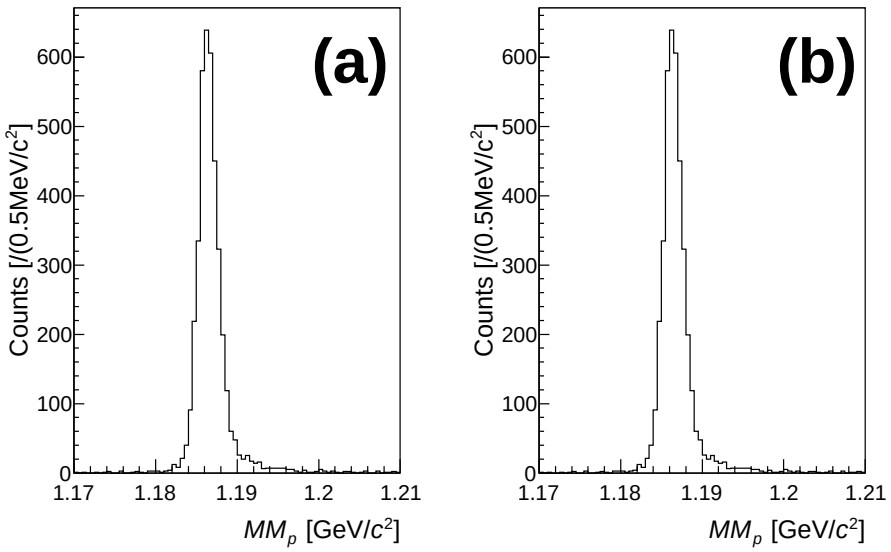

Figure 3.40: The obtained missing-mass spectra (MM_p) for the $p(\pi^+, K^+)\Sigma^+$. The spectra of the incident beam momenta of 1.58 GeV/c and 1.69 GeV/c are shown in (a) and (b), respectively.

Figure 3.41 shows the three kinematical lines as a function of particle momentum and scattering angle for the $p(\pi^+, K^+)\Sigma^+$ reactions at 1.58 GeV/c (solid line) and 1.69 GeV/c (dashed line) and the $d(\pi^+, K^+)K^-pp$ reaction at 1.69 GeV/c assuming the binding energy of 100MeV (dotted line). The acceptance of the SKS is also shown in this figure. The kinematical line of the Σ^+ production reaction at 1.58 GeV/c and the $d(\pi^+, K^+)K^-pp$ have a good overlap with the almost flat momentum acceptance region.

As shown in Figure 3.41, the kinematical lines of the Σ^+ productions at two different incident momenta run through different acceptance ares. In both cases, we obtained a reasonable agreement between our data and the previous ones within the large errors as shown in Figure 3.42 for 1.58 GeV/c and Figure 3.43 for 1.69 GeV/c. Since the old measurement was given in the center of mass system, these were transformed to the laboratory system for comparison.

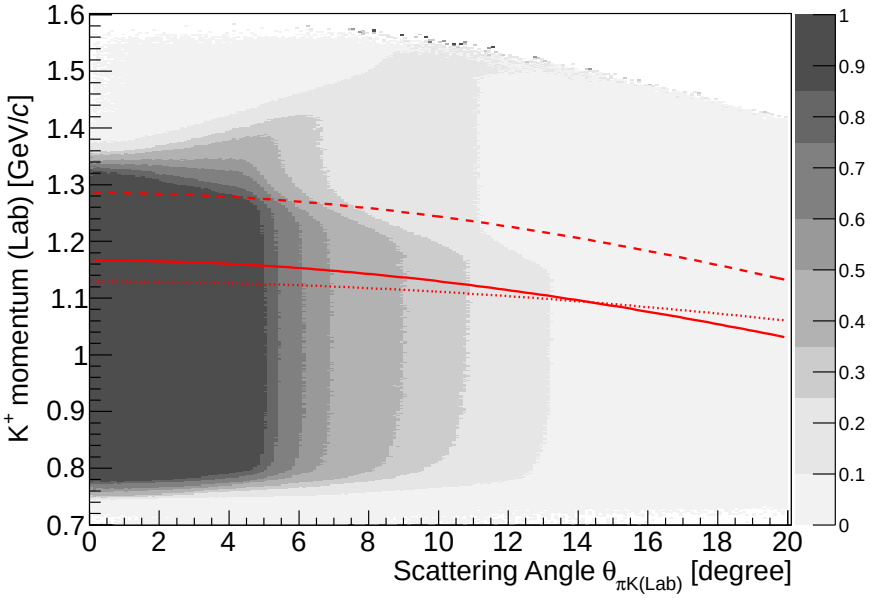

Figure 3.41: Three kinematical lines of K^+ for the $p(\pi^+, K^+)\Sigma^+$ reactions at 1.58 GeV/c (solid line) and 1.69 GeV/c (dashed line) and the $d(\pi^+, K^+)K^-pp$ reaction at 1.69 GeV/c assuming the binding energy of 100MeV (dotted line). Acceptance of the SKS is also shown. Taken from Ref. [93].

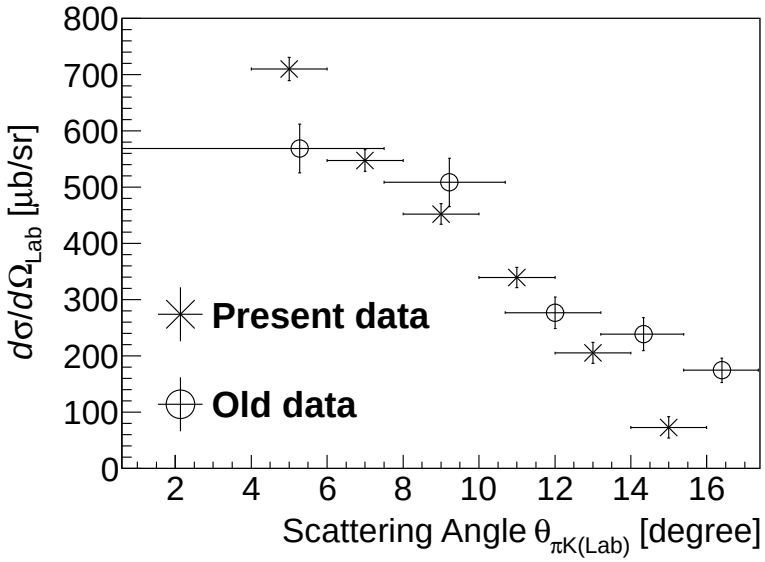

Figure 3.42: The differential cross section of Σ^+ production at $p_{\pi^+} = 1.58$ GeV/c. The present data and the referenced old ones [94] are shown by crosses with statistical errors and open circles, respectively.

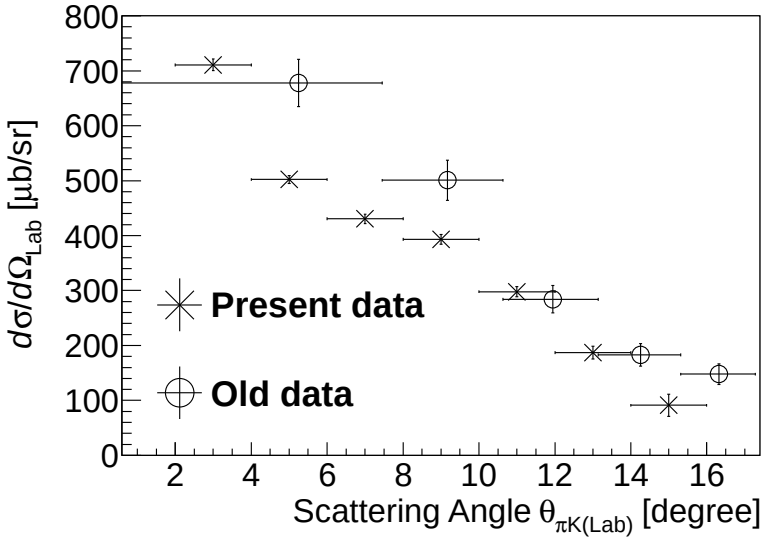

Figure 3.43: The differential cross section of Σ^+ production at $p_{\pi^+} = 1.69$ GeV/c. The present data and the referenced old ones [94] are shown by crosses with statistical errors and open circles, respectively. Taken from Ref. [93].

Chapter 4

Analysis II - Coincidence analysis

The analysis for RCA is discussed in this chapter. The goal of this part is to select the proton by using the information of RCA and determine the momentum of proton.

4.1 Outline

The RCA was composed of six segments of range counter array and each segment had five layers plastic scintillation counters, where the first two layers were segmented into two slabs. Every scintillation counter was read out from both up and down sides by phototubes (PMT). Thus, the RCA had total 84 PMT's and we read out the ADC and TDC information from every PMT. Each segment of RCA is analyzed with the same procedures.

In the RCA analysis, we measured the velocity (β) to determine the proton momentum as β = (path length)/(TOF$\cdot c$), where the path length was measured from the (π^+, K^+) vertex position and hit position on the first layer of RCA obtained from the time difference between the up and down PMT's, TOF was the time of flight between the BH2 and the first layer of RCA and c is the light velocity. The particle identification (proton selection) was carried out by using the particle identification parameter (PID), which was calculated using the information of the energy deposit, the velocity and stopping layer. Thus, the energy deposit information was used to obtain not the kinetic energy of the incident particles but the PID because the velocity had less uncertainties than the total energy deposit.

The analysis is carried out as the following procedures:

- The velocity of each particle was reconstructed by combining the information of TOF and the path length. TOF was measured from the time difference between BH2 and the first layer of RCA, whose time offset parameters were adjusted by using the π^+ ($\beta \sim 1$) from the $\Sigma^+ \to \pi^+ n$ decay in the $\pi^+ d \to K^+ \Sigma^+ X$ reaction. The path length was determined as $(path\ length) = \sqrt{(x_{RCA} - x_{\pi K})^2 + (y_{RCA} - y_{\pi K})^2 + (z_{RCA} - z_{\pi K})^2}$, where ($x_{\pi K}$, $y_{\pi K}$, $z_{\pi K}$) were the (π^+, K^+) vertex positions and (x_{RCA}, y_{RCA}, z_{RCA}) were the hit positions in the first layer of RCA.

- The energy gain of each layer of RCA was calibrated by using the information

of the pedestal and the pulse height for minimum ionization particles (MIP) and stopped proton events in the RCA. The particle identification parameter (PID) was set up from the energy deposit of each layer. The gain adjustment is important to correctly calculate the PID.

- Proton was selected by combining the information of the stopping layer of RCA, the velocity and the PID. The momentum of the proton was reconstructed from the velocity and the hit position of the first layer of RCA.

4.2 Velocity calibration

Velocity of a particle (β) was obtained as β = (path length)/(TOF$\cdot c$), where c was the light speed. TOF was the time-of-flight for each particle obtained from the hit timings of BH2 and the first layer of RCA.

The TDC values of these counters were converted to the time using the TDC conversion gain. A slewing correction was carried out to improve the time resolution. In this analysis, the parameters of this correction for BH2 were determined by using the beam π^+. In case of RCA, these parameters were tuned by using the information of the first and second layers in order to reduce the ambiguity of the flight path length. In this determination of the parameters, the high velocity ($\beta \sim 1$) and the small energy loss events corresponding to the MIP were selected for all layers of RCA. Figures 4.1 and 4.2 show a typical scatter plot between the ADC and flight time before/after the slewing correction for the BH2 and RCA, respectively. After this correction, the time resolution of the $\mathrm{TOF_{BH2-RCA}}$ was found to be 158 $\pm$ 16 ps.

The path length was obtained as,

$$(path\ length) \ = \ \sqrt{(x_{RCA} - x_{\pi K})^2 + (y_{RCA} - y_{\pi K})^2 + (z_{RCA} - z_{\pi K})^2}, \qquad (4.1)$$

where ($x_{\pi K}$, $y_{\pi K}$, $z_{\pi K}$) was vertex position of the (π^+, K^+) reaction and (x_{RCA}, y_{RCA}, z_{RCA}) was the hit position in the first layer. In this analysis, the horizontal hit position (x_{RCA} and z_{RCA}) was assumed to be the center of the scintillators and the vertical hit position (y_{RCA}) was obtained from the time difference between the up and down PMT's. The light velocity inside the scintillators was measured to be 14.4 $\pm$ 1.0 cm/ns by using the cosmic rays by changing the relative position defined by the small trigger counters. Thus, the vertical position resolution of RCA was about 8 mm. The time offset between the up and down PMT's corresponding to the center of the vertical position was determined by fitting the time difference spectrum with a Gaussian function as shown in Figure 4.3.

The time offset for each segment of RCA was properly adjusted by using the π^+ peak from the Σ^+ decay of the $\pi^+ d \to K^+\Sigma^+ n_s$ reaction, where n_s was the spectator neutron, by selecting the missing-mass (MM_d) region of $2.15 < MM_d < 2.22$ GeV/c^2 (see Figure 5.1). Figure 4.4 shows a typical obtained $1/\beta$ spectrum of this missing-mass region compared with the simulated one. In this comparison, a small energy-loss events corresponding to the MIP were selected to reject the other particles such as a proton from the Σ^+ decay. The accuracy of this time-offset adjustment was better than 100 ps, which was studied by using two-proton coincidence events described in Appendix B.

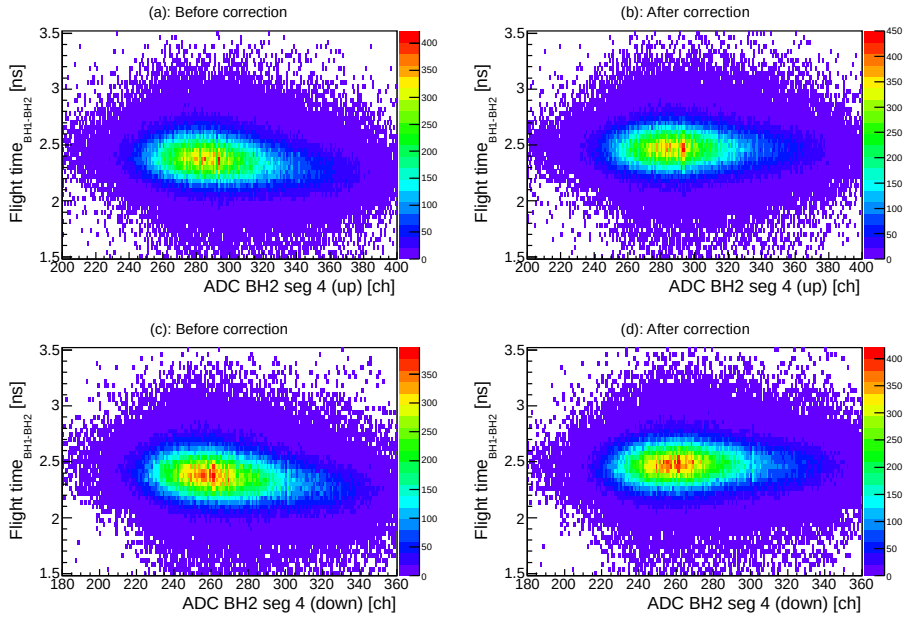

Figure 4.1: A typical scatter plot between the ADC of up and down PMT's of BH2 and flight time of BH1 to BH2. The scatter plot before the slewing correction are shown in (a): (ADC of up PMT) and (c): (ADC of down PMT). Similarly, the scatter plot after the slewing correction in (b) and (d).

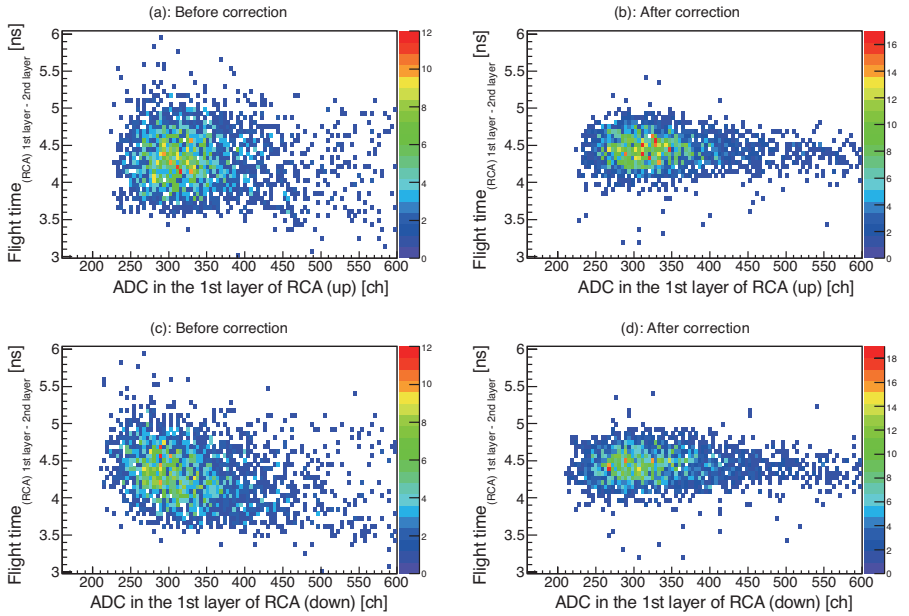

Figure 4.2: A typical scatter plot between the ADC of up and down PMT's of the first layer of RCA and flight time of the first layer to second layer of RCA. The scatter plot before the slewing correction are shown in (a): (ADC of up PMT) and (c): (ADC of down PMT). Similarly, the scatter plot after the slewing correction in (b) and (d).

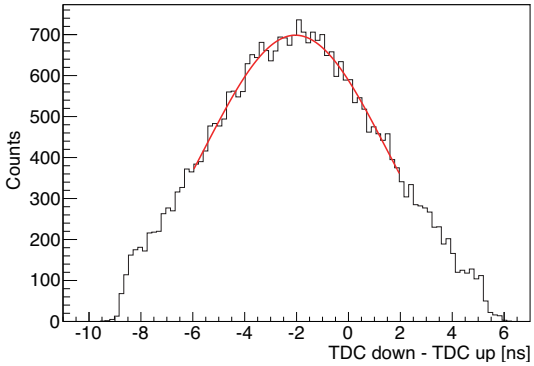

Figure 4.3: A typical time difference spectrum between the up and down PMT's of the first layer of RCA before the adjustment. The spectrum was fitted with a Gaussian function (red line) to obtain the time offset corresponding to the center of the vertical position of RCA.

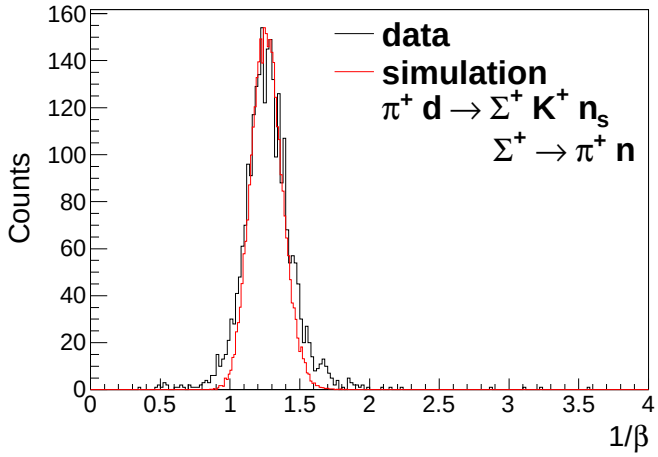

Figure 4.4: A typical $1/\beta$ spectrum around the quasi-free Σ production region of the $d(\pi^+, K^+)$ reaction compared with simulation. In this figure, the π^+ event from the Σ^+ decay was selected by requiring the small energy loss events.

4.3 Gain calibration

A light output of plastic scintillator is not necessarily proportional to the energy deposit because the light output tends to be saturated as the energy deposit becomes larger due to the quenching effect [95]. Thus, the relative gain of each PMT was corrected by using the ADC pedestal information and the peak pulse heights for MIP and for stopped proton events in the RCA, and fitted with a second order polynomial.

As the first step, we roughly adjusted the ADC value (ch) of each counter with a linear function by using two peaks corresponding to the pedestal and MIP. In the selection of the MIP event, the high velocity $\beta \sim 1$ and the vertical hit position around the center were chosen in order to reduce the ambiguity of the incident angle.

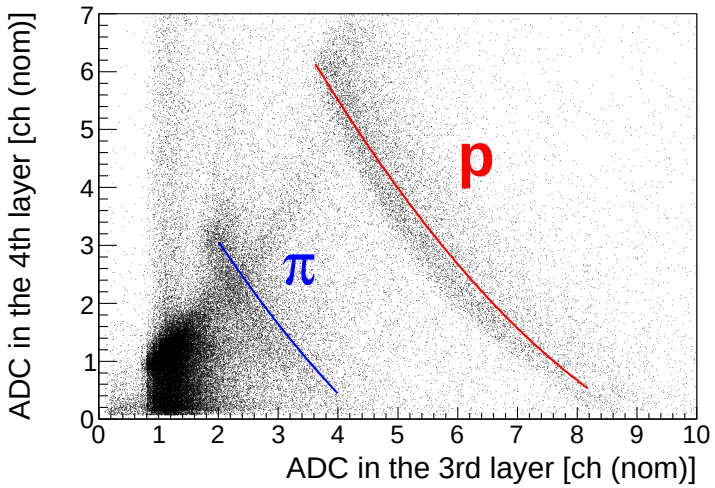

Figure 4.5: The correlation plot between the normalized ADC values of the third layer and fourth layer of RCA. We can see the stopped charged pion's and proton's clusters as shown in blue and red lines, respectively.

From the hit pattern of five layers, we can define the stopping layer, i_{stop}, for each RCA. Figure 4.5 shows a typical correlation plot between the normalized ADC values of the third layer and fourth layer of RCA for the events of $i_{stop} = 4$. In this figure, we can see the charged pion's and proton's clusters stopping at the fourth layer of RCA as shown in blue and red lines, respectively. Then, we obtained the maximum energy deposit for these proton events stopping at the forth layer by fitting with a function of $\frac{a}{1+d}\{d + \tanh(b(-x + c))\}$ as shown in Figure 4.6 (a). In this proton selection, the vertical hit position around the center ($< \pm$ 10 cm) was also chosen in order to select the perpendicular incident events. The same fitting procedure was applied to the simulated one constructed with Geant4 program [91], as shown in Figure 4.6 (b). The energy deposit at this maximum ADC channel was adjusted with the simulation value in MeV.

We could also obtain the maximum energy deposit of stopping protons in the other layers. Figure 4.7 (a) shows an obtained normalized ADC spectrum of the second layer of RCA for the proton events stopping at the fourth layer. The maximum value for

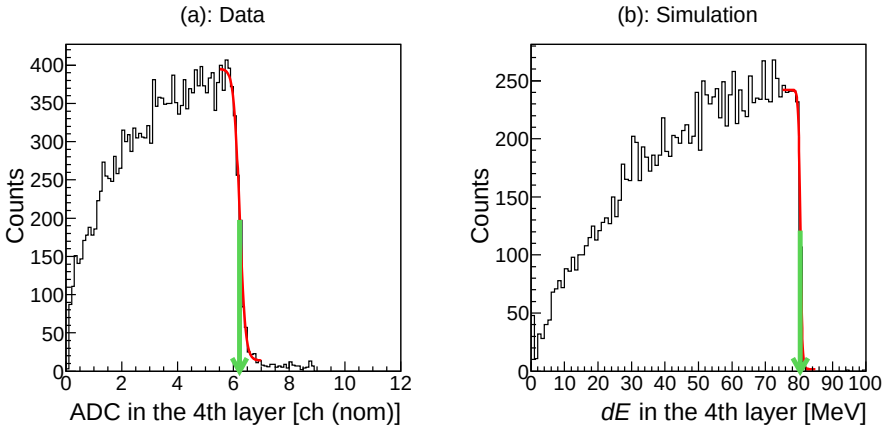

Figure 4.6: The obtained normalized ADC (a) and simulated energy deposit (b) spectra of the fourth layer of RCA for the stopping proton at this layer. The maximum energy deposit of this proton was found by fitting with the function of $\frac{a}{1+d}\{d+\tanh(b(-x+c))\}$ as shown in red lines.

these events was also obtained by fitting with the same function in Figure 4.6. The same fitting procedure was also tested for the simulated one as shown in Figure 4.7 (b). However, the maximum energy deposit of stopping proton was sometimes not clear. For instance, the maximum energy deposit in the second layer, where proton stopped in the third layer, was not clear. Thus, we did not take into account these unclear conditions for the energy correction.

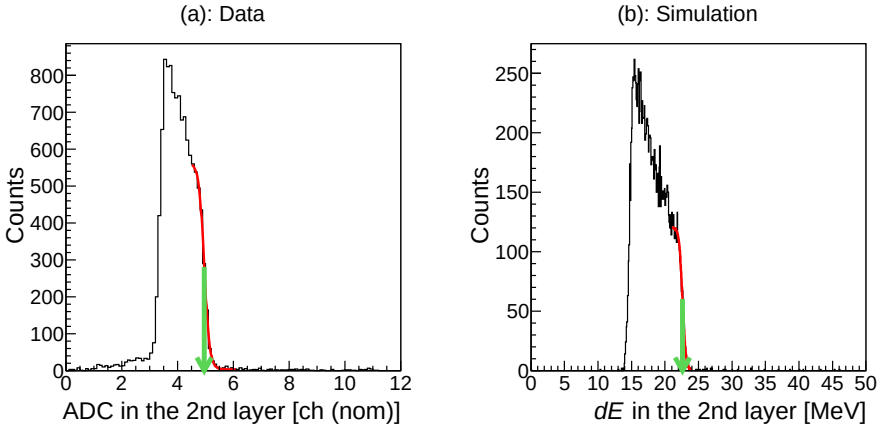

Figure 4.7: The obtained normalized ADC (a) and simulated energy deposit (b) spectra of the second layer of RCA for the stopping proton at the fourth layer. The maximum energy deposit of this proton was found by fitting with the same function of Figure 4.7 as shown in red lines.

Finally, the normalized ADC value of each layer was converted to the energy deposit by fitting with a second order polynomial. We show a case for the second and fourth layer in Figure 4.8. Here, we used the information of the penetrate events for this correction for small energy deposit region such as MIP. Therefore, we could not correct the ADC values validly for the particles stopping in this layer for the small energy loss events, although we corrected the ADC values validly for the penetrate particles.

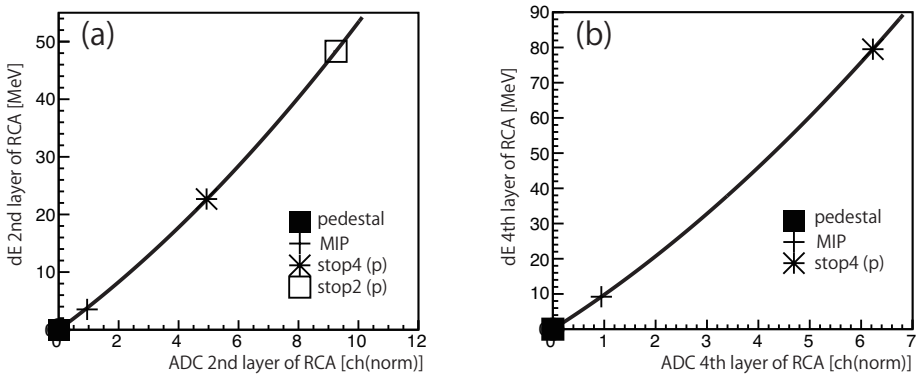

Figure 4.8: A typical correlation between the normalized ADC values and the energy deposits fitted with a second order polynomial indicated with the black lines for the second and fourth layer of RCA shown in (a) and (b), respectively.

4.3.1 PID parameter

In order to carry out the particle identification, we set up the particle identification parameter, PID, as

$$PID = \left((\widetilde{dE}_{i_{stop}} + \widetilde{dE}_{(i_{stop}-1)})^{\alpha} - (\widetilde{dE}_{i_{stop}})^{\alpha}\right) \cdot \cos\theta, \tag{4.2}$$

where $\widetilde{dE}_{i_{stop}}$ and $\widetilde{dE}_{i_{stop}-1}$ shows the energy deposit in the stopping layer, i_{stop}, and previous layer of the stopping one, respectively. The θ is the incident angle for RCA. The α is a constant parameter, whose typical value was 1.75. The PID corresponds to the thickness of the previous layer of the stopping one and it should depend on not momentum but charge number and mass of the particle[1].

Figure 4.9 shows a typical scatter plot between the energy deposit of the second layer and PID, where the α was set at 1.58 (a) and 1.73 (b), for the $i_{stop} = 2$ events. The parameter α was adjusted for each counter by fitting the PID for protons so as to have the minimum width (χ^2). Figure 4.9 with a constant value in order to reduce the correlation between the energy loss and the PID. The obtained χ^2 distribution as

[1]The range R can be described as $R \propto T^{\alpha}/(mZ^2)$, where T, m and Z are the kinetic energy, mass and charge number of the incident particle, respectively. Now, we defined the path length as b in the previous layer of the stopping one and x in the stopping layer. In this definition, the path length $b+x$ and x can be described as $b+x \propto (dE_{i_{stop}} + dE_{i_{stop}-1})^{\alpha}/(mZ^2)$ and $x \propto dE^{\alpha}_{i_{stop}}/(mZ^2)$. Thus, the PID parameter should depend on the thickness of the previous layer of the stopping one and the mass and charge of the incident particle as $PID = ((\widetilde{dE}_{i_{stop}} + \widetilde{dE}_{(i_{stop}-1)})^{\alpha} - (\widetilde{dE}_{i_{stop}})^{\alpha}) \cdot \cos\theta \propto mZ^2(b\cos\theta)$.

a function of α is shown in Figure 4.10. The optimum α parameter was determined by fitting it with a second order polynomial function.

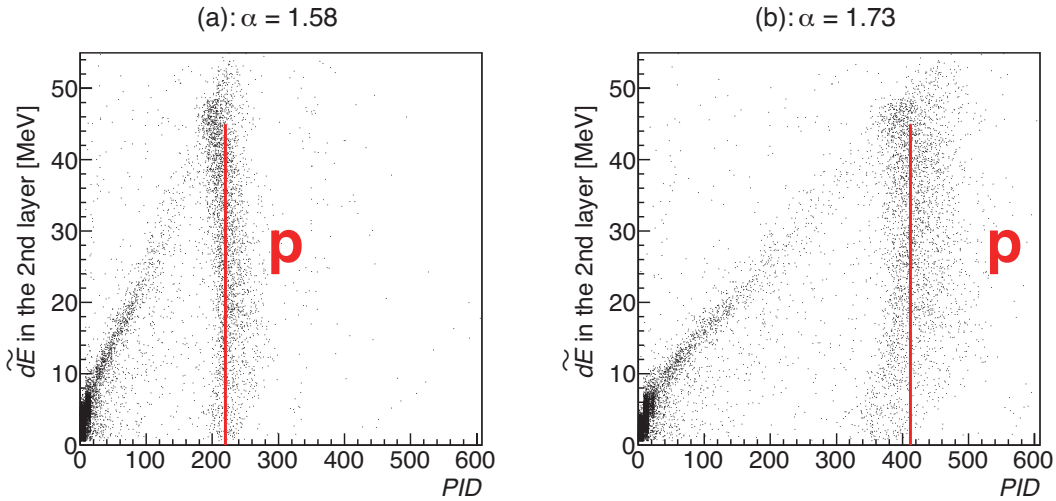

Figure 4.9: A typical scatter plot between the energy deposit of the second layer and PID for the $i_{stop} = 2$ event. In this figure, the parameter α was set at 1.58 and 1.73 in (a) and (b), respectively. The stopping proton cluster were fitted with the constant value shown as red lines.

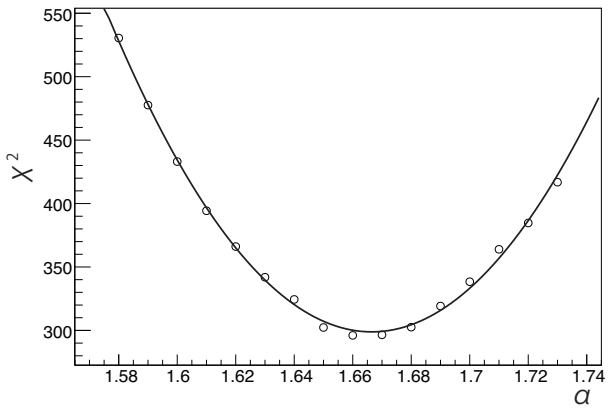

Figure 4.10: A typical χ^2 distribution as a function of α when we fit the scatter plot between the energy loss at stopping layer and PID with constant value as Figure 4.9. The optimum α parameter was determined by fitting with the second order polynomial function shown as a black line.

4.4 Particle identification in RCA

Proton was selected by combining the information of the stopping layer (i_{stop}), velocity and the PID parameter. In this section, we describe the proton selection scheme for each stopping layer. The scheme to evaluate the $\pi^{\pm}$ contamination yield for each stopping layer is also described in this section. In the proton-selection region, there are also some contamination from $\pi^{\pm}$ because the charged pions are influenced not only from electromagnetic processes but also strong interaction processes such as π^{-} nuclear absorption.

4.4.1 Analysis for stopping layer $i_{stop} = 2 \sim 4$

In the cases of the stopping layers from $i_{stop} = 2$ to $i_{stop} = 4$, proton events were selected with the information of $1/\beta$ and PID. Figure 4.11 shows scatter plots between $1/\beta$ and PID for each i_{stop} case. In these figures, we can see three clusters. A cluster in $1/\beta \sim 1$ was corresponding to leakage particles at the side edge of RCA and the others were originated from the charged pions and protons stopping at each layer. In this analysis, proton was selected as the gate of $\pm\, 3\sigma$ in PID and $\pm\, 2\sigma$ in $1/\beta$ shown in the red boxes. These σ's were obtained by fitting the proton distributions with Gaussian functions in the (π^{+}, π^{+}) and (π^{+}, p) reaction events obtained with the TOF-RCA trigger.

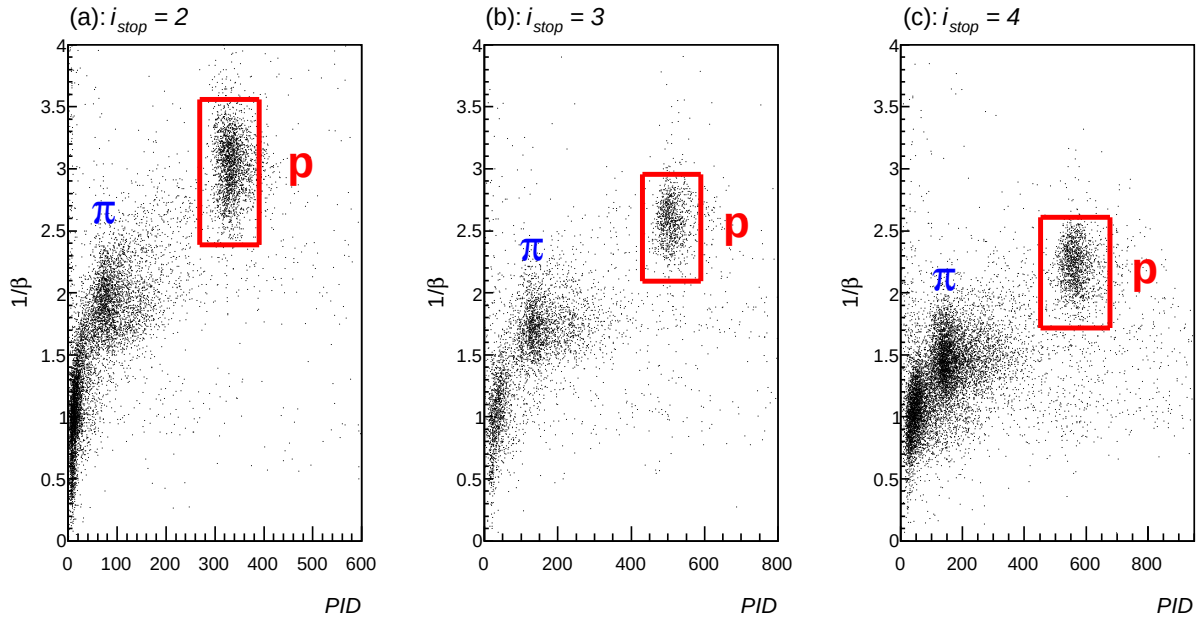

Figure 4.11: A typical scatter plots between the $1/\beta$ and PID for the i_{stop} = 2, 3 and 4 events shown in (a), (b) and (c), respectively. The proton selection gates are shown with the red boxes.

Figure 4.12 shows the PID spectra for each stopping layer; the black and gray histograms corresponding to the spectra with and without proton selection in $1/\beta$, respectively. The proton-selection region ($\pm$ 3σ) is also shown with red lines. The contamination yield of the $\pi^{\pm}$ in the proton selection region was investigated with the events in the $\pi^{\pm}$ contamination gates shown with black lines. The $\pi^{\pm}$ contamination gates were set from both higher and lower side region to keep the same gate width with the proton selection gate.

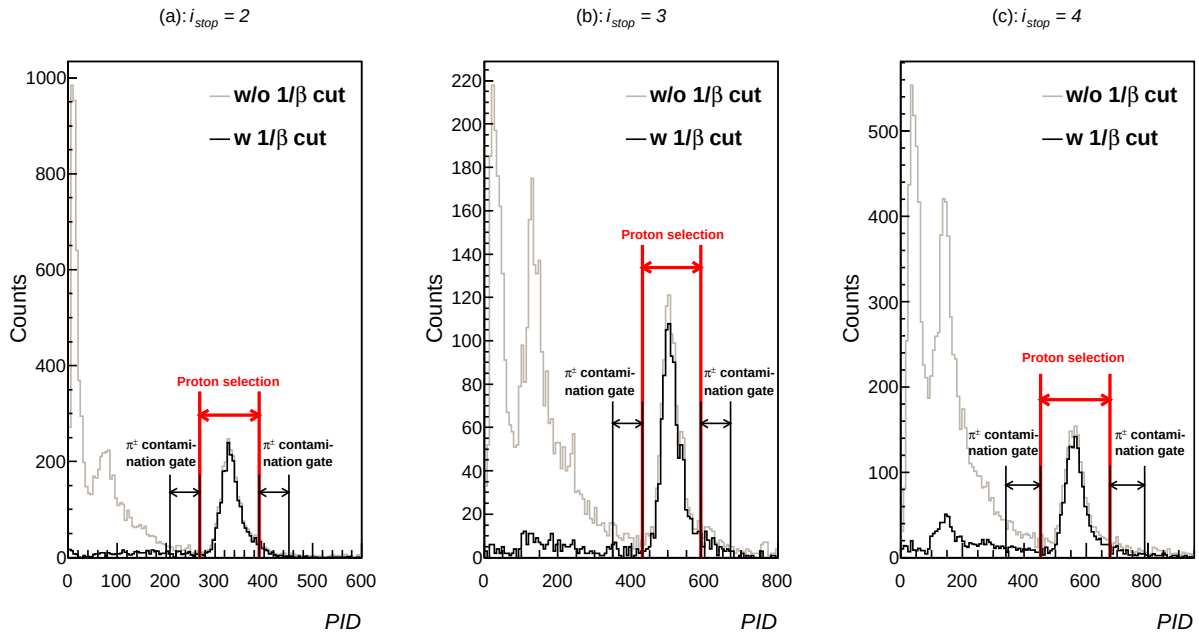

Figure 4.12: A typical PID spectra for the i_{stop} = 2, 3 and 4 events shown in (a), (b) and (c), respectively. The black and gray spectra are indicated with and without proton selection of the $1/\beta$, respectively. The proton selection gates and $\pi^{\pm}$ contamination gates are also shown in these figures.

4.4.2 Analysis for stopping layer $i_{stop} = 1$

In the case of stopping layer $i_{stop} = 1$, we can not define the PID because of a lack of energy deposit information in the second layer. Therefore, we selected proton by using the energy deposit in the first layer, which was same as the total energy, and the velocity $(1/\beta)$ only.

Figure 4.13 (a) shows a typical scatter plot between the $1/\beta$ and energy deposit in the first layer of RCA. In the figure, we can see a clear locus of a proton cluster stopping in the first layer. The correlation ($\widetilde{dE}$–$1/\beta$) was fitted with a second order polynomial in $1/\beta$ ($f(1/\beta)$) shown as a red line. We selected the proton stopping at the 1st layer in the gate of $\widetilde{dE}$ - $f(1/\beta)$ as shown in Figure 4.13 (b). Here, the small energy-loss events ($\widetilde{dE} < 2$ MeV) was rejected in order to reduce background.

In Figure 4.13, we can see another proton cluster which did not stop inside the RCA and leaked at the side edges of scintillator indicated with a green arrow. Therefore, we set the $\pi^{\pm}$ contamination gate only for higher $1/\beta$ side region for the stopping layer $i_{stop} = 1$ assuming the flat distribution shown as Figure 4.13 (b) in order to avoid these leakage protons.

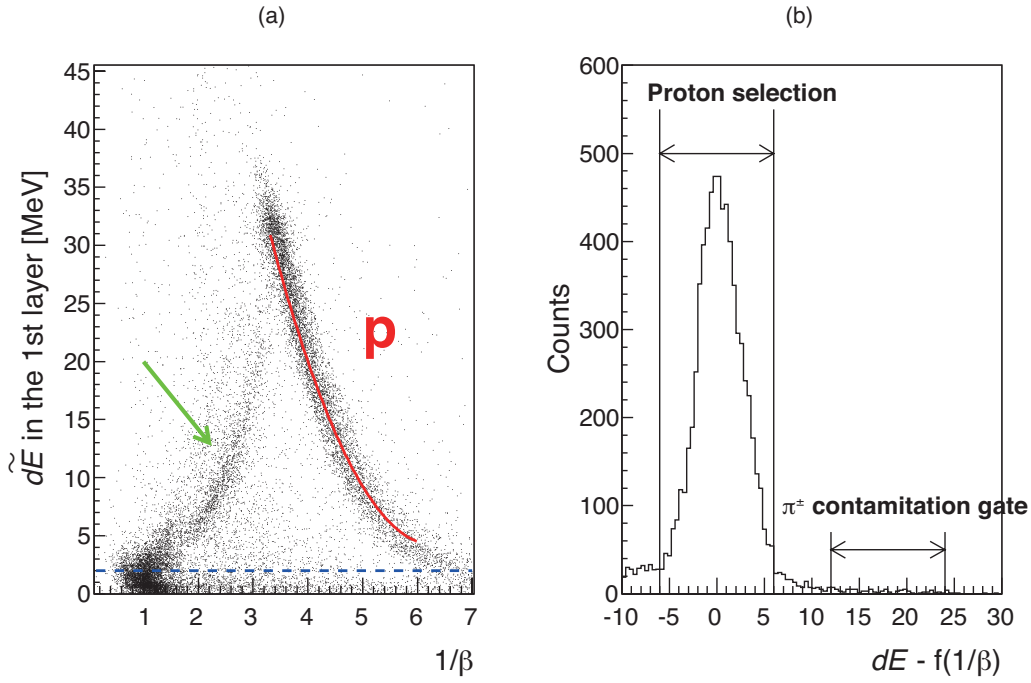

Figure 4.13: (a) A typical scatter plot between the $1/\beta$ and energy deposit of the first layer of RCA. (b) The proton selection gate and the side band region as the function of $\widetilde{dE}$ - $f(1/\beta)$. See the text for the detail.

4.4.3 Analysis for stopping layer $i_{stop} = 5$

In the analysis of $i_{stop} = 5$, we can not obtain the range information from the hit pattern in RCA because these events had the hits for all the layers of RCA. Thus, we identified the proton by using the information of β, PID and energy deposit of the fifth layer of RCA. As shown in Figure 2.20 (b), the expected maximum proton momentum from the K^-pp signal is almost 800 MeV/c, whose velocity is $\beta_p^{max} = 0.65$. We show the effective range, which is considered maximum incident angle to RCA, as a function of β for the pion and proton in Figure 4.14. In order to reach the fifth layer, the pion's velocity should be more than $\beta_\pi > 0.7$. Therefore, we could select the proton less than 800 MeV/c by choosing the event of $\beta < 0.65 = \beta_p^{max}$ for $i_{stop} = 5$ in principle.

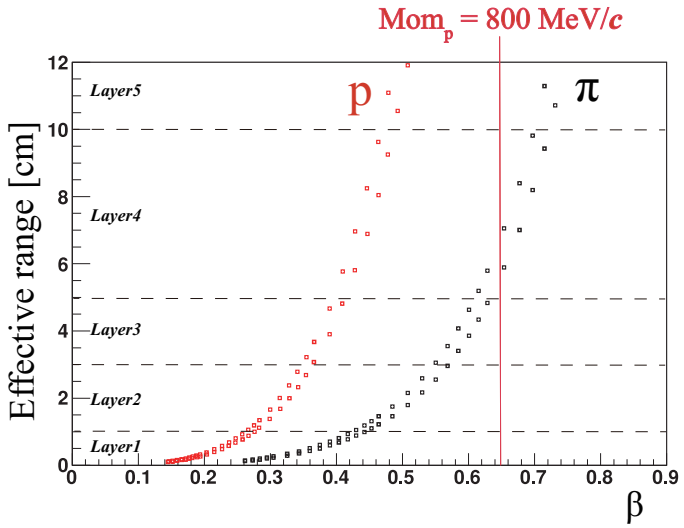

Figure 4.14: The effective range for the pion (black points) and proton (red points) as a function of β. In this figure, the depth for perpendicularly and maximum incident angle case are shown. The thickness of each layer of RCA is also indicated in the figure.

Figures 4.15 (a) and (b) show typical scatter plots between PID and energy deposit in the fifth layer of RCA without and with the $\beta < 0.65$ cut, respectively. In this figure, we can see three clusters. One is a cluster of pions, which penetrate all the layers, indicated by a blue arrow in Figure 4.15 (a). Next, we can see a cluster of protons, which penetrate all the layers, indicated by a red arrow in Figure 4.15 (b). The last cluster is corresponding to the proton stopping in the fifth layer indicated by a magenta arrow in Figure 4.15 (b).

Most of the pions could be suppressed by applying the $\beta < 0.65$ cut as shown in Figure 4.15 (a) and (b). However, some pions still remained as observed in Figure 4.15 (b) (blue ellipse region). These pions might be understood caused not only from the electromagnetic processes but also from strong interaction processes. Moreover, the muon from the $\pi^\pm$ decay in flight can also remain in the $\beta < 0.65$ cut. We chose the proton selected as the red points shown in Figure 4.15 (c) to avoid the penetrate pions. The $\pi^\pm$ contamination was estimated from the events in the side region of this selected region in the scatter plot.

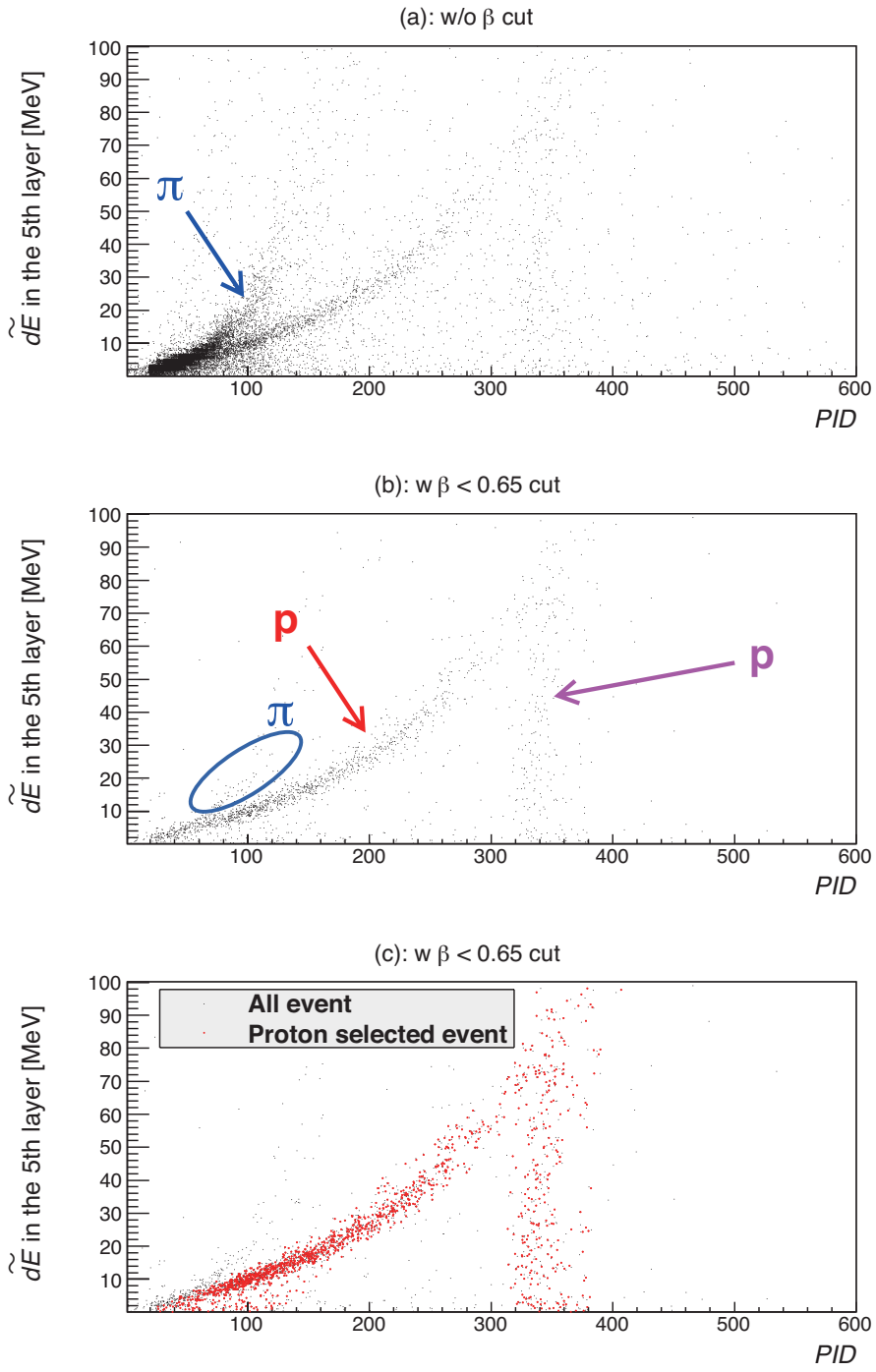

Figure 4.15: A typical scatter plot between PID and energy deposit of the fifth layer of RCA for the $i_{stop} = 5$ event. The scatter plot without and with $\beta < 0.65$ cut are shown in (a) and (b), respectively. The events selected as the proton is shown with the red points in (c).

4.5 Detection efficiency of RCA

The overall efficiency of the RCA for protons and pions was evaluated by using the $p(\pi^+, K^+)\Sigma^+$ reaction at $p_{\pi^+} = 1.69$ GeV/c. In this reaction, at first we can identify the Σ^+ production in the (π^+, K^+) missing-mass. Further, we can measure the proton and π^+ from the Σ^+ decay ($\Sigma^+ \to p\pi^0$ or $\Sigma^+ \to n\pi^+$) with RCA in coincidence. Since the velocities of the proton and π^+ from the Σ^+ decay are different, we can distinguish between proton and π^+ by using only the information of $1/\beta$ in this reaction.

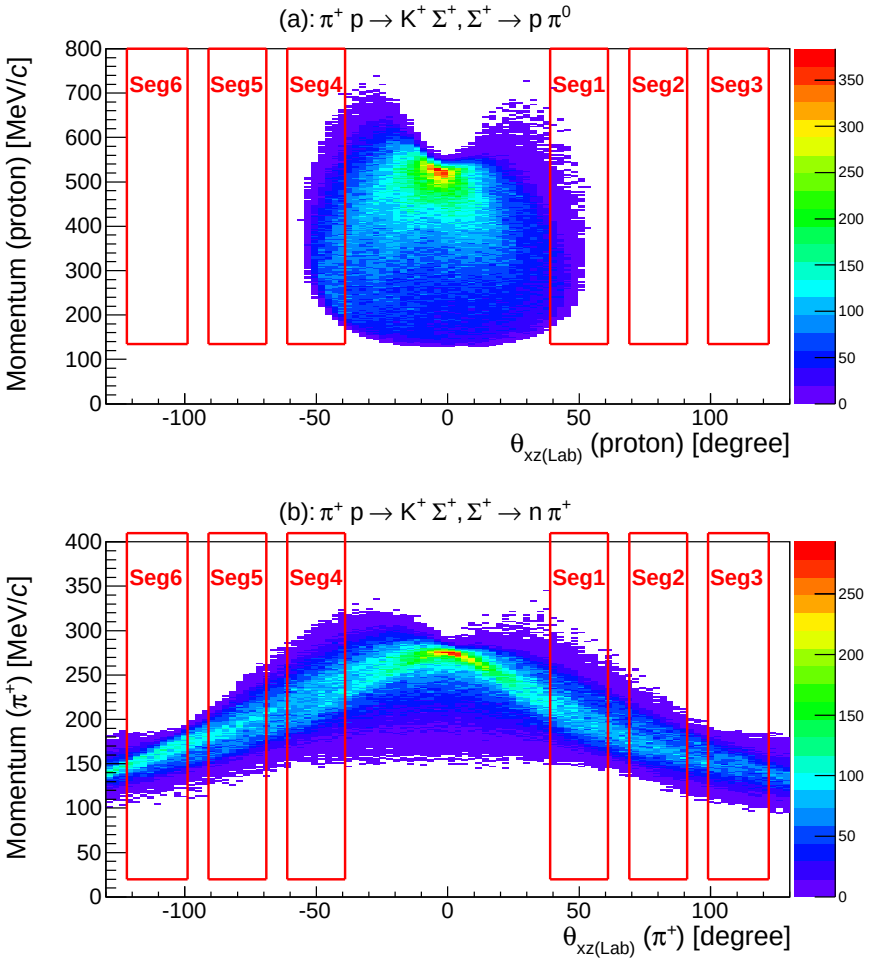

Figure 4.16: The simulated correlation plot between produced angle of the xz plane (θ_{xz}) and the momentum of proton and π^+ from the Σ^+ decay are shown in (a) and (b), respectively. The acceptance of each segment of RCA is also indicated as the red box.

Figure 4.16 shows the correlation between produced angle in the xz plane (θ_{xz}) and momentum of proton (a) and π^+ (b) estimated from a simulation taking account of elementary differential cross section. The acceptance of each segment is also indicated as a red box. In this plot, the emitted K^+ was required to be detected with the SKS and the asymmetry of the left and right originated from the asymmetry of the acceptance of the SKS for the K^+.

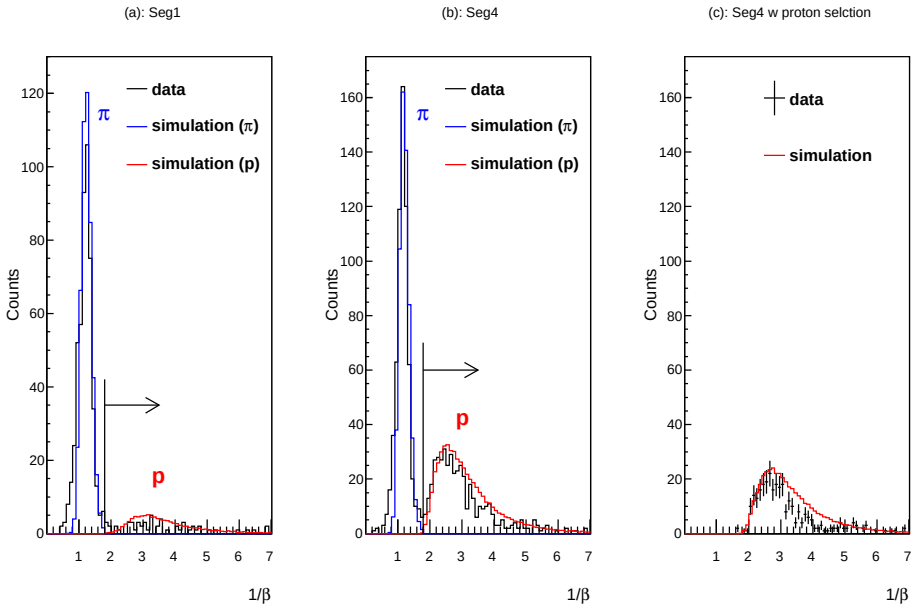

Figure 4.17: (a, b) The obtained $1/\beta$ spectrum for the Seg1 and 4 of RCA in coincidence with Σ^+ production shown. The simulated $1/\beta$ distributions of the proton and the other particles (dominant component was π^+) from the Σ^+ decay are also shown in red and blue lines, respectively. (c) The proton selection events in the scheme described in Sec. 4.4 for data and simulation shown in black points with error bar and red line, respectively.

As shown in Figure 4.16 (a), the proton from the Σ^+ decay can reach the Seg1 and 4, which are the most forward segments of RCA, while π^+ can reach all the segments.

Figures 4.17 (a) and (b) show the obtained $1/\beta$ spectra of the Seg1 and 4, respectively, in black lines. In this spectrum, the Σ^+ produced events were selected by checking the missing mass of $p(\pi^+, K^+)$ reaction. The simulated $1/\beta$ distributions of the proton and other particles, from the Σ^+ decay are also shown in red and blue lines, respectively. Since the dominant component of other particles was π^+, we describe such a component as the π^+ simply although gamma and electron were also contaminated with small fractions. In order to compare the data with simulation, we applied a cut for the energy loss in the first layer of RCA, $\widetilde{dE} > 1.3$ MeV, both in the simulation and data analysis. The π^+ and proton are separated in the $1/\beta$ shown as the arrow in these figures.

The yield of the simulation was normalized by adjusting the detected K^+ yield as same as the observed one. We found that the yield of π^+ and proton were almost consistent between data and simulation as shown in Figure 4.17 (a) and (b). A coincidence probability of π^+ (η_π) defined as,

$$\eta_\pi = \frac{N(\pi\ in\ RCA)}{N(\Sigma^+\ detected)} = \frac{1}{4\pi}\int_{\Omega_{RCA}} \epsilon_\pi \frac{d\sigma_\pi}{d\Omega} d\Omega, \tag{4.3}$$

where Ω_{RCA} is geometrical acceptance of RCA, $\frac{d\sigma_\pi}{d\Omega}$ is differential cross section of π^+ of the $\Sigma^+ \to n\pi^+$ decay including the branching ratio (48.3%). ϵ_π is efficiency to identify the π (assuming $\sim$100 % because we only use the information of the first layer), of each

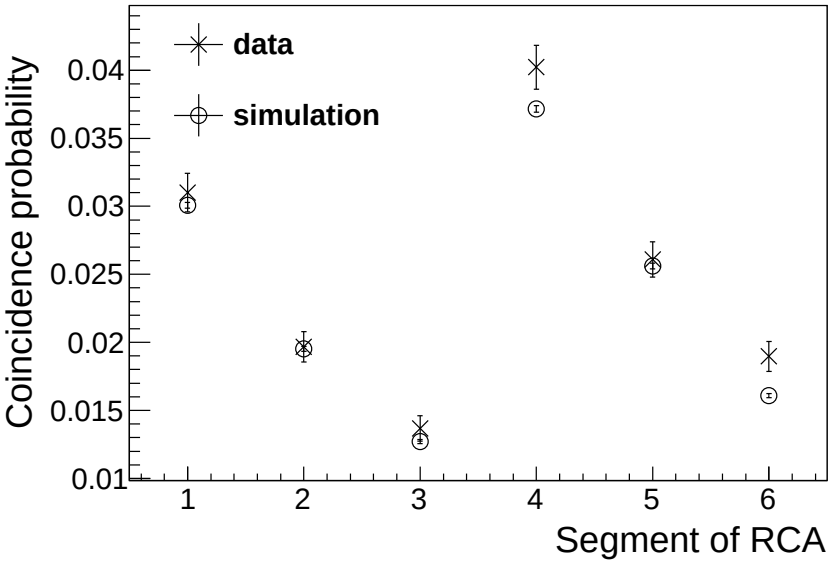

Figure 4.18: The π^+ coincidence probability, which is defined as Eq. 4.3, of each segment of RCA. The present data and simulated one are shown by crosses and open circles, respectively.

segment of RCA for data and simulation is summarized in Figure 4.18. These values for data and simulation are almost consistent with each other. Thus, we understand the geometical acceptance of RCA reasonably well.

Next, we discuss the proton coincidence probability by using the Seg4 because the yield of proton in Seg1 is limited. In the $p(\pi^+, K^+)$ reaction, we can separate π^+ and proton by using only the $1/\beta$ information shown as the arrow in Figure 4.17 (b). Thus, we defined the coincidence probability of proton for the first layer ($\eta_{p(1st)}$) as,

$$\eta_{p(1st)} = \frac{N(p\ in\ RCA)}{N(\Sigma^+\ detected)} = \frac{1}{4\pi}\int_{\Omega_{RCA}} \epsilon_{p(1st)} \frac{d\sigma_p}{d\Omega} d\Omega, \tag{4.4}$$

where $N(p\ in\ RCA)$ is the number of proton events to be detected in the first layer of RCA shown in Figure 4.17 (b) and $\epsilon_{p(1st)}$ is the efficiency to identify the proton in the first layer assumed to be $\sim$100 % in this analysis. $\frac{d\sigma_p}{d\Omega}$ is differential cross section of proton from the $\Sigma^+ \to p\pi^0$ decay including the branching ratio (51.6%). The coincidence probabilities for the first layer obtained from the data and simulation are 2.8 $\pm$ 0.1% and 3.4%, respectively.

Fig. 4.17 (c) shows the proton events in the scheme as described in Sec. 4.4 for the data and simulation in black points with error bars and a red line, respectively. The overall proton coincidence probability (η_p) is defined as,

$$\eta_p = \frac{N(p\ selected\ in\ RCA)}{N(\Sigma^+\ detected)} = \frac{1}{4\pi}\int_{\Omega_{RCA}} \epsilon_p \frac{d\sigma_p}{d\Omega} d\Omega, \tag{4.5}$$

where $N(p\ selected\ in\ RCA)$ is the number of proton events selected with the scheme described in Sec. 4.4 shown in Figure 4.17 (c) and ϵ_p is the detection efficiency for the proton in RCA. In this Σ^+ analysis, we could estimate the proton detection efficiency ϵ_p as,

$$\epsilon_p = \frac{N(p\ selected\ in\ RCA)}{N(p\ in\ RCA)}, \tag{4.6}$$

where $N(p\ in\ RCA)$ is the number of proton events identified with only the first layer of RCA same as Eq. 4.4. The overall proton coincidence probabilities (η_p) of Seg4 for the data and simulation are $1.8 \pm 0.1\%$ and 2.7%, respectively. The detection efficiency (ϵ_p) for the data and simulation are 65% and 78%, respectively. The main component of an inefficiency of ϵ_p originates from the leakage of proton at the side edge of RCA and it strongly depends on the incident angle to the RCA. As shown in Figure 4.16 (a), the protons produced from the Σ^+ decay concentrate in the forward angle and we can detect only a tail part of this Σ^+ decay. Thus, the discrepancy of the proton detection efficiency between the data and simulation by 20% may originate from not an ambiguity of the proton detection efficiency itself but the reproducibility of the proton incident angle distribution. From this study, we found that the absolute detection efficiency might be overestimated by 20%. We discuss the uncertainty of the cross section caused from this ambiguity in Sec. 5.2.6.

Chapter 5

Experimental results and discussion

The experimental results are separated into two parts; namely the inclusive analysis results and the coincidence analysis results. At first, we discuss the inclusive spectra of the $d(\pi^+, K^+)X$ reaction by comparing the Monte Carlo simulations based on a simple quasi-free picture. In the next section, the coincidence analysis results with RCA are discussed.

5.1 Inclusive analysis: results and discussion

5.1.1 Inclusive missing-mass spectra of the $d(\pi^+, K^+)$ reaction

As mentioned in Sec. 3.1, we can define MM_d and MM_p as follows

$$MM_{d(p)} = \sqrt{(E_\pi + M_{d(p)} - E_K)^2 - (p_\pi^2 + p_K^2 - 2p_\pi p_K \cos\theta_{\pi K})}, \tag{5.1}$$

where MM_d and MM_p are the missing mass calculated assuming the deuteron and proton at rest as a target, respectively. Here, M_d and M_p are the rest mass of deuteron and proton, respectively.

Figures 5.1 (a) and 5.2 (a) show missing-mass spectra in the scattering angle of 2° to 16° in the laboratory system, before corrections with experimental efficiency and the acceptance of the SKS, in the $d(\pi^+, K^+)$ reaction expressed as the MM_d and MM_p, respectively. Figures 5.1 (b) and 5.2 (b) show the double differential cross sections after the corrections with experimental efficiency and acceptance of the SKS as described in Eq. 3.30. The spectra are shown with a bin width of 2 MeV/c^2 per bin.

In these spectra, we can find three major peak structures around 2.08 (1.12) MeV/c^2, 2.17 (1.19) MeV/c^2 and 2.40 (1.37) MeV/c^2 in the MM_d (MM_p) spectrum. These regions are shown as I, II and III in Figures 5.1 and 5.2. These peaks can be considered as originating from the Λ, Σ and hyperon resonance (Y^*) productions in the quasi-free processes.

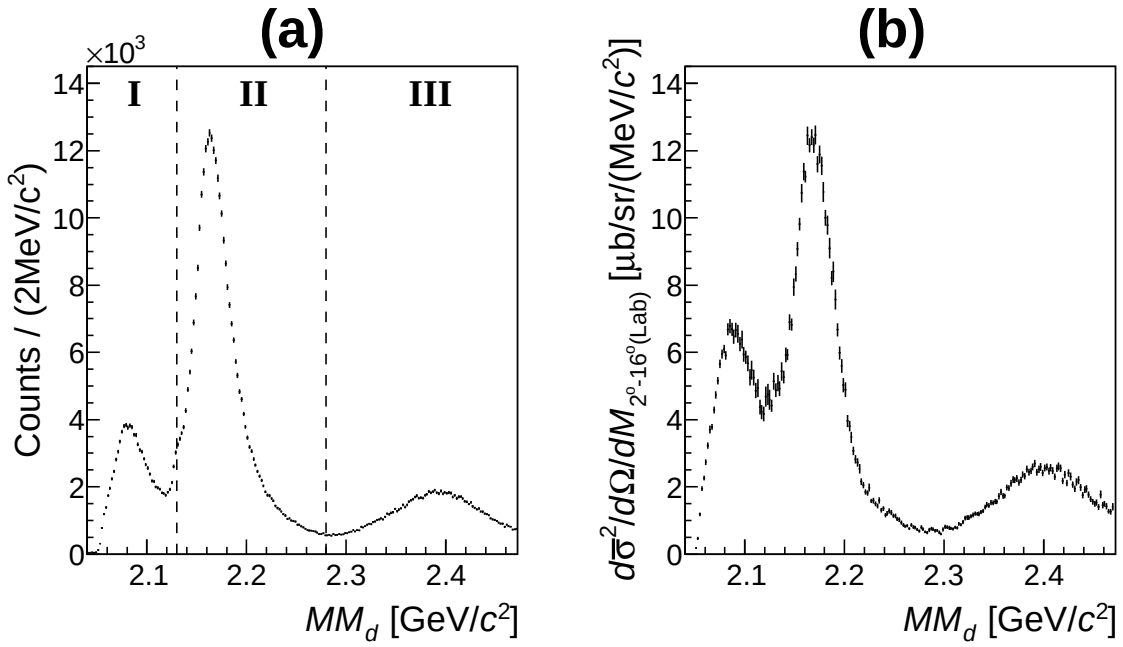

Figure 5.1: The obtained inclusive missing-mass spectra of the $d(\pi^+, K^+)$ reaction at 1.69 GeV/c as a function of missing mass MM_d. The spectra of raw missing-mass and double differential cross section are shown in (a) and (b), respectively.

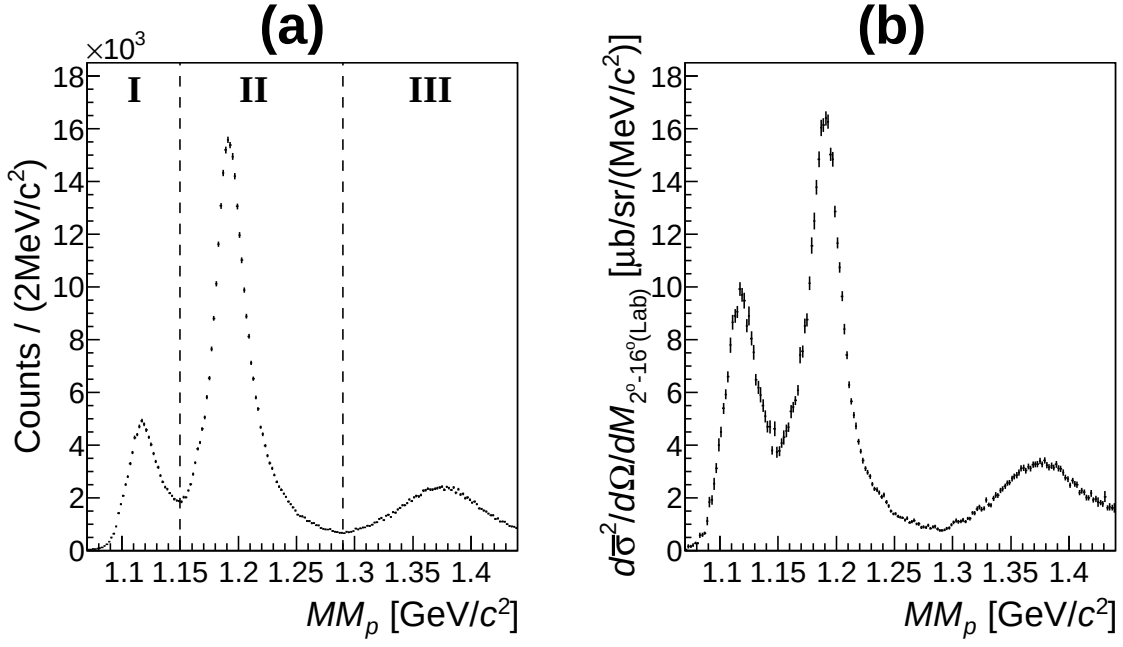

Figure 5.2: The obtained inclusive missing-mass spectra of the $d(\pi^+, K^+)$ reaction at 1.69 GeV/c as a function of missing mass MM_p. The spectra of raw missing-mass and double differential cross section are shown in (a) and (b), respectively.

5.1.2 Quasi-free processes in the $d(\pi^+, K^+)$ reactions

In the $d(\pi^+, K^+)$ reaction at $p_\pi = 1.69$ GeV/c, there are several quasi-free processes known from old elementary process data. Here, we considered the quasi-free hyperon productions of Λ (Region I) and $\Sigma^{+/0}$ (Region II),

$$\pi^+ \text{“}n\text{”} \to K^+\Lambda, \tag{5.2}$$

$$\pi^+ \text{“}p\text{”} \to K^+\Sigma^+; \quad \pi^+ \text{“}n\text{”} \to K^+\Sigma^0, \tag{5.3}$$

hyperon resonance (Y^*) productions of $\Lambda(1405)$ and $\Sigma(1385)^{+/0}$ (Region III),

$$\pi^+ \text{“}n\text{”} \to K^+\Lambda(1405), \tag{5.4}$$

$$\pi^+ \text{“}p\text{”} \to K^+\Sigma(1385)^+; \quad \pi^+ \text{“}n\text{”} \to K^+\Sigma(1385)^0, \tag{5.5}$$

and non-resonant productions of $\Lambda\pi$ and $\Sigma\pi$ (Region III),

$$\pi^+ \text{“}N\text{”} \to K^+\Lambda\pi; \quad \pi^+ \text{“}N\text{”} \to K^+\Sigma\pi. \tag{5.6}$$

The “n” and “p” indicate a neutron and a proton in a deuteron, respectively. The cross sections of elementary processes have already been measured [65, 19] and these total cross sections σ are listed in Table.5.1.

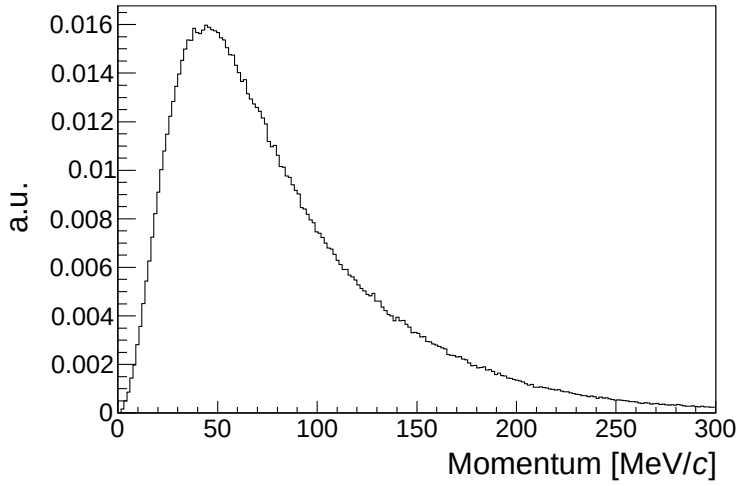

Figure 5.3: The momentum distribution of a nucleon inside of deuteron obtained from the Bonn Potential [97].

We made an attempt to reproduce the double differential cross section $d^2\bar{\sigma}/d\Omega/dM$ with a Monte Carlo simulation by using the differential cross sections $d\sigma/d\Omega$ of each elementary reaction obtained in the past experiments with a smearing by the nucleon Fermi motion in a deuteron. We assumed there are no rescattering of all the final state particles such as K^+ , hyperon, Y^*'s *etc.* Here, we used a deuteron wave-function derived from the Bonn potential [97], of which nucleon momentum distribution (p_F) is shown

in Figure 5.3. In this simulation, the participant nucleon mass, M_p^*, was assumed to be in the off-mass by taking into account the Fermi motion, p_F, as:

$$M_p^{*2} = \left(M_d - \sqrt{M_s^2 + p_F^2} \right)^2 - p_F^2, \tag{5.7}$$

where M_d and M_s are deuteron and spectator on-shell nucleon mass, respectively (spectator model [100]). The emitted K^+ momentum, p_K, was distributed according to the reaction kinematics with the mass of the the participant nucleon M_p^* and its momentum $\vec{p_F}$. Then, the missing mass MM_d was calculated as $MM_d^2 = (E_\pi + M_d - E_K)^2 - |\vec{p_\pi} - \vec{p_K}|^2$.

Table 5.1: Elementary total cross sections of hyperon productions. The cross sections of $\pi^+ p$ reaction at 1.7 GeV/c are listed in the left [65]. The cross sections of $\pi^+ n$ reaction at 1.69 GeV/c, which is assumed the isospin symmetry, are listed in the right [19].

Reaction($\pi^+ p$)	Cross section (μb)	Reaction($\pi^+ n$)	Cross section (μb)
		$\pi^+ n \to K^+ \Lambda$	174 ± 14
$\pi^+ p \to K^+ \Sigma^+$	470 ± 39	$\pi^+ n \to K^+ \Sigma^0$	121 ± 10
		$\pi^+ n \to K^+ \Lambda(1405)$	20.6 ± 1.0
$\pi^+ p \to K^+ \Sigma(1385)^+$	124 ± 20	$\pi^+ n \to K^+ \Sigma(1385)^0$	76.7 ± 10
$\pi^+ p \to K^+ \Lambda \pi$	40.0 ± 28	$\pi^+ n \to K^+ \Lambda \pi$	13.7 ± 1.8
$\pi^+ p \to K^+ \Sigma \pi$	40.0 ± 6.0	$\pi^+ n \to K^+ \Sigma \pi$	19.3 ± 1.0

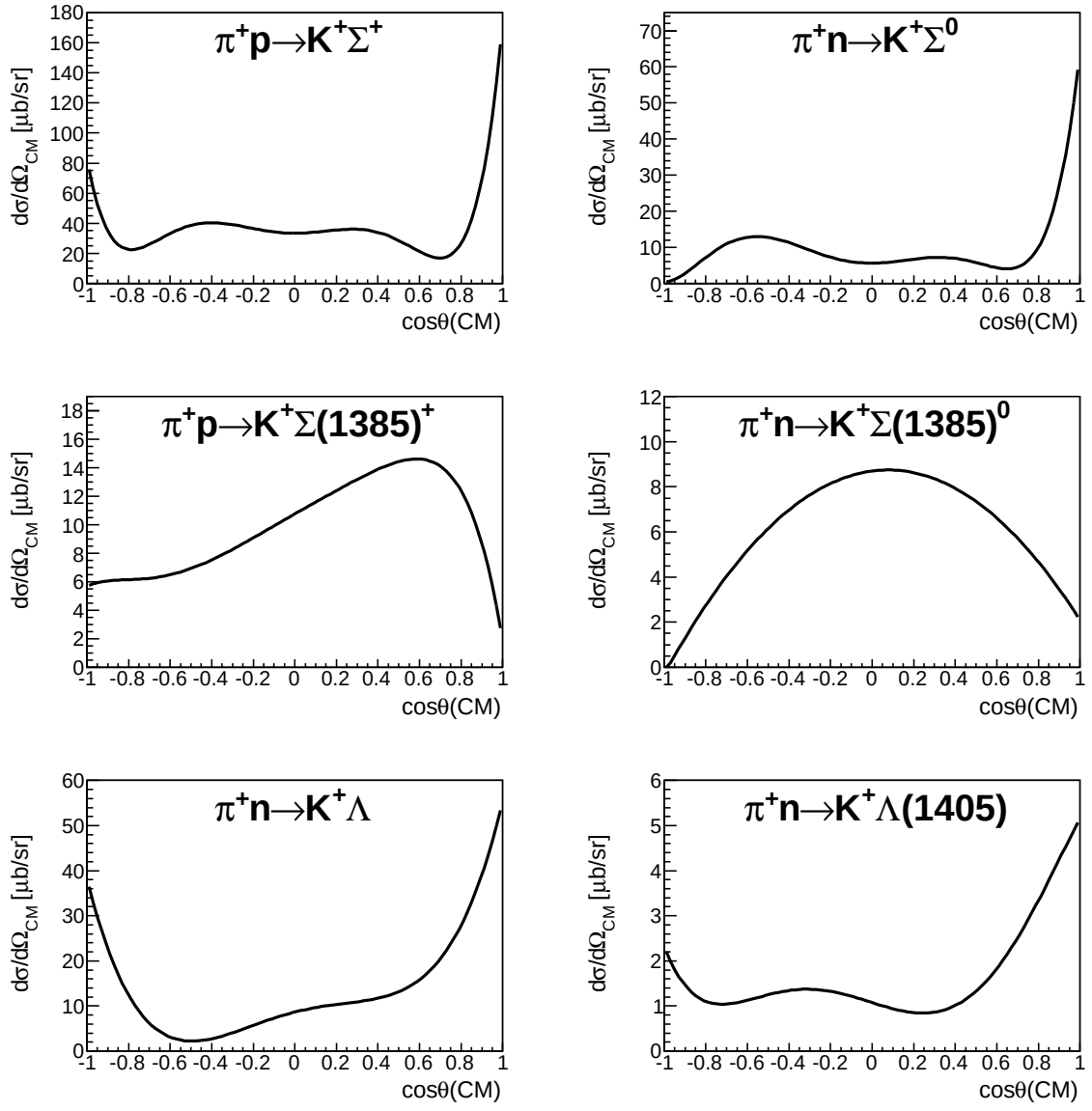

Figure 5.4: Considered elementary differential cross sections of the two-body reactions for the quasi-free processes obtained from the Ref. [65, 19]. These values are plotted in the center of mass system.

For the $\pi^+ +$ "n" reactions, we used the cross sections and angular distributions of $\pi^- + p$ reactions in Ref. [19] assuming isospin symmetry. For the $\pi^+ +$ "p" reactions, we used the values in Ref. [65]. The angular distributions were expressed as Legendre polynomial functions as, $d\sigma/d\Omega = \sum A_n P_n(\cos\theta)$, in the past experiments. Here, in the cases of $\pi^+ p \to K^+\Sigma^+$ and $\pi^+ p \to K^+\Sigma(1385)^+$ reactions, fit results with a Legendre polynomial function were not given in Ref. [65]. Therefore, we estimated these parameters by ourselves by fitting the listed data in Ref. [65]. The fit reproduces the measured differential cross sections of the $p(\pi^+, K^+)$ reaction at 1.69 GeV/c reasonably well.

All considered elementary differential cross sections of the two-body reactions are summarized in Figure 5.4. Three-body reactions such as $\pi^+ n \to K^+\Lambda\pi$ reaction were assumed to be distributed in a three-body phase space. Moreover, the elementary differential cross section for the Σ^0 production processes [19, 98, 99] features rather large errors in the forward scattering angles as shown in Figure 5.5. Therefore, an adjustment of the normalization of the cross section of the quasi-free Σ component was applied within the measurement errors in the present simulation.

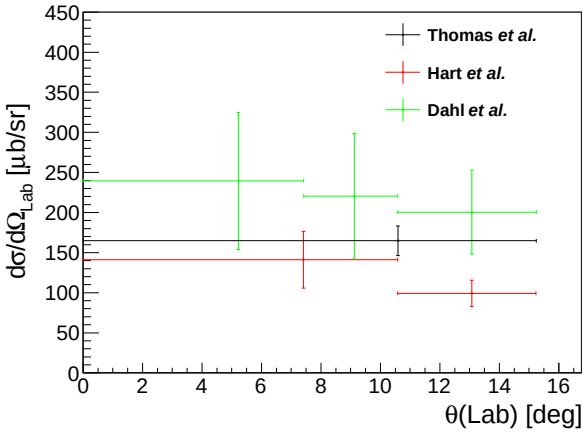

Figure 5.5: The differential cross sections of the Σ^0 production in the $p(\pi^-, K^0)\Sigma^0$ reaction for the forward scattering angle obtained from the Ref. [19, 98, 99].

A simulated spectrum as a sum of each quasi-free process is shown in Figure 5.6. An enlarged spectra in Region III is also shown in Figure 5.7.

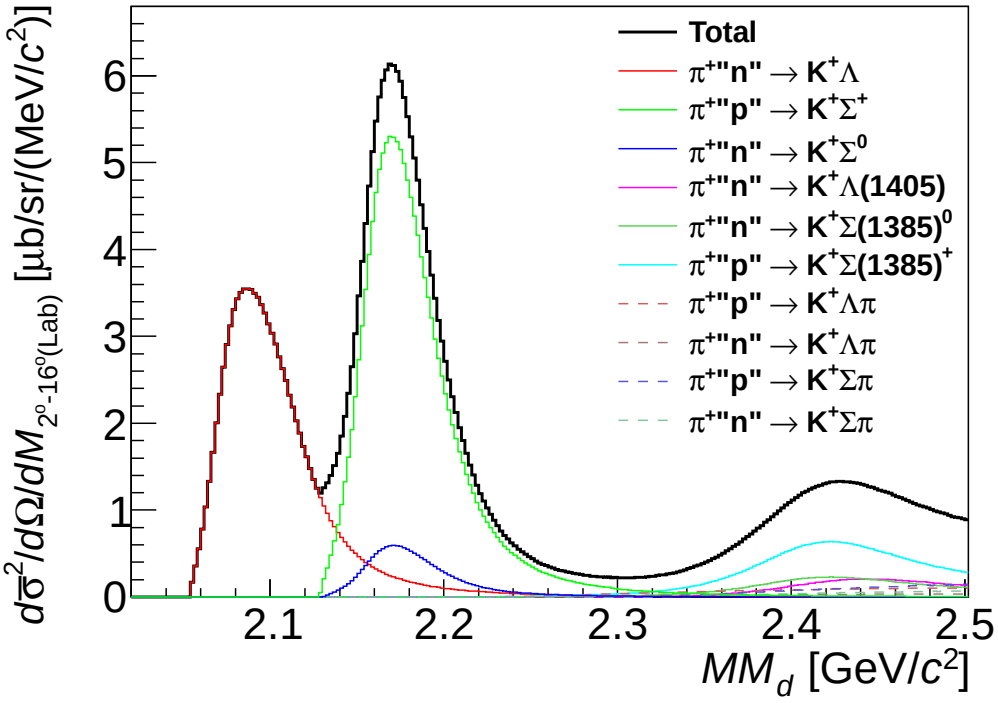

Figure 5.6: A simulated differential cross section of the $d(\pi^+, K^+)$ reaction for the quasi-free processes. Each process is shown in the figure with different colors and line styles.

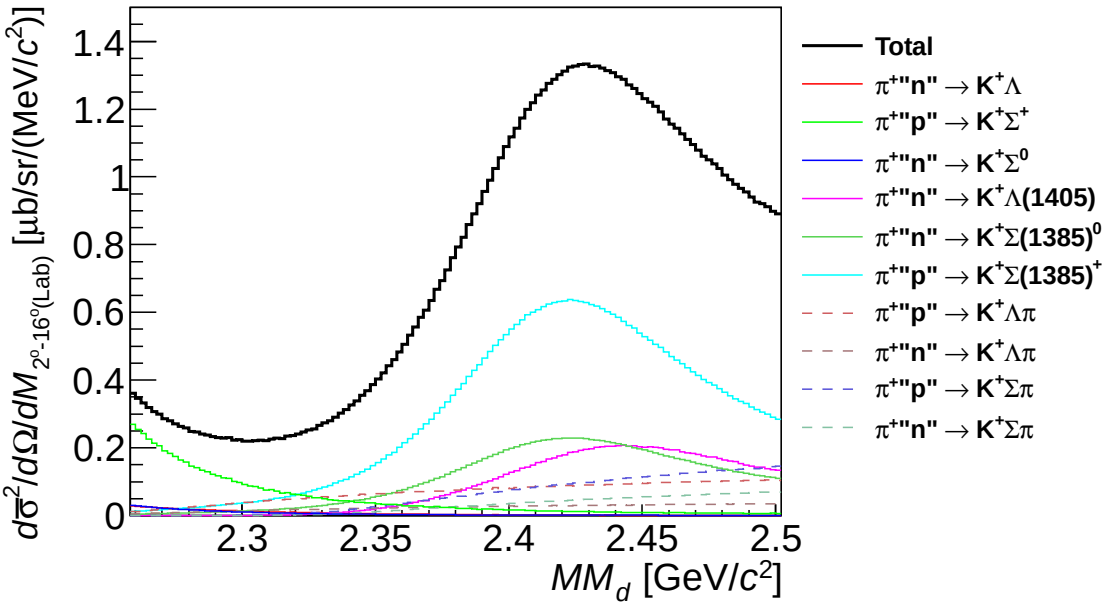

Figure 5.7: An enlarged spectrum of Figure 5.6 in Region Ⅲ.

5.1.3 Discussion on inclusive spectra

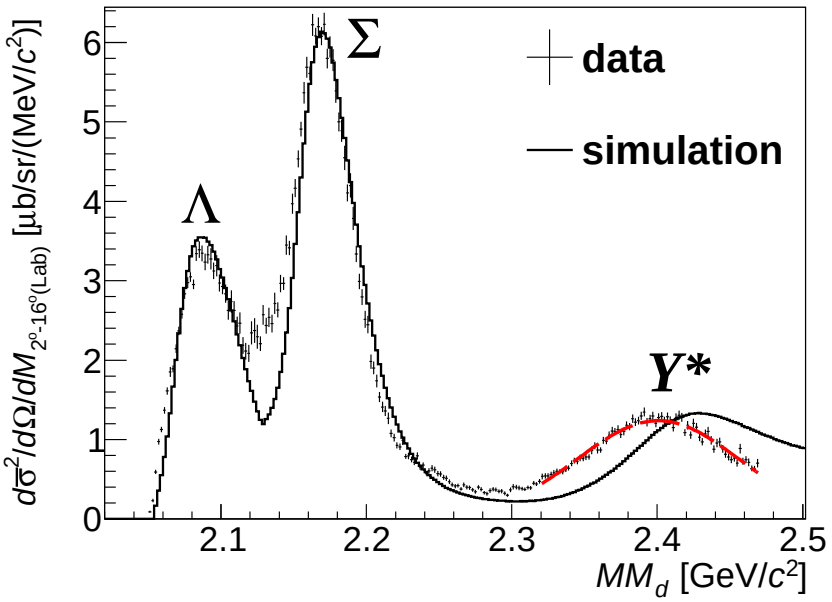

Figure 5.8: The missing-mass spectrum (MM_d) of the $d(\pi^+, K^+)$ reaction for the scattering angle from 2° to 16° in the laboratory system per 2 MeV/c^2. The crosses and solid line show the experimental data and the simulated spectrum, respectively. The result of the Y^* peak fitting is also shown with a dashed red line for the experimental data. Taken from Ref. [93].

Figure 5.8 shows the obtained double differential cross section (crosses) compared with the simulated spectrum (solid line). We find an overall structure of the spectrum is well reproduced expect for two distinct differences. One difference is a cusp structure observed around 2.13 GeV/c^2. The other difference is a "shift" of the broad bump position for the Y^* production in Region Ⅲ.

ΣN cusp

A magnified view of the missing-mass spectrum in Region I is shown in Figure 5.9 (a) for the forward scattering angle from 2° to 8° in the laboratory frame. A peak around ΣN thresholds (2.1289 GeV/c^2 for $\Sigma^+ n$ and 2.1309 GeV/c^2 for $\Sigma^0 p$) is prominent in the figure. When we chose the scattering angle larger than 8°, the cusp is less prominent due to the large quasi-free Λ and Σ backgrounds as shown in Figure 5.9 (b).

Generally, when a new threshold opens, a cusp structure can appear in order to conserve the flux and the associated unitarity of the S-matrix. However, such a cusp structure can not always be observed at the threshold experimentally. On the other hand, similar cusp structure can also be seen when a pole exists near the threshold [101]. In case of the ΣN system, it is theoretically suggested that the pole exists near the ΣN threshold in a second and third quadrant of the complex plane of the ΣN relative momentum using

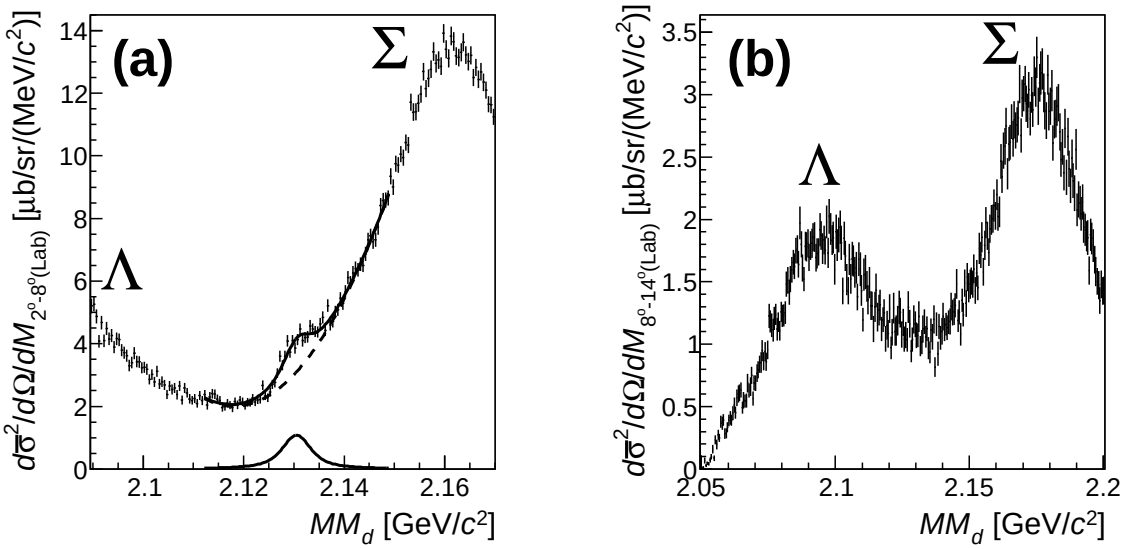

Figure 5.9: (a)The missing-mass spectrum (MM_d) in 2.09 to 2.17 GeV/c^2 region for the forward scattering angle from 2° to 8°(Lab) per 0.5 MeV/c^2, which is shown by crosses. The fitting results are shown by solid and dashed lines ($\chi^2/ndf = 1.11$). Taken from Ref. [93]. See the text for the detail. (b)The missing-mass spectrum (MM_d) in 2.05 to 2.20 GeV/c^2 region for the backward scattering angle from 8° to 14°(Lab) per 0.5 MeV/c^2 shown by crosses. The cusp is less prominent due to the large quasi-free backgrounds when we select the backward scattering angle.

the several YN potential models by Miyagawa and Yamamura [102]. Thus, the structure at the ΣN threshold would not be a simple threshold effect but could originate from a pole near the ΣN threshold. Experimentally, a cusp structure at the ΣN threshold was observed in $K^- d \to \pi^- \Lambda p$ reaction more than 40 years ago [103, 104]. Figure 5.10 shows the obtained Λp invariant-mass spectrum in the $K^- d \to \pi^- \Lambda p$ reaction at rest in Ref. [103]. A clear peak corresponding to the ΣN cusp is seen around 2.13 GeV/c^2. Recently, the ΣN cusp has been intensively investigated in the $pp \to K^+ \Lambda p$ reaction at COSY [105, 106]. These results were listed in Ref. [107].

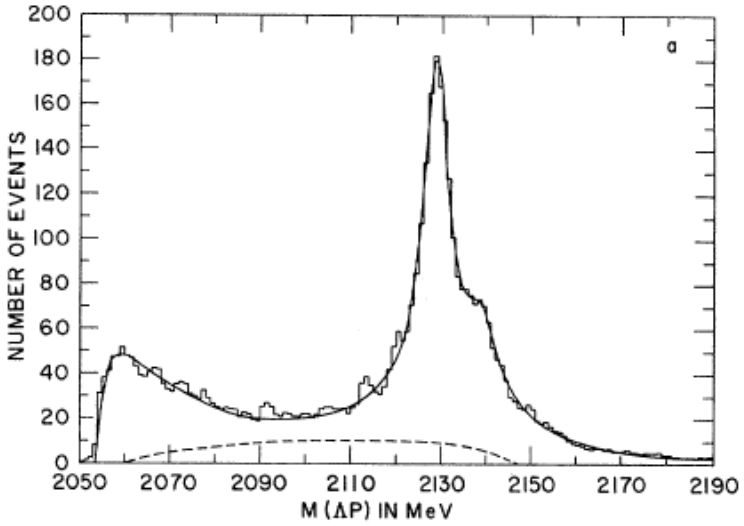

Figure 5.10: The obtained Λp invariant mass spectrum of the old experiment in the $K^- d \to \pi^- \Lambda p$ reaction at rest taken from Ref. [103]. The clear structure corresponding to the ΣN cusp is seen around 2.13 GeV/c^2.

Although this ΣN cusp may not necessarily distribute according to a Lorentzian function, here we fit the cusp structure with this function in order to compare with the previous results summarized in Ref. [107]. Through a fit of the Lorentzian function folded with the resolution of 1.4 MeV/c^2. in σ for the cusp (solid line) and a third-order polynomial function for a continuum background (dashed line), we obtained the peak position at 2130.5 ± 0.4 (stat.) $\pm$ 0.9 (syst.) MeV/c^2, the width of $\Gamma = 5.3\ ^{+1.4}_{-1.2}$ (stat.) $^{+0.6}_{-0.3}$ (syst.) MeV and the differential cross section of $d\bar{\sigma}/d\Omega = 10.7 \pm 1.7$ μb/sr.

The statistical errors were estimated from the χ^2 distribution of the fitting as a function of the peak position and width of the cusp shown in Figure 5.11. In this fit, there were seven parameters, which correspond to the peak position, the width and the normalization factor for the Lorentzian function (ΣN cusp) and four parameters for the third order polynomials (continuum background). Thus, the χ^2 value was calculated by adjusting the parameters except for the peak position and the width to vary for minimizing χ^2 for each combination of the peak position and the width. The systematic errors of these values were estimated in σ taking into account uncertainties in the absolute momentum scale of $\pm$ 1.1 MeV/c fitting ranges, the missing-mass resolution ($\pm$ 0.08 MeV/c^2), the binning of the missing-mass spectrum and background functional shapes by changing

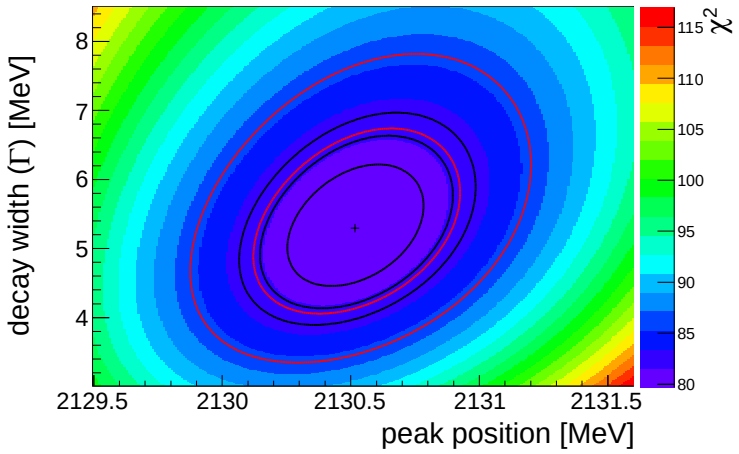

Figure 5.11: The contour plot of the χ^2 of the fitting shown in Figure 5.9 (a) as a function of the peak position and width. The black lines show $\Delta\chi^2 = +1$, $+2$ and $+3$ regions from the minimum χ^2 value shown in a cross. The red lines show the 1σ and 2σ deviations.

the third to fifth order polynomials. The χ^2/ndf of this fitting was 1.11. This result is the first observation of the ΣN cusp structure in the inclusive spectrum of the $d(\pi^+, K^+)$ reaction.

In Ref. [107], the obtained spectrum from these past experiments were fitted with a Lorentzian function after subtracting the continuum background. The obtained peak position and width from this fitting are shown in Figure 5.12 [107]. Furthermore, since existence of a shoulder at about 10 MeV higher mass was reported in several reactions, they also tried to fit with two Lorentzian functions. The obtained peak positions and widths corresponding to two Lorentzian functions are listed in Figure 5.13 [107].

The obtained peak position from the present analysis is consistent with the mean value shown in Figure 5.12, which is the one Lorentzian fitting result, within the errors. The same was true with the lower peak (m_{01}) shown in Figure 5.13 for two Lorentzian fitting results. Here, we can conclude nothing on the existence of the shoulder structure (higher peak m_{02}) from the present data because of the large quasi-free Σ backgrounds.

In addition, the width seems to be smaller than the averaged value of 12.2 ± 1.3 MeV in other reactions shown in Figure 5.12, although there is no large difference between the width of lower peak (Γ_1) in Figure 5.13. In order to discuss the possible pole position and the difference between the other reaction data, we need realistic theoretical calculations taking into account the (π^+, K^+) reaction mechanism. Such a detailed studies including the present data would reveal the information of the ΣN–ΛN coupling strength.

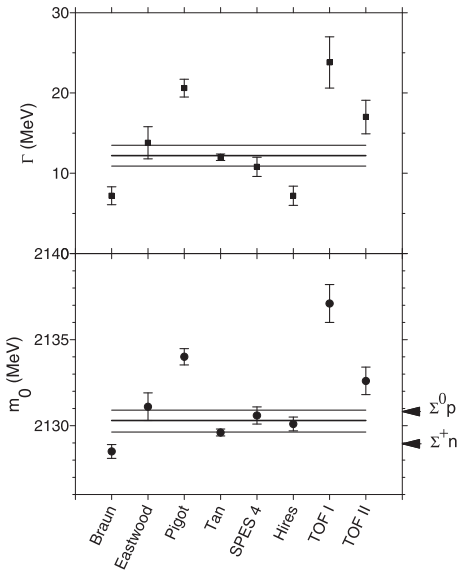

Figure 5.12: A summary of the peak positions (m_0) and widths (Γ) from the fit with one Lorentzian function by the author of Ref. [107]. The values for the data set from Braun *et al.* [104], Eastwood *et al.* [108], Pigot *et al.* [109], Tan [103], SPES4 [110], HIRES [105] and TOF [106] are shown. The lines show the mean (thick line) and variance (thin line). The arrows show the indicated thresholds.

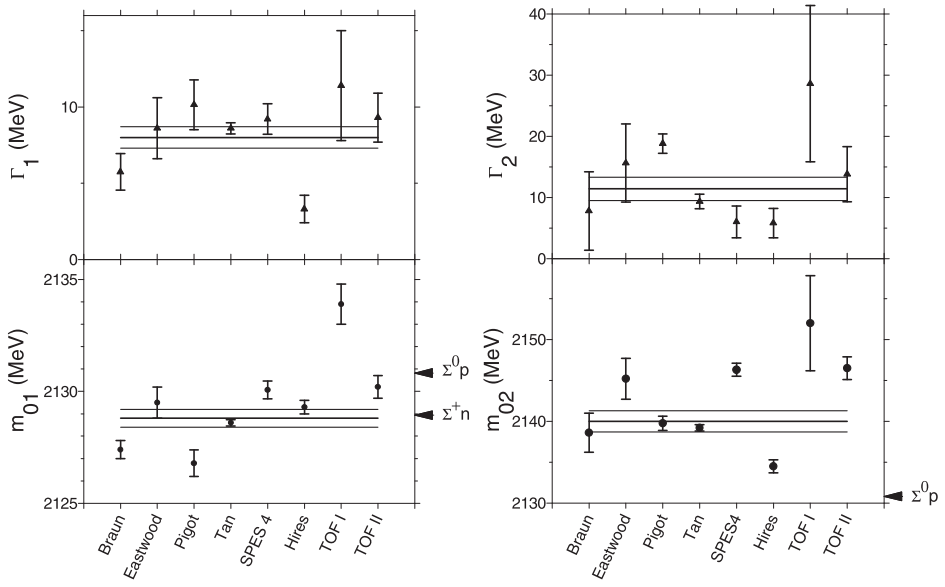

Figure 5.13: A summary of the peak positions (m_{01}, m_{02}) and widths (Γ_1, Γ_2) from the fit with two Lorentzian functions by the author of Ref. [107]. The used data sets are same as in Figure 5.12. The lines show the mean (thick line) and variance (thin line). The arrows show the indicated thresholds.

"Shift" of Y^* peak

In Region Ⅲ, the contributions of $\Sigma(1385)^{+/0}$ and $\Lambda(1405)$ overlap each other, and it is not possible to disentangle them in the inclusive measurement. Here, we treat the bump structure as one component.

When we fitted the bump with a Gaussian function, we obtained the peak position at 2400.6 ± 0.5 (stat.) ± 0.6 (syst.) MeV/c^2 for the present data and at 2433.0 $^{+2.8}_{-1.6}$ (syst.) MeV/c^2 for the simulation as shown in Figure 5.8. The systematic error for the simulation was estimated taking into account uncertainties of the differential cross sections of Y^*, the Y^* mass and fitting ranges. The same fitting procedure was applied for a MM_p spectrum. We obtained the peak position at 1376.1 ± 0.4 (stat.) ± 0.5 (syst.) MeV/c^2 and 1398.5 $^{+2.6}_{-1.6}$ (syst.) MeV/c^2, respectively. The amount of the peak shift for the scattering angle of 2° to 16° is 32.4 ± 0.5 (stat.) $^{+2.9}_{-1.7}$ (syst.) (22.4 ± 0.4 (stat.) $^{+2.7}_{-1.7}$ (syst.)) MeV/c^2 for the MM_d (MM_p) spectra to the low mass side.

Even if the peak position of the simulated spectrum was adopted instead of the fitted one, the difference is only reduced by just 4 MeV/c^2. There could be an additional uncertainty by several MeV additionally to the low-mass side arising from our simple spectator model in the simulation, which was estimated from the difference of the peak positions when the balance of the off-shellness between the participant and spectator nucleons was changed. The small difference of about 3 MeV/c^2 for the quasi-free Σ productions is within this uncertainty. More sophisticated theoretical analyses taking into account Y^*N interactions in the final state might explain the observed puzzling "shift".

Next, we discuss the comparison of the Y^* bump for each scattering angle between the obtained data and the simulation. Figures 5.14 and 5.15 show the spectra obtained from data and simulation for the MM_d and MM_p, respectively, for every 2° between 2° and 16°. The peak positions of Y^* for the present data are shifted to low mass side for all the scattering angles. The same fitting procedure as for the angle averaged spectra in the whole scattering angle was applied for each spectrum.

The obtained peak positions are summarized in Figure 5.16. The peak position of the simulation for MM_p spectra (black points with error bars in Figure 5.16 (b)) decrease as the scattering angle becomes larger. It is because the elementary cross section of $\Lambda(1405)$ is larger (smaller) than that of $\Sigma(1385)$ in the very forward (backward) region. So that the peak position is larger in the forward scattering angle. However, this effect shifts the peak by at most 10 MeV. Here, the peak position of the present data for MM_p spectra (red points with error bars in Figure 5.16 (b)) does not decrease as the scattering angle becomes larger. On the other hand, the peak positions for MM_d spectra (black points with error bars in Figure 5.16 (a)) increase as the scattering angle becomes larger because the momentum transfer increases when we select the backward scattering angle. This increase is seen for the peak position of the present data for MM_d spectra (red points with error bars in Figure 5.16 (a)).

It should be noted that the LEPS group recently reported a similar inclusive spectrum for the $d(\gamma, K^+\pi^-)$ reaction at a 1.5–2.4 GeV photon energy region and found no significant shift in the Y^* region [51]. Moreover, there is an old experiment using a deuterium bubble chamber [111]. They measured the invariant mass spectrum of

$\Lambda\pi^+$ in the $\pi^+ d \to K^+\Lambda\pi^+(n_s)$ reaction at incident beam momenta between 1.1 and 2.4 GeV/c^2. The measured mass and width for the $\Sigma(1385)^+$ are 1386.6 $\pm$ 4.4 MeV/c^2 and 49 $\pm$ 11 MeV, respectively. Thus, the $\Sigma(1385)^+$ mass measured by the invariant mass of $\Lambda\pi^+$ is not shifted to the low-mass side.

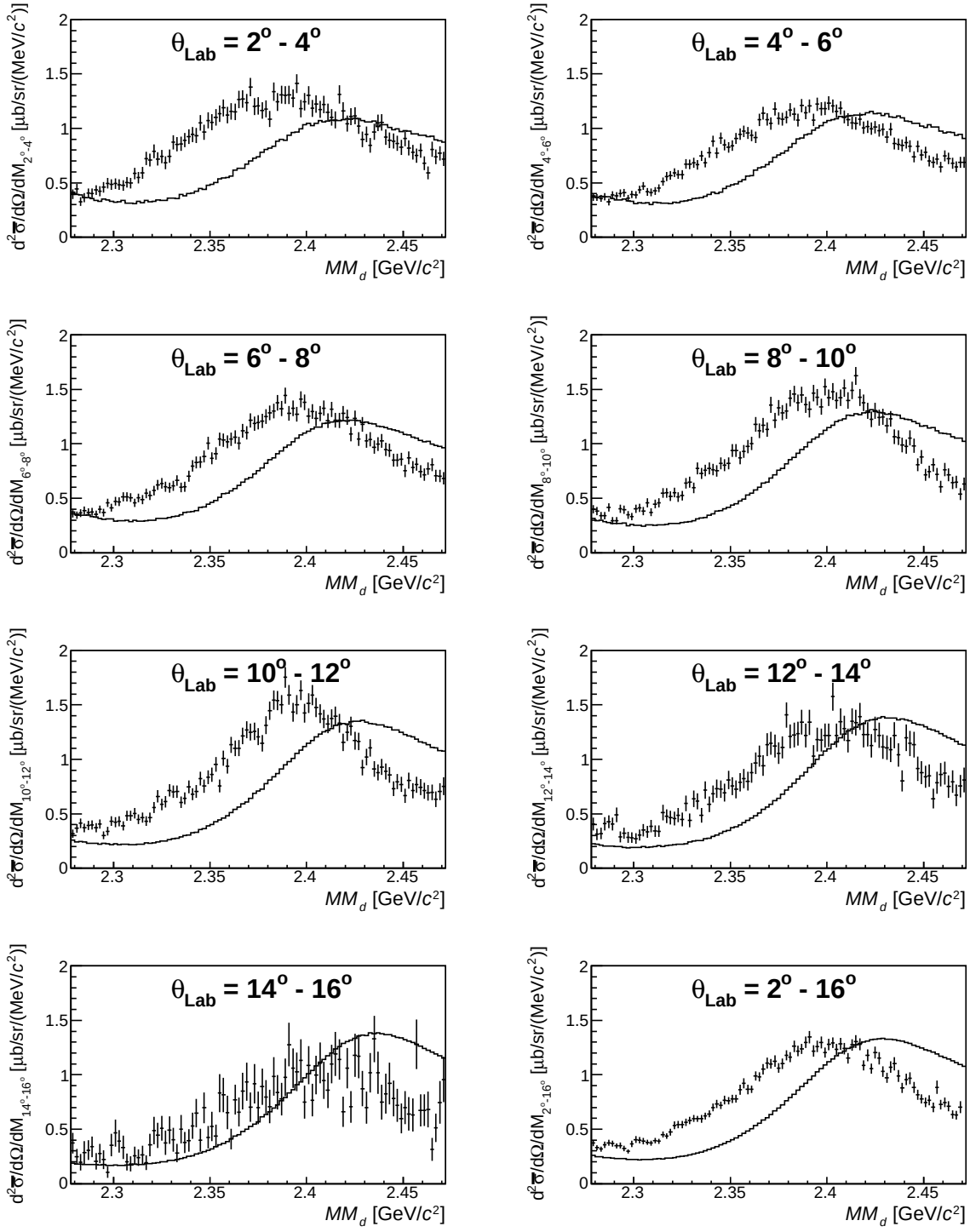

Figure 5.14: The obtained double differential cross section (crosses) of the $\pi^+ d \rightarrow K^+X$ reaction shown with MM_d for each scattering angle compared with the simulated spectra (solid lines).

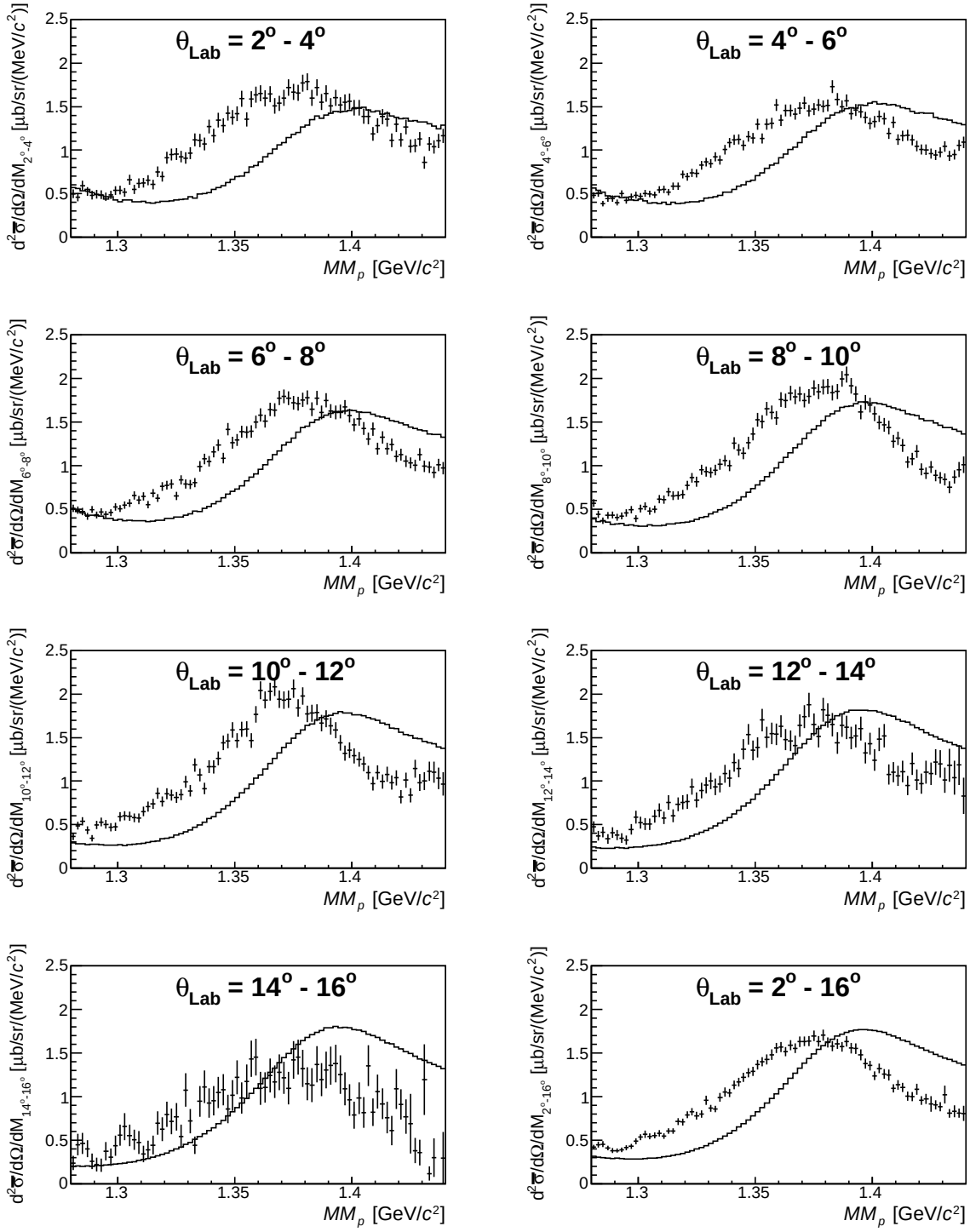

Figure 5.15: The obtained double differential cross section (crosses) of the $\pi^+ d \rightarrow K^+X$ reaction shown with MM_p for each scattering angle compared with the simulated spectra (solid lines).

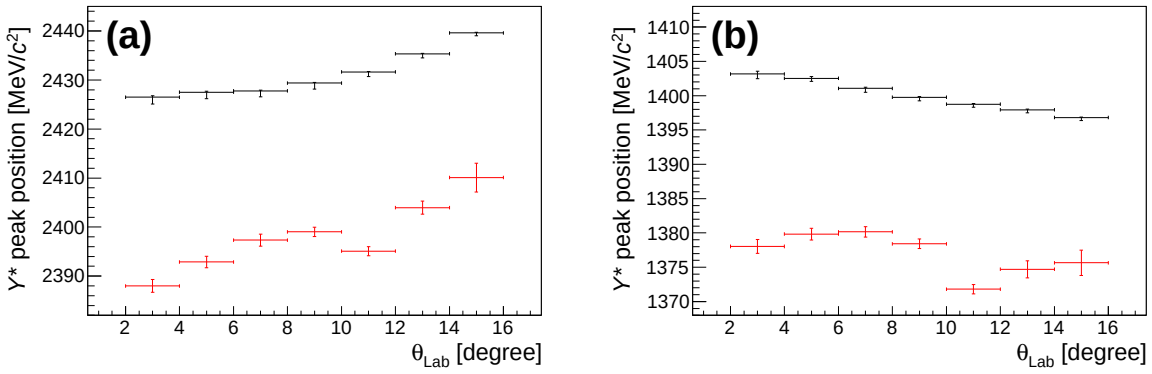

Figure 5.16: The peak positions of the Y^* bump for each scattering angle obtained from the present data (red) and simulated spectra (black) The values obtained for MM_d and MM_p are shown with (a) and (b), respectively.

5.2 Coincidence analysis: results and discussion

5.2.1 π coincidence analysis

According to our Monte Carlo simulation, a proton emitted from hyperon produced from the quasi-free processes as Eq. 5.2 $\sim$ 5.6 rarely hits the RCA. However, pions from these quasi-free processes can reach all the segments of RCA. This is the same as in the $p(\pi^+, K^+)\Sigma^+$ reaction described in Sec. 4.5 (especially in Figure 4.16).

Thus, we compared the obtained π coincidence spectra of the $d(\pi^+, K^+)$ reaction and the simulation of the quasi-free hyperon and hyperon resonance production processes, whose assumptions were same as described in Sec. 5.1.2. Here, we assigned the events, which had the hit at least in the first layer of RCA and was not assigned as proton, as π. The other particles such as gammas should be included in our pion selections, although the main component is pion. Such other particles were also included in the simulation and the same cut condition for the energy loss at the first layer of RCA ($\widetilde{dE} > 1.3$ MeV) was applied both in the simulation and data analysis.

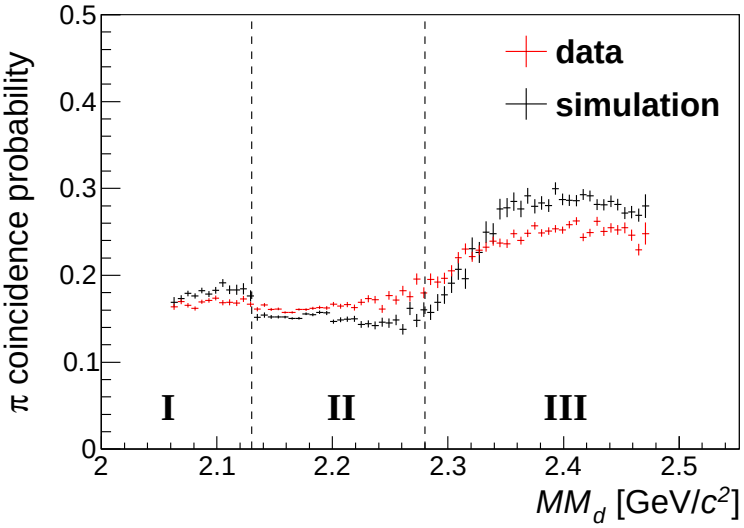

Figure 5.17: A comparison of the π coincidence probability spectra between data and simulation is shown in red and black lines, respectively. The regions of the quasi-free productions of Λ (I), Σ (II) and Y^*'s (III), which are same as Figure 5.1, are also indicated in the figure.

Figure 5.17 shows a comparison of the π coincidence probability spectra as a function of MM_d between data and simulation. In the spectra, three regions I, II and III are shown in the figure for different quasi-free processes. The difference originated from the decay branch to emit the charged pion and the number of the produced charged pions.

For instance, $\Sigma(1385)^+$ mainly decays to $\Sigma(1385)^+ \to \Lambda\pi^+ \to p\pi^-\pi^+$ (55.6%). On the other hand, Σ^+ can decay to $n\pi^+$ (48.3%). Then, the pion coincidence probability of $\Sigma(1385)^+$ should be higher than the one of Σ^+ because $\Sigma(1385)^+$ and Σ^+ can produce

two and one pion(s), respectively. Such a tendency can be seen in the obtained data shown in red crosses. Moreover, the pion coincidence probabilities of obtained data and simulation in the Λ (I) and Σ (II) regions are almost consistent. However, in the Y^* (III) region, they do not always go together. This difference might be due to the same origin of the observed "shift" of Y^* peak in the inclusive spectrum.

5.2.2 One-proton coincidence analysis

A proton emitted from the quasi-free processes rarely hits the RCA: only small fraction in the forward segments (Seg1, 4). Moreover, the spectator proton in a deuteron rarely exceeds the analysis threshold momentum of 250 MeV/c. Therefore, we can expect a good suppression of the quasi-free processes in one-proton coincidence spectrum.

Here, we show the detection efficiency of one proton as a function of missing mass (MM_d) in each segment of RCA in Figure 5.18 produced from a simulation. In this figure, the efficiency of Λp and $\Sigma^0 p$ final state mode is shown with red and black crosses, respectively, and the mass threshold of the $K^- pp$ system is also shown with a green line. The detection efficiency of the proton gradually increases from the production threshold of each final state mode and it reaches to an almost flat region. We can see that the forward (Seg1, 4) and middle (Seg2, 5) segments have an almost flat and wide acceptance with respect to the $K^- pp$ mass threshold, although the acceptance of the backward segments (Seg3, 6) is limited. Therefore, we discuss the one-proton

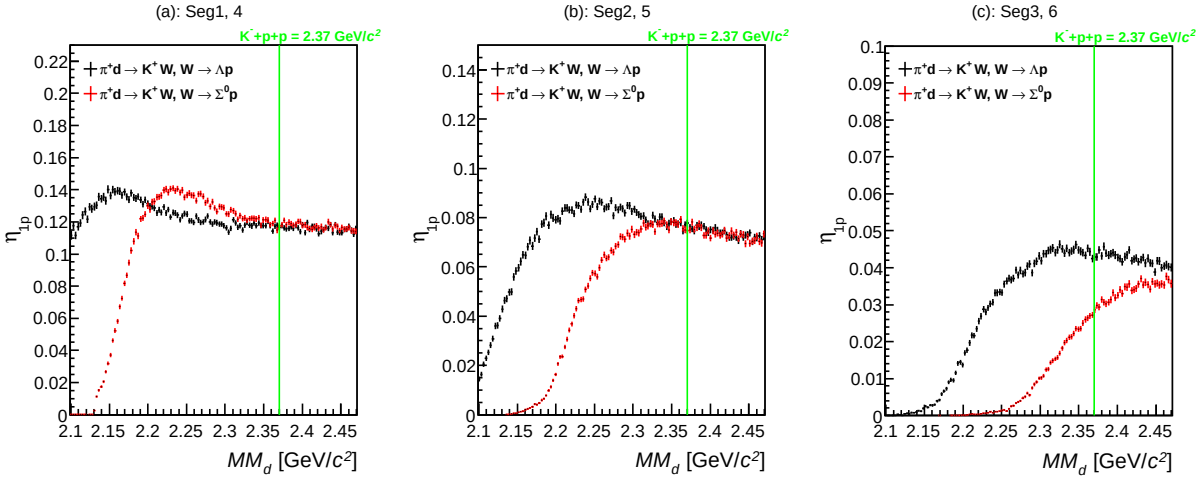

Figure 5.18: The detection efficiency of a proton for each segment of RCA as a function of MM_d. The efficiency for the forward segment (Seg1, 4), the middle segment (Seg2, 5) and the backward segment (Seg3, 6) is shown in (a), (b) and (c), respectively. The cases of Λp and $\Sigma^0 p$ final state modes are indicated with black and red crosses, respectively.

coincidence spectrum for the middle segments (Seg2, 5) of RCA. Note that there would be no quasi-free contributions in this spectrum according to the simulation.

Figure 5.19 (b) shows a coincide spectrum with one proton in the middle segments of RCA and Figure 5.19 (c) shows the coincidence probability spectrum, which was obtained

by dividing the coincidence spectrum (Figure 5.19 (b)) with the inclusive spectrum (Figure 5.19 (a)). These spectra are without acceptance correction for the RCA. The contamination from the misidentification of $\pi^{\pm}$ in RCA, which is estimated by the side-band events in PID described in Sec. 4.4, is shown with hatched spectra in the figure. The contamination fraction of this component is about 7% around the $MM_d \sim 2.27$ GeV/c^2.

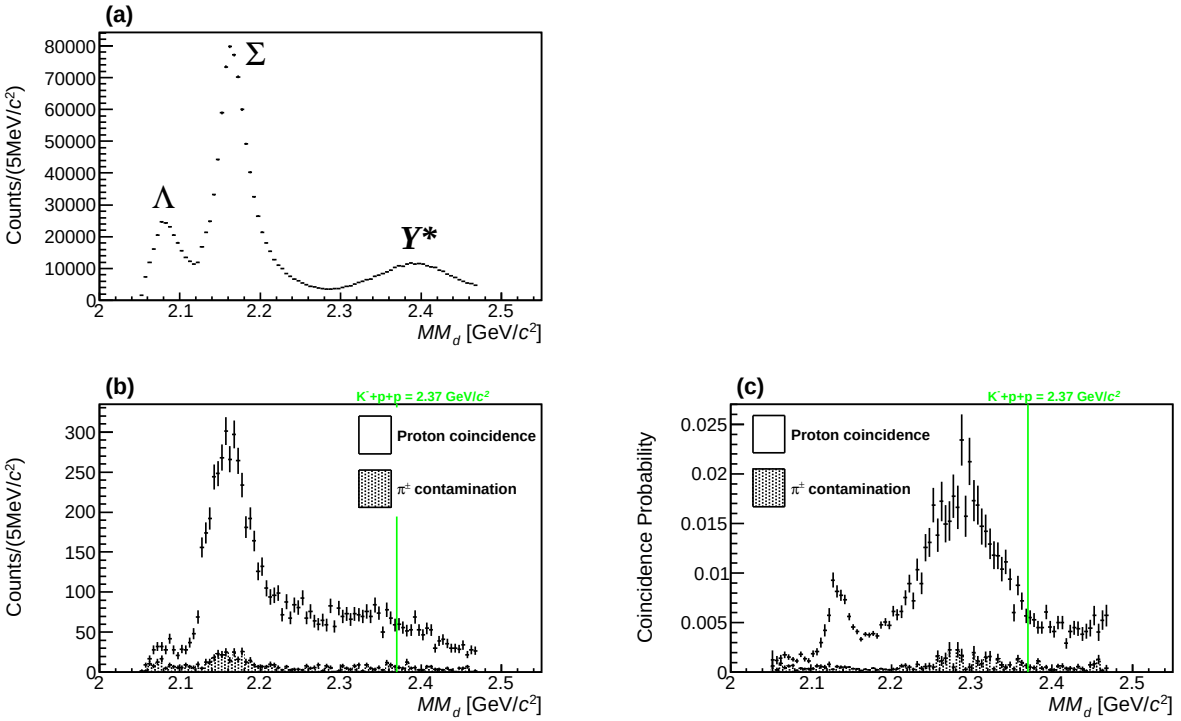

Figure 5.19: (a) Inclusive missing-mass spectrum of the $d(\pi^+, K^+)$ reaction. (b) Missing-mass spectrum of the $d(\pi^+, K^+)$ reaction with one proton in the middle of the RCA in each side (Seg2, 5). (c) The coincidence probability of a proton obtained by dividing the coincidence spectrum (b) with the inclusive spectrum (a). Hatched spectra show the $\pi^{\pm}$ contamination in RCA.

In these spectra, there are possible non-quasi-free contributions of the ΣN threshold cusp, the K^-pp signal emitting through $K^-pp \to \Lambda(\Sigma^0)p$, and quasi-free hyperons and hyperon resonances productions followed by conversions such as $\Sigma N \to \Lambda N$. Here, we notice there are two prominent structures in Figure 5.19 (c): one at the threshold cusp position (2.13 GeV/c^2) and the other broad bump at around 2.27 GeV/c^2, which can be the signal of the "K^-pp"-like structure. In the quasi-free production region of Σ (II) and Y^* (III), the proton coincidence probability is smaller than the two prominent structures and stays rather constant.

5.2.3 Two-proton coincidence analysis

We present the two proton coincidence analysis result, which is also free from the quasi-free background. Figures 5.20(b) and (c) show the two-proton coincidence and coincidence probability spectra same as Figure 5.19. At this stage, the acceptance of RCA is not taken into account. The component of the $\pi^{\pm}$ contamination is also shown with hatched spectra in the figure. The two-proton coincidence probability spectrum also has the two prominent structures, which are at the threshold cusp position (2.13 GeV/c^2) and the other broad bump at around 2.27 GeV/c^2 similar to the one-proton coincidence probability spectrum.

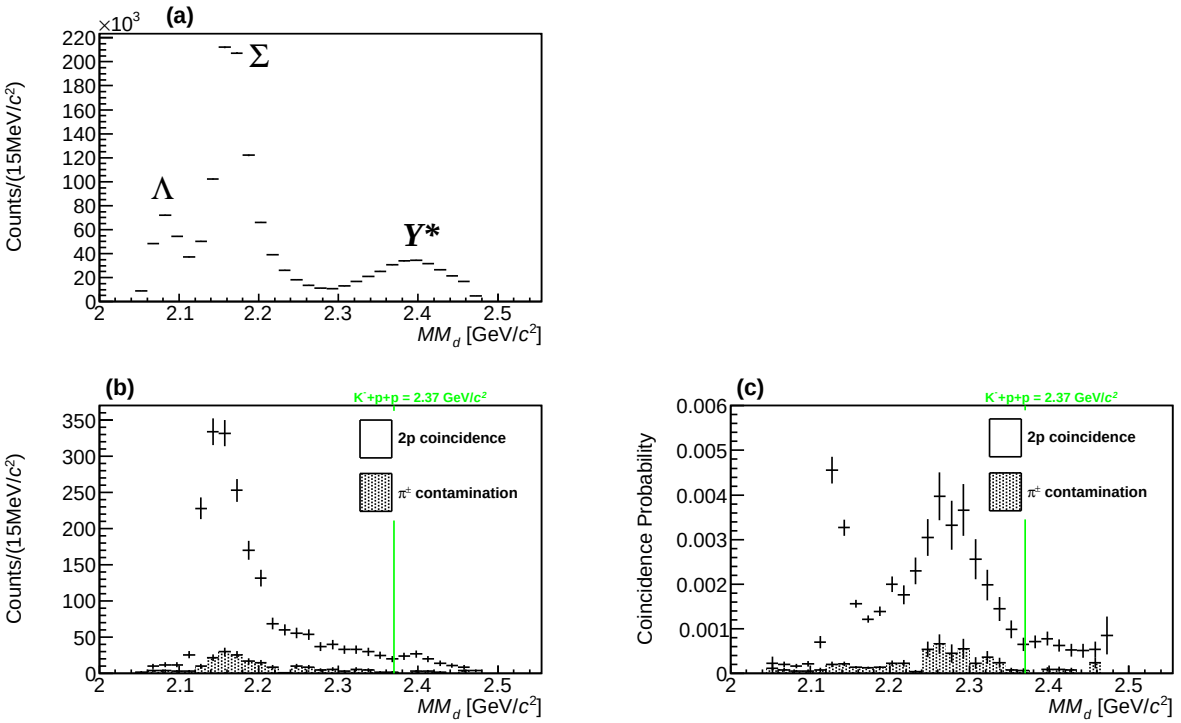

Figure 5.20: (a) Inclusive missing-mass spectrum of the $d(\pi^+, K^+)$ reaction. (b) Missing-mass spectrum of the $d(\pi^+, K^+)$ reaction with two protons coincidence in RCA. (c) The coincidence probability of two protons obtained by dividing the coincidence spectrum (b) with the inclusive spectrum (a). Hatched spectra show the $\pi^{\pm}$ contamination in RCA.

5.2.4 Identification of final states in two-proton coincidence

In order to take into account the acceptance of our range counter system, we need information of the final state of the W in the $\pi^+ d \to K^+ W$ reaction. This study was carried out by requiring coincidence of two protons in the RCA's.

In order to detect the two protons in our system, the final state of W should be a) Λp, $\Lambda \to p\pi^-$, b) $\Sigma^0 p, \Sigma^0 \to \Lambda\gamma \to p\pi^-\gamma$, and c) $Y\pi p \to pp\pi\pi(\gamma)$, where Y is hyperon as Λ and Σ. We identified such a final state by measuring the missing-mass squared spectra of X in the $d(\pi^+, K^+pp)X$ process by measuring the momenta of two protons in the

decay of ppX system, of which mass is MM_d. In this analysis, the absolute value of the momenta of protons were obtained from the velocity and emitted angles estimated from the vertex position of the (π^+, K^+) reaction point and hit position of the first layer of RCA. The first two modes, a) and b), are non-mesonic and the X is one pion (and γ). The last one, c), is mesonic and the X is two pions. Therefore, the missing-mass squared spectrum of M_X^2 should show different distribution for each decay mode.

Figure 5.21 shows such missing-mass squared spectrum of M_X^2 for each MM_d region. The obtained data is indicated in black points with error bars. These points were shown after subtraction of the $\pi^\pm$ contamination fraction, whose distributions were almost flat in the M_X^2. The colored dashed-lines in Figure 5.21 show the Λp, $\Sigma^0 p$ and $Y\pi p$ final-state components, whose normalization factors were adjusted by a template fit. The total fit results are also displayed with the black lines.

These templates were made from the simulation, which assumed the reaction of $\pi^+ d \to K^+ W, W \to pY(pY\pi)$ with uniform productions. In the Λp and $\Sigma^0 p$ modes (pY), we assumed the uniform decay distributions in the center of mass system because the $K^- pp$ is considered as spin $J = 0$. In case of $Y\pi p$ modes, there are many possible decay distributions because they are three-body systems. When the $K^- pp$ decays to $Y\pi p$ modes, the proton momentum in the center of mass system may become small corresponding to the Fermi momentum in the deuteron [96]. Thus, in the fitting of Figure 5.21, we assumed the weighted decay distribution for the $Y\pi p$ modes, whose proton's momentum was small as the Fermi momentum in the deuteron. Moreover, the templates for the $Y\pi p$ modes were made by mixing of the $\Sigma^+\pi^- p$, $\Sigma^0\pi^+ p$ and $\Lambda\pi^0 p$ components because the M_X^2 distributions for such $Y\pi p$ modes had only small differences and it is difficult to distinguish between each other. The mixture ratio was estimated from the elementary cross-section of Y^*'s (see Sec. 5.1.2) and decay branches of Y^*'s to $Y\pi$ modes.

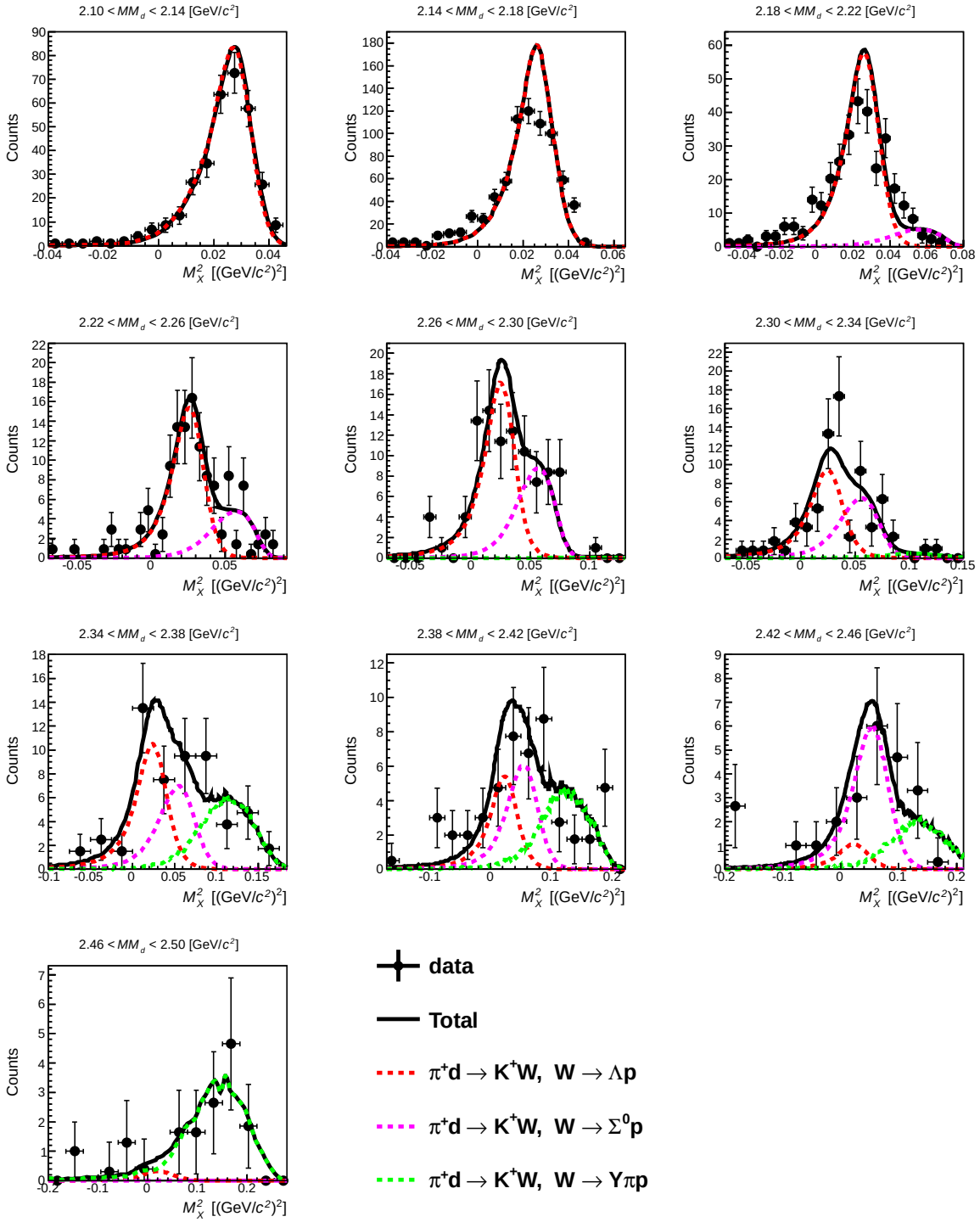

Figure 5.21: Missing-mass squared spectra of X obtained from the two proton coincidence events in the reaction of the $d(\pi^+, K^+pp)X$. Each spectrum shows the mass square of X for the different MM_d region shown in the figure. The spectra were fitted with three components of Λp (red dashed-line), $\Sigma^0 p$ (magenta dashed-line) and $Y\pi p$ (green dashed-line) modes.

5.2.5 Cross section in two-proton coincidence

The missing mass spectrum is obtained as a double differential cross section of $d^2\bar{\sigma}/d\Omega/dM$ averaged over the scattering angle of the (π^+, K^+) reaction from 2° to 14° for the two proton coincidence events[1]. We reconstructed the double differential cross section only for the Λp and $\Sigma^0 p$ modes because the $Y\pi p$ modes had the large ambiguities such as the mixture of each mode and decay distributions. The double differential cross section of each final state was calculated as,

$$\frac{d^2\bar{\sigma}^i_{2^\circ-14^\circ}}{d\Omega dM} = \frac{A}{N_A(\rho x)N_{beam}\Delta\Omega_K}\sum_{j=0}^{N_{K\times 2p}}\frac{Br(MM_d, M_X^2)^i_j}{\epsilon_{\pi K_j}\eta^i_{2p}(MM_d, \theta_{\pi K})_j}, \tag{5.8}$$

where A is the target mass number, N_A the Avogadro constant, ρx the target mass thickness, N_{beam} the number of beam pions on the target, $\Delta\Omega_K$ the solid angle of SKS, $\epsilon_{\pi K}$ the overall experimental efficiency for the (π^+, K^+) measurements same as the ϵ in Eq. 3.30, $N_{K\times 2p}$ the number of detected kaons with two protons in the missing-mass interval ΔM_X and j indicates the event number. $Br^i(MM_d, M_X^2)$ is the probability for each final state estimated from the fitting as in Figure 5.21. The probability $Br^i(MM_d, M_X^2)$ is normalized as,

$$Br^{\Lambda p}(MM_d, M_X^2) + Br^{\Sigma^0 p}(MM_d, M_X^2) + Br^{Y\pi p}(MM_d, M_X^2) + Br^{Contami}(MM_d) = 1, \tag{5.9}$$

where $Br^{Contami}$ is the probability of the $\pi^\pm$ contamination in the proton selection region.

$\eta^i_{2p}(MM_d, \theta_{\pi K})$ is the detection efficiency of two protons in RCA for each final state calculated by a Geant4 [91] based Monte Carlo simulation. Figures 5.22 (a) and (b) show the detection efficiency ($\eta^i_{2p}(MM_d, \theta_{\pi K})$) for the Λp and $\Sigma^0 p$ modes, respectively. Figure 5.23 is the projection spectra of Figures 5.22. The η_{2p} is almost constant in the missing mass (MM_d) except near the production threshold. In this analysis, we did not use the small η_{2p} region to avoid the miss-assignment of the final state. The standard cut-off value was $\eta_{2p} = 0.01$, which was about 1/3 of the acceptance in the constant region as shown in Figure 5.23. $\eta^i_{2p}(MM_d, \theta_{\pi K})$ was corrected event-by-event by checking the MM_d and scattering angle $\theta_{\pi K}$.

[1]The obtained number of events for the $\theta_{\pi K} = 14^\circ \sim 16^\circ$ region was small due to the limited acceptance of the SKS for K^+ detection. Therefore, we did not use such large scattering angle events for the coincidence analysis.

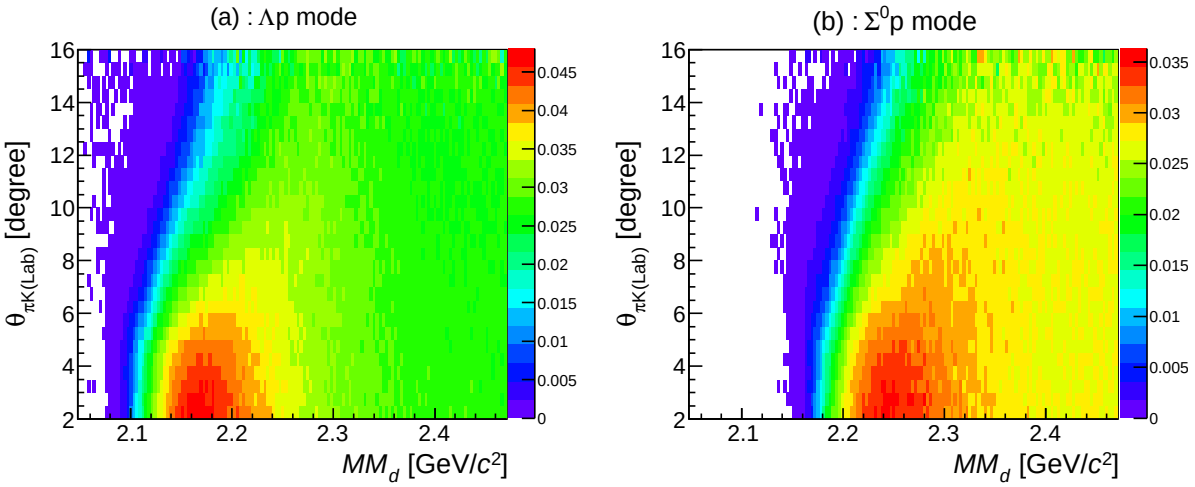

Figure 5.22: Detection efficiency of two protons η^{2p} for Λp and $\Sigma^0 p$ modes are shown in (a) and (b), respectively. The efficiency was corrected event-by-event by checking the MM_d and $\theta_{\pi K}$.

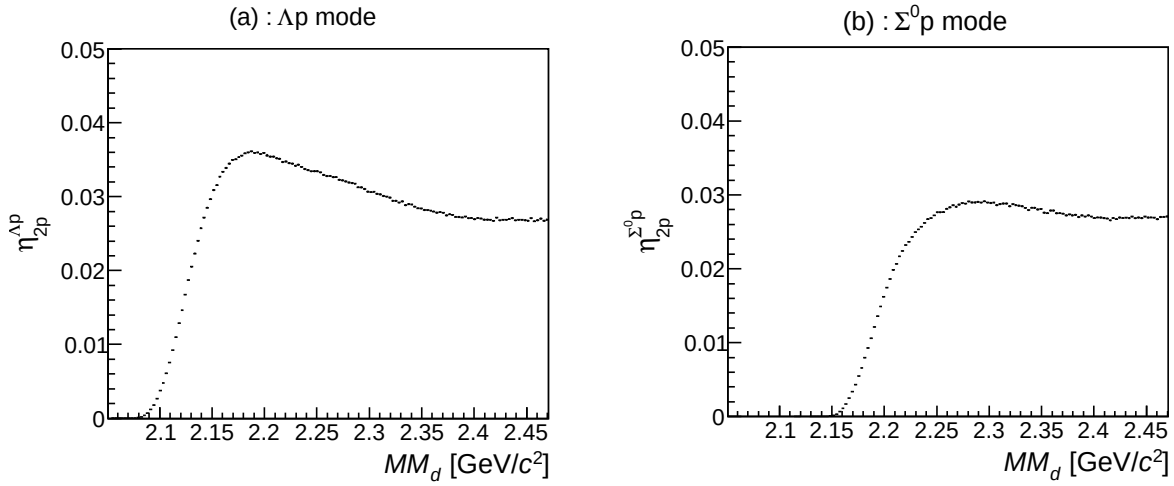

Figure 5.23: Detection efficiency of two protons η^{2p} for Λp (a) and $\Sigma^0 p$ (b) modes as a function of MM_d. These are the projection spectra of Figure 5.22.

Figure 5.24 (a) and (b) show the obtained double differential cross section $(d^2\bar{\sigma}/d\Omega/dM)$ averaged over the scattering angle from 2° to 14° for the Λp and $\Sigma^0 p$ modes, respectively. The errors in those spectra were determined by the statistical error of two-proton coincidence events ($N_{K\times 2p}$). They also include the ambiguity of the fraction of $\pi^{\pm}$ contamination ($Br^{Contami}$ in Eq. 5.9), and the statistical error of the final state determination (Br^i in Eq. 5.8) shown in Figure 5.21.

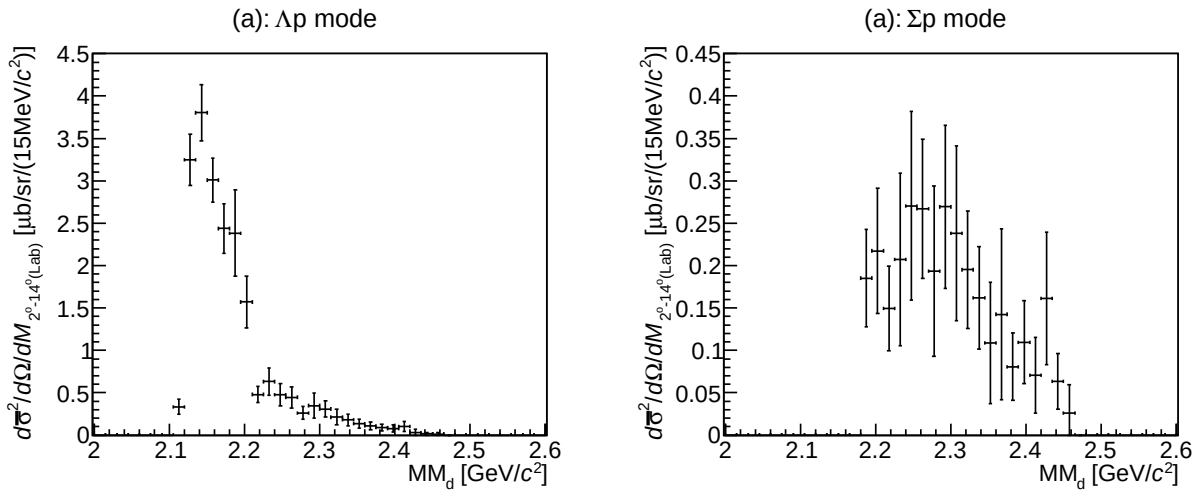

Figure 5.24: The double differential cross section for the Λp (a) and $\Sigma^0 p$ (b) final state modes estimated from the fitting of M_X^2 as shown in Figure 5.21. These spectra are obtained from the two-proton coincidence events.

5.2.6 Results on proton coincidence spectra

We have observed a broad enhancement in the $\Sigma^0 p$ spectrum as shown in Figure 5.24 (b). Here, we call the obtained broad enhancement as a "$K^- pp$"-like structure. In this $\Sigma^0 p$ spectrum, there is no considerable background processes. On the other hand, in the Λp spectrum in Figure 5.24 (a), there is a large component around 2.13 GeV/c^2, while the component around 2.28 GeV/c^2 corresponding to the "$K^- pp$"-like structure is also seen. Therefore, we did not use Λp spectrum for the fit to evaluate the mass and width of the "$K^- pp$"-like structure. The large component around 2.13 GeV/c^2 is interpreted as the ΣN cusp and the conversion process of $\Sigma N \to \Lambda p$ reaction. The detail discussion for this component in the Λp spectrum is described in Appendix C.

We fitted the $\Sigma^0 p$ spectrum to evaluate the mass and width of the "$K^- pp$"-like structure with a relativistic Breit-Wigner function as,

$$f(MM_d) = \frac{(2/\pi) MM_d m_0 \Gamma(q)}{(m_0^2 - MM_d^2)^2 + (m_0 \Gamma(q))^2}. \tag{5.10}$$

The mass-dependent width was $\Gamma(q) = \Gamma_0(q/q_0)$, in which q (q_0) is the momentum of the Σ^0 and proton in the $\Sigma^0 p$ rest frame at mass MM_d (m_0). Note that we did not use the Λp spectrum for the evaluation of the mass and width of the "$K^- pp$"-like structure. Figure 5.25 (b) shows the fit result of the $\Sigma^0 p$ spectrum with the relativistic Breit-Wigner function.

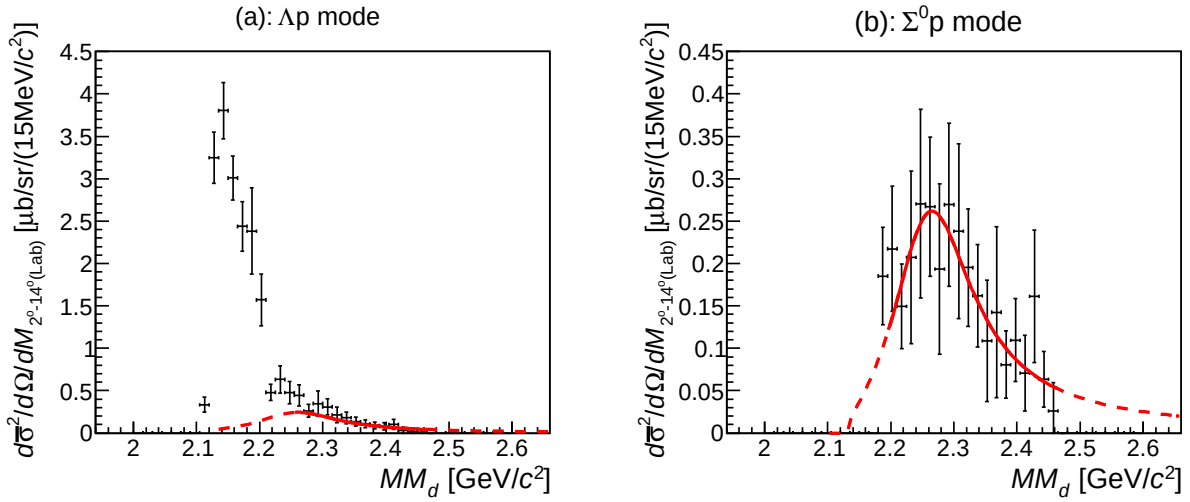

Figure 5.25: The double differential cross section for the Λp (a) and $\Sigma^0 p$ (b) final state modes fitted with the relativistic Breit Winger function. These cross section spectra are same as Figure 5.24. The solid lines and dashed lines show the obtained relativistic Breit Wigner function of the fitted region and whole region, respectively. The evaluation of the mass and width was carried out only using the $\Sigma^0 p$ spectrum. The determination of the branching fraction of the "$K^- pp$"-like structure was carried out by fitting with the Λp and $\Sigma^0 p$ spectra with the common parameters assuming the same mass distribution of MM_d. (b) is taken from Ref. [112].

The mass, width and these statistical errors were estimated from the χ^2 distribution of the fit as a function of the mass (m_0) and width (Γ_0) of the "K^-pp"-like structure shown in Figure 5.26. The χ^2-determination scheme is same as the one for the ΣN-cusp analysis (Figure 5.11). The mass and width of the "K^-pp"-like structure were found to be 2275 $^{+17}_{-18}$ (stat.) MeV/c^2 and 162 $^{+87}_{-45}$ (stat.) MeV, respectively. It corresponds to the binding energy of the K^-pp system to be 95 $^{+18}_{-17}$ (stat.) MeV.

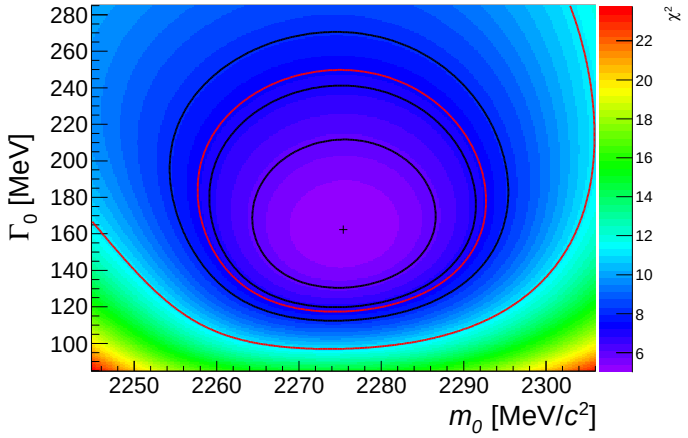

Figure 5.26: The contour plot of the χ^2 of the fitting as a function of the mass (m_0) and width (Γ_0) of the "K^-pp"-like structure. The black lines show $\Delta\chi^2 = +1$, $+2$ and $+3$ regions from the minimum χ^2 value shown in a cross. The red lines show the 1σ and 2σ deviations.

Next, we estimated the systematic uncertainty of the mass and width for the "K^-pp"-like structure. The systematic error of the width is larger than the one for the mass same as the statistical error. In this analysis, we identified the final state in two-proton coincidence by fitting with the template functions of the missing-mass squared M_X^2 of the $d(\pi^+, K^+pp)X$ reaction. In order to estimate the uncertainty of the final state determination method, we carried out the template fit with not only the M_X^2 spectrum but also missing-energy (E_X) spectra. The uncertainties of the width and mass originating from this ambiguity were 61 MeV and 9 MeV/c^2, respectively. This uncertainty is the largest component of the systematic error. The analysis using the E_X spectra is described in Appendix D. Moreover, since we used the template fit to identify the final state, the shape of the mass distribution might be changed when we used the different templates from different assumptions. Since the Λp and $\Sigma^0 p$ modes are two body systems, we have less assumptions to make the templates. On the other hand, we made the $Y\pi p$ templates with different assumptions of the decay distributions and mixture ratio for each component. In this analysis, we assumed the weighted decay distributions, whose proton's momentum was small as the Fermi-motion in the deuteron, for the $Y\pi p$ modes. In order to estimate the systematic error of this assumption, we changed the decay distribution to the three-body phase-space distribution. The systematic errors of the width and mass of this ambiguity were 33 MeV and 10 MeV/c^2, respectively. We

also changed the different mixture ratio for the $Y\pi p$ modes. In the simulation, we made the $Y\pi p$ template functions by mixing of the $\Sigma^+\pi^-p$, $\Sigma^0\pi^0p$ and $\Lambda\pi^0p$ components according to the elementary cross-section of Y^*'s. We carried out another template fit by changing the $Y\pi p$ mixed template to single $\Lambda\pi^0p$ and $\Sigma\pi p$ ($\Sigma^+\pi^-p$: $\Sigma^0\pi^0p$ = 1 : 1) templates to estimate the ambiguity from this assumption. The systematic errors of the width and mass of this assumption were 25 MeV and 2 MeV/c^2, respectively. We also estimated the ambiguity originating from the fitting function. For this estimation, we performed the mass fit using the Lorentzian function instead of the relativistic Breit Wigner function. The systematic errors of the width and mass originating from this uncertainty were 19 MeV and 3 MeV/c^2, respectively. The ambiguities originating from the binning and fit region were 20 MeV (width) and 9 MeV/c^2 (mass). The systematic uncertainty of each component is shown in full width. Finally, the mass and width of the "K^-pp"-like structure were estimated to be 2275 $^{+17}_{-18}$ (stat.) $^{+21}_{-30}$ (syst.) MeV/c^2 and 162 $^{+87}_{-45}$ (stat.) $^{+66}_{-78}$ (syst.) MeV, respectively. It corresponds to the binding energy of the K^-pp system to be 95 $^{+18}_{-17}$ (stat.) $^{+30}_{-21}$ (syst.) MeV.

The production cross section of the "K^-pp"-like structure decaying to Σ^0p was estimated from the fit of the Σ^0p spectrum by using the evaluated mass and width of the "K^-pp"-like structure. The evaluated production cross section was $d\sigma/d\Omega_{K^-pp\to\Sigma^0p}$ = 3.0 ± 0.3 (stat.) μb/sr. A branching fraction of the "K^-pp"-like structure of $\Gamma_{\Lambda p}/\Gamma_{\Sigma^0p}$ was estimated by fitting the Λp and Σ^0p spectra with the common parameters as shown in Figure 5.25 (a) and (b), respectively. The mass distribution of the Λp mode was assumed to be same as the Σ^0p one. Here, the Λp spectrum has the large component around 2.13 GeV/c^2 corresponding to the ΣN cusp and $\Sigma N \to \Lambda p$ conversion. Thus, we did not use such low missing-mass region of the Λp spectrum for the fit. We evaluated the branching fraction to be $\Gamma_{\Lambda p}/\Gamma_{\Sigma^0p}$ = 0.92 $^{+0.16}_{-0.14}$ (stat.).

For the production cross section and the branching fraction, we also estimated the systematic error. The origins of these systematic error were almost same as the ones for the mass and width. The systematic errors caused from the final state determinations, which was estimated by changing the fitting spectrum to E_X, were obtained to be 0.7 μb/sr for the production cross section and 0.21 for the branching fraction. The uncertainties originating from the assumption of the decay distributions of the $Y\pi p$ modes were 0.8 μb/sr ($d\sigma/d\Omega_{K^-pp\to\Sigma^0p}$) and 0.42 ($\Gamma_{\Lambda p}/\Gamma_{\Sigma^0p}$). The systematic errors originating from the assumption of the mixture ratios of the $Y\pi p$ modes were found to be 0.1 μb/sr ($d\sigma/d\Omega_{K^-pp\to\Sigma^0p}$) and 0.17 ($\Gamma_{\Lambda p}/\Gamma_{\Sigma^0p}$). In case of the systematic-error estimation of the differential cross section and the branching fraction, we did not take into account the ambiguity of the fit using the Lorentzian function. Moreover, we estimated the systematic error caused from the uncertainties of the mass and width by changing these values within the evaluated errors. These systematic uncertainties were 0.1 μb/sr ($d\sigma/d\Omega_{K^-pp\to\Sigma^0p}$) and 0.33 ($\Gamma_{\Lambda p}/\Gamma_{\Sigma^0p}$). The systematic uncertainty of each component is also shown in full width. Finally, we evaluated the production cross section and the branching fraction to be $d\sigma/d\Omega_{K^-pp\to\Sigma^0p}$ = 3.0 ± 0.3 (stat.) $^{+0.7}_{-1.1}$ (syst.) μb/sr and $\Gamma_{\Lambda p}/\Gamma_{\Sigma^0p}$ = 0.92 $^{+0.16}_{-0.14}$ (stat.) $^{+0.60}_{-0.42}$ (syst.), respectively. Furthermore, there is additional uncertainty for the differential cross section $d\sigma/d\Omega_{K^-pp\to\Sigma^0p}$ of $^{+1.3}_{-0.0}$ μb/sr arising from the discrepancy of the proton detection efficiency of the $p(\pi^+, K^+)\Sigma^+$ analysis as described in Sec. 4.5.

5.2.7 Discussion on proton coincidence spectra

We compare the "K^-pp"-like structure with the elementary cross sections. A comparison of the double differential cross sections between the inclusive and "K^-pp"$\rightarrow \Sigma^0(\Lambda)p$ spectra is shown in Figure 5.27. A differential cross section of the Y^* region (Region I Ⅱ) of the inclusive spectrum is evaluated to be $d\sigma/d\Omega_{Y^*} = 168.6 \pm 6.3$ μb/sr. Here, the elementary differential cross section of the $\Lambda(1405)$ production was found to be 36.9 ± 1.8 μb/sr, which was measured in Ref. [19]. Thus, the production probabilities of the "K^-pp"-like structure, which decays to $\Sigma^0 p$ mode, for the inclusive differential cross section of the Y^* region and the elementary differential cross section of $\Lambda(1405)$ are found to be $(d\sigma/d\Omega_{K^-pp\rightarrow\Sigma^0 p})/(d\sigma/d\Omega_{Y^*}) = 1.8 \pm 0.2$ (stat.) $^{+0.4}_{-0.7}$ (syst.) % and $(d\sigma/d\Omega_{K^-pp\rightarrow\Sigma^0 p})/(d\sigma/d\Omega_{\Lambda(1405)}) = 8.2 \pm 1.0$ (stat.) $^{+1.9}_{-3.0}$ (syst.) %. These values correspond to the probabilities of the "K^-pp"$\rightarrow \Lambda p$ mode of about 1.6% for the $d\sigma/d\Omega_{Y^*}$ and about 7.5% for the $d\sigma/d\Omega_{\Lambda(1405)}$. Since we only measured the mass spectra of the "K^-pp"-like structure for the $\Sigma^0 p$ and Λp modes, we can evaluate the lower limit of the sticking probability of the $\Lambda(1405)p \rightarrow$"$K^-pp$" reaction to be $\gtrsim 15.7\%$, where we assume the "K^-pp"-like structure can be produced only from the $\Lambda(1405)$ doorway process. This lower limit of the sticking probability is large compared with a theoretical value about 1% [69]. This discrepancy might originate from the incorrect assumption that the K^-pp bound state is formed through the $\Lambda(1405)$ doorway K^-pp formation as the $\Lambda(1405)$ doorway and/or the nature of "K^-pp"-like structure, which might be not the simple K^-pp bound state but the other possibilities like a dibaryon as $\pi\Lambda N$–$\pi\Sigma N$ bound states [2], a $\Lambda^* N$ bound states [3], and a lower $\pi\Sigma N$ pole of the K^-pp [113].

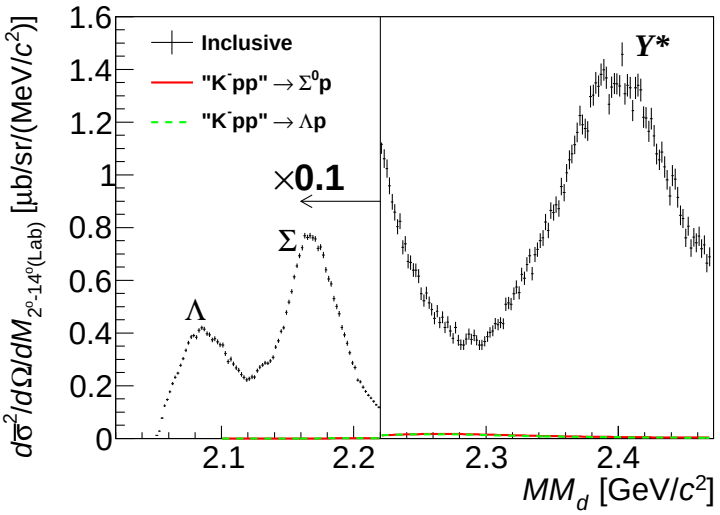

Figure 5.27: Comparison of the double differential cross sections between the inclusive spectrum and "K^-pp"-like structure. The black crosses show the obtained inclusive spectrum. The red line and green dashed-line show the mass spectrum of the "K^-pp"-like structure, which decays to the $\Sigma^0 p$ and Λp modes respectively. In the $MM_d <$ 2.22 GeV/c^2 region, these spectra were multiplied by 0.1.

Next, we try to understand the coincidence probability spectrum of the one-proton coincidence analysis shown in Figure 5.19 (c) with the evaluated K^-pp mass distribution of $f(MM_d)$. By using the mass distribution for the "K^-pp"-like structure and the double differential cross section of the inclusive (π^+, K^+) process $\frac{d^2\sigma}{d\Omega dMM_d}(MM_d)_{Inclusive}$ shown in Figure 5.1 (b), we can obtain the coincidence probability spectrum as shown in Figure 5.28 as a plot colored in magenta, which is calculated as,

$$R_p(MM_d) = \frac{C \times f(MM_d) \times \eta_{1p}(MM_d)}{(\frac{d^2\sigma}{d\Omega dMM_d}(MM_d))_{Inclusvie}}, \tag{5.11}$$

where C is the normalization constant, and $\eta_{1p}(MM_d)$ is the detection efficiency of a proton in the middle segments of the RCA (Seg2, 5) shown in Figure 5.18 (b). A blue line in Figure 5.28 is an assumed flat component representing the conversion processes and the $\pi^\pm$ contamination due to the misidentification of $\pi^\pm$ in RCA. Red points with error bars in Figure 5.28 are the sum of the magenta points and blue line. The normalization constant C and the amplitude of the flat component (blue line) were adjusted to minimize the differences between the black and red points. Thus, the obtained one proton coincidence probability spectrum of the broad enhanced region could be reproduced by the "K^-pp" and flat background.

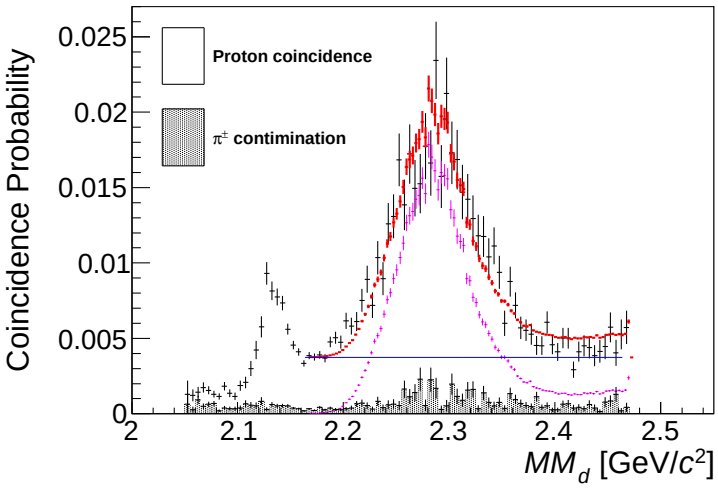

Figure 5.28: The one proton coincidence probability spectrum of the middle segment of RCA same as Figure 5.19 (c) with the interpreted spectrum shown in colored spectra. A magenta spectrum was obtained from the Eq. 5.11 corresponding to the component of the "K^-pp"-like structure. A blue line indicated the flat component representing the conversion processes and $\pi^\pm$ contamination. Red points with error bars are the sum of the magenta points and blue line.

What is the nature of the "K^-pp"-like structure? Since we used the $\pi^+ d \rightarrow K^+$ "K^-pp", "K^-pp" $\rightarrow \Sigma^0(\Lambda)\, p$ reaction, the "K^-pp"-like structure should be strangeness -1 and baryon number $B = 2$, so that the hyper charge $Y = 1$. The K^-pp is theoretically considered as the $J^P = 0^-$, where a K^- couple with a spin-singlet ($S = 0$) p-p pair in S-wave ($L = 0$). The possible theoretical interpretation as a $\Lambda^* p$ bound state also predicted to be $J^P = 0^-$ for the bound state [3]. There is also a theoretical prediction of a dibaryon as $\pi\Lambda N$–$\pi\Sigma N$ bound state, whose quantum number is $(Y, I, J^P) = (1, 3/2, 2^+)$ [2]. However, from the isospin point of view, the isospin of the system should be 1/2 not 3/2, because we have observed the Λp mode.

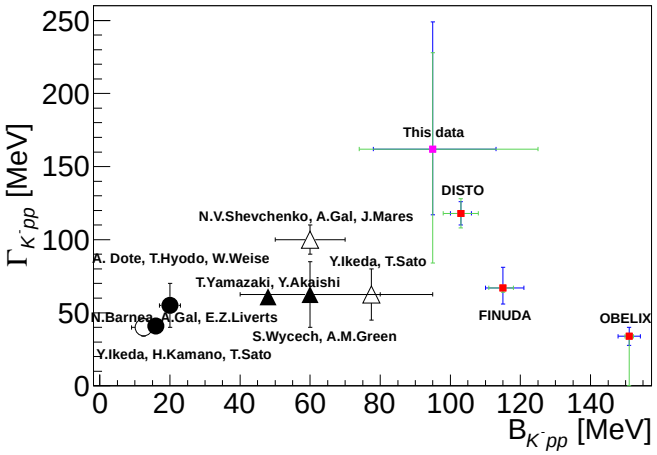

Figure 5.29: Comparison of the binding energy and width of the K^-pp. The calculated binding energy and width using the chiral SU(3)-based energy dependent potentials are shown with circles and the ones calculated with the energy independent potentials are indicated with triangles (same as Figure 1.15). The experimental values evaluated from the FINUDA [43], DISTO [46] and OBELIX [49] experiments are indicated with red squares. The values obtained from this data are shown with a magenta square. For the experimental values, the statistical and systematic errors are shown with the blue and green lines, respectively.

Our obtained mass corresponding to the K^-pp binding energy of about 100 MeV and broad width are not inconsistent with the values evaluated from the FINUDA and DISTO experiment within the error as shown in Figure 5.29. However, theoretical calculation for the K^-pp is difficult to reproduce such a deep binding energy about 100 MeV. In this view, recently Maeda, Akaishi and Yamazaki reported an interesting study [114]. They studied some kaonic nuclei such as the K^-pp with the phenomenological $\bar{K}N$ potential [1, 40] using the Faddeev and Faddeev-Yakubovsky method. They conducted an analysis on the effect of the partial restoration of chiral symmetry on the $\bar{K}N$ interaction on the basis of the "clearing QCD vacuum" model of Brown, Kubodera and Rho [115]. Finally, they pointed out that the renormalized interaction strength of $\bar{K}N$ system due to the partial restoration of the chiral symmetry can reproduce such a large K^-pp binding energy about 100 MeV. There is also an interesting theoretical study,

which was reported by Dóte, Inoue and Myo recently [113]. They proposed a new calculation method where the coupled-channel complex scaling method and the Feshbach projection were combined, and applied it to the K^-pp system. The evaluated binding energy of the K^-pp using the chiral SU(3)-based energy dependent potential was about 27 MeV. On the other hand, when they calculated using NRv2c potential (one of the chiral SU(3)-based energy dependent potentials) they always obtained another quasi self-consistent solution corresponding to the $\bar{K}NN$ resonance near the $\pi\Sigma N$ threshold, which was equivalent of the K^-pp binding energy of about 100 MeV, with large decay width. Those quasi-consistent solutions are considered as related to the lower pole of $\Lambda(1405)$, while the solutions described above must be related to the higher pole. In other words, the K^-pp might have the double pole structure as same as the $\Lambda(1405)$. These theoretical suggestions seem to be interesting to understand the obtained "K^-pp"-like structure.

The branching fraction of the K^-pp bound state of $\Gamma_{\Lambda p}/\Gamma_{\Sigma^0 p}$ was discussed from a theoretical point in Ref. [116]. In this paper, it was found that the branching fraction of these modes strongly depends on the ratio between the couplings $\Lambda(1405)$-$\bar{K}N$ and $\Lambda(1405)$-$\pi\Sigma$. A larger $\Lambda(1405)$-$\bar{K}N$ coupling leads to an enhancement of Λp decay mode. Furthermore, this ratio was predicted to be $\Gamma_{\Lambda p}/\Gamma_{\Sigma^0 p} \sim 1.2$ using the chiral unitary approach. The predicted value is not in-consistent with the obtained value within the error.

In the next step, further experiment with high statistics and a larger acceptance detector system is important to reduce both statistic and systematic errors and improve the sensitivities for the "K^-pp"-like structure. One of the detector systems to carry out the further experiment using the same reaction is large-acceptance Hyperon spectrometer with TPC (HypTPC) to detect the decay particles and KURAMA spectrometer to measure the K^+ momenta [117]. This detector system will be used by the J-PARC E42 experiment to search for the H-dibaryon at J-PARC K1.8 beam line [117]. Since HypTPC ($\sim 2\pi$) and KURAMA spectrometer ($\sim$200 msr) have the large acceptance, we will be able to improve the statistics more than 10 times than the present experiment. Moreover, we will be able to obtain not only the missing-mass spectrum but also the invariant-mass spectra because HypTPC can measure the momenta of the decay charged particles with the magnetic system. Thus, we can measure not only the non-mesonic decay modes such as Λp and $\Sigma^0 p$ but also the mesonic ($Y\pi p$) decay modes. In addition, we can search the origin of the obtained "shift" of the Y^* region by reconstructing the invariant-mass spectrum. After we establish the "K^-pp"-like structure in this detector system, we are going to search the further systems such as K^-ppp and K^-K^-pp by using the $^3\mathrm{He}(\pi^+, K^+)$ and $d(K^-, K^0)$ reactions.

Chapter 6

Conclusion

The strange dibaryon systems ($S = -1$, $B = 2$) beyond the octet baryon pair (ΛN, ΣN) are experimentally not well explored, yet. A recently interested system of $\bar{K}NN$ is such an example. Theoretically a bound state of K^-pp is expected to exist, but maybe a broad resonance. However, the experimental status is still not conclusive although some experimental evidences are reported.

In order to improve the situation, we have newly investigated the strange dibaryon system with the $d(\pi^+, K^+)$ reaction at the pion incident momentum of 1.69 GeV/c. The reaction can produce a broad energy range of excitation spectrum from Λ, Σ hyperons to $\Lambda(1405)$, $\Sigma(1385)$ excited hyperon resonances as well as $\bar{K}N$. The involved elementary processes of the $\pi^+ + p/n$ reactions are rather well known at this energy, so that we can fully explore exotic states in the wide energy range.

The J-PARC E27 experiment was carried out at the K1.8 beam line of the hadron experimental hall at J-PARC to search for the K^-pp bound state by using the $d(\pi^+, K^+)$ reaction at 1.69 GeV/c. In this reaction, the K^-pp is expected to be formed through the $\Lambda(1405)$ production as a doorway [69]. In this experiment, we measured the missing-mass spectrum of the $d(\pi^+, K^+)$ reaction by analyzing the incident beam π^+ and emitted K^+ momenta. Furthermore, the coincidence measurement was also performed by detecting proton(s) in order to suppress the quasi-free hyperon production processes.

We obtained the inclusive missing-mass spectrum at the laboratory scattering angle between 2° and 16° in high statistics and high energy resolution for the first time. The present data cover a wide missing-mass range from the Λ production threshold to the $\Lambda(1405)/\Sigma(1385)$ region. The overall structure was understood with a simple quasi-free picture based on the known elementary processes. However, there were two peculiar deviations from this picture. One observation is the ΣN cusp, of which mass was found to be 2130.5 $\pm$ 0.4 (stat.) $\pm$ 0.9 (syst.) MeV/c^2 with the width of $\Gamma = 5.3\ ^{+1.4}_{-1.2}$ (stat.) $^{+0.6}_{-0.3}$ (syst.) MeV. The peak position is consistent with previous measurements. Further detailed theoretical studies including the present data would reveal the information on the ΣN-ΛN coupling strength and the pole position. Another observation is that the centroid of the broad bump structure in the Y^* production region was significantly shifted to low mass side as compared with a simple quasi-free simulation, by about 32.4 ± 0.5 (stat.) $^{+2.9}_{-1.7}$ (syst.) (22.4 ± 0.4 (stat.) $^{+2.7}_{-1.7}$ (syst.)) MeV/c^2 for MM_d (MM_p) spectra. In order to clarify the origin of the peak shift, further experiments to measure

not only the missing-mass spectra but also invariant-mass spectra and theoretical studies are necessary.

We have measured the missing-mass distributions of $d^2\bar{\sigma}/d\Omega/dM$ in the $\pi^+ d \rightarrow K^+ W$, $W \rightarrow \Sigma^0(\Lambda)p$ reactions in the scattering angle between 2° and 14° for the first time. Here, the final states of $\Sigma^0 p$ and Λp were identified using the missing-mass squared M_X^2 distribution of $d(\pi^+, K^+pp)X$ reaction by measuring the two protons in the RCA. A broad enhancement have been observed in the missing-mass distribution of the $\Sigma^0 p$ mode around 2.27 GeV/c^2 corresponding to the "K^-pp"-like structure. The mass and width of the "K^-pp"-like structure were evaluated to be 2275 $^{+17}_{-18}$ (stat.) $^{+21}_{-30}$ (syst.) MeV/c^2 and 162 $^{+87}_{-45}$ (stat.) $^{+66}_{-78}$ (syst.) MeV, respectively, by fitting with the relativistic Breit Wigner function. These obtained mass and width are not inconsistent with the values evaluated from the FINUDA and DISTO experiments within the errors, although our statistical and systematic errors are large. If the observed structure originates from the K^-pp bound state, the binding energy of the K^-pp system corresponds to be 95 $^{+18}_{-17}$ (stat.) $^{+30}_{-21}$ (syst.) MeV. Such a large binding energy together with a large width is difficult to reproduce in the present theoretical models. The other possibilities like a dibaryon as $\pi\Lambda N$–$\pi\Sigma N$ bound states [2], a $\Lambda^* N$ bound states [3], and a lower $\pi\Sigma N$ pole of the K^-pp [113] might be considered as alternatives. In this view, the isospin of the "K^-pp"-like structure should be 1/2 not 3/2, while a dibaryon as $\pi\Lambda N$–$\pi\Sigma N$ bound state [2] is expected to be isospin $I = 3/2$. Furthermore, we have measured the branching fraction between the Λp and $\Sigma^0 p$ decay modes of the "K^-pp"-like structure to be $\Gamma_{\Lambda p}/\Gamma_{\Sigma^0 p} = 0.92\ ^{+0.16}_{-0.14}$ (stat.) $^{+0.60}_{-0.42}$ (syst.), for the first time. The obtained branching fraction is not in-consistent with the theoretically predicted value of $\Gamma_{\Lambda p}/\Gamma_{\Sigma^0 p} \sim 1.2$ [116] using the chiral unitary approach within the error, although our error is large. In order to reduce these errors, further experiments with higher statistic and larger acceptance detector system is important.

Acknowledgements

I would like to express my sincere gratitude to Prof. Tomofumi Nagae who is my supervisor and the spokesperson of the present experiment. He suggested me to join the experiment and gave me the opportunity to write this doctoral thesis. He always encouraged me and gave me the fruitful suggestions. The discussions with him are the irreplaceable treasure for me. But for his shrewd advice and helpful suggestions, I would have never been able to complete this work.

During doctor course, I belong to the "Research Group for Hadron Physics" at Advance Science Research Center (ASRC) of Japan Atomic Energy Agency (JAEA). I would like to deeply acknowledge Prof. Ken'ichi Imai, who is a leader of this group and suggested me to join this group. He always helped me when I was in trouble. His warm advice and sharp insight for physics were quite helpful for me.

I would like to express my thanks to Dr. Hiroyuki Fujioka. He always gave me comments about data analyses and physics. I have learned various things from him and they will help me in my life as a physicist.

I would like to thank the J-PARC E27 collaborators and all the people who worked with me. In particular, I am grateful to Dr. Atsushi Tokiyasu, who was my colleague at the graduate school. He gave me the first instruction on the experimental techniques. Moreover, I would like to thank Mr. Hiroyuki Ekawa. He worked hardly to construct and install the RCA for the present experiment. Without his efforts, it is difficult to succeed the present experiment. I also acknowledge Dr. Kotaro Shirotori and Mr. Tomonori Takahashi, who were pioneers of J-PARC K1.8 beam line groups. I have learned many experimental techniques and analysis methods from them. I wish to acknowledge Dr. Ryuta Kiuchi, Prof. Takeshi Koike, Dr. Koji Miwa, Prof. Atsushi Sakaguchi, Prof. Hirokazu Tamura, Prof. Kiyoshi Tanida, and Dr. Mifuyu Ukai. They gave me fruitful advice and suggestions based on their profound knowledge and experience. I also thanks Mr. Shuhei Hayakawa, Dr. Ryotaro Honda, Mr. Changwoo Joo, Mr. Yuki Matsumoto, Mr. Ryosuke Ota, Mr. Toshiyuki Tanaka, Mr. Takeshi Yamamoto, and Mr. Seongbae Yang. I owed the success of the present experiment to their strong help. Moreover, I could enjoy my life with them at J-PARC.

I have spent my graduate school days as a member of the "Experimental Nuclear and Hadron Physics Laboratory (NH)" in Kyoto University. I would like to acknowledge Prof. Takahiro Kawabata, Prof. Megumi Naruki, Dr. Tetsuya Murakami, Dr. Masayuki Niiyama, and Dr. Toshiyuki Gogami for the help and encouragement. I wish to express my thanks to Dr. Manabu Moritsu, Mr. Shunsuke Kanatsuki, Mr. Nobuaki Amano and Mr. Kohei Takenaka. I worked at K1.8 beam line and enjoyed the experiment with them.

I have also belonged to the "Research Group for Hadron Physics" in JAEA during the doctor course. I am grateful to Prof. Hiroyuki Sako, Prof. Toshiki Maruyama, Prof. Shoichi Hasegawa, Prof. Susumu Sato, Dr. Hwang Sanghoon, and Dr. Kenji Hosomi to give me warm advise. I also wish to thank Dr. Hitoshi Sugimura and Dr. Tong-Gyu Lee. I enjoyed the discussion and spent good days with them in Tokai.

I have joined two experiments, J-PARC E19 and E10 experiments, which were carried out at J-PARC K1.8 beam line. I acknowledge all the members of J-PARC E19 and E10 collaborations.

The present experiment was successfully carried out owing to the staffs of J-PARC and KEK. I would like to thank the Hadron beam channel group, accelerator group, and cryogenics section in J-PARC for their great efforts on stable machine operation and beam quality improvement. Especially, I would like to acknowledge Prof. Toshiyuki Takahashi and Prof. Masaharu Ieiri to plan the schedule of beam time. Moreover, I would like to thank Prof. Shigeru Ishimoto and Prof. Shoji Suzuki for the stable operation of the liquid hydrogen and deuterium target.

Finally, but not the least, I want to express my best thanks to my parents, Keiichiro Ichikawa and Junko Ichikawa. Their supports throughout my 28 years life led my dream come true.

Appendix A

BH1 filter tracking

In finding the BC1, 2 track, we applied the hit position gate for each layer by checking consistency of hit position with the BH1 hit segment (BH1Filter) as Figure A.1. When there were multi-hits in BH1 segment, the true hit segment which has the proper timing was selected by requiring the least |Beam TOF| segment. For example, the hits within the red lines in Figure A.1 were included to the track candidates. Figure A.2 shows the typical hit position gate for BH1Filter. In this case, it is shown that the hit position gate of BC1-X layer with the BH1 Seg5 hit. Moreover, the hit profile of this layer under the low rate ($\sim$10k pion/spill) and the high rate ($\sim$3.5M pion/spill) beam condition are also shown in the black and red line, respectively. Here, the black and red spectrum was required the single hit in BH1 Seg5 and at least one hit in BH1 Seg5, respectively. Thus, the BH1Filter helps to search the true track which made the trigger with a good time resolution of BH1, 2 and improve the single track efficiency.

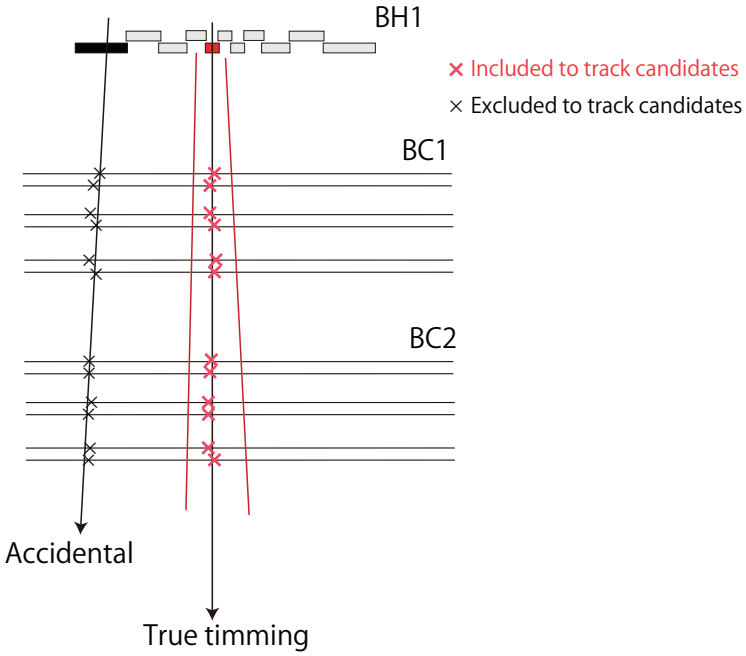

Figure A.1: Schematic view of BH1Filter. The hits within the red line gate were included to the track candidates.

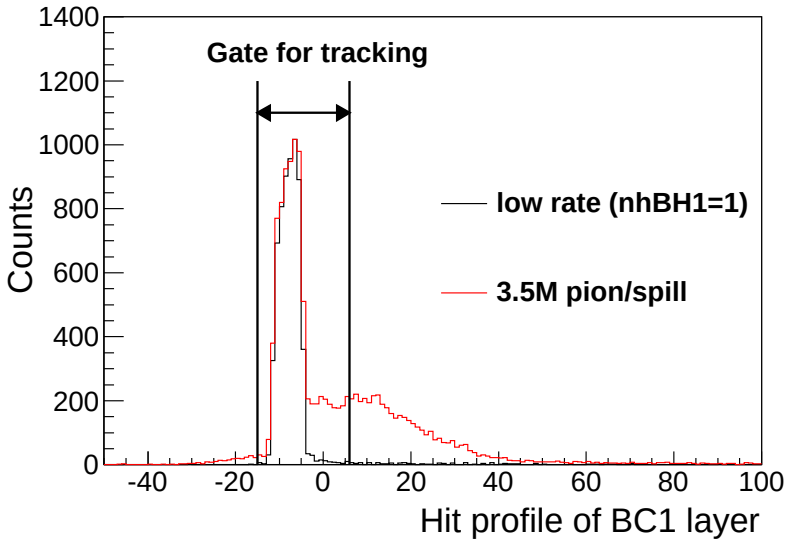

Figure A.2: Typical hit position gate of BH1Filter tracking. The hit profile of BC1-X layer of each condition is also shown. See the text for the detail.

Appendix B

Accuracy of time offset of RCA

The time offset for each segment of RCA was adjusted by using the π^+ peak from the $\Sigma^+ \rightarrow \pi^+ n$ decay in the $\pi^+ d \rightarrow K^+ \Sigma^+ X$ reaction described in Sec. 4.2. The accuracy of the time-offset adjustment was studied by using the two protons coincidence event. As described in Sec. 5.2.4, when we select the missing-mass region of $2.1 < MM_d < 2.22$ GeV/c^2, the almost all component of the final state of the W in the $\pi^+ d \rightarrow K^+ W$ reaction should be Λp. Thus, the mass-square spectrum of M_X^2 of the $d(\pi^+, K^+ pp)X$ reaction of this missing-mass region should sit on the π^- region.

In this study, we additionally applied the time offset of (-0.30, -0.15, $+0.15$, $+0.30$) ns and compared the peak position of the M_X^2 spectrum for each time offset condition with the simulated spectrum. Figure B.1 (a, b, c, d, e) show the obtained M_X^2 spectrum for the missing-mass region of $2.1 < MM_d < 2.22$ GeV/c^2 with the additional time offset of (-0.30, -0.15, 0.00, $+0.15$, $+0.30$) ns, respectively. The peak position of the M_X^2 spectrum for each time-offset condition was evaluated by fitting with the Gaussian function as shown in red lines in Figure B.1. Thus, the peak position of the M_X^2 spectrum decreases as the time-offset parameter is increased. The simulated M_X^2 spectrum for the Λp final state mode is shown in Figure B.1 (f). The obtained peak position for each time offset condition is summarized in Figure B.1 (g), where the peak position of the simulated spectrum is indicated with the black line. Therefore, the obtained peak position of the M_X^2 spectrum without additional time-offset parameter is consistent with the simulation within the error bar. Moreover, we found that the accuracy of the time-offset parameter of RCA was less than 0.1 ns.

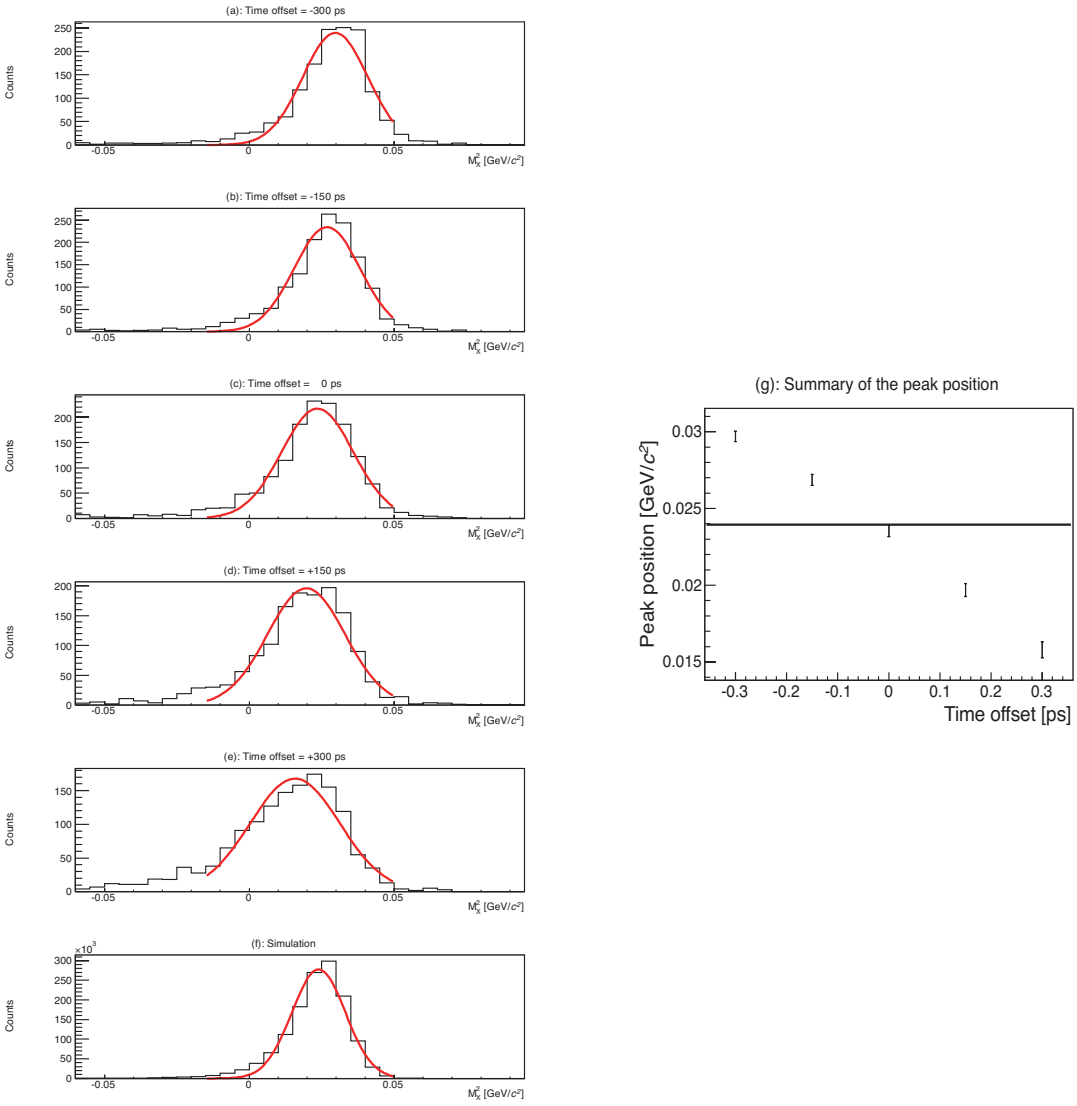

Figure B.1: (a, b, c, d, e) The obtained M_X^2 spectrum for the missing-mass region of $2.1 < MM_d < 2.22$ GeV/c^2 with the additional time offset of (-0.30, -0.15, 0.00, $+0.15$, $+0.30$) ns. (f) The simulated M_X^2 spectrum for the Λp final state mode. These spectra was fitted with the Gaussian function as the red lines. (g) The summary of the peak position of M_X^2 spectrum obtained from the Gaussian fitting for each time-offset condition. The peak position of the simulated spectrum is shown with the black line.

Appendix C

ΣN cusp for two-proton coincidence analysis

The obtained double differential cross section of the Λp final state mode evaluated from two-proton coincidence events has a large component around 2.13 GeV/c^2 as shown in Figure 5.24 (a). It is interpreted as the ΣN cusp and the conversion process of $\Sigma N \to \Lambda p$. Figure C.1 (α) show an enlarged view around 2.13 GeV/c^2 when we select the forward scattering angle of $\theta_{\pi K(Lab)} = 2°$–$8°$. Note that the Λp spectrum around 2.13 GeV/c^2 does not depend on the final state identification because almost all of the component around this low missing-mass region is Λp mode.

In Figure C.1 (α), we notice two prominent components as the ΣN cusp and the conversion process of $\Sigma N \to \Lambda p$. We fitted with the Lorentzian function folded with the resolution of 1.4 MeV/c^2 in σ for the cusp (green line) and a Gaussian function for the $\Sigma N \to \Lambda p$ conversion (blue line). The total fitting function is also shown in a red line. In this fitting, the parameters of the Lorentzian function of the peak position and the width as well as the differential cross section $(d\sigma/d\Omega)$ were set as the values obtained from the fitting of the inclusive spectrum described in Sec. 5.1.3. Thus, the ΣN cusp signal in two-proton coincidence analysis can be understood by the result of the inclusive analysis.

The similar structure, ΣN cusp and $\Sigma N \to \Lambda p$ conversion, was observed a past experiment [109]. In this experiment, they also used the $d(\pi^+, K^+)$ reaction, although the incident beam momentum was 1.4 GeV/c (our beam momentum is 1.69 GeV/c). They measured the missing-mass spectrum using the magnetic spectrometer with the multiplicity counter surrounding the deuterium target. The observed missing-mass spectra by requiring the multiplicity 1, 2 and 3 are shown in Figure C.1 (a), (b) and (c), respectively. The spectra with multiplicity 1 and 3 (Figure C.1 (a) and (c)) can compare with our inclusive and two proton coincidence Λp spectrum, respectively. The missing-mass distributions, which corresponds to be ΣN cusp and $\Sigma N \to \Lambda p$ conversion, between our Λp spectrum (Figure C.1 (α)) and their multiplicity 3 spectrum (Figure C.1 (c)) are similar. Thus, we consider that our obtained Λp spectrum around this low missing-mass region is reasonable.

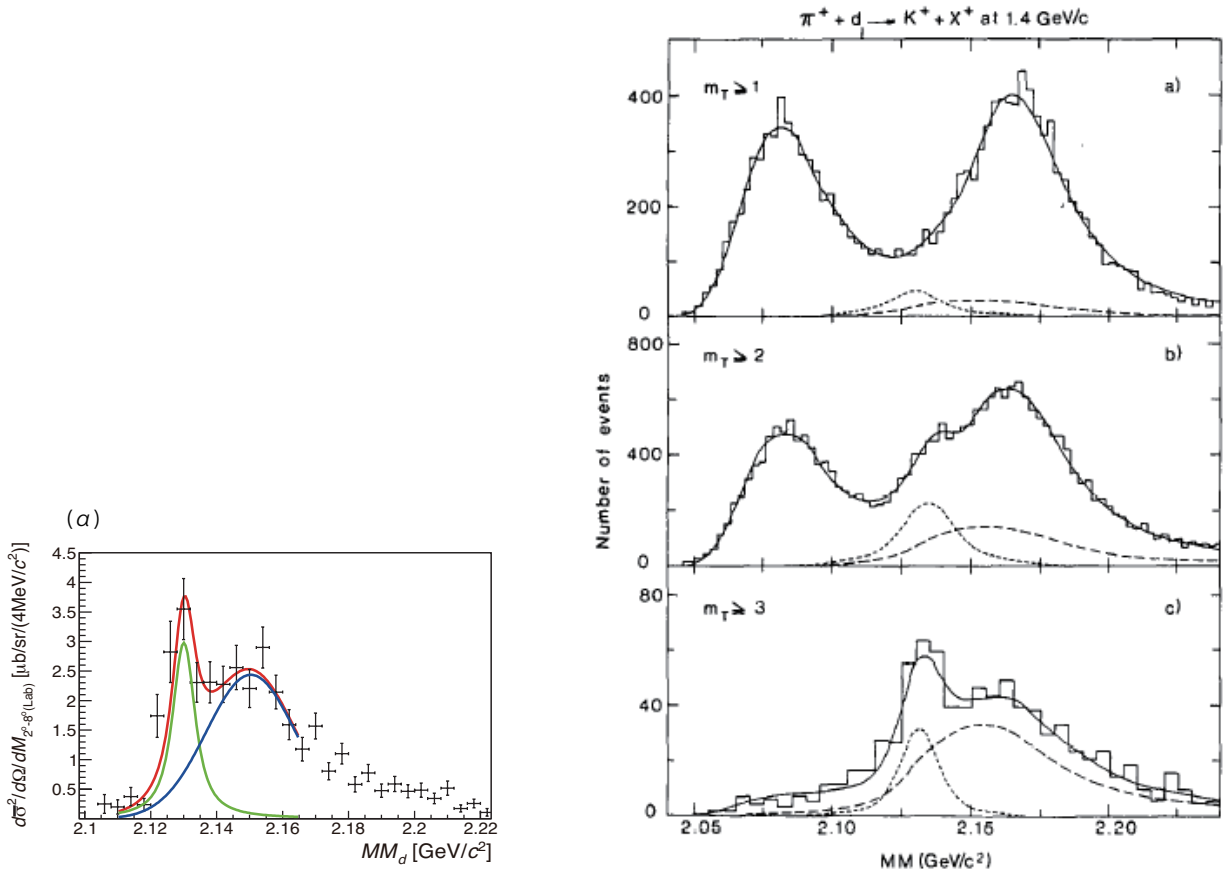

Figure C.1: (α) The double differential cross section for the Λp final state mode around 2.13 GeV/c^2 for the forward scattering angle of $\theta_{\pi K(Lab)} = 2°$–$8°$. This spectrum was fitted with a Lorentzian function folded with the resolution of 1.4 MeV/c^2 in σ for the ΣN cusp (green line), and a Gaussian function for the $\Sigma N \rightarrow \Lambda p$ conversion (blue line). The total fitting function is also shown in the red line. (a, b, c) are the missing mass spectra by requiring the multiplicity 1, 2 and 3, respectively, of the past experiment taken from Ref. [109]. The multiplicity 1 and 3 spectra correspond to the our inclusive and Λp final state spectra, respectively. In this reference, the narrow peak around 2.13 GeV/c^2 shown in dotted-line was interpreted as a resonance, which is understood as the ΣN cusp nowadays, a broad peak around 2.15 GeV/c^2 indicated in dashed-line was taken into account as the component of $\Sigma N \rightarrow \Lambda p$ conversion.

Appendix D

Two-proton coincidence analysis using the E_X spectrum

In order to check the validity of this final state determination method of the two-proton coincidence analysis, we fitted not only missing-mass squared M_X^2 but also missing energy E_X spectra of the $d(\pi^+, K^+pp)X$ reaction. In this appendix, we show the two-proton coincidence analysis result by using the E_X spectrum in the $d(\pi^+, K^+pp)X$ reaction to identify the final state for the systematic study. Figure D.1 shows the missing energy spectrum of E_X for each MM_d region. The obtained data is indicated in black points with error bars, whose points are after subtraction of the $\pi^\pm$ contamination fraction. The template fits results for the Λp, $\Sigma^0 p$ and $Y\pi p$ modes are also shown in the figure with colored dashed-lines. These templates were constructed by the simulation with the same assumption of Figure 5.21. As shown in Figure D.1, the separations of the templates between Λp and $\Sigma^0 p$ modes seems to be worse than the case of M_X^2 spectra (Figure 5.21). Thus, the result estimated from the M_X^2 is used for the main analysis.

From this E_X template fit, we also evaluated the double differential cross section using the same analysis scheme described in Sec. 5.2.5. The double differential cross sections for the Λp and $\Sigma^0 p$ modes estimated from the fit of E_X spectrum are shown in Figure D.2 (a) and (b) respectively. In the systematic error evaluation, we took into account the ambiguity for the final state determination method.

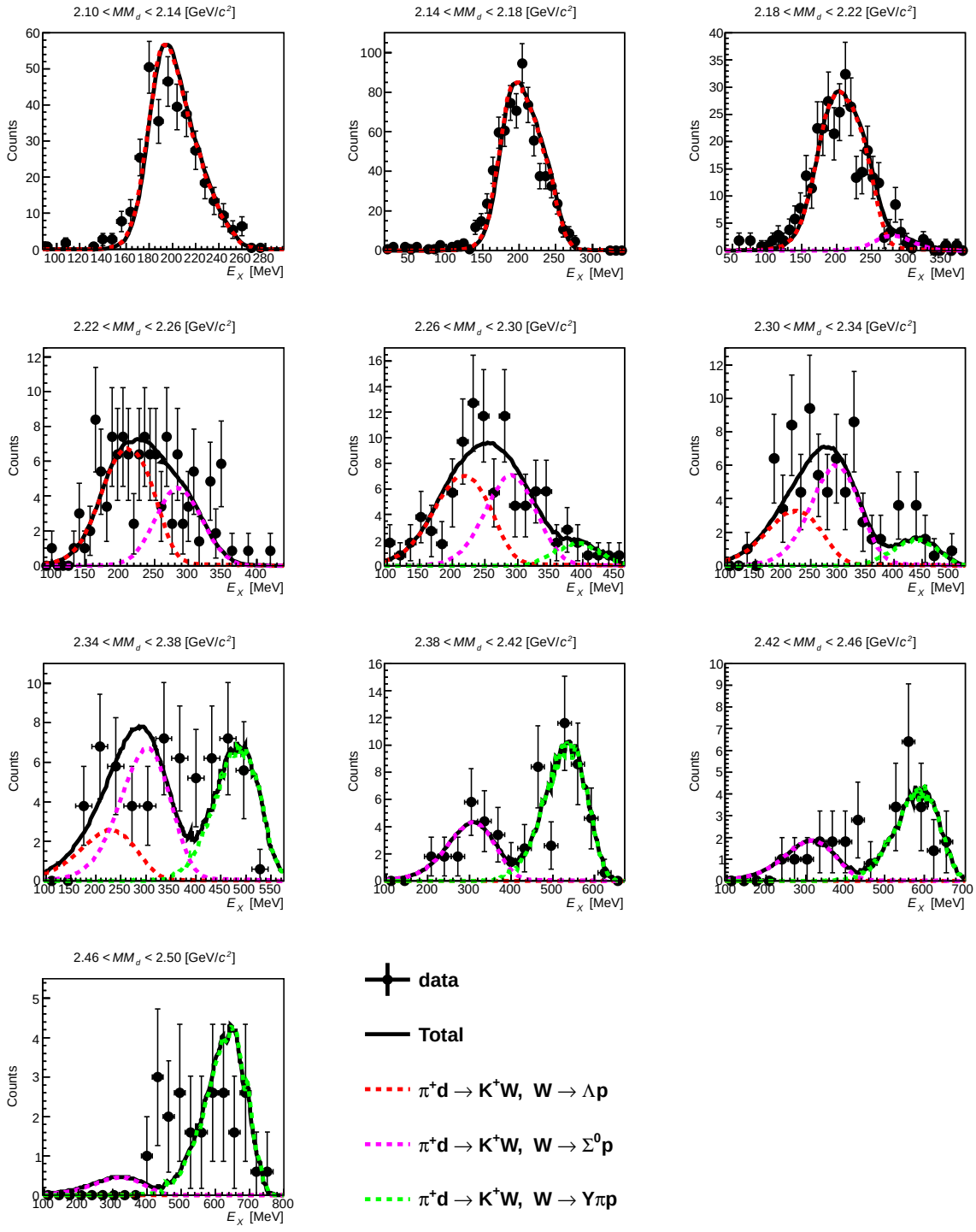

Figure D.1: Energy spectra of X obtained from the two proton coincidence events in the reaction of the $d(\pi^+, K^+pp)X$. Each spectrum shows the energy of X for the different MM_d region shown in the figure. The spectra were fitted with three components of Λp (red dashed-line), $\Sigma^0 p$ (magenta dashed-line) and $Y\pi p$ (green dashed-line) modes same as Figure 5.21. This fitting was carried out to check the systematic ambiguity of this final-state determination method.

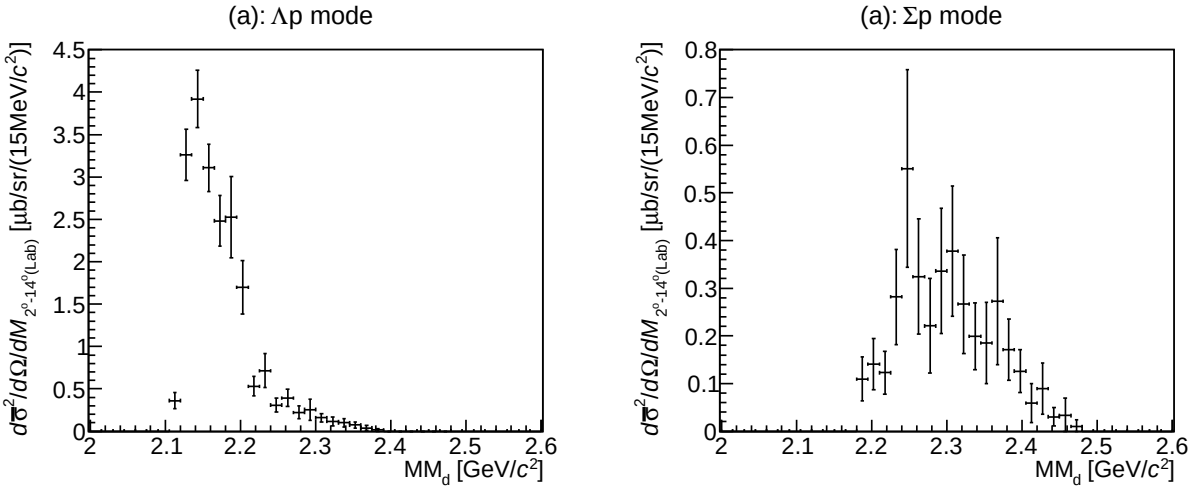

Figure D.2: The double differential cross section for the Λp (a) and $\Sigma^0 p$ (b) final state modes estimated from the fitting of E_X as shown in Figure D.1. These spectra are obtained from the two protons coincidence events.

Bibliography

[1] Y. Akaishi and T. Yamazaki, Phys. Rev. C **65**, 044005 (2002).

[2] H. Garcilazo and A. Gal, Nucl. Phys. A **897**, 167 (2013).

[3] T. Uchino, T. Hyodo and M. Oka, Nucl. Phys. A **868**, 53 (2011).

[4] P.K. Saha *et al.*, Phys. Rev. C **70**, 044613 (2004).

[5] A.D. Martin, Nucl. Phys. **B179**, 33 (1981).

[6] S. Deser, M. Goldberger, K. Baumann and W.E. Thirring, Phys. Rev. **69**, 774 (1954).

[7] T. Trueman, Nucl. Phys. **26**, 57 (1961).

[8] M. Iwasaki *et al.*, Phys. Rev. Lett. **78**, 3067 (1997).

[9] G. Beer *et al.*, Phys. Rev. Lett. **94**, 212302 (2005).

[10] M. Bazzi *et al.*, Phys. Lett. **B704**, 113 (2011).

[11] Y. Ikeda, T. Hyodo and W. Weise, Phys. Lett. **B706**, 63 (2011).
Y. Ikeda, T. Hyodo and W. Weise, Nucl. Phys. A **881**, 98 (2012).

[12] M. Mai and U.-G. Meissner, Nucl. Phys. A **900**, 51 (2013).

[13] A. Cieplý and J. Smejkal, Nucl. Phys. A **881**, 115 (2012).

[14] Z.-H. Guo and J.A. Oller, Nucl. Phys. Rev. C **87**, 035202 (2013).

[15] T. Hyodo, Nucl. Phys. A **914**, 260 (2013).

[16] N. Isgur, G. Karl, Nucl. Phys. Rev. D **18**, 4187 (1978).

[17] R.H. Dalitz, T.C. Wong and G. Rajasekaran, Phy. Phys. **153**, 1617 (1967).

[18] D. Jido *et al.*, Nucl. Phys. A **725**, 181 (2003).

[19] D.W. Thomas *et al.*, Nucl. Phys. **B56**, 15 (1973).

[20] R.J. Hemingway, Nucl. Phys. B **253**, 742 (1985).

[21] I. Zychor *et al.*, Phys. Lett. **B660**, 167 (2008).

[22] G. Agakishiev *et al.*, Phys. Rev. C **85**, 035203 (2012).

[23] J.K. Ahn *et al.*, Nucl. Phys. A **721**, 715 (2003).

[24] M. Niiyama *et al.*, Phys. Rev. C **78**, 035202 (2008).

[25] K. Moriya *et al.*, Phys. Rev. C **87**, 035206 (2013).

[26] S. Okada *et al.*, Phys. Lett. **B653**, 387 (2007).

[27] M. Bazzi *et al.*, Phys. Lett. **B714**, 40 (2012).

[28] C. Batty, E. Friedman and A. Gal, Phys. Rept. **287**, 385 (1997).

[29] T. Wass, N. Kaiser and W. Weise, Phys. Lett. **B365**, 12 (1996).

[30] A. Cieplý, E. Friedman, A. Gal and J. Mareš, Nucl. Phys. A **696**, 173 (2001).

[31] A. Ramos and E. Oset, Nucl. Phys. A **671**, 481 (2000).

[32] J. Mareš, E. Friedman and A. Gal, Nucl. Phys. A **770**, 84 (2006).

[33] N. Barnea and E. Friedman, Phys. Rev. C **75**, 022202(R) (2007).

[34] E. Friedman and A. Gal, Nucl. Phys. A **899**, 60 (2013).

[35] M. Agnello *et al.*, Phys. Lett. **B698**, 219 (2011).

[36] A. Cieplý, E. Friedman, A. Gal and V. Krejčiřík, Phys. Lett. **B698**, 226 (2011).

[37] T. Kishimoto *et al.*, Prog. Theor. Phys. **118**, 181 (2007).

[38] V. Magas *et al.*, Phys. Rev. C **81**, 024609 (2010).

[39] T. Kishimoto, Phys. Rev. Lett. **83**, 4701 (1999).

[40] T. Yamazaki and Y. Akaishi, Phys. Lett. **B535**, 70 (2002).

[41] M. Sato *et al.*, Phys. Lett. **B659**, 107 (2008).

[42] H. Yim *et al.*, Phys. Lett. **B688**, 43 (2010).

[43] M. Agnello *et al.*, Phys. Rev. Lett. **94**, 212303 (2005).

[44] V. Magas, E. Oset, A. Ramos and H. Toki, Phys. Rev. C **74**, 025206 (2006).

[45] T. Nagae, Nucl. Phys. A **881**, 141 (2012).

[46] T. Yamazaki *et al.*, Phys. Rev. Lett. **104**, 132502 (2010).

[47] P. Kienle *et al.*, Eur. Phys. J. A **48**, 183 (2012).

[48] G. Bendiscioli *et al.*, Nucl. Phys. A **789**, 222 (2007).

[49] G. Bendiscioli *et al.*, Eur. Phys. J. A **40**, 11 (2009).

[50] S. Piano *et al.*, Nucl. Phys. A **835**, 35 (2010).

[51] A.O. Tokiyasu *et al.*, Phys. Lett. **B728**, 616 (2014).

[52] L. Fabbietti *et al.*, Nucl. Phys. A **914**, 60 (2013).

[53] G. Agakishiev *et al.*, arXiv:1410.8188.

[54] T. Hashimoto *et al.*, arXiv:1408.5637.

[55] The AMADEUS Collaboration, http://www.lnf.infn.if/sis/preprint/pdf/getfile.php?filename=LNF-07-024(IR).pdf

[56] K. Suzuki and M. Berger, Prog. Theor. Phys. Suppl, **186**, 351 (2010).

[57] N. Barnea, A. Gal and E.Z Liverts, Phys. Lett. **B712**, 132 (2012).

[58] A. Doté, T. Hyodo and W. Weise, Nucl. Phys. A **804**, 197 (2008).
A. Doté, T. Hyodo and W. Weise, Phys. Rev. C **79**, 014003 (2009).

[59] Y. Ikeda, H. Kumano and T. Sato, Prog. Theor. Phys. **124**, 533 (2008).

[60] N.V. Shevchenko, A. Gal and J. Mareš, Phys. Rev. Lett. **98**, 082301 (2007).
N.V. Shevchenko, A. Gal, J. Mareš and J. Revai, Phys. Rev. C **76**, 044004 (2007).

[61] Y. Ikeda, and T. Sato, Phys. Rev. C **76**, 035203 (2007).
Y. Ikeda, and T. Sato, Phys. Rev. C **79**, 035201 (2009).

[62] S. Wycech, and A.M. Green, Phys. Rev. C **79**, 014001 (2009).

[63] A. Gal, Nucl. Phys. A **914**, 270 (2013).

[64] A.O. Tokiyasu *et al.*, PoS **Hadron2013**, 180 (2013).

[65] Y.-L. Pan and F.L. Forman, Nucl. Phys. **B21**, 395 (1970);
Y.-L. Pan *et al.*, Phys. Rev. D **2**, 449 (1970).

[66] K. Agari *et al.*, Prog. Theor. Exp. Phys. **2012**, 02B009 (2012).

[67] K. H. Tanaka *et al.*, The technical report of the hadron experimetal facility, KEK internal 2007-1.

[68] S. Nagamiya, Prog. Theor. Exp. Phys. **2012**, 02B001 (2012).

[69] T. Yamazaki and Y. Akaishi, Phys. Rev. C **76**, 045201 (2007).

[70] M. Ikegami, Prog. Theor. Exp. Phys. **2012**, 02B002 (2012).

[71] H. Hotchi *et al.*, Prog. Theor. Exp. Phys. **2012**, 02B003 (2012).

[72] T. Koseki *et al.*, Prog. Theor. Exp. Phys. **2012**, 02B004 (2012).

[73] K. Agari *et al.*, Prog. Theor. Exp. Phys. **2012**, 02B008 (2012).

[74] K. L. Brown *et al.*, CERN 80-04 (1980).

[75] T. Takahashi *et al.*, Nucl. Phys. A **835**, 88 (2010).

[76] Digital Teslameter 151 (DTM-151), http://www.group3technology.com/meters/dtm151.php

[77] O. Sasaki and M. Yoshida, IEEE Trans. Nucl. Sci., vol **46**, 1871 (1999).

[78] Y. Igarashi IEEE Trans. Nucl. Sci., vol **52**, 2866 (2005).

[79] H. Hotchi *et al.*, Phys. Rev. C **64**, 044302 (2001).

[80] T. Fukuda *et al.*, Nucl. Instrum. Methods. A **361**, 483 (1995).

[81] EFM-3000AX, http://echo-denshi.co.jp/nmr_magnetic.htm

[82] R.W. Stotzer *et al.*, Phys. Rev. Lett. **78**, 3646 (1997).

[83] K.Miwa *et al.*, Phys. Rev. C **77**, 045203 (2008).

[84] http://www.srim.org/

[85] http://lambda.phys.tohoku.ac.jp/takahasi/TUL-8040/

[86] Y. Igarashi IEEE Trans. Nucl. Sci., vol **57**, 618 (2010).

[87] S. Morinobu, privete communication.

[88] J. Myrheim and L. Bugge, Nucl. Instr. Meth. **160**, 43 (1979).

[89] K.L. Brown, Ch. Iselin, D.C. Carey: Decay Turtle, CERN 74-2 (1974), Urs Rohrer: Compendium of Decay Turtle Enhancements.

[90] ANSYS, htpp://www.ansys.com

[91] S. Agostinelli *et al.*, Nucl. Instrum. Methods. A **506**, 250 (2003).

[92] J. Beringer *et al.* (Particle Data Group), Phys. Rev. D **86**, 01001 (2012).

[93] Y. Ichikawa *et al.*, Prog. Theor. Exp. Phys. **2014**, 101D03 (2014).

[94] D.J. Candlin *et al.*, Nucl. Phys. B **226**, 1 (1983).

[95] Phys. Lett. **B667**/1-5, 285 (2008).

[96] P. Kienle, Y. Akaishi and T. Yamazaki, Phys. Lett. **B632**, 187 (2006).

[97] R. Machleidt, K. Holinde and Ch. Elster, Phys. Rep. **149**, 1 (1987).

[98] J.C. Hart *et al.*, Nucl. Phys. **B166**, 73 (1980).

[99] O.I. Dahl *et al.*, Phys. Rev. **163**, 1430 (1967).

[100] M. Abdel-Bary *et al.*, Eur. Phys. J. A **29**, 353 (2006).

[101] A.M. Badalian, L.P. Kok, M.I. Polikarpov and Yu.A. Simonov, Phys. Rep. **82**, 31 (1982).

[102] K. Miyagawa and H. Yamamura, Phys. Rev. C **60**, 024003 (1999).

[103] T.H. Tan, Phys. Rev. Lett. **23**, 395 (1969).

[104] O. Braun *et al.*, Nucl. Phys. **B124**, 45 (1977);

[105] A. Budzanowski *et al.*, Phys. Lett. **B692**, 10 (2010).

[106] S. Abd El-Samad *et al.*. Eur. Phys. J. A **49**, 41 (2013).

[107] H. Machner *et al.*, Nucl. Phys. **A901**, 65 (2013).

[108] D. Eastwood *et al.*, Phys. Rev. D **3**, 2603 (1971).

[109] C. Pigot *et al.*, Nucl. Phys. **B249**, 172 (1985).

[110] R. Siebert *et al.*, Nucl. Phys. **A567**, 819 (1994).

[111] D.W. Davies *et al.*, Phys. Rev. D **2**, 506 (1970).

[112] Y. Ichikawa *et al.*, arXiv:1411.6708.

[113] A. Doté, T. Inoue and T. Myo, arXiv:1411.0348.

[114] S. Maeda, Y. Akaishi and T. Yamazaki, Proc. Jpn. B **89**, 418 (2013).

[115] G.E. Brown, K. Kubodera and M. Rho, Int. J. Mod. Phys. A **22**, 365 (2007).

[116] T. Sekihara, D. Jido and Y, Kanada-En'yo, Phys. Rev. C **79**, 062201(R) (2009).

[117] J.K. Ahn *et al.*, http://j-parc.jp/researcher/Hadron/en/pac_1201/pdf/KEK_J-PARC-PAC2011-06.pdf